OCS Study
BOEM 2019-009

Marine ARctic Ecosystem Study (MARES): Moorings on the Beaufort Sea shelf, 2016-2017

May 2019

Authors:
Francis K. Wiese
Carin Ashjian
Frank Bahr
Michael Fabijan
Dave B. Fissel
Rowenna D. Gryba
Jeremy Kasper
Natalie Monacci
John Nelson
Robert Pickart
Ed Ross
Kate Stafford
Daniel Torres
Chris Turner

Prepared under M14PC00008 M17PD00006
By
Stantec Consulting Services Inc.
4500 Daley Dr., Suite 100
Chantilly, VA 20151-3724

US Department of the Interior
Bureau of Ocean Energy Management
Alaska

DISCLAIMER

Study concept, oversight, and funding were provided by the US Department of the Interior, Bureau of Ocean Energy Management (BOEM), Environmental Studies Program, Washington, DC, under Contract Number M14PC00008. This report has been technically reviewed by BOEM, and it has been approved for publication. The views and conclusions contained in this document are those of the authors and should not be interpreted as representing the opinions or policies of the US Government, nor does mention of trade names or commercial products constitute endorsement or recommendation for use.

REPORT AVAILABILITY

To download a PDF file of this report, go to the US Department of the Interior, Bureau of Ocean Energy Management Data and Information Systems webpage (http://www.boem.gov/Environmental-Studies-EnvData/), click on the link for the Environmental Studies Program Information System (ESPIS), and search on 2019-009. The report is also available at the National Technical Reports Library at https://ntrl.ntis.gov/NTRL/.

CITATION

Wiese FK, Ashjian C, Bahr F, Fabijan M, Fissel DB, Gryba RD, Kasper J, Monacci N, Nelson J, Pickart R, Ross E, Stafford K, Torres D, Turner C. 2019. Marine Arctic Ecosystem Study (MARES): Moorings on the Beaufort Sea shelf, 2016-2017. Anchorage (AK): US Department of the Interior, Bureau of Ocean Energy Management. OCS Study BOEM 2019-009. xx p.

ABOUT THE COVER

[Optional for cover graphic/photo credit]

ACKNOWLEDGMENTS

We would like to acknowledge the support provided by the Stantec MARES team: Diane Ingraham, Jeff Green, Cathy Finnie, Barry Keough, and Melissa Gandy. We would like to also acknowledge COR, Heather Crowley, and the cruise support provided by H. Melling and the crew of the *CCGC Sir Wilfrid Laurier*.

Contents

LIST OF FIGURES

LIST OF TABLES

LIST OF ABBREVIATIONS AND ACRONYMS

ADCP	Acoustic Doppler Current Profilers
AZFP	Acoustic Zooplankton and Fish Profiler
AURAL	Autonomous Underwater Recorder for Acoustic Listening
BOEM	Bureau of Ocean Energy Management
CSE	Council of Science Editors
CTD	conductivity, temperature, depth
DOI	US Department of the Interior
ESP	Environmental Studies Program
ESPIS	Environmental Studies Program Information System
HTC	Hunters and Trappers Committee
IPS	Ice Profiling Sonar
MARES	Marine Arctic Ecosystem Study
MMP	McLane Moored Profiler
PAR	Photosynthetically Active Radiation
QA/QC	quality assurance/quality control
SAMI	Submersible Autonomous Moored Instrument
SUNA	Ultraviolet Nitrate Analyzer

1 OVERVIEW

1.1 BACKGROUND

The Department of the Interior, Bureau of Ocean Energy Management (BOEM) and its partners, Office of Naval Research (ONR), National Oceanographic Partnership Program (NOPP), Shell Oil Company, US Artic Research Commission (USARC), US Coast Guard (USCG), seek to advance knowledge of the arctic marine ecosystem. The Marine ARctic Ecosystem Study (MARES) arose from increased attention on climate change, energy development, and related sustainability issues in the arctic. Results from this study are intended to inform government, industry, and communities on regulatory needs, operational challenges and resource management, and provide important context for economic development, environmental protection, sustainability of local communities, and health and safety.

The focus area of MARES is the eastern Beaufort Sea shelf from Kaktovik to the Mackenzie Delta coastline to a depth of 1,000 m. The overarching scientific goal of MARES, as initially envisioned, was to increase our understanding of the impact of physical drivers (ocean, ice, atmosphere) on the trophic structure and function of the marine ecosystem on the Beaufort shelf with special attention to the implications on marine mammals and local communities. The intent was to implement an integrated, multidisciplinary study combining retrospective analyses, field studies, modeling, and synthesis spanning atmosphere, ice, physical, chemical, and biological oceanography from benthos to fish, marine mammals, and people.

1.2 BIOPHYSICAL AND CHEMICAL PROGRAM

The Biophysical and Chemical Program supports the broader MARES objectives through three linked components:

1. *Moving platforms*: Collect, describe and analyze physical, biological, and chemical observations collected by a glider in the same region of the Eastern Beaufort Sea as the mooring deployment
2. *Benthic sampling:* Sample and analyze sediment samples for benthic carbon near the moorings that transected the Mackenzie River-Yukon Shelf
3. *Moored platforms:* Deploy a high-resolution cross-shelf mooring array for two years to provide a continuous biophysical and chemical time series, as well as calibration data for the glider sensors.

Components 1 and 2 have previously been reported (Wiese et al. 2018) and include the set up and deployment of the Year 1 mooring array in October 3–7, 2016 (Figure 1). The present report focuses on the recovery and demobilization of the previously deployed moorings, redeployment of the Year 2 mooring array, and preliminary data analysis of Year 1 data. As such, the work described here represents a collaborative effort between Stantec, Kavik-Stantec, ASL Environmental Sciences (ASL), the Woods Hole Oceanographic Institution (WHOI), the University of Alaska Fairbanks (UAF), the University of Washington (UW), AXIOM Data Science, SeaStar Biotech, and Canadian Department of Fisheries and Oceans (DFO).

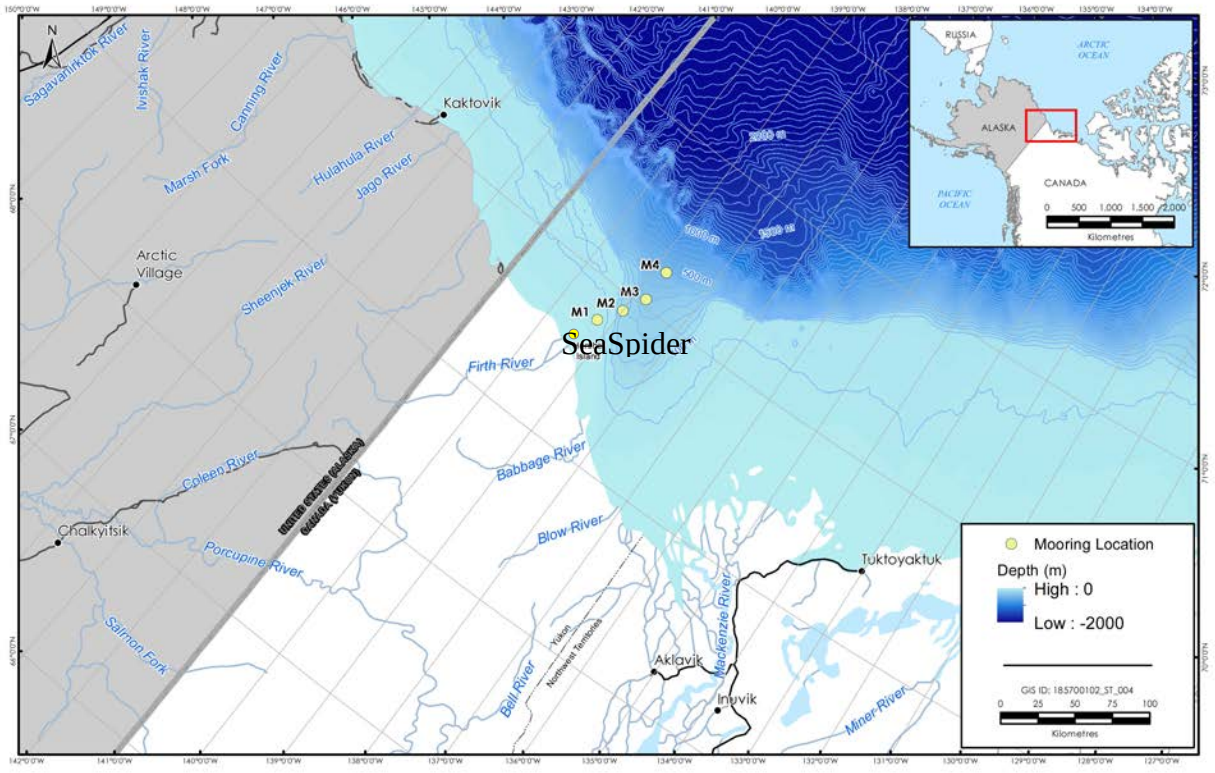

Figure 1. Location of the MARES Year 1 mooring array.

1.3 GOALS AND OBJECTIVES

The specific goals and objectives of this MARES component were to:

- Retrieve moorings deployed in the eastern Beaufort Sea in October 2016
- Redeploy a mooring array to extend the data series for a second year (October 2017-2018)
- Perform appropriate quality assurance/quality control (QA/QC) on Year 1 data
- Conduct preliminary analysis and interpretation of the data (general characteristics of the data) collected during the first year of deployment to the extent possible within this budget.

Subsequent retrieval of the Year 2 moorings in 2018, integrated data analysis and synthesis across years and other MARES study components will be documented in a subsequent report.

1.4 REGIONAL SETTING

In Canada, the MARES program is entirely within the Inuvialuit Settlement Region (ISR) established in the Inuvialuit Final Agreement (IFA) through the Canadian Federal Government's 1984 "Western Arctic Claims (Inuvialuit) Settlement Act" (Department of Indian and Northern Affairs Canada, 1984).

The Environmental Impact Screening Committee (EISC) reviews projects to determine if they meet the IFA definition of development and have the potential for a significant negative environmental impact. The screening process includes feedback from and consultation with the appropriate Inuvialuit co-management bodies (e.g., Fisheries Joint Management Committee [FJMC]), Inuvialuit organizations (e.g., community Hunters and Trappers Committees [HTCs] and the Inuvialuit Game Council [IGC]), communities and government and regulatory bodies. Only after this process is complete can permitting agencies issue permits to the project. In addition, research in the Northwest Territories is permitted by the Government of the Northwest Territories through the Northwest Territories Scientist Act, administered by the Aurora Research Institute (ARI) which issues the Northwest Territories Scientific Research Licence. Issuance of this licence requires input from Inuvialuit organizations, government agencies and project approval from the EISC.

1.5 COMMUNITY CONSULTATION

EISC and ARI consultation requirements for the MARES program, being conducted in the Canadian Beaufort, were met by meeting with the Inuvialuit Game Council that represents the Inuvialuit regionally on wildlife, habitat and environmental interests and the local Hunters and Trappers Committees in the communities of Aklavik, Inuvik and Tuktoyaktuk that were potentially affected by the program (Table 1). A record of these meetings was included in the EISC and ARI applications.

In 2015 and 2016 Kavik-Stantec Inc. consulted with the IGC and HTCs. The IGC and HTCs did not have any concerns with the program and asked to be updated on the project's progress and results. Consultations in 2017 were conducted to meet ARI permit requirements and update the committees on the project. Stantec submitted a Memo to the IGC on June 9, 2017, which provided requested information on the Alaska Ocean Observing System (AOOS) and data access after completion of the program. The IGC and HTCs have requested a presentation on the program results upon its completion.

1.6 PERMITTING

Stantec and Kavik-Stantec Inc. gathered all necessary permits and permissions as outlined in the contract agreement including applicable permits from the Northwest Territories (ARI) (Table 1).

The program was conducted by adding MARES to a collaborative agreement with DFO Canada already established by ASL to conduct oceanographic research in the Canadian Beaufort Sea. Confirmation to conduct all activities under this scope were received. The EISC determined that the MARES program did not meet the definition of development, as defined under the IFA, and was therefore not subject to an environmental impact screening. With this approval, the ARI issued a Northwest Territories Scientific Research license. This license was renewed annually.

Table 1.

Consultation meetings and permits for MARES work in the Canadian Beaufort Sea.

Date	Group	Permit
Consultation Meetings		
2015-12-18	Inuvialuit Game Council	
2016-06-22	Inuvik HTC	
2016-06-23	Tuktoyaktuk HTC	
2016-06-24	Aklavik HTC	
2017-03-17	Inuvialuit Game Council	
2017-04-12	Tuktoyaktuk HTC	
2017-04-13	Aklavik HTC	
2017-04-20	Inuvik HTC	
Permits		
2016-08-02	EISC	Project pre-screening approval
2016-08-18	ARI - GNWT	Northwest Territories Scientific Research Licence
2017-01-12	ARI - GNWT	Northwest Territories Scientific Research Licence
2018-07-19	ARI - GNWT	Northwest Territories Scientific Research Licence
HTC = Hunters and Trappers Committee EISC = Environmental Impact Screening Committee ARI GNWT = Aurora Research Institute - Government of the Northwest Territories, Canada		

2 METHODS AND EQUIPMENT

2.1 MOORING RETRIEVAL ACTIVITIES

On September 19, 2017, the ASL mooring team boarded the vessel CCGS *Sir Wilfrid Laurier* at Kugluktuk, NU and mobilized replacement equipment on board in the days leading up to the mooring recovery operations. Replacement equipment was provided for many of the mooring components to allow for faster mooring turnaround and to provide additional equipment in the event of loss or damage of the recovered moorings.

A required step in the mobilization of Acoustic Doppler Current Profilers (ADCPs) was the calibration of the onboard magnetic compasses in geomagnetic field conditions that are similar to the target deployment location. This calibration was carried out at Herschel Island (69°34’11”N, 138°54’45”W) for the seven ADCPs to be deployed. In addition, a 300 kHz ADCP from M2 that was not calibrated in 2016 was, as previously planned, post-calibrated.

Recovery of the moorings that were deployed in 2016 commenced on September 27, 2017 (see Figure 2, Figure 3 and Figure 4 for the mooring configurations deployed in 2016). Rough seas and gale force winds prevented the recoveries of moorings located at sites M4, M3 and M2; however, M1 was sheltered enough to recover on September 27. Recoveries of M2, M3 and M4 were done on September 28 when weather conditions had somewhat improved. In addition to the challenging weather, the vessel also suffered from propulsion issues which prevented the captain from taking the vessel into shallow waters or near shore. This delayed recovery of the UAF SeaSpider until October 3 when these issues were resolved (see Table 2 for summary of recovery efforts).

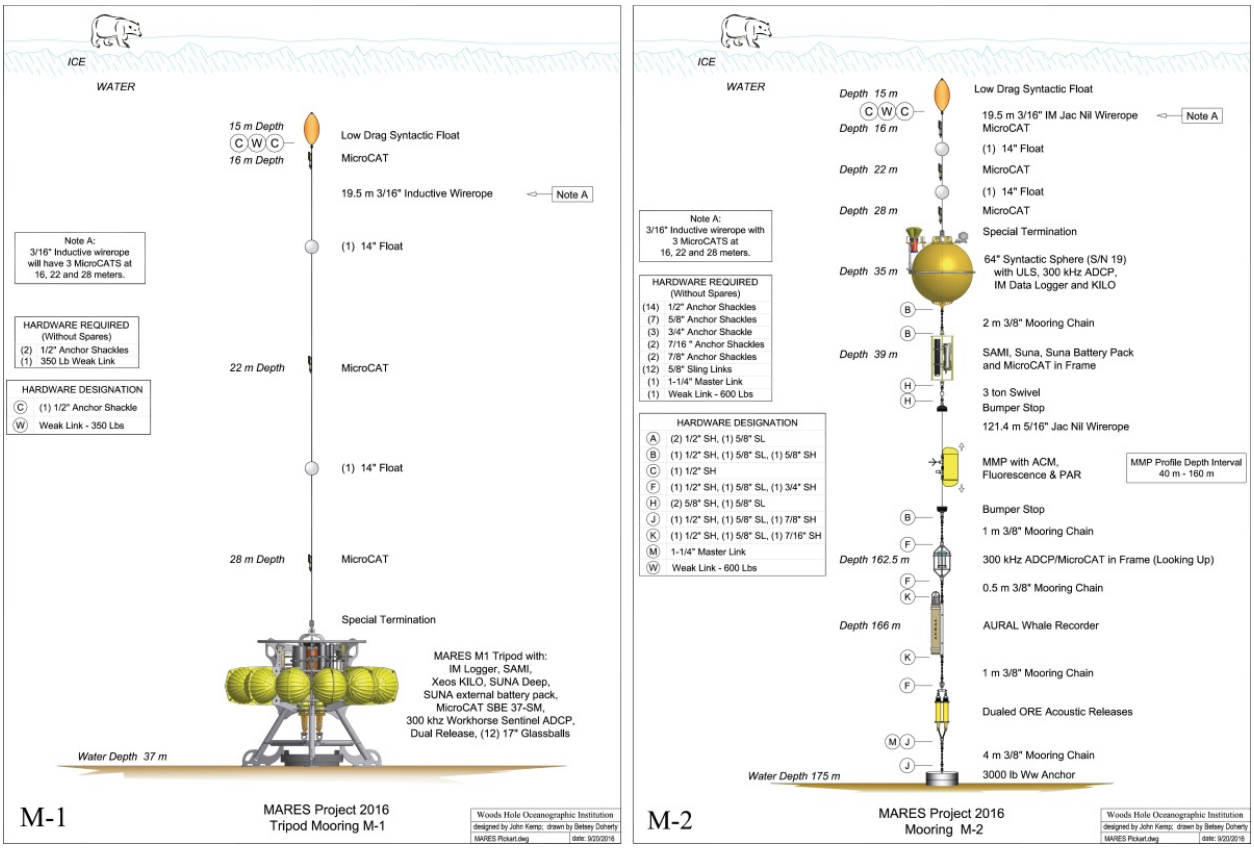

Figure 2. WHOI moorings M1 and M2.

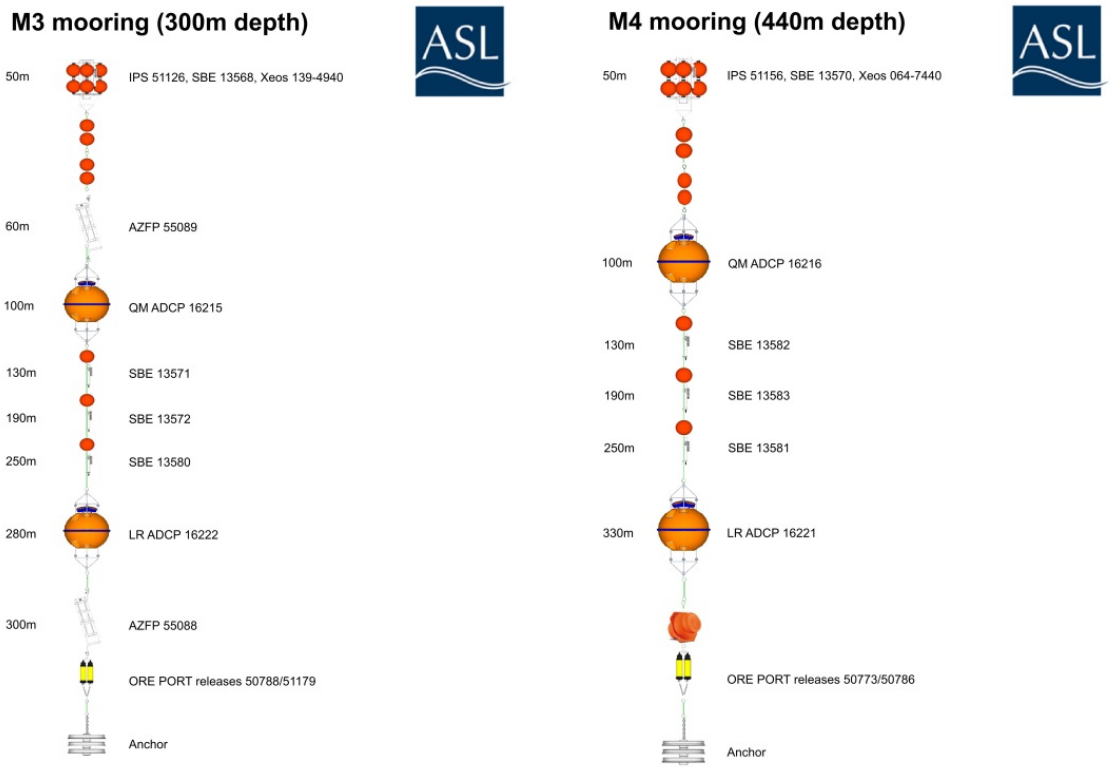

Figure 3. ASL Moorings M3 and M4.

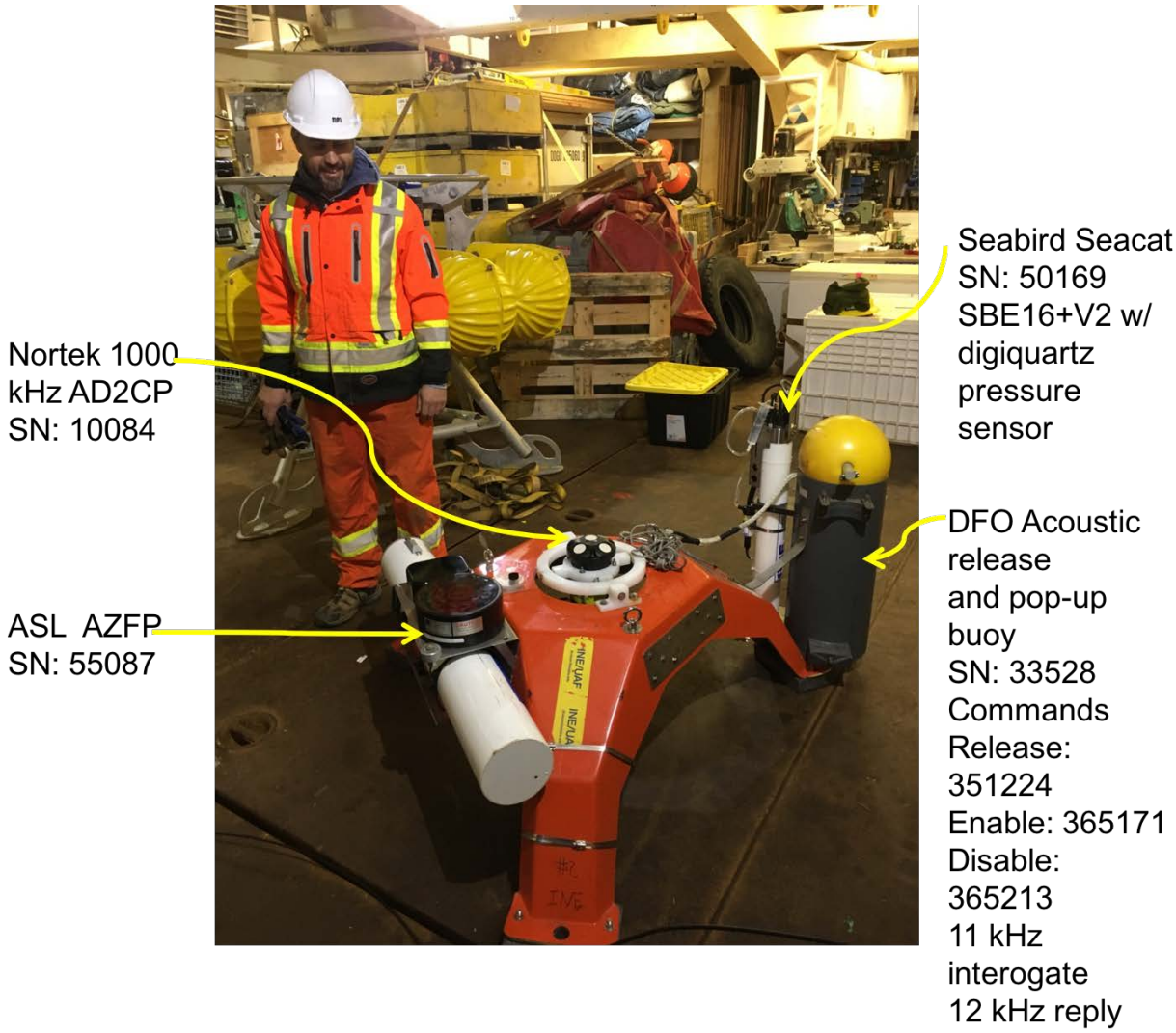

Figure 4. SeaSpider mooring deployed in 13 m water depth showing sensor components.

Table 2.

Summary of the recovery efforts of moorings deployed in October 2016.

Mooring	Operator	Latitude	Longitude	Water depth (m)	Retrieval Date (yyyy-mm-dd)	Retrieval Time (hh:mm) [UTC]
M1	WHOI	69° 46.235´	139° 15.286´	40	2017-09-27	23:05
M2	WHOI	69° 54.478´	138° 59.925´	175	2017-09-28	20:52
M3	ASL	70° 02.909´	138° 47.691´	300	2017-09-28	19:15
M4	ASL	70° 15.101´	138° 47.626´	440	2017-09-28	15:33
SeaSpider	UAF	69° 36.426´	139° 42.925´	14	2017-10-03	17:35

The water depth was determined using observations from the vessel's sounder which were corrected for the sound speed depth profile using the results of a CTD cast.

Upon recovery, the physical condition of all sensors was inspected and found to be in good working condition. Only one small float on the top of the M1 mooring was lost, possibly due to the impact of a sea ice feature. Data sets from all but four sensors were downloaded and inspected for integrity (Table 3). Data quality issues discovered are detailed in the table below, and, where possible, lessons learned were immediately integrated into the redeployed mooring array (see Section 2.2). As anticipated, data from four sensors that were just being retrieved were not downloaded as the field team was not equipped with the necessary communication hardware; this includes the SeaSpider AD2CP and three CTDs on M1 and M2. As required, BOEM was immediately notified on the status of sensors and integrity of data and approved the planned mooring redeployment.

Table 3.

Summary of the recovered mooring components.

Mooring	Equipment	Serial number	Depth (m)	Start date	End date	Data size	Re-deploy	Comments
SeaSpider	AZFP	55087	14	2016-10-01	2017-10-03	11.2 GB	no	
	SBE-16 V2	50169	14	2016-10-05	2017-10-03	1.07 MB	no	
	Nortek AD2CP	10084	14	2016-10-07	2017-10-03	10.9 GB	no	
M1	IM Logger	2	39	-	-	-	no	Downloaded from SBEs directly
	Seabird CTD	13541	16	2016-10-03	2017-09-28	34,518 samples	no	
	Seabird CTD	13540	22	2016-10-03	2017-09-28	34,513 samples	no	
	Seabird CTD	13539	28	2016-10-03	2017-09-27	34,152 samples	no	
	SAMI	n/a	39	2016-09-28	2017-09-28	83 KB	no	
	SUNA	253	39	2016-10-06	2017-07-17	434 MB	yes	Battery exhausted early
	Seabird CTD	2131	39	-	-	-	no	To be extracted after return to WHOI
	300 kHz ADCP	15358	39	2016-10-06	2017-09-27	1.6 GB	no	
M2	IM Logger	1	35	-	-	-	no	Downloaded from SBEs directly
	Seabird CTD	13538	20	2016-10-03	2017-09-28	34,605 samples	no	
	Seabird CTD	13537	26	2016-10-03	2017-09-28	34,606 samples	no	
	Seabird CTD	13536	31	2016-10-03	2017-09-28	34,607 samples	no	
	IPS4	1042	35	2016-10-01	2017-06-11	1.8 MB	no	Data acquisition ended early
	300 kHz ADCP	2131	35	2017-10-07	2017-09-29	1.3 GB	no	Time check 24hrs off
	SAMI	60029	39	2016-09-28	2017-09-29	87 KB	no	
	SUNA	252	39	2017-10-05	2017-09-29	446 MB	yes	

Mooring	Equipment	Serial number	Depth (m)	Start date	End date	Data size	Re-deploy	Comments
M2 (cont'd)	Seabird CTD	2135	39	-	-	-	no	To be extracted after return to WHOI
	MMP CTD	134	40-160	2016-10-07	2017-07-20	39 MB	no	CTD sensor failed
	MMP ACM	-	40-160	2016-10-07	2017-09-26	119 MB	no	2124 profiles @ 4 hour intervals
	MMP Fluorescence, PAR, Turbidity	-	40-160	2016-10-07	2017-09-26	-	no	2124 profiles @ 4 hour intervals
	300 kHz ADCP	14159	162.5	2016-10-06	2017-09-28	1.8 GB	no	Compass post-calibrated at Herschel Island.
	Seabird CTD	2136	162.5	-	-	-	no	To be extracted after return to WHOI
	AURAL	134DEFC	166	2016-10-07	2017-09-10	297 GB	yes	
M3	IPS5	51126	50	2016-10-05	2017-07-30	1.6 GB	no	
	Seabird CTD	13568	50	2016-10-01	2017-09-30	34,796 samples	no	
	AZFP	55089	60	2016-10-05	2017-09-29	22.4 GB	no	
	150 kHz ADCP	16215	100	2016-10-05	2017-09-28	317 MB	no	
	Seabird CTD	13571	130	2016-10-01	2017-09-30	34,794 samples	no	
	Seabird CTD	13572	190	2016-10-01	2017-09-30	34,792 samples	no	
	Seabird CTD	13580	250	2016-10-01	2017-09-30	34,792 samples	no	
	75 kHz ADCP	16222	280	2016-10-05	2017-09-28	115 MB	no	Episodes of limited range in winter
	AZFP	55088	300	2016-10-01	2017-09-29	21.6 GB	yes	

Mooring	Equipment	Serial number	Depth (m)	Start date	End date	Data size	Re-deploy	Comments
M4	IPS5	51156	50	2016-10-05	2017-06-09	1.4 GB	no	
	Seabird CTD	13570	50	2016-10-01	2017-09-30	34,774 samples	no	
	150 kHz ADCP	16216	100	2016-10-05	2017-09-28	42 MB	no	Faulty data card. Missing data on 2017-07-16 and 2017-07-22.
	Seabird CTD	13582	130	2016-10-01	2017-09-30	34,772 samples	no	
	Seabird CTD	13583	190	2016-10-01	2017-09-30	34,771 samples	no	
	Seabird CTD	13581	250	2016-10-01	2017-09-30	34,770 samples	no	
	75 kHz ADCP	16221	330	2016-10-05	2017-09-28	122 MB	no	Episodes of limited range in winter

The depth of each component was determined using the full water depth reported in Table 1 and the height off the sea bottom according to measurements taken from the final mooring assembly.

During retrieval activities, conductivity-temperature-depth (CTD) casts were performed at each mooring site using the CTD/rosette equipment onboard the vessel, and water samples were collected at sites M1 and M2 (Table 4). Water samples were collected for the measurement of dissolved inorganic carbon (DIC) and total alkalinity at the depth and location of Submersible Autonomous Moored Instrument (SAMI) pCO_2 sensors on the recovered moorings. Water samples were also collected for the measurement of nitrate at the depth and location of Submersible Ultraviolet Nitrate Analyzer (SUNA) sensors on the recovered moorings. Water samples were frozen in the onboard wetlab freezer during the transit of the ship back to Victoria. They were transported in a cooler to ASL, which is about a half-hour drive, where they were at once placed into a freezer until they were shipped to the lab in Burnaby. The samples were held in a cool room until analysis.

Table 4.

Summary of CTD casts and water samples acquired during mooring retrieval.

Mooring	CTD cast time [yyyy-mm-dd hh:mm:ss UTC]	Latitude	Longitude	Water sample collection and planned analyses	Water Sample Depth (m)	Maximum Depth at location (m)
M1	2017-09-27 22:20:05	69° 46.43´	139° 15.93´	DIC Total alkalinity Nitrate	36.3	36.6
	2017-10-02 23:21:42	69° 46.24´	139° 14.88´	DIC Total alkalinity Nitrate	35.9	36.6
M2	2017-09-28 21:49:04	69° 54.19´	139° 00.04´	DIC Total alkalinity Nitrate	39.0	39.6
	2017-10-03 23:12:21	69° 54.37´	138° 59.52´	Nitrate	40.0	171.2
M3	2017-09-28 18:22:41	70° 03.12´	138° 47.17´	-	-	294.8
	2017-10-02 21:10:22	70° 02.86´	138° 48.18´	-	-	296.7
M4	2017-09-27 17:52:39	70° 15.66´	138° 48.54´	-	-	445.9
	2017-10-03 18:27:18	70° 15.30´	138° 47.06´	-	-	436.1
SeaSpider	2017-10-03 17:56:10	69° 36.54´	139° 42.89´	-	-	13.9

2.2 MOORING REDEPLOYMENT

Refurbishment was carried out on the equipment to be redeployed, including SUNA sensors, an Acoustic Zooplankton and Fish Profiler (AZFP), and an Autonomous Underwater Recorder for Acoustic Listening (AURAL) sound recorder. The assembly of the moorings to be deployed at sites M3 and M4 was finalized and the moorings were deployed on October 2. 2017. Redesigned moorings were prepared for M1 and M2 which were deployed on October 2 and 3, respectively. As closely as possible, sensor heights within the water column were maintained for continuity of the sampling performed in the previous year despite the redesign of the moorings. Table 5 summarizes the deployed moorings.

Table 5.

Summary of moorings deployed for Year 2 data collection (2017-2018).

Mooring	Operator	Latitude	Longitude	Water depth (m)*	Date	Time [UTC]
M1	ASL	69° 46.306´	139° 15.491´	40	2017-10-02	23:45
M2	ASL	69° 54.528´	138° 59.914´	175	2017-10-03	22:31
M3	ASL	70° 02.912´	138° 47.295´	300	2017-10-02	20:29
M4	ASL	70° 15.089´	138° 47.358´	440	2017-10-02	17:48

*The water depth was determined using observations from the vessel's sounder which were corrected for the sound speed depth profile using the results of a CTD cast.

All moorings were deployed top first. Once all mooring components were on the surface of the water the anchor was lowered over the side and released using a cut-line which caused the mooring to free fall into position on the sea floor. In the case of M2, M3 and M4, the vessel's fast response craft (FRC) was used to tow the mooring by the uppermost component away from the vessel. For these three longer moorings, their positions were triangulated by transponding on the acoustic releases installed on the moorings following deployment to determine their final position on the sea floor. CTD casts and water sampling were performed at the time of deployment at each site as described above.

Table 6 to Table 9 list the components integrated into each of the moorings deployed. Mooring diagrams for each of the deployed moorings are provided in Figure 5 and Figure 6.

The Seabird CT sensors were set to acquire measurements at 15-minute intervals, while the RBR CTs were set to sample every 5 minutes. The exception to this was the RBR CTD 17111 which was set to sample every 45 minutes at 143 m depth at M2. At M3 and M4, the Long Ranger 75 kHz ADCPs were set to ping at 18.75 second intervals and record an ensemble every 10 minutes, while the 150 kHz Quartermaster ADCPs were set to ping at 10.71 second intervals and record an ensemble every 2.5 minutes. These sampling schemes were modified from the Year 1 deployment because it was found that the range of the ADCP observations was lower than that estimated by the manufacturer's configuration software. This was likely due to the lack of acoustic scatterers in the water column, particularly through the winter. At M1, the 300 kHz ADCP was set to ping at 10-second intervals and record an ensemble every 1 minute. At M2, both 300 kHz ADCPs were set to ping at 12-second intervals and record an ensemble every 1 minute. The AZFPs

will sample continuously at 8-second intervals at M3 and 9-second intervals at M2. The SUNA sensors on M1 and M2 were set to sample at 2-hour intervals. This sampling rate was reduced from the Year 1 deployment when it was discovered that one of those sensors stopped recording early due to battery exhaustion. The SAMI sensor was set to sample at 3-hour intervals. The AURAL sensor was set to sample for 15 minutes every hour. This interval constituted a reduction from 20 minutes every hour in the Year 1 deployment because the sensor stopped recording slightly early in that case. The sampling scheme for the IPS sensors varies throughout the deployment and is typically recording at 1 to 3 second intervals.

Table 6.

Summary of mooring components deployed on M1, anchored at 40 m.

Component	Serial number	Depth (m)	Mount type	In-water time [yyyy-mm-dd hh:mm UTC]
RBR CTD	15282	16	Line Clamp	2017-10-02 23:42
RBR CTD	9658	22	Line Clamp	2017-10-02 23:42
RBR CTD	17096	28	Line Clamp	2017-10-02 23:42
300 kHz ADCP (upward facing)	18071	34	ASL Dual-Cage	2017-10-02 23:45
SUNA	253	36	WHOI-Cage	2017-10-02 23:45
SAMI	0026	36	WHOI-Cage	2017-10-02 23:45
Seabird CT	12123	36	WHOI-Cage	2017-10-02 23:45
PORT Release	50920	38	-	2017-10-02 23:45
PORT Release	50921	38	-	2017-10-02 23:45

Table 7.

Summary of mooring components deployed under on M2, anchored at 175 m.

Component	Serial number	Depth (m)	Mount type	In-water time [yyyy-mm-dd hh:mm UTC]
IPS (upward facing)	51049	40	ASL Dual-Cage	2017-10-03 22:25
SUNA	252	40	ASL Dual-Cage	2017-10-03 22:25
Seabird CT	11312	40	ASL Dual-Cage	2017-10-03 22:25
Xeos Beacon	9950	40	ASL Dual-Cage	2017-10-03 22:25
RBR CTD	17308	57	Line clamp	2017-10-03 22:26
300 kHz ADCP (upward facing)	10985	59	ASL Dual-Cage	2017-10-03 22:26
RBR CTD	60176	74	Line clamp	2017-10-03 22:27
RBR CTD	17365	91	Line clamp	2017-10-03 22:27
RBR CTD	60177	109	Line clamp	2017-10-03 22:27
RBR CTD	60175	126	Line clamp	2017-10-03 22:27
RBR CTD	17111	143	Line clamp	2017-10-03 22:27
300 kHz ADCP (upward facing)	6593	162	ASL Dual-Cage	2017-10-03 22:31
Seabird CT	11311	162	ASL Dual-Cage	2017-10-03 22:31
Aural	93LF	164	Strong back	2017-10-03 22:31
AZFP (upward facing)	55120	166	ASL 15° Cage	2017-10-03 22:31
PORT Release	43089	168	-	2017-10-03 22:31
PORT Release	43090	168	-	2017-10-03 22:31

Table 8.

Summary of mooring components deployed on M3, anchored at 300 m.

Component	Serial number	Depth (m)	Mount type	In-water time [yyyy-mm-dd hh:mm UTC]
IPS (upward facing)	51092	52	ASL Dual-Cage	2017-10-02 20:21
Seabird CT	11313	52	ASL Dual-Cage	2017-10-02 20:21
Xeos Beacon	8510	52	ASL Dual-Cage	2017-10-02 20:21
AZFP (upward facing)	55054	59	ASL 15° Cage	2017-10-02 20:21
150 kHz ADCP (upward facing)	17898	104	M40	2017-10-02 20:22
Seabird CT	12282	132	Line clamp	2017-10-02 20:23
Seabird CT	13569	192	Line clamp	2017-10-02 20:25
Seabird CT	10754	252	Line clamp	2017-10-02 20:26
75 kHz ADCP (upward facing)	12962	283	M40	2017-10-02 20:27
AZFP (upward facing)	55088	288	ASL 15° Cage	2017-10-02 20:27
PORT Release	49431	290	-	2017-10-02 20:29
PORT Release	49432	291	-	2017-10-02 20:29

Table 9.

Summary of mooring components deployed on M4, anchored at 440 m.

Component	Serial number	Depth (m)	Mount type	In-water time [yyyy-mm-dd hh:mm UTC]
IPS (upward facing)	51089	51	ASL Dual-Cage	2017-10-02 17:31
Seabird CT	13186	51	ASL Dual-Cage	2017-10-02 17:31
Xeos Beacon	5290	51	ASL Dual-Cage	2017-10-02 17:31
150 kHz ADCP (upward facing)	16157	101	M40	2017-10-02 17:35
Seabird CT	13689	130	Line clamp	2017-10-02 17:35
Seabird CT	10755	190	Line clamp	2017-10-02 17:36
Seabird CT	10756	250	Line clamp	2017-10-02 17:37
75 kHz ADCP (upward facing)	17441	331	M40	2017-10-02 17:38
PORT Release	50790	429	-	2017-10-02 17:48
PORT Release	46375	429	-	2017-10-02 17:48

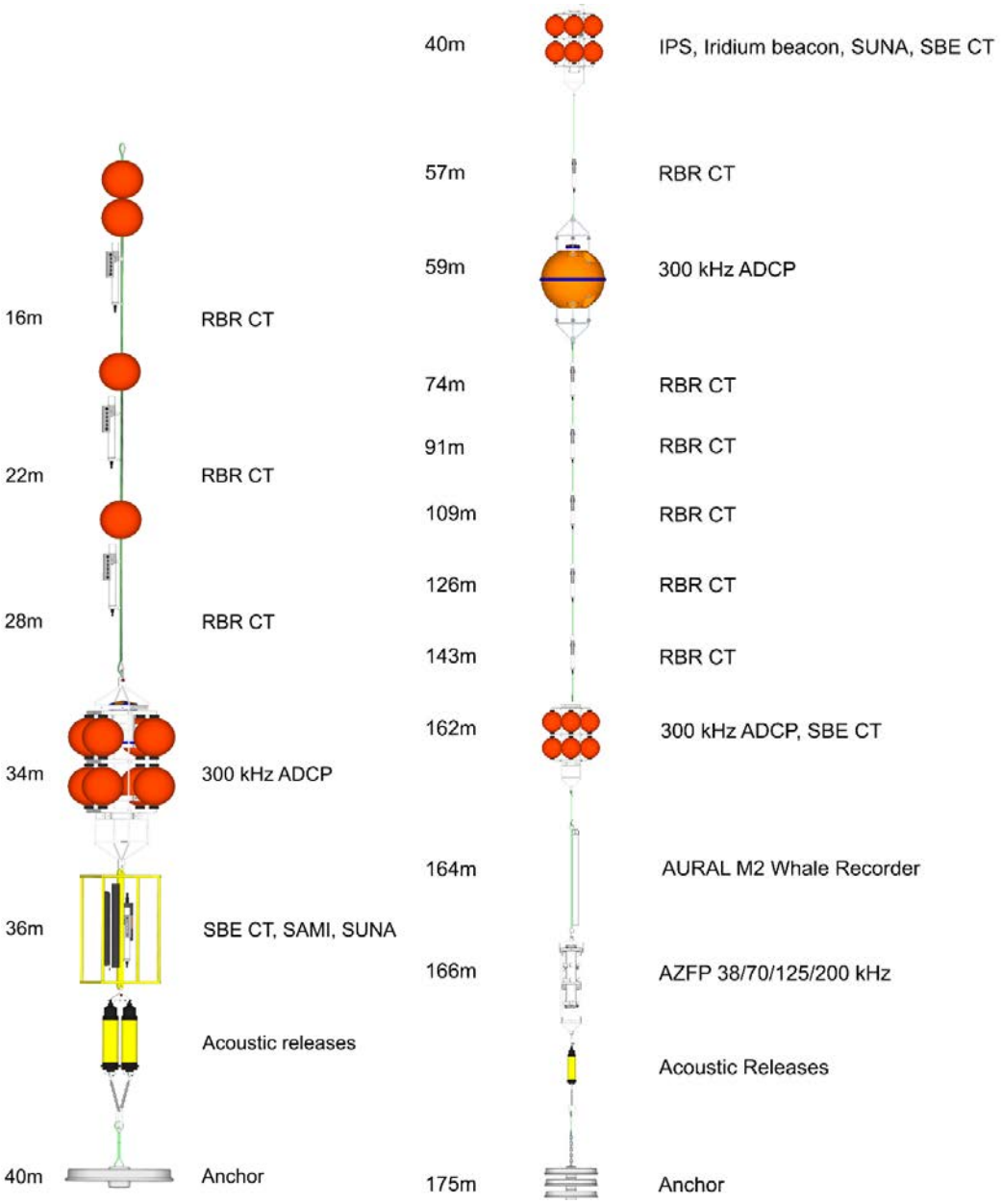

Figure 5. Mooring diagrams for M1 (left) in 40 m water depth and M2 (right) in 175 m water depth.

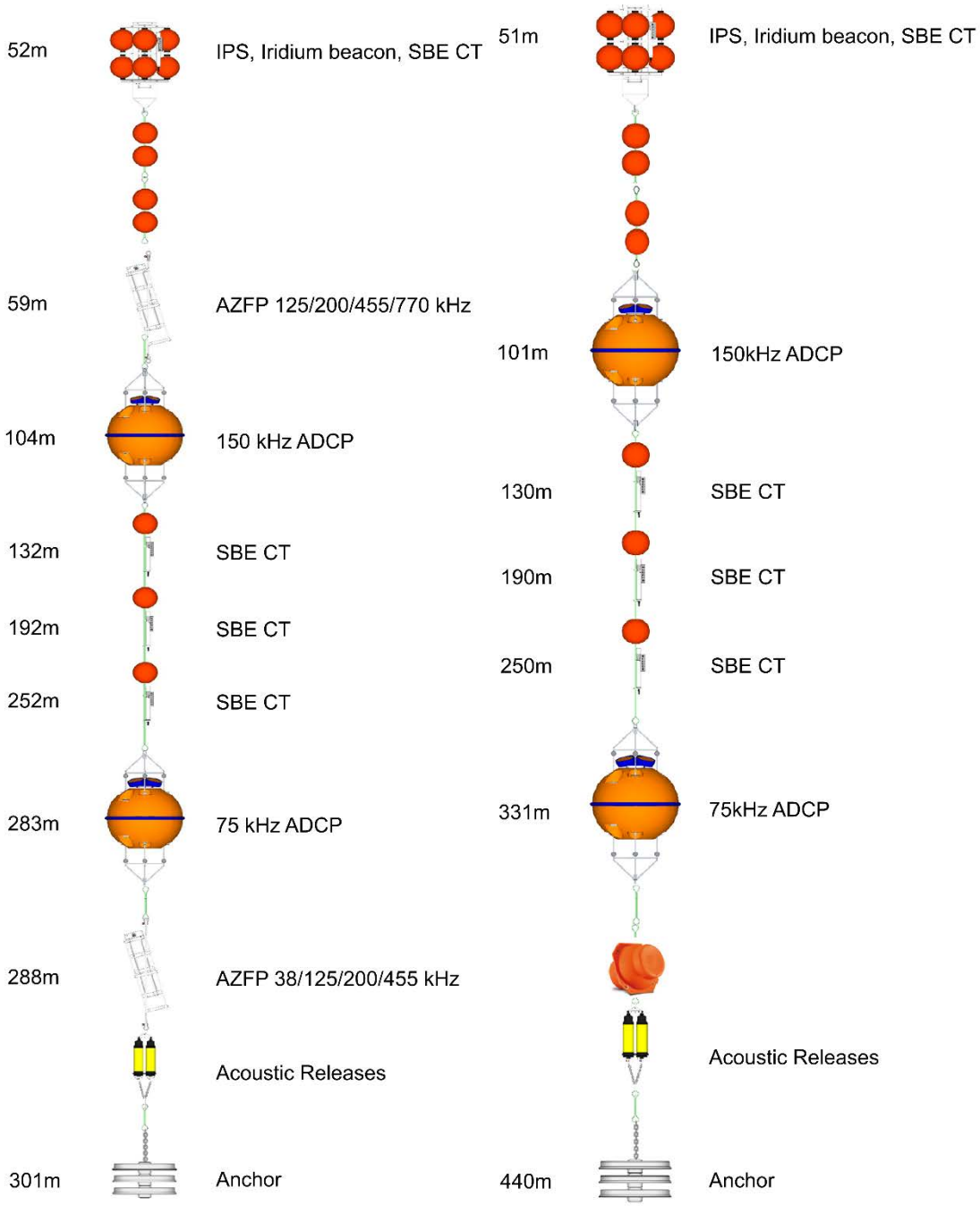

Figure 6. Mooring diagrams for M3 (left) in 300 m water depth and M4 (right) in 440 m water depth.

The mooring team disembarked from the vessel, with the Year 1 raw mooring data, in Nome, Alaska, on October 9, 2017, and returned to Victoria, BC the following morning. The data were transported by the field team to Victoria, BC and uploaded to the MARES data management system at AXIOM on October 18, 2017. The vessel returned to its home port of Sidney, BC on October 18, 2017 and all the retrieved mooring equipment was offloaded at the Institute of Ocean Sciences (IOS). The equipment used on the M3 and M4 MARES moorings operated by ASL during Task Order 3 was prepared for shipment back to ASL's facility in Victoria, BC. The shipment arrived, and all equipment was demobilized. Equipment from the M1 and M2 moorings operated by WHOI was packed by ASL staff, using crates provided by WHOI and stored at IOS until WHOI was ready to have it shipped to their facility on November 8, 2017. Water samples were shipped to ASL Environmental in Burnaby, BC for analysis. MARES partners University of Washington (UW) and University of Alaska Fairbanks (UAF) received their data on October 20, 2017 and October 17, 2017, respectively.

2.3 DATA MANAGEMENT

Key objectives for the data management were to adaptively update and produce a data management plan, oversee data ingestion into the MARES Research Workspace, and archive and publish data in appropriate locations. With these ends in mind, the data management workflow began prior to Year 1 mooring deployment and will conclude with MARES datasets delivered to BOEM, made publicly available via interactive visualizations in the AOOS Arctic Data Portal, and archived in an appropriate data repository, e.g., the Research Workspace DataONE Member Node[1] or the National Center for Environmental Information (NCEI)[2].

2.3.1 Data Management Workflow

Data management tasks were divided into three semi-overlapping focuses: planning and orientation; raw data; and preliminary data and metadata.

2.3.2 Planning and orientation

In the planning and orientation phase of data management tasks, the data management team at Axiom Data Science reviewed deployment plans for the moorings to understand planned instrumentation, expected data types, and science team responsibility for each mooring and instrument. With this information, Axiom staff updated project data management plans and internal project management notes to be ready to receive data once it had been recovered from the retrieved moorings. Data management personnel hosted several small-group or one-on-one calls and webinars to provide an introduction and orientation to the Research Workspace (Workspace) for MARES scientists and program administrators.

These information calls demonstrated the use and navigation of the Research Workspace, a web-based data management platform, described below; and discussed project structure, organization, and membership. After mooring retrieval, the data management team hosted

[1] https://search.dataone.org/#profile/RW
[2] https://www.ncei.noaa.gov/

additional webinars to orient all project scientists to the Workspace while demonstrating features and reviewing the data handling processes and the management workflow.

The Workspace is a web-based platform developed at Axiom Data Science for collaboratively managing science projects through the entire data lifecycle. It allows research scientists, data managers, and program administrators a secure way to store and organize data within individual projects and research campaigns; to create, share, and execute reproducible numerical workflows; and to generate robust metadata, and to publish finalized data products to custom data catalogs and national data archives. Projects within the Workspace can be shared with selected users, with research campaigns, or with entire organizations. Specific permissions may be set on an individual or group basis. This allows preliminary results and interpretations to be shared by geographically- or scientifically-diverse individuals working together on a project or program before the data are shared with the public, which gives program leads and other stakeholders a front-row view of how their programs are progressing through time. From the beginning, the MARES program has used the Workspace to store, share, track, and document data generated under each task order.

2.3.3 Raw Data

Upon return from the mooring retrieval cruise in September 2017, an FTP site was set up from which the data management team ingested the data into the Workspace, where it was organized by mooring and instrument. Notifications were sent to the MARES teams that raw data were now available for QA/QC and preliminary analysis.

From the Year 1 moorings and related activities, 4220 raw data files were uploaded into the Workspace (Table 10 and Table 11). These represented biophysical data collected from 36 distinct instruments on the 4 MARES moorings, the UAF SeaSpider mooring, from CTD casts and water samples acquired during the 2017 mooring recovery and deployment cruises, and from the meteorological station on Herschel Island.

Table 10.

Summary of MARES Year 1 mooring data size and volume, by platform

	Total Raw Files	Total Raw Volume	Total Preliminary Files	Total Preliminary Volume
M1	379	2.084 GB	17	1.993 GB
M2	3,145	323.530 GB	45	3.853 GB
M3	336	15.343 GB	67	1.462 GB
M4	283	1.783 GB	40	1.220 GB
UAF Sea Spider	31	19.434 GB	4	2.130 MB
Cruise Sampling	46	12.481 MB	23	3.279 MB
Met Station	0	0 MB	2	0.650 MB

Table 11.

Summary of MARES Year 1 dataset by instrument and parameter

Instrument Type	Raw Data Files	Raw Data Volume	Preliminary Data Files	Preliminary Data Volume	Parameters
ADCP	27	17.271 GB	29	5.928 MB	ocean currents
MicroCATs	63	35.213 MB	27	41.200 MB	conductivity (salinity), temperature
SAMI	4	0.674 MB	5	0.988 MB	pCO_2
SUNA	741	913.978 MB	13	4.135 MB	nitrate
AURAL	2,712	319.814 GB	0[1]	0.000 MB	passive acoustics
AZFP	6	21.020 GB	3	10.037 GB	zooplankton, fish profiles
IPS	587	3.001 GB	76	2.530 GB	sea ice profile
MMP	30	117.472 MB	9	24.844 MB	conductivity (salinity), temperature, pressure, oxygen, fluorescence, turbidity, PAR
CTD Casts	40	11.422 MB	12	2.741 MB	temperature, conductivity (salinity), pressure
Water Samples	10	1.374 MB	11	0.537 MB	meiofauna abundance, diversity, biomass; inorganic nutrients; nitrate
Met Station	0	0.000 MB	2	0.655 MB	air temperature, atmospheric pressure, wind velocity

[1] Data is owned by UW collaborator. Preliminary results are included in this report.

2.3.4 Preliminary data and metadata

Members of the MARES science team downloaded raw data from the Workspace to their local workstations to perform quality control processes and begin their analyses. Throughout the preliminary data phase, the data management team remained in contact with MARES scientists to provide reminders about expected data and metadata, to advise on data formatting to meet BOEM requirements and ensure datasets are ready for long-term preservation, and to review and provide feedback on metadata authored by scientists. Once quality-controlled data were delivered (182 files, see Table 11), the data management team ensured that datasets were documented with descriptive, standards-compliant ISO 19115/19139 metadata. This work ensured that data collected, produced or consolidated through the MARES effort was managed throughout its lifecycle using an established and agreed upon data administration system for storage and organization during the project; and that data will be archived according to BOEM requirements. The data management team also created and maintained a data and metadata inventory to provide the project management team with a status update on data delivery and metadata generation.

2.4 QUALITY ASSURANCE/QUALITY CONTROL (QA/QC) ON YEAR 1 DATA

2.4.1 Acoustic Doppler Current Profiler (ADCP)

ADCPs provide precise measurements of both horizontal and vertical components of ocean currents at many levels within the water column. The ADCP instruments measure velocity by detecting the Doppler shift in acoustic frequency, arising from water current or ice movements, of the backscattered returns of four upward transmitted acoustic pulses slanted 20º from vertical. The ADCPs deployed at the four mooring sites differed among mooring locations. The ADCPs at M1 and M2 were 300 kHz ADCPs (RDI Workhorse). One was deployed on a bottom-mounted tripod (M1) at 40 m seafloor depth, nominally 2 m off of the bottom so at 38 m water depth and surveyed the full water column. Two of the instruments (M2a and M2b) were deployed on a single mooring (railroad wheel weight, mooring string) located at 175 m water depth, placed nominally at 39 m (M2a) and 162.5 m (M2b) water depth. During the year, the depth of the transducers varied slightly as the mooring chain tilted in the prevailing currents but the shallow instruments (M1a, M2a) remained at average ~39 m water depth and the deeper ADCP was at average ~160 m. All instruments had beam angles of 20° and were set to a blanking interval of 1.76 m. Timing settings are outlined in Table 12. All three ADCPs were set for single ping ensembles in burst sample mode. The ADCPs were set to ping once every 5 seconds for 7.5 minutes (90 pings) every 30 minutes. The idea was to later average these pings into 30-minute ensembles. Saving every ping allowed us to edit single pings for a more robust average. Additionally, ADCPs M1a and M2a were both configured with WM15 surface track firmware. This firmware allows ADCP to bottom track using the water track ping. In this case, the bottom track is actual tracking the ice velocity and distance to surface. From distance to surface one can derive ice draft.

Table 12.

Parameters used in calculation of volume backscattering (S_V) and settings used for each ADCP during deployment. *

ADCP	Bandwidth %	C (dB)	E_r (4-Beam Mean)	α	P_{DBW}	L_{DBM}	q (Beam Angle, °)	B (Blank, m)	L (Pulse Length, m)	D (Bin Length, m)	N (# Bins)
M1a	6.25	-151.64	32.5225	0.069	14	3.6361	20	1.76	2.31	2	40
M2a	25	-140.87	18.348	0.069	14	3.8021	20	1.76	2.4	2	30
M2b	6.25	-151.64	33.5425	0.069	14	6.3144	20	1.76	4.28	4	50
Source	D.Torres	Mullison	Data	Deines	Mullison	Data	RDI	Data	Data	Data	Data

*The source of each parameter is indicated (Deines, 1999; Mullison, 2017; Data from the instrument). Parameters used in the absolute backscatter equation are defined in section 2.4.2.

At M3 and M4 two ADCPs were used: a 150 kHz Workhorse Quartermaster and a 75 kHz Workhorse Long Ranger. The ADCP instruments, operating in conventional water column data acquisition mode with bottom-tracking mode enabled, provided time-series measurements of three-dimensional currents and ice velocity. The 150 kHz Workhorse Quartermaster ADCPs collected data at 2-minute sampling intervals with a vertical resolution of 2 m. They were both deployed at approximately 100-metre water depth in an upward-looking configuration. The 75 kHz Workhorse Long Ranger ADCPs collected data at 5-minute sampling intervals with a vertical resolution of 8 m. Both were deployed near the ocean floor in an upward-looking configuration; on M3 at approximately 280 m water depth and on M4 at approximately 330 m water depth.

2.4.1.1 M1a Processing

ADCP M1a heading was mounted on a tripod and should therefore have been fixed at a single direction. Several events resulted in movement of the tripod, however, changing its heading (Figure 7). In addition, even during the times when the ADCP was motionless, there was still considerable variability in the heading data (Figure 8). It was discovered that the heading data were corrupted by spikes, which were subsequently corrected through a series of steps. Correction was possible because single pings had been recorded instead of the usual ensemble averages. First a spike filter was applied that removed most of the large spikes (example shown in Figure 9) in each 30-minute burst. A median filter was then applied to get a single heading for each burst sample. A heading correction was then applied to the ADCP velocity data which also included correction for magnetic declination. The resultant corrected heading (Figure 10) was applied to all velocity and bottom track data.

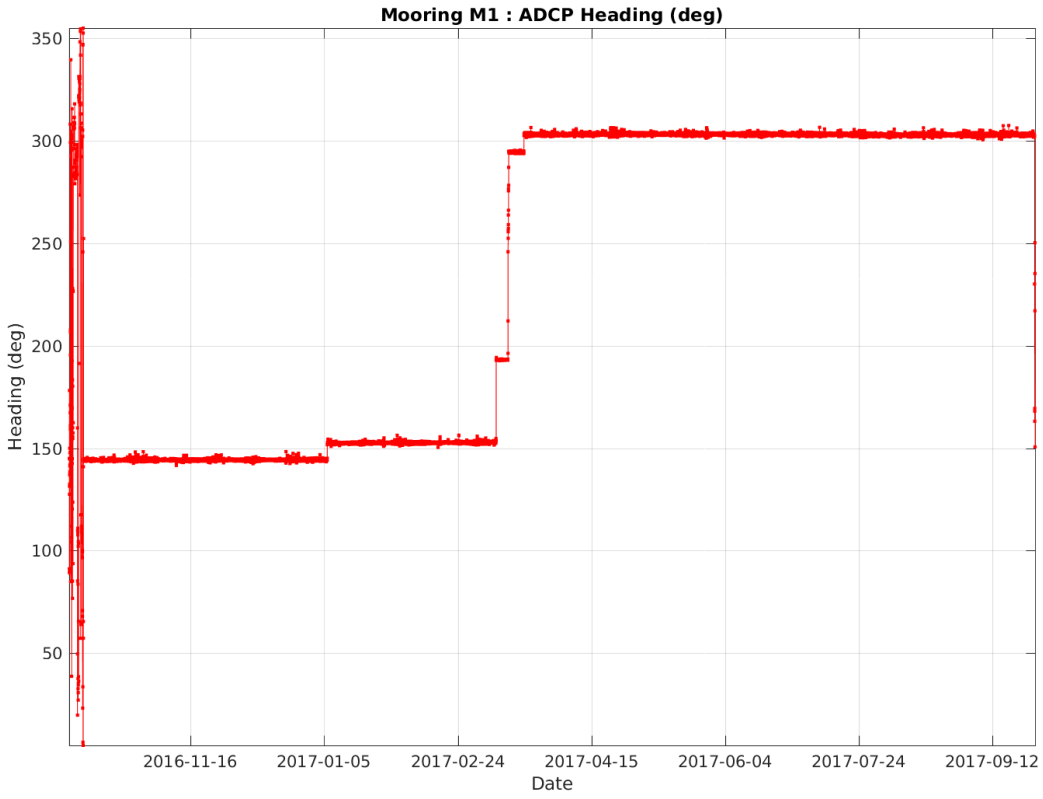

Figure 7. Raw ADCP heading data before correction.

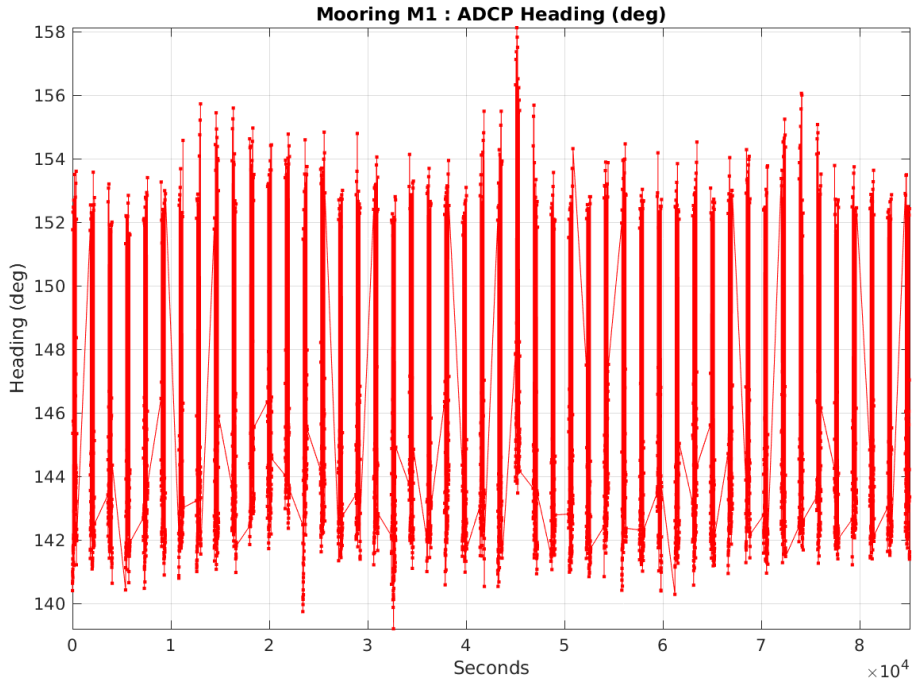

Figure 8. Example of raw ADCP Heading during a 24-hour period

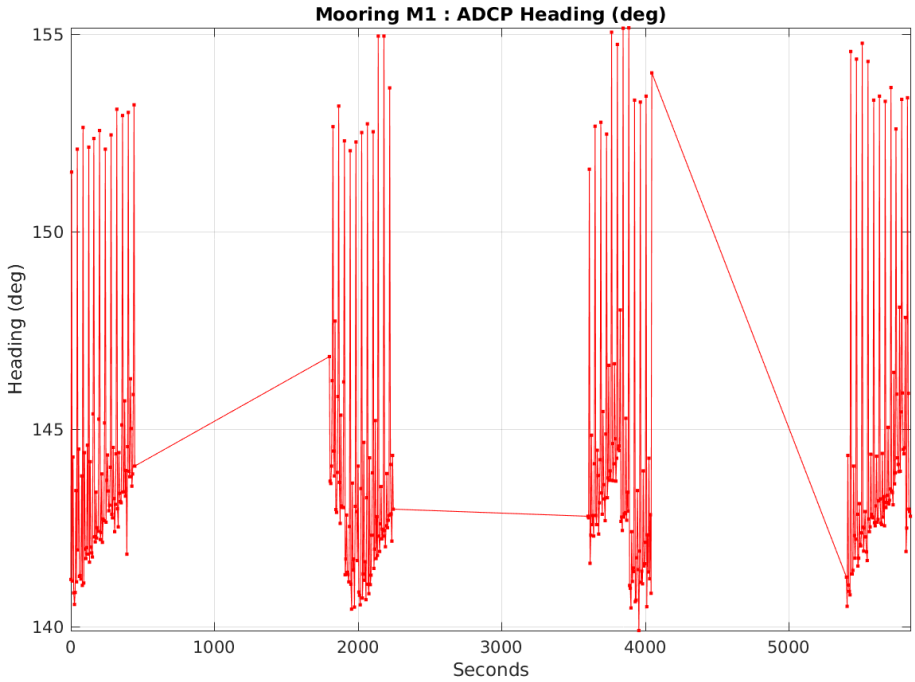

Figure 9. Spike Filter application on ADCP Heading—2 hours; 90 pings per burst; four 30-minute bursts. Pings 5 seconds apart.

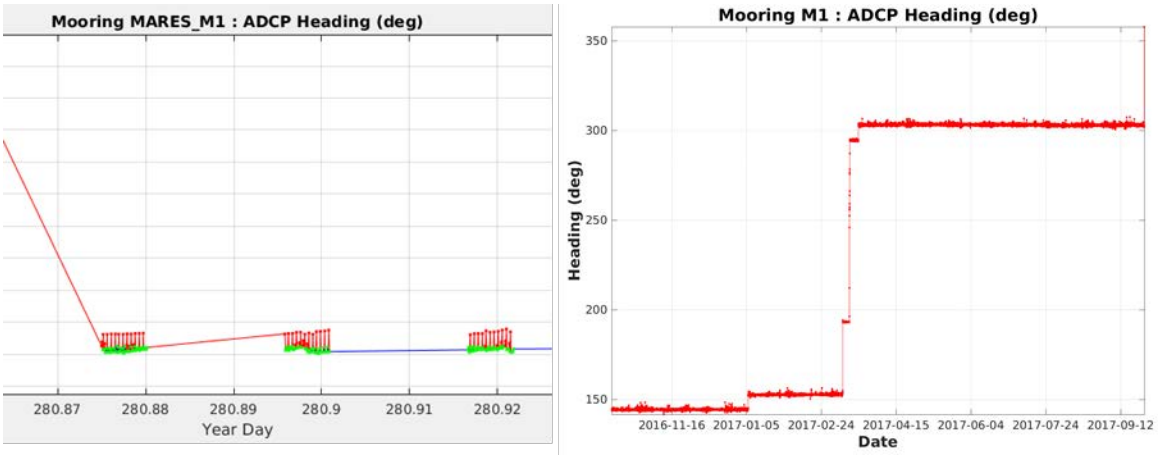

Figure 10. (left) New corrected heading (green dots) before averaging; (right) Final corrected heading.

The rest of the raw single ping data were averaged into 30-minute ensembles to reduce velocity standard deviation. Error criteria of minimum 20% good pings and maximum 8 cm/s error velocity were applied for velocity data screening. The M1 mooring design consisted of a bottom mounted tripod with a tether attached that was held up by a series of floats. A string of Seabird MicroCATs were attached to the tether at varying depths. Investigation of the raw data showed interference of the floats with the ADCP at those depths, so those data were flagged for the entire deployment. The upper flotation was lost on 2017/03/20, 18:30:00 (likely due to passing ice keels), so from that point on, those data were no longer biased by that float.

2.4.1.2 M2a Processing

Mooring M2 had two ADCPs. The shallower ADCP (M2a) was mounted on the subsurface syntactic foam sphere at ~39 m depth facing up. A tether with floats and MicroCATs was also attached to the sphere. As for M1a several data bins were affected by the tether floats, and these were flagged for the duration of the deployment. The exception was the uppermost flotation which was lost due to ice on 2017-03-10, 21:30:00 after which time those data were clean. Similar editing procedures were applied to M2a as M1a.

2.4.1.3 M2b Processing

M2b was the deeper (~162.5 m) of the two ADCPs deployed on mooring M2. Due to an instrument failure at the time of deployment, the initial ADCP was swapped out. The installed instrument was the same as the planned instrument except it did not have ice tracking firmware installed. Therefore, the data from this instrument does not have any ice information. Other than that, similar processing methods were applied to this instrument as described for the other two. None of the instruments installed on the mooring tether above this ADCP seemed to influence the velocity measurements, so no data from this ADCP had to be systematically flagged.

2.4.1.4 M3 and M4 Processing

On recovery of the four ADCPs mounted on M3 and M4, the actual time and the time read from the instrument clock were recorded to determine clock drift. As is common occurrence, the

instrument clocks drifted slightly over this year-long deployment. The time drift was assumed to occur linearly and was compensated by adjusting the sample interval (Table 13). The instrument depth values were referenced to the mean of the ADCP-measured pressure and converted to depth using water density. The distance to bin 1 values (distance from the head of the ADCP to the first acquired current bin) are instrument and configuration dependent and were recorded by each instrument in the raw data file. The raw data value count (total number of ensembles acquired during the deployment) were also recorded.

Table 13.

Selected M3 and M4 ADCP configuration parameters.

	M3 150 kHz Quartermaster	M4 150 kHz Quartermaster	M3 75 kHz LongRanger	M4 75 kHz LongRanger
Instrument clock drift	4 minutes slow	2:20 minutes slow	6:05 minutes slow	6:11 minutes slow
Configured sample interval	120 second ensemble (7 pings / ensemble)	120 second ensemble (7 pings / ensemble)	300 second ensemble (20 pings / ensemble)	300 second ensemble (20 pings / ensemble)
Sample interval corrected for clock drift [s]	120.2109	120.0005	300.0035	300.0035
Instrument depth [m]	105	94	284	334
Bin size [m]	2	2	8	8
Distance to bin 1 [m]	6.39	6.39	15.82	15.87
Raw data value count	257,285	257,321	103,081	103,075

2.4.1.5 Ocean current time-series

The ADCPs at M1 and M2 collected 357 and 358 days, respectively, of ocean current time-series measurements. The ADCPs at M3 and M4 collected approximately 358 days of ocean current time-series measurements.

Combining the results from the Workhorses on moorings M1 and M2, current measurements were obtained from near-bottom to near-surface. Table 14 lists the ocean current bin indices and their associated depth for each instrument. Actual depths were determined using a pressure sensor from a Seabird MicroCAT SM58 co-located with each ADCP. Pressure from the MicroCAT was converted to depth and then interpolated onto the ADCP time record to determine ADCP transducer depth. Then a depth profile was determined for each ADCP 30-minute average ensemble from the transducer to the center of each bin. Variations in sea surface height (and thus pressure) along with mooring blow-over result in variable depth profiles for each ensemble. Table 14 below is a representation of the average depth for each profile throughout the full time series. Actual depths can vary substantially from this table, especially during substantial blow-over events.

Table 14.

Bin depth referenced to mean sea level as derived from the pressure time-series measured by each MicroCAT CTD co-located with each ADCP.

Bin index	Bin bottom boundary depth [m]*		
	M1a 300 kHz Workhorse	M2a 300 kHz Workhorse	M2b 300 kHz Workhorse
39			2.3
38			6.3
37			10.3
36			14.3
35			18.3
34			22.3
33			26.3
32			30.3
31			34.3
30			38.3
29			42.3
28			46.3
27			50.3
26			54.3
25			58.3
24			62.3
23			66.3
22			70.3
21			74.3
20			78.3
19			82.3
18	1.3		86.3
17	3.3	0.6	90.3
16	5.3	2.6	94.3
15	7.3	4.6	98.3
14	9.3	6.6	102.3
13	11.3	8.6	106.3
12	13.3	10.6	110.3
11	15.3	12.6	114.3
10	17.3	14.6	118.3
9	19.3	16.6	122.3
8	21.3	18.6	126.3
7	23.3	20.6	130.3
6	25.3	22.6	134.3
5	27.3	24.6	138.3
4	29.3	26.6	142.3
3	31.3	28.6	146.3
2	33.3	30.6	150.3
1	35.3	32.6	154.3

*The depth is the center of each bin; for example, bin index 8 for the M1a Workhorse spans a depth of 22.3 to 20.3 m

Combining the results from the LongRanger and Quartermaster on these moorings, current measurements were obtained from near-bottom to near-surface. Table 15 lists the ocean current bin indices and their associated depth for each instrument.

Table 15.

Bin depth referenced to mean sea level as derived from the pressure time-series measured by each ADCP.

Bin index	Bin bottom boundary depth [m]*			
	M3 150 kHz Quartermaster	M4 150 kHz Quartermaster	M3 75 kHz LongRanger	M4 75 kHz LongRanger
46	8.6	-	-	-
45	10.6	-	-	-
44	12.6	-	-	-
43	14.6	-	-	-
42	16.6	-	-	-
41	18.6	7.6	-	-
40	20.6	9.6	-	-
39	22.6	11.6	-	-
38	24.6	13.6	-	-
37	26.6	15.6	-	30.1
36	28.6	17.6	-	38.1
35	30.6	19.6	-	46.1
34	32.6	21.6	-	54.1
33	34.6	23.6	12.5	62.1
32	36.6	25.6	20.5	70.1
31	38.6	27.6	28.5	78.1
30	40.6	29.6	36.5	86.1
29	42.6	31.6	44.5	94.1
28	44.6	33.6	52.5	102.1
27	46.6	35.6	60.5	110.1
26	48.6	37.6	68.5	118.1
25	50.6	39.6	76.5	126.1
24	52.6	41.6	84.5	134.1
23	54.6	43.6	92.5	142.1
22	56.6	45.6	100.5	150.1
21	58.6	47.6	108.5	158.1
20	60.6	49.6	116.5	166.1
19	62.6	51.6	124.5	174.1
18	64.6	53.6	132.5	182.1
17	66.6	55.6	140.5	190.1
16	68.6	57.6	148.5	198.1
15	70.6	59.6	156.5	206.1
14	72.6	61.6	164.5	214.1
13	74.6	63.6	172.5	222.1
12	76.6	65.6	180.5	230.1
11	78.6	67.6	188.5	238.1
10	80.6	69.6	196.5	246.1
9	82.6	71.6	204.5	254.1

Bin index	Bin bottom boundary depth [m]*			
	M3 150 kHz Quartermaster	M4 150 kHz Quartermaster	M3 75 kHz LongRanger	M4 75 kHz LongRanger
8	84.6	73.6	212.5	262.1
7	86.6	75.6	220.5	270.1
6	88.6	77.6	228.5	278.1
5	90.6	79.6	236.5	286.1
4	92.6	81.6	244.5	294.1
3	94.6	83.6	252.5	302.1
2	96.6	85.6	260.5	310.1
1	98.6	87.6	268.5	318.1

*The depth is the middle of each bin; for example, bin index 8 for the M3 Quartermaster spans a depth of 81.6 to 83.6 m

The extracted ADCP time-series were subjected to quality control procedures. The steps in the error detection and removal procedures were as follows:

1. The currents were screened for Correlation < 64, Amplitude < 50 m/s and VError > 30 cm·s-1.
2. The current direction time-series was compass corrected using a heading-dependent compass calibration polynomial obtained from performing a dry land compass calibration routine. Also, a magnetic declination rotation factor was applied to each instrument based on coordinates of deployment. This step establishes horizontal motion vectors referenced to geographic (true) north and corrects the data for the inaccuracies of the compass. The resulting current velocity components are herein referred to as VEast and VNorth.
3. The sample interval was adjusted for the observed time drift.
4. Current measurements that were determined to be compromised by the obstruction of other components further up the mooring were replaced with flag values.
5. Current measurements determined to be compromised by the water surface and presence of ice were replaced with flag values.
6. Unreasonable first-difference values in the current time-series were automatically identified. Thresholds for each bin were automatically determined using a multiple of the standard deviation of the time-series for the bin after the application of a high pass filter.
7. Values of measured horizontal components of current that had absolute values exceeding an out-of-bound threshold were identified. This threshold is calculated as the rounded maximum of the high pass filtered absolute current speed plus fifty standard deviations plus the mean current speed.
8. All suspect values found in steps 6 and 7 were replaced by linear interpolation.

9. The current time-series was block averaged using a ~20-minute sample interval to reduce standard error but retain enough resolution for the expected timescales of relevant phenomena.
10. The data was visually inspected, and data found to be unreliable based on reduced signal strength and inconsistent with the immediately surrounding data was replaced with a flag value of -9999. Modifications in this step were made in both the VEast and VNorth data channels.

The count of records modified in the V_{East} and V_{North} data channels for each current bin up to step 8 is shown in Figure 11 and listed in Table 16. The data are presented with the shallowest/highest bin at the top. Similar to float interference at M1 and M2, the IPS5 instrument located at ~60 m depth at M3 created interference in the raw ADCP data at this level, as shown through inconsistencies such as drastic direction changes and very high signal strength. As a result, measurements at this depth were replaced with flagged values. In addition, there was a substantial amount of data flagged in the shallowest bins of the water column due to the presence of the surface and ice. These processing summaries include data records that were replaced by linearly interpolated values and records that were assigned a value of -9999.

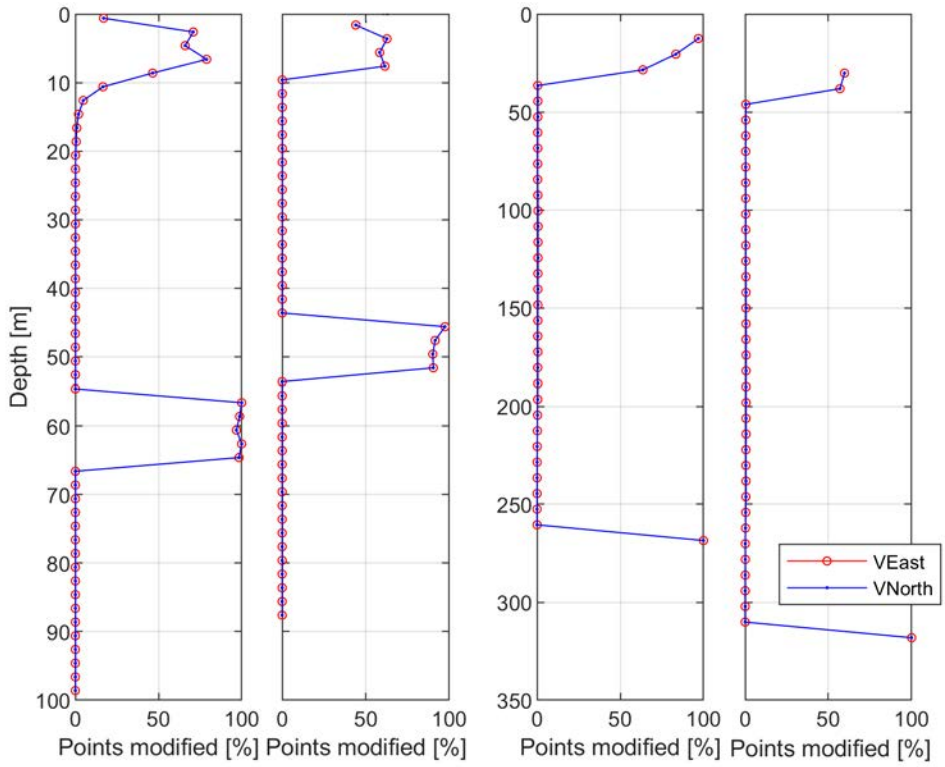

Figure 11. Fraction of data records modified before time-averaging for the (from left to right) M3 Quartermaster, M4 Quartermaster, M3 LongRanger, and M4 LongRanger.

Table 16.

Count and fraction of data records modified before time-averaging for each ocean current bin.

Bin index	Count (fraction) of modified records							
	M3 150 kHz Quartermaster		M4 150 kHz Quartermaster		M3 75 kHz LongRanger		M4 75 kHz LongRanger	
	V_{East}	V_{North}	V_{East}	V_{North}	V_{East}	V_{North}	V_{East}	V_{North}
50	43,726 (17%)	43,726 (17%)	-	-	-	-	-	-
49	182,247 (71%)	182,247 (71%)	-	-	-	-	-	-
48	169,811 (66%)	169,811 (66%)	-	-	-	-	-	-
47	202,958 (79%)	202,959 (79%)	-	-	-	-	-	-
46	119,582 (47%)	119,591 (47%)	-	-	-	-	-	-
45	42,777 (17%)	42,901 (17%)	-	-	-	-	-	-
44	12,338 (5%)	12,339 (5%)	113352 (44%)	113,352 (44%)	-	-	-	-
43	5,088 (2%)	5,065 (2%)	161,429 (63%)	161,429 (63%)	-	-	-	-
42	2,256 (1%)	2,261 (1%)	150,166 (58%)	150,166 (58%)	-	-	-	-
41	1,404 (1%)	1,446 (1%)	158,230 (62%)	158,230 (62%)	-	-	-	-
40	384 (<0.5%)	407 (<0.5%)	246 (<0.5%)	217 (<0.5%)	-	-	-	-
39	320 (<0.5%)	332 (<0.5%)	211 (<0.5%)	197 (<0.5%)	-	-	-	-
38	281 (<0.5%)	283 (<0.5%)	206 (<0.5%)	174 (<0.5%)	-	-	-	-
37	279 (<0.5%)	274 (<0.5%)	175 (<0.5%)	140 (<0.5%)	-	-	61,526 (60%)	61,526 (60%)
36	249 (<0.5%)	243 (<0.5%)	187 (<0.5%)	153 (<0.5%)	-	-	58,703 (57%)	58,703 (57%)
35	246 (<0.5%)	233 (<0.5%)	193 (<0.5%)	171 (<0.5%)	-	-	423 (<0.5%)	422 (<0.5%)
34	250 (<0.5%)	269 (<0.5%)	182 (<0.5%)	152 (<0.5%)	-	-	412 (<0.5%)	339 (<0.5%)

Bin index	Count (fraction) of modified records							
	M3 150 kHz Quartermaster		M4 150 kHz Quartermaster		M3 75 kHz LongRanger		M4 75 kHz LongRanger	
	V_{East}	V_{North}	V_{East}	V_{North}	V_{East}	V_{North}	V_{East}	V_{North}
33	219 (<0.5%)	231 (<0.5%)	196 (<0.5%)	155 (<0.5%)	99,913 (97%)	99,913 (97%)	370 (<0.5%)	401 (<0.5%)
32	210 (<0.5%)	250 (<0.5%)	166 (<0.5%)	159 (<0.5%)	85,961 (83%)	85,961 (83%)	338 (<0.5%)	310 (<0.5%)
31	224 (<0.5%)	220 (<0.5%)	157 (<0.5%)	133 (<0.5%)	65,559 (64%)	65,559 (64%)	356 (<0.5%)	380 (<0.5%)
30	228 (<0.5%)	210 (<0.5%)	141 (<0.5%)	132 (<0.5%)	472 (1%)	513 (1%)	336 (<0.5%)	363 (<0.5%)
29	221 (<0.5%)	206 (<0.5%)	109 (<0.5%)	115 (<0.5%)	528 (1%)	517 (1%)	394 (<0.5%)	385 (<0.5%)
28	211 (<0.5%)	205 (<0.5%)	103 (<0.5%)	103 (<0.5%)	486 (1%)	540 (1%)	327 (<0.5%)	372 (<0.5%)
27	185 (<0.5%)	210 (<0.5%)	94 (<0.5%)	85 (<0.5%)	446 (<0.5%)	494 (1%)	385 (<0.5%)	354 (<0.5%)
26	198 (<0.5%)	211 (<0.5%)	99 (<0.5%)	91 (<0.5%)	467 (1%)	412 (<0.5%)	374 (<0.5%)	436 (<0.5%)
25	210 (<0.5%)	206 (<0.5%)	68 (<0.5%)	89 (<0.5%)	432 (<0.5%)	456 (<0.5%)	416 (<0.5%)	388 (<0.5%)
24	192 (<0.5%)	214 (<0.5%)	95 (<0.5%)	56 (<0.5%)	396 (<0.5%)	440 (<0.5%)	480 (1%)	480 (1%)
23	188 (<0.5%)	189 (<0.5%)	82 (<0.5%)	94 (<0.5%)	508 (1%)	557 (1%)	550 (1%)	520 (1%)
22	257,078 (100%)	257,078 (100%)	250,734 (98%)	250,734 (97%)	611 (1%)	633 (1%)	530 (1%)	546 (1%)
21	253,907 (100%)	253,907 (99%)	235,592 (92%)	235,592 (92%)	638 (1%)	611 (1%)	538 (1%)	579 (1%)
20	248,976 (97%)	248,976 (97%)	231,953 (90%)	231,953 (90%)	610 (1%)	630 (1%)	549 (1%)	653 (1%)
19	257,100 (100%)	257,100 (100%)	232,744 (90%)	232,744 (90%)	610 (1%)	644 (1%)	620 (1%)	586 (1%)
18	253,040 (99%)	253,040 (99%)	24 (<0.5%)	22 (<0.5%)	551 (1%)	592 (1%)	587 (1%)	562 (1%)
17	175 (<0.5%)	158 (<0.5%)	30 (<0.5%)	23 (<0.5%)	521 (1%)	563 (1%)	544 (1%)	527 (1%)
16	133 (<0.5%)	150 (<0.5%)	28 (<0.5%)	21 (<0.5%)	536 (1%)	560 (1%)	603 (1%)	542 (1%)
15	144 (<0.5%)	157 (<0.5%)	25 (<0.5%)	27 (<0.5%)	537 (1%)	493 (1%)	540 (1%)	572 (1%)

Bin index	Count (fraction) of modified records							
	M3 150 kHz Quartermaster		M4 150 kHz Quartermaster		M3 75 kHz LongRanger		M4 75 kHz LongRanger	
	V_{East}	V_{North}	V_{East}	V_{North}	V_{East}	V_{North}	V_{East}	V_{North}
14	148 (<0.5%)	173 (<0.5%)	14 (<0.5%)	26 (<0.5%)	461 (<0.5%)	433 (<0.5%)	591 (1%)	602 (1%)
13	134 (<0.5%)	131 (<0.5%)	22 (<0.5%)	25 (<0.5%)	541 (1%)	488 (1%)	486 (1%)	505 (1%)
12	119 (<0.5%)	144 (<0.5%)	19 (<0.5%)	23 (<0.5%)	436 (<0.5%)	494 (1%)	451 (<0.5%)	450 (<0.5%)
11	119 (<0.5%)	135 (<0.5%)	21 (<0.5%)	12 (<0.5%)	514 (1%)	534 (1%)	515 (1%)	532 (1%)
10	136 (<0.5%)	145 (<0.5%)	13 (<0.5%)	15 (<0.5%)	398 (<0.5%)	439 (<0.5%)	428 (<0.5%)	512 (1%)
9	134 (<0.5%)	144 (<0.5%)	16 (<0.5%)	8 (<0.5%)	315 (<0.5%)	300 (<0.5%)	359 (<0.5%)	326 (<0.5%)
8	119 (<0.5%)	159 (<0.5%)	14 (<0.5%)	9 (<0.5%)	242 (<0.5%)	250 (<0.5%)	241 (<0.5%)	223 (<0.5%)
7	127 (<0.5%)	142 (<0.5%)	9 (<0.5%)	5 (<0.5%)	103 (<0.5%)	100 (<0.5%)	127 (<0.5%)	122 (<0.5%)
6	147 (<0.5%)	153 (<0.5%)	9 (<0.5%)	5 (<0.5%)	81 (<0.5%)	96 (<0.5%)	131 (<0.5%)	135 (<0.5%)
5	149 (<0.5%)	176 (<0.5%)	6 (<0.5%)	7 (<0.5%)	53 (<0.5%)	72 (<0.5%)	63 (<0.5%)	46 (<0.5%)
4	137 (<0.5%)	151 (<0.5%)	5 (<0.5%)	4 (<0.5%)	33 (<0.5%)	29 (<0.5%)	47 (<0.5%)	50 (<0.5%)
3	129 (<0.5%)	149 (<0.5%)	5 (<0.5%)	4 (<0.5%)	13 (<0.5%)	30 (<0.5%)	26 (<0.5%)	36 (<0.5%)
2	112 (<0.5%)	132 (<0.5%)	4 (<0.5%)	1 (<0.5%)	37 (<0.5%)	22 (<0.5%)	21 (<0.5%)	14 (<0.5%)
1	91 (<0.5%)	110 (<0.5%)	6 (<0.5%)	5 (<0.5%)	103,063 (100%)	103,063 (100%)	103,059 (100%)	103,059 (100%)

After the current time-series was averaged to 20-minute intervals there were remaining suspect records near the surface. The values with high associated error velocities and low beam correlation were removed using an ADCP full water column visual editing tool. The number of records modified in step 9 is shown in Figure 11 and Table 17. This processing step was applied to both the V_{North} and V_{East} velocity components and so only the count of vector velocity records is listed for each instrument in Table 17. Table 17 also lists the count and fraction of flagged values in both the V_{North} and V_{East} channels of the final quality-controlled time-series. The Quartermaster instruments are missing data in the 55 m to 65 m and 45 m to 52 m depth bins at M3 and M4, respectively. This is due to interference with the shallower IPS instrument on the same mooring. The Quartermasters are also missing data shallower in the water column due to low signal strength

caused by an episodic lack of scatterers such as bubbles and passively moving biology which otherwise scatter the acoustic sonar pulse and return a fraction of this energy to the instrument. Turbulence in the near-surface layer reduces data quality in corresponding depth bins. The LongRangers also contain missing data records due to a lack of scattering in the water column. This occurs mostly during the winter and spring when the ice concentration is high and concentration of biological scatterers are low.

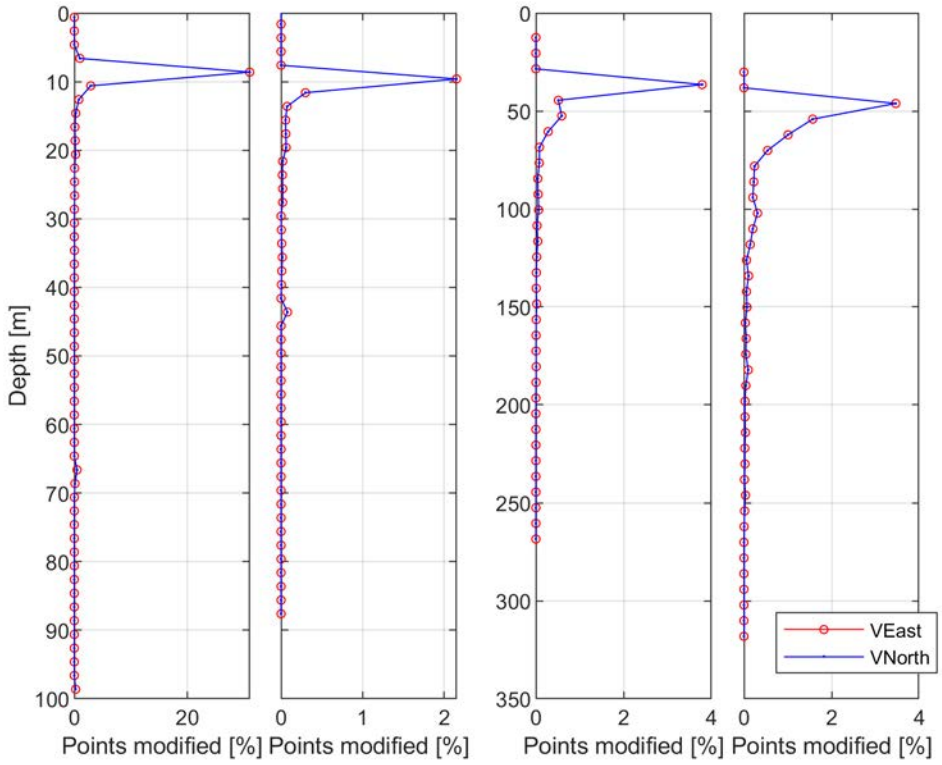

Figure 12. Fraction of data records modified before time-averaging for the (from left to right) M3 Quartermaster, M4 Quartermaster, M3 LongRanger, and M4 LongRanger.

Table 17.

Count and fraction of data records modified after time-averaging for each ocean current bin.

Bin index	Count (percent) of modified records				Count (percent) of flagged records			
	M3 150 kHz Quarter-master	M4 150 kHz Quarter-master	M3 75 kHz Long-Ranger	M4 75 kHz Long-Ranger	M3 150 kHz Quarter-master	M4 150 kHz Quarter-master	M3 75 kHz Long-Ranger	M4 75 kHz Long-Ranger
50	0 (<0.5%)	0 (<0.5%)	-	-	25,728 (100%)	-	-	-
49	0 (<0.5%)	0 (<0.5%)	-	-	25,728 (100%)	-	-	-
48	0 (<0.5%)	0 (<0.5%)	-	-	25,728 (100%)	-	-	-
47	253 (1%)	0 (<0.5%)	-	-	25,728 (100%)	-	-	-
46	7,984 (31%)	0 (<0.5%)	-	-	25,728 (100%)	-	-	-
45	748 (3%)	0 (<0.5%)	-	-	10,919 (42%)	-	-	-
44	205 (1%)	0 (<0.5%)	-	-	7,199 (28%)	25,732 (100%)	-	-
43	67 (<0.5%)	0 (<0.5%)	-	-	6,390 (25%)	25,732 (100%)	-	-
42	27 (<0.5%)	0 (<0.5%)	-	-	5,902 (23%)	25,732 (100%)	-	-
41	40 (<0.5%)	0 (<0.5%)	-	-	5,451 (21%)	25,732 (100%)	-	-
40	59 (<0.5%)	553 (2%)	-	-	5,010 (20%)	4,974 (19%)	-	-
39	15 (<0.5%)	77 (<0.5%)	-	-	4,606 (18%)	3,973 (15%)	-	-
38	14 (<0.5%)	19 (<0.5%)	-	-	4,179 (16%)	3,401 (13%)	-	-
37	17 (<0.5%)	14 (<0.5%)	-	0 (<0.5%)	3,776 (15%)	2,972 (12%)	-	25,768 (100%)
36	4 (<0.5%)	15 (<0.5%)	-	0 (<0.5%)	3,451 (13%)	2,650 (10%)	-	25,768 (100%)
35	4 (<0.5%)	16 (<0.5%)	-	892 (4%)	3,149 (12%)	2,307 (9%)	-	12,493 (49%)

Bin index	Count (percent) of modified records				Count (percent) of flagged records			
	M3 150 kHz Quarter-master	M4 150 kHz Quarter-master	M3 75 kHz Long-Ranger	M4 75 kHz Long-Ranger	M3 150 kHz Quarter-master	M4 150 kHz Quarter-master	M3 75 kHz Long-Ranger	M4 75 kHz Long-Ranger
34	0 (<0.5%)	5 (<0.5%)	-	404 (2%)	2,789 (11%)	2,027 (8%)	-	12,678 (49%)
33	8 (<0.5%)	4 (<0.5%)	0 (<0.5%)	259 (1%)	2,611 (10%)	1,842 (7%)	25,770 (100%)	13,369 (52%)
32	1 (<0.5%)	5 (<0.5%)	0 (<0.5%)	139 (1%)	2,419 (9%)	1,646 (6%)	25,770 (100%)	13,672 (53%)
31	1 (<0.5%)	5 (<0.5%)	0 (<0.5%)	62 (<0.5%)	2,251 (9%)	1,475 (6%)	25,770 (100%)	13,949 (54%)
30	0 (<0.5%)	0 (<0.5%)	977 (4%)	58 (<0.5%)	2,086 (8%)	1,288 (5%)	10,555 (41%)	14,121 (55%)
29	2 (<0.5%)	1 (<0.5%)	132 (1%)	52 (<0.5%)	1,972 (8%)	1,137 (4%)	10,068 (39%)	14,073 (55%)
28	0 (<0.5%)	2 (<0.5%)	152 (1%)	80 (<0.5%)	1,909 (7%)	970 (4%)	10,979 (43%)	14,093 (55%)
27	2 (<0.5%)	4 (<0.5%)	72 (<0.5%)	52 (<0.5%)	1,936 (8%)	902 (4%)	11,732 (46%)	13,835 (54%)
26	3 (<0.5%)	2 (<0.5%)	21 (<0.5%)	37 (<0.5%)	1,929 (8%)	779 (3%)	11,962 (46%)	13,563 (53%)
25	3 (<0.5%)	1 (<0.5%)	20 (<0.5%)	15 (<0.5%)	1,801 (7%)	663 (3%)	11,656 (45%)	13,295 (52%)
24	2 (<0.5%)	0 (<0.5%)	11 (<0.5%)	27 (<0.5%)	1,634 (6%)	569 (2%)	11,262 (44%)	12,664 (49%)
23	3 (<0.5%)	20 (<0.5%)	13 (<0.5%)	15 (<0.5%)	1,260 (5%)	738 (3%)	10,780 (42%)	11684 (45%)
22	0 (<0.5%)	0 (<0.5%)	16 (<0.5%)	18 (<0.5%)	25,728 (100%)	25,732 (100%)	10,271 (40%)	10,712 (42%)
21	0 (<0.5%)	0 (<0.5%)	7 (<0.5%)	8 (<0.5%)	25,728 (100%)	25,732 (100%)	9,634 (37%)	9,514 (37%)
20	0 (<0.5%)	0 (<0.5%)	11 (<0.5%)	13 (<0.5%)	25,728 (100%)	25,732 (100%)	8,354 (32%)	8,196 (32%)
19	0 (<0.5%)	0 (<0.5%)	5 (<0.5%)	11 (<0.5%)	25,728 (100%)	25,732 (100%)	7,682 (30%)	6,775 (26%)
18	0 (<0.5%)	0 (<0.5%)	3 (<0.5%)	25 (<0.5%)	25,728 (100%)	465 (2%)	6,506 (25%)	5,523 (21%)

Bin index	Count (percent) of modified records				Count (percent) of flagged records			
	M3 150 kHz Quarter-master	M4 150 kHz Quarter-master	M3 75 kHz Long-Ranger	M4 75 kHz Long-Ranger	M3 150 kHz Quarter-master	M4 150 kHz Quarter-master	M3 75 kHz Long-Ranger	M4 75 kHz Long-Ranger
17	126 (1%)	0 (<0.5%)	2 (<0.5%)	11 (<0.5%)	875 (3%)	444 (2%)	5,398 (21%)	4,509 (18%)
16	29 (<0.5%)	0 (<0.5%)	5 (<0.5%)	6 (<0.5%)	693 (3%)	432 (2%)	4,467 (17%)	3,874 (15%)
15	2 (<0.5%)	0 (<0.5%)	2 (<0.5%)	6 (<0.5%)	583 (2%)	415 (2%)	3,647 (14%)	3,274 (13%)
14	2 (<0.5%)	0 (<0.5%)	1 (<0.5%)	9 (<0.5%)	474 (2%)	405 (2%)	2,915 (11%)	2,551 (10%)
13	0 (<0.5%)	0 (<0.5%)	1 (<0.5%)	5 (<0.5%)	353 (1%)	396 (2%)	2,228 (9%)	1,862 (7%)
12	0 (<0.5%)	0 (<0.5%)	2 (<0.5%)	6 (<0.5%)	295 (1%)	390 (2%)	1,536 (6%)	1,163 (5%)
11	0 (<0.5%)	0 (<0.5%)	1 (<0.5%)	3 (<0.5%)	264 (1%)	389 (2%)	814 (3%)	598 (2%)
10	2 (<0.5%)	0 (<0.5%)	0 (<0.5%)	9 (<0.5%)	218 (1%)	389 (2%)	451 (2%)	252 (1%)
9	0 (<0.5%)	0 (<0.5%)	0 (<0.5%)	4 (<0.5%)	148 (1%)	384 (2%)	238 (1%)	127 (1%)
8	0 (<0.5%)	0 (<0.5%)	0 (<0.5%)	1 (<0.5%)	125 (1%)	385 (2%)	124 (1%)	72 (<0.5%)
7	0 (<0.5%)	0 (<0.5%)	0 (<0.5%)	0 (<0.5%)	91 (<0.5%)	383 (2%)	91 (<0.5%)	49 (<0.5%)
6	0 (<0.5%)	0 (<0.5%)	0 (<0.5%)	0 (<0.5%)	70 (<0.5%)	384 (2%)	55 (<0.5%)	39 (<0.5%)
5	0 (<0.5%)	0 (<0.5%)	0 (<0.5%)	0 (<0.5%)	52 (<0.5%)	383 (2%)	33 (<0.5%)	29 (<0.5%)
4	0 (<0.5%)	0 (<0.5%)	0 (<0.5%)	0 (<0.5%)	3 (<0.5%)	383 (2%)	14 (<0.5%)	11 (<0.5%)
3	0 (<0.5%)	0 (<0.5%)	0 (<0.5%)	0 (<0.5%)	0 (<0.5%)	384 (2%)	7 (<0.5%)	4 (<0.5%)
2	0 (<0.5%)	0 (<0.5%)	0 (<0.5%)	0 (<0.5%)	0 (<0.5%)	383 (2%)	2 (<0.5%)	0 (<0.5%)
1	60 (<0.5%)	0 (<0.5%)	0 (<0.5%)	0 (<0.5%)	60 (<0.5%)	383 (2%)	25,770 (100%)	25,768 (100%)

2.4.1.6 Ice velocity time-series

Ice velocity measurements were made with the M3 and M4 Quartermaster ADCPs using the bottom-tracking feature. The following methodology was used when processing the raw ADCP ice velocity time-series data:

1. Extract the bottom-tracking time-series from the bottom-tracking variable in the raw data file.
2. Time-drift information recorded by the field crew is used to calculate a revised sample interval, assuming a linear time drift of the instrument clock.
3. Average data to ~20-minute sample interval to reduce Doppler noise but keep enough time resolution for expected ice velocity phenomena.
4. Trim to the in-water portion of the deployment.
5. Identify episodes of probable open water and anomalous velocity values in each data record. Use supplemental information to identify these episodes, including IPS time-series, ice charts, satellite imagery as well as instrument-recorded data quality indicators including error velocity, vertical velocity, correlation and echo amplitude. For these episodes, set the values of the horizontal ice velocity components to flag values of -9999.
6. Identify remaining horizontal ice velocity values exceeding the out-of-bound threshold in absolute value (150 cm·s-1).
7. For all suspect values found in steps 5 and 6, the values are replaced by linear interpolation over individual segments with durations of less than one hour. For longer data gaps coincident with substantial ice floes recorded by the IPS, construct ice velocity records using upper water column velocities, surface winds, interpolation and smoothing with short-term moving averages. If the ice velocities cannot be reconstructed, then flag the values as unreliable using -9999.
8. Identify sections of higher error velocity and higher velocity variability and apply a moving average filter.
9. Plot the edited ice velocity time-series, evaluate, and repeat editing steps as required.

Table 18 details the number of points modified at each site for each ice velocity component. This includes the automatic detection and interpolation of outliers and spikes as well as manual review and adjustment of data.

Table 18.

Summary of edited ice velocity time-series records for the M3 and M4 Quartermasters.

	M3 150 kHz Quartermaster		M4 150 kHz Quartermaster	
	VEast	VNorth	VEast	VNorth
Automatically despiked	295	295	0	0
Smoothed via moving average	927	642	189	189
Manually edited	351 (1%)	259 (1%)	392 (2%)	371 (1%)
Manually edited and <1 cm·s-1	163 (1%)	96 (<0.5%)	57 (<0.5%)	48 (<0.5%)
Total edited	646 (3%)	554 (2%)	392 (2%)	371 (1%)
Flagged	10,076 (39%)	10,076 (39%)	10,223 (40%)	10,223 (40%)
Total time-series length	25,728	25,728	25,732	25,732

2.4.2 ADCP Backscatter

As a first step, the measured return signal strength amplitude (Mullison, 2017) for each beam was compared between the four beams of each ADCP to ensure that the signal strengths were relatively compatible and that there was no drift or deviation in one of the four beams over the period (~1 year) of the deployment. To do this, the signal strengths for all four beams were plotted together for all the bins in the profile at 12 evenly spaced periods during the deployment period. Some variation between beams was expected. None of the instruments displayed substantial deviations in the signal strengths for the individual beams over the deployment period. As a result, all four beams were included in the average signal strength amplitudes for the deployment. This analysis also identified periods with bad data at the start and end of the record that were collected while the instrument was on deck before and after deployment; these ensembles were removed in subsequent analyses.

Calculation of "absolute" backscatter

"Absolute" backscatter was calculated for using measured return signal strength amplitude (counts) from the four beams or each instrument according to the updated equation in Mullison (2017). Mullison (2017) updated the equation of Deines (1999) to include the correct calculation of signal to noise and to be more correct for very low backscatter environments. Accordingly, the equation is:

Equation 1 $$S_v = C + 10\log((T_x + 273.16)R^2) - L_{DBM} - P_{DBW} + 2\alpha R + 10\log(10^{kc(E-Er)/10}-1)$$

where S_v is the absolute backscatter equation, C is an RDI ADCP model specific constant that depends on the bandwidth used, Tx is the transducer temperature for profile x, k_c is a factor used to convert counts to decibels (dB) that is specific for each beam for each instrument, R is the along-beam range, E is the return strength signal indicator (counts), E_r is the measured return strength in the absence of any signal, L_{DBM} is 10log(pulse length), and P_{DW} is 10logTransmit power. P_{DBW} are from Mullison (2017), and α is from Deines (1999), and L_{DBM}, R and E_r are calculated from the data and settings of the instrument. For these data, E_r for each instrument was calculated as the minimum E recorded for the period of the deployment; for all instruments, this minimum was collected from the furthest bin from the instrument (a similar approach was taken using an Acoustic

Zooplankton Fish Profiler (AZFP) by Kitamura et al. 2017). As a check, the minimum E was also determined for each beam from bins located below the sea surface; the E_r values from these calculations were very similar to the minima calculated from the entire data set. Values of K_c for each beam for each instrument were obtained from Teledyne. Range (R) was calculated according to equation (3) in Deines 1999 using the blank, bin length, pulse length, beam angle, and bin number. After the absolute backscatter was calculated for each beam, those values were averaged for the four beams.

Despite S_v being termed "absolute backscatter" (Mullison, 2017), there remains sufficient uncertainty in the calculation to still consider it as a type of relative backscatter, albeit carefully calculated.

Editing of spurious data

Once the backscatter was calculated, additional editing was conducted for each data set to remove spurious data resulting from backscatter off of sea ice, off of floats suspending instruments shallower on the mooring string than the ADCP (M2a), and from unknown but obvious interference. For each data set (the mean S_v from the four beams), all points at depths shallower than the surface, including a few meters to remove scattering from the surface, were removed. Since the velocity data had already been checked for QA/QC as explained in Section 2.4.1, the velocity arrays provided a useful template to blank out data contaminated by backscatter from sea ice in the upper water column. The ADCP M2a was deployed below three floats supporting other instrumentation; these floats produced spurious data in one or more depth bins that also had to be blanked out. Each profile then was smoothed using a 5-point running average; for depths where a single or several observations had been removed by the blanking (such as for the floats), the smoothing produced a meaningful value. The smoothing also had the effect of adding large spurious values at depths where sea ice had been present; these were removed either by re-applying the velocity derived mask to blank out those data or to convert the very high values to blanks. Smoothed backscatter was used for all analyses.

Generating common depth horizons

Because the actual depths of the instruments varied according to the angle of the mooring string in the water, each profile had a unique set of depth intervals. To generate common depth intervals across the entire record for each instrument, the mean depth was calculated for each bin from all of the profiles in the record. That mean depth was then used as the depth of the bin for subsequent analyses. Variation was quite small, with standard deviations of 0.1464 m, 0.1336 m, and 0.0912 m for instruments M1a, M2a, and M2b, respectively. The end result is an array for each re-gridded variable of the same size as the original data but with common depth horizons for each profile.

Winds

Winds frequently drive physical processes on the Beaufort Shelf. Associations between winds, currents, and backscatter were explored using National Centers for Environmental Prediction (NCEP) reanalysis winds. Winds also were available from Herschel Island, but these data were much noisier. The two data sets compared well in gross features but the higher variability in the Herschel Island data resulted in correlation only of about 0.5 for both wind direction and wind magnitude.

Detecting Diel Vertical Migration (DVM)

Examination of the 10-day rough plots of backscatter revealed changes in vertical distribution of backscatter on a daily basis during some periods that were characteristic of diel vertical migration (DVM). A method was developed to detect periods of DVM that was similar to the approach of Ashjian et al. (1998, 2002). Rather than using the median depth to detect diel patterns, as was done in those analyses, here the backscatter at an indicator depth was examined. Backscatter at 17 m and at 82 m were extracted for moorings M1a and M2b, respectively. These depths were in the middle of the range of the depth data for each instrument and for some periods showed a daily periodicity in magnitude. The times of each profile in the data was converted to local Alaskan time by subtracting 8 hours from the UCT time (daylight savings time was not considered). This placed the time of sunrise and sunset within the 24 hours of a single day for most of the period of the deployment. Times of sunrise and sunset for each day were calculated. For each day in the data records, the time of the data points was adjusted so that the times of sunrise was set to 6 AM and of sunset at 6 PM and noon and midnight remained set, with points in between these four fixed points proportionally adjusted. This adjustment meant that a typical diel signal in the vertical distribution could be approximated using a sinusoidal curve. Also for each day, the magnitude of backscatter was standardized to the maximum value so that the range varied from 0 to 1. A sinusoid curve was calculated for each 24-hour period, using the cosine function and converting times from that day into degrees from 0 to 360. Both the standardized backscatter and the values of the sinusoid curve were adjusted to share a common range of -0.5 to 0.5. For each day, the deviation of the observed pattern in backscatter from the sinusoid was expressed as the sums of squares of the hourly differences between backscatter and the reference curve:

Equation 2 $$SS = \sum_{0}^{23}(\boldsymbol{Sv} - \boldsymbol{Sincurve})^2/(\boldsymbol{n} - \mathbf{1})$$

where:
SS is sums of squares
S_v is absolute backscatter
Sincurve is reference sinusoid curve
n is the number of observations

Good adherence to the sinusoid curve yielded SS values of ~0.15 or less.

2.4.3 Ice Profiling Sonar (IPS)

The IPS instrument is an upward-looking ice profiling sonar, which provides the high-resolution ice thickness, or more correctly, ice draft data required for characterizing the winter oceanic environment. The IPS operates in a pulsed mode with its acoustic beam directed toward zenith. A multi-faceted algorithm (Melling et al. 1995) identifies the target, which may be the underside of sea-ice or the air-water interface. Targets are detected using the range, amplitude and persistence parameters. From this initial selection, up to 5 targets of longest persistence are recorded. Choice of the control parameters must be carried out with a view to minimizing the likelihood that the algorithm will select echoes from sources within the water-column as opposed to the ice under-surface. The ice keel depth is determined from the return travel time of an acoustic pulse (420 kHz; 1.8° beam at -3 dB) reflected off the underside of the sea ice. The return time is converted to an acoustic range value using the speed of sound in seawater. A pressure sensor

(Paroscientific Digiquartz) is used to determine water level changes due to tidal and wind forcing, as well as apparent water level changes arising from depression/tilt of the mooring. A pitch/roll sensor enables correction of instrument tilt effects on the measured target ranges. A temperature sensor provides an estimate of the ambient water temperature near the instrument.

There are three primary concerns when configuring an IPS prior to deployment. Firstly, the sampling scheme for an IPS can be varied throughout a deployment using sampling phases. Each phase spans a set time episode and employs distinct sample intervals for the acquisition of acoustic and ancillary measurements. Secondly, the IPS firmware performs on-board target detection and requires setting of echo amplitude target parameters for each phase. Thirdly, the IPS employs multiple sensors including sonar, pressure, tilt, and temperature. Each sensor has a unique set of calibration coefficients determined during the manufacture and testing of an IPS unit. Table 19 and Table 20 list the key configuration parameters for the IPS units used at M3 and M4, respectively. Unfortunately, the IPS on M2 malfunctioned. Examining the data recovered, the ranges looked reasonable for a few days after deployment assuming open water. However, pressure and roll/pitch looked faulty. After a few days, ranges went unrealistic as well and it was determined the IPS failed. As a result, data processing was not pursued any further for the M2 IPS. The M3 and M4 IPS stopped recording earlier than planned on 2017-07-25 and 2017-06-09, respectively. The cause for both instruments was battery exhaustion as is evident in Figure 13. The following sections explain the supplemental data and methods used in pre-processing the multi-sensor IPS data channels.

Table 19.

Key M3 IPS configuration parameters:

Parameter	Phase				
	1	2	3	4	5
Start [yyyy-mm-dd UTC]	2016-10-01	2016-11-01	2016-12-15	2017-09-01	2017-10-04
End [yyyy-mm-dd UTC]	2016-10-31	2016-12-14	2017-08-31	2017-10-03	Continuous
Ping interval [sec]	5	1	1	5	5
Ancillary interval [sec]	60	10	10	60	60
Profile interval [sec]	7,200	600	600	7,200	7,200
Target start amplitude [counts]	10,000	10,000	7,000	10,000	10,000
Target stop amplitude [counts]	9,000	9,000	6,000	9,000	9,000
Minimum persistence [µsec]	62.5	62.5	62.5	62.5	62.5
Blanking range [m]	10	10	10	10	10
Maximum range [m]	85	85	85	85	85

Ping interval is the duration between successive acoustic pings.

Ancillary interval is the duration between successive pressure, tilt, temperature and battery voltage acquisitions. Profile interval is the duration between successive storage of the full echo profile corresponding to an acoustic ping. Target start amplitude is the threshold that must be exceeded to be considered a target.

Target stop amplitude is the threshold that defines the end of a target.

Minimum persistence is the duration between the target start and stop amplitudes that must be exceeded to be considered a target.

Blanking range and Maximum range are the minimum and maximum distances within which acoustic backscatter amplitudes are detected.

Table 20.

Key M4 IPS configuration parameters.

Parameter	Phase				
	1	2	3	4	5
Start [yyyy-mm-dd UTC]	2016-10-01	2016-11-01	2016-12-15	2017-09-01	2017-10-04
End [yyyy-mm-dd UTC]	2016-10-31	2016-12-14	2017-08-31	2017-10-03	Continuous
Ping interval [sec]	5	1	1	5	5
Ancillary interval [sec]	60	10	10	60	60
Profile interval [sec]	7200	600	600	7200	7200
Target start amplitude [counts]	10000	10000	7000	10000	10000
Target stop amplitude [counts]	9000	9000	6000	9000	9000
Minimum persistence [µsec]	62.5	62.5	62.5	62.5	62.5
Blanking range [m]	10	10	10	10	10
Maximum range [m]	85	85	85	85	85

Ping interval is the duration between successive acoustic pings.

Ancillary interval is the duration between successive pressure, tilt, temperature and battery voltage acquisitions. Profile interval is the duration between successive storage of the full echo profile corresponding to an acoustic ping. Target start amplitude is the threshold that must be exceeded to be considered a target.

Target stop amplitude is the threshold that defines the end of a target.

Minimum persistence is the duration between the target start and stop amplitudes that must be exceeded to be considered a target.

Blanking range and Maximum range are the minimum and maximum distances within which acoustic backscatter amplitudes are detected.

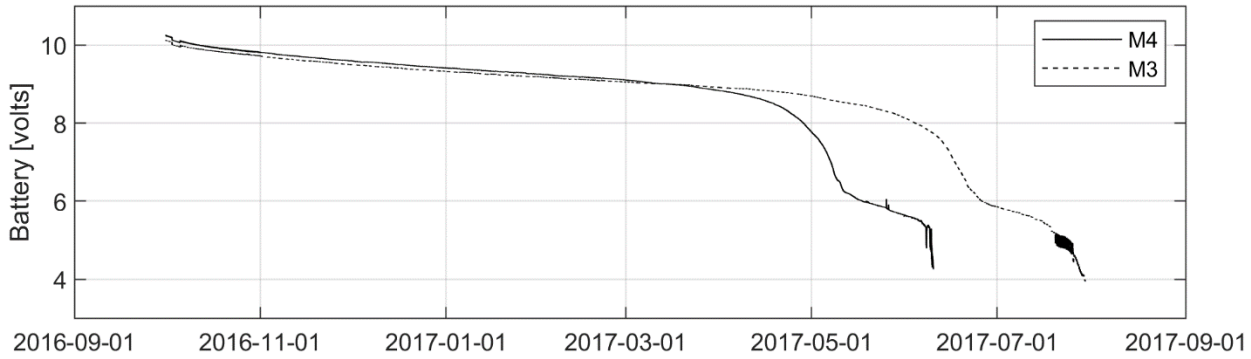

Figure 13. The M3 and M4 IPS battery voltage over the full deployment.

2.4.3.1 Supplemental data

The processing of an IPS dataset involves consideration of the regional oceanographic, meteorological and ice conditions throughout the deployment. This is particularly important when calibrating the IPS measurements for variations in seawater sound speed, distinguishing episodes of thin ice from open water, and accounting for ice motion. Additionally, the sea level atmospheric pressure at the measurement location is required in deriving an ice draft time-series from an IPS dataset.

To aid in the processing of the M3 and M4 IPS data, the following supplemental datasets were used:

- Meteorology from the Herschel Island meteorological station operated by Environment and Climate Change Canada, Meteorological Service of Canada (ECCC-MSC) (Hourly Data Report…2017). The relevant parameters included atmospheric pressure, wind speed and direction, and air temperature. Data was acquired from 2016-09-01 through 2017-10-30 and required the following processing steps:
  - Corrected the atmospheric pressure to sea level by assuming a hydrostatic conversion using an elevation of 1.2 m, air density of 1.3 $kg \cdot m^{-3}$, and local gravitational acceleration of 9.825834 $m \cdot s^{-2}$.
  - Linearly interpolated gaps in the sea level pressure time-series that spanned less than or equal to 10 hours.
  - Three gaps remained in the sea level pressure time-series that were longer than 10 hours in duration. The sea level pressure time-series acquired at the ECCC-MC Pelly Island meteorological station was considered for filling these gaps. The Pelly Island record demonstrated that linear interpolation approximated the sea level pressure change over two of these gaps. The third gap was filled using the Pelly Island record with an adjustment for phase and amplitude differences of -7 hours and +0.02 dbar, respectively.
- Sea ice charts from the Canadian Ice Service from 2016-09-05 through 2017-10-23 for the Western Arctic region (Archive Search 2017).

- Aqua/MODIS satellite imagery including the Corrected Reflectance (True Color) and Brightness Temperature (Band 31-Day) data products (NASA Worldview 2017).
- Ice velocity time-series from moored Acoustic Doppler Current Profilers (see Section 2.4.1.6).
- Ocean temperature and salinity from moored conductivity-temperature (CT) time-series and conductivity-temperature-depth casts (CTD) (see Section 3.1.3)

2.4.3.2 Pre-processing

IPS data pre-processing consists of the following steps in accordance with a methodology that has been developed since the 1990s (ASL Environmental Sciences Inc., 2017; Fissel et al., 2008; Melling et al., 1995); however, every data set is unique and the general processing procedures outlined below were customized as necessary:

1. Converting raw IPS data from binary form in instrument units to nominal engineering units using the IPS5Extract desktop application. The raw time-series data are plotted, and summary statistics are calculated. These are reviewed for major quality issues including instrument failure, large data gaps, high fractions of anomalous data values and ice events within the blanking range. Distinct events in the raw data such as the entry into and exit from the water are compared to field notes of the timing of these events to verify consistency with external observations. Events, such as mooring pull-down, that are evident in the range and pressure time-series are compared to verify the internal consistency of the time values associated with each raw data time-series.
2. Correcting the timing characteristics of the IPS data files for the effects of instrument clock time drift. The correction is derived from a comparison of instrument start and stop times with times from an independent clock recorded on start-up and shut-down of the instrument.
3. Automatically correcting for double bounce effects. The acoustic signal transmitted by the IPS can transit the water column multiple times. Under certain deployment conditions, this effect is recorded resulting in range measurements that are too high. If available in the target data, these records are replaced with more appropriate targets; otherwise, the range value is corrected arithmetically or by linear interpolation.
4. Removing unnecessary data at the start and end of the data record related to out-of-water time before deployment and after recovery.

5. Automated editing of range records associated with no targets. The IPS records the maximum amplitude and corresponding range for every ping regardless of the target detection results. For those pings that do not realize a target, this information can often be used to approximate a target range. All pings that realize a single target with moderate maximum amplitude, defined as the start amplitude plus 10,000 counts, are selected. The range difference between the start amplitude crossing point and the maximum amplitude is calculated for each of these selected targets. The average range difference is computed and is used to correct the range at maximum amplitude for those pings that did not realize a target but whose maximum amplitude exceeded 500 counts. Any gaps remaining after this null target replacement step that are shorter than 10 seconds are linearly interpolated. Figure 14 shows an example data segment containing range drop-outs.

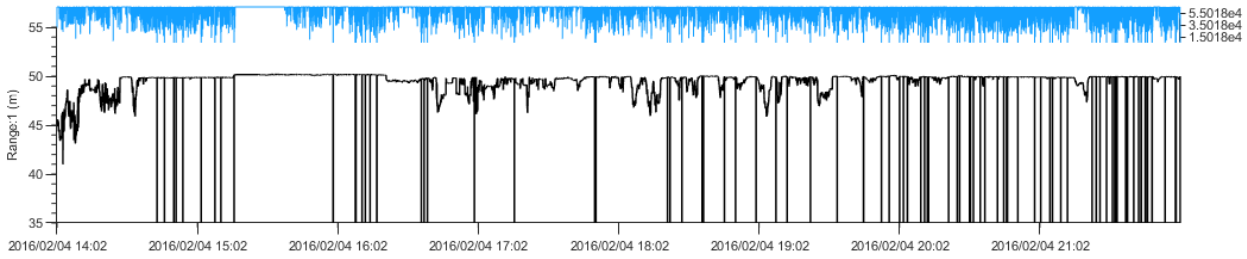

Figure 14. An example of unedited range and amplitude data measured by an IPS, showing a period characterized by sea-ice floes and some range "drop-outs".

1. Automated editing of range values considered to be too high. The detection threshold for high range values is calculated as: instrument depth at high tide + buffer. The buffer value avoids clipping of wave peaks and is determined through a manual review of the raw data.
2. Masking of segments of range data that show evidence of large waves. This prevents the records corresponding to the wave extremes from being identified as spikes in the later automated despiking steps. Figure 15 shows an example data segment containing large waves.

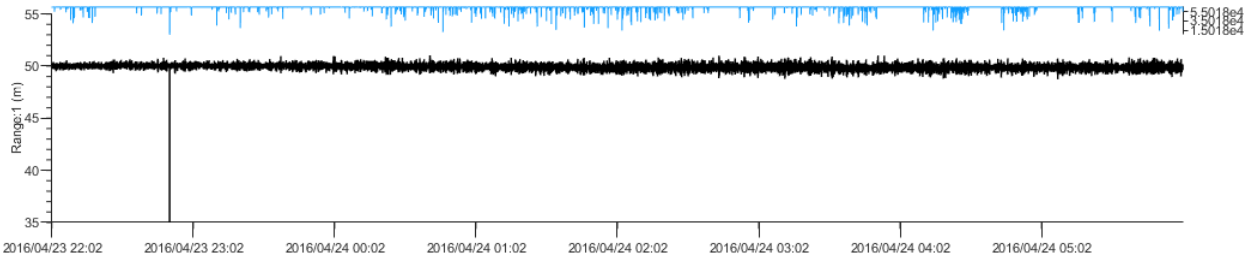

Figure 15. An example of unedited range and amplitude data measured by an IPS, showing a period following the main part of the ice season.

This is an example of 'rough open water' in which the returns obtained from targets below mean sea level are believed to result from the troughs of ocean waves and from bubbles located beneath the surface.

1. Automated removal of anomalous range and ancillary values based on first-difference values. This includes at least two iterations to remove anomalous features in the range data with lengths of one to four records. The thresholds are refined through trial despiking iterations and reviews of the results. Initial first difference thresholds for the range data is determined through the horizontal distance traveled by the average ice velocity over one IPS range sample interval.
2. Patching of the previously masked segments of range data back into the data record.
3. Manually reviewing the edited data for any additional spikes or suspect values. These may include targets within the lockout range and short duration targets due to bubbles associated with strong winds and large waves. The amplitude data is often helpful in classification of range features during this step.
4. Any remaining data gaps in the range, pressure and tilt time-series are reviewed and edited manually.
5. If available, the pressure measured by the IPS when the instrument is vertical and out of the water is compared to coincident and independent measurement of the sea level pressure. The pressure head due to the oil within the IPS pressure sensor must be accounted for. Any resulting offset is applied as a correction to the IPS pressure.

The extent of editing that resulted from the above pre-processing steps is summarized for the M3 and M4 IPS datasets in Table 21 and Table 22, respectively.

Table 21.

Summary of the two main stages of IPS processing.

	Phase	1	2	3
	Start date/time [yyyy-mm-dd hh:mm:ss UTC]	2016-10-05 21:10:09	2016-12-15 00:01:51	2015-12-15 00:01:59
	Stop date/time [yyyy-mm-dd hh:mm:ss UTC]	2016-10-31 23:58:57	2016-12-14 00:00:52	2017-07-25 19:19:55
	Sample interval [sec]	4.9999853	0.9999972	0.9999973
Target	Replaced multiple transit [# records]	0	0	0
	Replaced null targets [# records]	80	128,775	109,008
	Interpolated null targets [# records]	0	0	0
	Interpolated out-of-bound [# records]	0	0	0
	Interpolated single spikes [# records]	0	2,572	14,331
	Interpolated double spikes [# records]	0	562	1,010
	Interpolated triple spikes [# records]	0	54	24
	Interpolated quadruple spikes [# records]	0	4	4
	Interpolated manually [# records]	1	0	78,696
Ice draft	Interpolated manually [# records]	0	70	3,012
	Identified open water (-200) [# records]	451,308 (100%)	389307 (10%)	4,096,473 (21%)
	Total data [# records]	451,308	3,801,671	19,250,330
	Identified poor-quality data (-9999) [#records]	0	0	0
	Total edited data [# records]	81 (<1%)	132,037 (3%)	206,085 (1%)

Range time-series and ice draft time-series for M3, giving number of data records having errors that were detected and edited. Distinction is made between those records that have been interpolated and those that have been replaced by other measurement data. The instrument stopped recording before Phase 4 began.

Table 22.

Summary of the two main stages of IPS processing.

	Phase	1	2	3
	Start date/time [yyyy-mm-dd hh:mm:ss UTC]	25-10-05 23:08:11	2016-11-01 00:00:52	2016-12-15 00:02:02
	Stop date/time [yyyy-mm-dd hh:mm:ss UTC]	2016-10-31 23:59:29	2016-12-15 00:01:57	2017-06-09 10:01:46
	Sample interval [sec]	5.00003549	1.00001208	1.00001215
Target	Replaced multiple transit [# records]	0	0	0
	Replaced null targets [# records]	0	0	140
	Interpolated null targets [# records]	38	28,034	17,956
	Interpolated out-of-bound [# records]	0	0	0
	Interpolated single spikes [# records]	0	0	9
	Interpolated double spikes [# records]	0	2,780	12,487
	Interpolated triple spikes [# records]	0	390	1,180
	Interpolated quadruple spikes [# records]	0	18	27
	Interpolated manually [# records]	0	4	0
Ice draft	Interpolated manually [# records]	0	158	1,452
	Identified open water (-200) [# records]	449,894 (100%)	404,496 (11%)	150,984 (1%)
	Total data [# records]	449,894	3,801,620	15,242,200
	Identified poor-quality data (-9999) [#records]	0	0	0
	Total edited data [# records]	38 (<1%)	31,654 (1%)	33,251 (<1%)

Range time-series and ice draft time-series for M4, giving number of data records having errors that were detected and edited. Distinction is made between those records that have been interpolated and those that have been replaced by other measurement data. The instrument stopped recording before Phase 4 began.

2.4.4 SeaBird MicroCATs and McLane Moored Profiler (MMP)

Time series of temperature, conductivity, and pressure at the M1 tripod and M2 moorings were made by a series of SBE37 MicroCATs (MCs) and one McLane Moored Profiler (MMP, M2 mooring only). In addition to T, C, and P, the MMP also made optical measurements of turbidity, fluorescence, and photosynthetically available radiation (PAR).

2.4.4.1 MicroCATs

Following a pre-deployment laboratory calibration at the manufacturer (SeaBird), the M1 and M2 MicroCATs were prepared for sea at the Woods Hole Oceanographic Institution (WHOI). They were deployed on October 6, 2016 and recovered on September 27 (M1) and 28 (M2), 2017. Following recovery, the data were downloaded from the instruments, which were then sent to SeaBird for a post-deployment calibration. Data processing of the MicroCATs started with the conversion of the downloaded ascii records into MATLAB-readable form, followed by the

removal on-deck readings of temperature and conductivity (set to "nan"). We retained on-deck readings of pressure (or depth) as a deployment marker. Next, we edited for outlier spikes. Particularly the conductivity sensor can be affected by instrument contaminations that distort the readings. We made use of nearby MC readings to help distinguish between sharp short-term signals and contamination spikes. Lastly, we adjusted the pressure, temperature, and conductivity records for calibration changes as detected by pre- and post-cruise calibration differences. Without additional evidence, we assumed that sensor drifts occurred linearly in time over the course of the deployment. Both temperature and conductivity adjustments were small for the nine MCs on M1 and M2. Pressure did not need adjustment for any of these instruments. From the final data, we derived salinity as function of temperature, conductivity, and pressure using standard oceanographic algorithms.

Four SeaBird MicroCATs were deployed on each of the M3 and M4 moorings. All measured temperature and conductivity and four additionally measured pressure. All eight CT sensors were equipped with pumps to aid in correcting the measured conductivity values for thermal lag effects. Table 23 lists important parameters related to the deployment of each CT sensor on these moorings.

Table 23.

Key deployment parameters for the CT sensors used on the M3 and M4 moorings.

Mooring	Depth [m]	Measured	Sample Interval [s]
M3	50	Temperature, Conductivity	900
	130	Temperature, Conductivity	900
	190	Temperature, Conductivity	900
	250	Temperature, Conductivity, Pressure	900
M4	50	Temperature, Conductivity	900
	130	Temperature, Conductivity, Pressure	900
	190	Temperature, Conductivity, Pressure	900
	250	Temperature, Conductivity, Pressure	900

The measurement data from the eight CT sensors were subjected to the following quality control pre-processing steps:

1. Decode binary data. The data files downloaded from the instruments were converted from their raw format to an ASL .dat/.hdr file pair in scientific units.
2. Correcting the timing characteristics of the CT data files for the effects of instrument clock time drift. The correction is derived from a comparison of instrument start and stop times with times from an independent clock recorded on start-up and shut-down of the instrument.
3. Time-series cropping. The CT measurement data time-series are trimmed to only those times when the instrument was in the water and the mooring was stable on the seabed.
4. Automated anomaly detection and removal. Data spikes based on first-difference thresholds within the measurement data time-series were detected and linearly interpolated.
5. For those CT instruments without pressure sensors, the pressure time-series measured by a nearby instrument on the same mooring was used to add a pressure channel to the salinity and temperature time-series. All pressure time-series were corrected to remove the contribution from sea-level pressure so that the final.

2.4.4.2 McLane Moored Profiler (MMP)

Profiles of a set of hydrographic variables were collected by a vertical profiler, which traveled every six hours along the M2 mooring wire between the depths of 44 and 164 meters. The variables included conductivity, temperature, and pressure from a SeaBird SBE52 CTD, oxygen from a SeaBird SBE43, fluorescence and turbidity from two Seapoint sensors, and Photosynthetically Available Radiation (PAR) from a Biospherical Instruments photosynthetically active radiation (PAR) sensor.

The M2 MMP was prepared for sea at the Woods Hole Oceanographic Institution (WHOI) and was deployed on Oct 7, 2016. Following its recovery on September 27, 2017, the data were downloaded and converted from binary into ascii using the McLane's "Unpacker" software. The ascii data of temperature (T), conductivity (C), pressure, oxygen sensor frequency readings, as well as voltages from the analog sensors measuring turbidity, fluorescence, and PAR were made available to us on the project web site. We derived salinity (S) as well as water density from conductivity, temperature, and pressure using standard oceanographic formulae. Subsequent data processing included: remove sensor "warm-up" periods from each profile prior to and following the instruments crawl up- or down the mooring wire; edit for outlier spikes, primarily in conductivity; investigate the conductivity cell for calibration changes; vertically average into 2-dbar bins (T, S, P, and DO only).

The MMP conductivity sensor can be affected by contaminations that distort its readings. We made use of oceanographic properties to identify outliers, such as the unlikeliness of vertical density inversions, or anomalous T versus S characteristics compared to nearby MicroCATs. Vertical density decreases larger than 0.005 kg/m^3 triggered a warning flag. In some cases, modifying sensor lag times from their standard values, or the time constant and amplitude of the "thermal lag" effect - a known concern for SeaBird sensors, where the thermal mass of the instruments affects the conductivity readings in ways undetected by the temperature sensor, thus causing salinity and therefore density errors - alleviated the problem. More substantial contaminations required the removal of raw conductivity data. This affected 23 out of 2,153 profiles, eliminating 1,591 out of 1,345,629 total conductivity readings, or about 0.1 percent.

2.4.5 Acoustic Zooplankton Fish Profiler (AZFP)

The Acoustic Zooplankton Fish Profiler (AZFP) is calibrated to multiple frequencies to characterize the presence and abundance of zooplankton and fish in the water column. The storage and power capabilities of the AZFP allow for continuous acquisition at frequent sampling intervals over long deployments. Each acoustic ping realizes a profile of the acoustic backscatter over the water column. The maximum range is dependent on several factors but is most limited by the frequency of each transducer. The configuration of an AZFP enables the division of a deployment plan into several phases, each with their distinct set of sampling parameters.

Two AZFPs were housed on M3 at 59 m and 288 m water depth and one AZFP was placed on the UAF Sea Spider at approximately 13 m water depth. All AZFPs were deployed in an upward-looking configuration and employed sonar transducers with the following frequencies:

- UAF SeaSpider 13 m—38 kHz
- M3 59 m—125, 200, 455, and 769 kHz
- M3 288 m—38 kHz

The 38 kHz echosounder primarily detects adult and larval Arctic cod while zooplankton are tracked with the higher frequencies, although sound attenuation will limit the effective ranges. Differential backscatter among the four frequencies are used to differentiate targets (Korneliuss and Ona, 2002; Kitamura et al., 2017). Table 24 lists key parameters used in the configuration of each AZFP.

Table 24.

Key AZFP configuration parameters.

Parameter	M3 288 m	M3 59 m	UAF SeaSpider 13 m
Start [yyyy-mm-dd UTC]	2016-09-30 12:00:00	2016-09-25 12:00:00	2016-10-01 15:20:18
End [yyyy-mm-dd UTC]	2017-11-29 11:59:59	2017-11-24 11:59:59	2017-11-30 15:20:17
Ping interval [sec]	8	8	8
Bin averaging [m]	0.467	0.216	0.467
Blanking range [m]	0	0	0
Maximum range [m]	500	65	500

Ping interval is the duration between successive acoustic pings. Bin averaging is the depth distance span over which multiple acoustic backscatter acquisitions are averaged. Blanking range and Maximum range are the minimum and maximum distances within which acoustic backscatter amplitudes are detected. The same parameters apply to all employed frequencies.

2.4.5.1 Acoustic backscatter comparison

Acoustic data for zooplankton studies are occasionally collected using ADCPs (see Section 2.4.1), despite the ADCP being designed for current profiling rather than for zooplankton assessment. This repurposing of an instrument raises questions about its suitability for this purpose. To evaluate performance differences and to inform future study designs, a preliminary comparison of water column data between an AZFP with two Teledyne Marine Workhorse Quartermaster ADCPs was performed.

The rationale and methods for using the AZFP as a performance benchmark in this comparison is presented in sections 2.4.5.2 and 2.4.5.3. The preliminary comparison between AZFP and ADCP performance in the application of zooplankton study is presented in Section 3.4.2.1. Conclusions are drawn, and recommendations are made regarding the use of ADCPs for zooplankton studies in Section 3.4.2.1.

2.4.5.2 AZFP as a performance benchmark

The AZFP S/N 55089 mounted on M3 provides a suitable performance benchmark for comparison against the ADCPs located on M3 and on M4. Firstly, the AZFP interrogated the water column at center frequencies including 125 kHz and 200 kHz, which straddle the 150 kHz center frequency of the ADCPs. Additionally, the AZFP was located a few meters below multiple sets of mooring floats which provide persistent and consistent targets that can then be used to verify the consistency of the backscatter intensity as seen by the AZFP.

AZFPs are calibrated instruments and are specifically designed to maintain a consistent source level throughout the course of their operation. This implies that a persistent target, with a consistent target strength that does not substantially move throughout the beam will appear to have a consistent target strength throughout the course of the deployment. In contrast, a device such as

the deployed ADCPs that does not maintain a consistent source level will see a reduction in apparent target strength as the battery is depleted (2018 personal communication with Todd Mudge, ASL Environmental Sciences Inc.).

The first target within the AZFP data record appeared at a tilt-corrected vertical range of 3.3 m, corresponding to a slant range of 3.4 m. The second target appeared at a tilt-corrected range of 5.4 m, corresponding to a slant range of 5.6 m. Plots of the relevant AZFP data are presented in Section 3.4.2.2, where the received signal intensity in A/D counts and the volume backscattering intensity, S_v, in units of dB ref. 1 $m^2\ m^{-3}$ are shown for the 12-month time series.

A similar comparison between AZFP 55088 at a center frequency of 38 kHz and the deployed Teledyne Marine Workhorse Long Ranger ADCP at 75 kHz is possible; however, the relatively smaller frequency difference between AZFP 55089 and the Workhorse Quartermaster ADCPs is preferred when intercomparing.

2.4.5.3 Preliminary performance comparison

The preliminary performance comparison is facilitated by considering the backscatter intensity that was observed by all three instruments from a similar portion of the water column. This decision was made because the ADCPs did not observe a suitable single target (e.g. mooring floatation) that is common with the AZFP, and the comparison should involve either a common target or targets. In lieu of a common single target, a 25 m wide swath of the water column was chosen as the basis for this comparison.

The chosen swath extends from approximately 25 m to 50 m below the surface of the water. Within this region the acoustic backscatter did not include direct acoustic returns from mooring equipment, and largely excluded backscatter from ice floes. To facilitate the comparison, backscatter from within this swath was heavily averaged such that a single data point representing backscatter intensity is produced approximately once every 24 hours for both the ADCPs and AZFP. In the case of the ADCPs, this required averaging across all four beams, across range bins corresponding to the chosen swath, and across multiple ensembles. Ensemble averaging was performed such that a single data point was produced approximately each day after the data have been dropped to exclude mooring deployment and recovery. This resulted in a time series of 356 daily data points. The AZFP has a single 125 kHz channel, and a single 200 kHz channel, so the averaging for the AZFP was simply across range bins and across pings for each frequency. The averaging has been performed across pings in the AZFP such that similar time series of 356 data points were produced.

For a meaningful comparison, backscatter data from the AZFP and the ADCP are reported in units of decibels, for which a reference is required. The AZFP is a calibrated instrument that calculates volume backscattering intensity levels, S_v, in units of dB referenced to 1 m^2 m^{-3} directly; no manual adjustment or calculation is required, and S_v is reported on an absolute scale. ADCP backscatter data may be converted from A/D counts into decibels, but in this case the reference is 0 A/D counts, i.e., it is not an absolute reference. To compare ADCP data to AZFP data, an offset was introduced such that the ADCP backscattering data may be brought into approximate registration with AZFP data. The conversion of ADCP echo level, EL, in A/D counts into decibels has been accomplished in the following manner:

Equation 3

$$BI = \left(EL * \frac{127.3}{T}\right) + 20\log_{10} R + 2\alpha R + C$$

where BI is the relative backscatter intensity in units of dB referenced to 0 A/D counts before the offset C is applied, and T is the ADCP temperature reading in degrees Kelvin at each ensemble. Compensation is made for transmission loss consisting of spreading loss of $20\log_{10} R$ and acoustic absorption of $2\alpha R$, where α is the acoustic absorption term for seawater. A fixed offset C was introduced to bring the ADCP relative backscatter intensity measurement into approximate registration with the AZFP S_v output. In this analysis, C was determined empirically to be -158 dB through comparison of the AZFP and ADCP backscatter measurements during the initial part of each dataset. Two factors led to this offset being empirical: (1) the ADCPs are not calibrated and (2) it was expected that the ADCP transmit signal would weaken as the batteries deplete.

2.4.5.4 AZFP acoustic analysis

All acoustic analyses were performed with Myriax Echoview (version 8.0), R (version 3.5.1) and MATLAB (version 8.5). Acoustic data were converted to volume backscattering strength (S_v) as follows:

Equation 4

$$S_v = EL_{max} - \frac{2.5}{a} + \frac{N}{26214a} - TVR - 20logV_{TX} + 20logR + 2\alpha R - 10log\left(\frac{c\tau\varphi}{2}\right) \qquad (1)$$

where EL_{max} is the echo level (in dB re 1 µPa) at the transducer that produces full-scale output; N, in counts, is the digital recorded value and is linearly related to the received voltage (vin) after it has been amplified, bandpass filtered, and passed through a so-called "detector'' whose output is a function of log(vin2); a is the slope of the detector response; TVR is the transmit voltage response of the transducer in dB re 1 µPa/volt at 1 m range; VTX is the voltage amplification factor before it is sent out; α is the absorption coefficient, c is the speed of sound; and τ is the pulse length. R is the range calculated as R = ct/2. 20log R + 2αR represents the time-varied-gain (TVG) applied to compensate for transmission loss (TL). ϕ, the equivalent beam angle, is approximated by

$$\varphi = 1.4\pi(1 - cos\theta) \qquad (2)$$

where θ is half the full -3 dB beam angle of the transducer.

The density of targets per unit area is defined as:

$$\rho_a = \frac{NASC}{4\pi \times \sigma_{bs}} \quad (3)$$

where σbs is the backscattering cross-section (m^2). NASC, the nautical area scattering coefficient (m^2nmi-2), is a vertical integration of the volume backscattering strength over the sampled depth:

$$NASC = 4\pi \times 1852^2 \times 10^{\frac{Sv}{10}} \times T \quad (4)$$

T is the vertical extent of the analysis domain, and S_v the mean volume backscattering strength. In this study, we use NASC as an index of abundance, since it is proportional to fish density.

Acoustic noise from several sources was found in the acoustic data and needed to be removed prior to analysis. Impulse noise was removed using the Impulsive Noise (IN) algorithm (Ryan et al., 2015) implemented in Echoview. The algorithm was applied on a 5 x 5 window using a 10 dB threshold, and the thresholded data was replaced by the mean.

Background noise was removed by linear subtraction using Echoview's Background Noise Removal algorithm (DeRobertis and Higginbottom, 2007). Thresholds for maximum estimated noise were -140 dB at 125 kHz, -135 dB at 200 kHz, -123 dB at 455 kHz, and -113 dB at 769 kHz. These values were determined empirically. A signal-to-noise ratio of 10 dB specified the acceptable limit for a signal to be deemed distinguishable from noise.

Strong echoes corresponding to ice, as well as bubbles originating from surface waves, were often found near the surface. To exclude this signal from the analysis, an exclusion line was generated from the 125 kHz data using Echoview's maximum S_v algorithm. The exclusion line was reviewed and corrected manually. Data above this line, as well as data below a 7 m distance from the transducer's face, where side lobes had more effect, were excluded from the analysis.

Acoustic targets were separated into three classes: "Copepod", "Juvenile arctic cod", and "Adult arctic cod". Arctic Cod (*Boreogadus Saida*) is by far the most abundant fish in the Beaufort Sea (Benoit et al., 2008). Adults are found at deeper depth (> 100 m) whereas juvenile cod are found in the epipelagic layer (Parker-Stetter et al., 2011; Benoit et al., 2013). The single-frequency, inverted 38 kHz AZFP mounted near the bottom was used to detect adult cod. The analysis domain was 23 m to 188 m range above the echo-sounder (approximately 112 to 277 m depth). Beyond this, the signal-to-noise ratio was too high, and the acoustic signal was lost.

The shallower multi-frequency AZFP was used to detect juvenile cod and copepods in the epipelagic layer. The 125 and 200 kHz frequencies were used to separate the two classes. The data was re-sampled (1 m by 3 minutes) before subtracting data at 200 kHz from data at 125 kHz. A threshold of -1 dB < 125–200 kHz < 1 dB was used for juvenile cod and 125-200 kHz < -4 dB was used for copepods (Korneliuss and Ona, 2002; Kitamura et al., 2017).

2.4.6 Submersible Autonomous Moored Instrument (SAMI)

Submersible Autonomous Moored Instrument for CO_2 (SAMI-CO2) were deployed at the M1 and M2 mooring sites. SAMI 0009 was deployed at M1 at 39 m water depth and SAMI 0021 was

deployed at M2 at 39 m water depth. The SAMI-CO2 is a wet-chemical spectrophotometric system, using an indicator dye to determine concentration when CO_2 in the seawater diffuses across a permeable membrane. Collected data consists of temperature (°C) and partial pressure of carbon dioxide (pCO_2) (μatm). Data were downloaded from the SAMI-CO2 upon recovery and parsed using the software provided by the manufacturer, Sunburst Sensors. No additional manipulation was performed on the parsed data.

Discrete water samples were collected upon recovery at both sensor sites to validate the autonomous measurements. Sample collection and analysis followed best practices protocols (Dickson et al., 2007; Mathis et al., 2011). Seawater samples were drawn from Niskin bottles into pre-cleaned 200 mL borosilicate bottles using a tube to prevent gas exchange during sample transfer. Bottles were rinsed with the sample three times and filled, then immediately fixed with saturated mercuric chloride ($HgCl_2$) to halt biological activity, sealed, and returned to the laboratory for analysis.

Water samples were analyzed for Dissolved Inorganic Carbon (DIC) and Total Alkalinity (TA) at the Ocean Acidification Research Center (OARC) at UAF. The DIC and TA analyses were performed on a Marianda AIRICA and VINDTA, respectively. These instruments are routinely calibrated using Certified Reference Materials (CRMs) supplied by A.G. Dickson at the Scripps Institute of Oceanography, ensuring accuracy and stability of sample readings over time. For comparison to the mooring data, these discrete DIC and TA values were used to calculate a reference pCO_2 using the CO2CALC software (Robbins et al., 2010). These were shown to provide the best comparison between calculated system variables and discrete samples for pCO_2 in the arctic (Evans et al., 2015).

2.4.7 Submersible Ultraviolet Nitrate Analyzer (SUNA)

The SUNA instrument is an optical, chemical-free sensor that measures nitrate concentration by detecting the absorption of certain wavelengths across a beam path based on in-situ spectroscopy. The instrument employs a total of 256 wavelength channels. The nitrate processing uses the 217 nm to 240 nm wavelength range, corresponding to 35 of the measured channels. The SUNA instruments housed on the MARES moorings (M1 and M2) used a path length of 5 mm. For the 5 mm path length, the instrument has an accuracy of 4 μM (0.056 $mg \cdot N \cdot L^{-1}$) and a precision of 2.4 μM (0.034 $mg \cdot N \cdot L^{-1}$) in seawater. The instruments were configured to collect five samples at the beginning of every hour with three seconds between samples.

The SUNA gave an estimate of nitrate concentration by applying a multi-variate linear regression. The calculation of the nitrate concentration was determined primarily from four inputs: nitrate, bromide, lamp-temperature, and other absorbing species (other matter that absorbs light outside of the 217 nm to 240 nm band). The instrument also featured adaptive sampling such that extended conditions of high turbidity (or optically dense conditions) result in the lamp integration time being extended beyond the typical duration of 300 to 500 ms. This increase in the lamp-time can prematurely deplete the instrument battery.

The absorbance at the sensor is defined as:

Equation 5

$$A_\lambda = -\log\left(\frac{I_\lambda - I_D}{I_{\lambda,0} - I_D}\right)$$

where I_λ is the detector intensity at wavelength λ for light passing through a sample, $I_{\lambda,0}$ is the detector intensity at wavelength λ for light passing through DIW, and I_D is the intensity of the dark spectrum. The dark spectrum is sampled when the lamp is turned off to account for ambient illumination.

If the absorption of the sample is too high for the proxy wavelengths 254 nm and 350 nm (outside the nitrate absorption range), exceeding 1.3 absorption units (AU), then the instrument cannot collect sufficient light to make a measurement, and the model can no longer be used to effectively calculate the nitrate concentration. In this scenario, the root mean square error (RMSe) of the SUNA was used to make an estimate of the wellness of the nitrate spectral fit. The RMSe should typically be less than 10^{-3}. If it was higher it may indicate the presence of colored dissolved organic matter (CDOM) that adversely impacts the nitrate estimate.

The lamp and other optical components in the sensor drift with time resulting in changes to the measured nitrate concentration. This drift requires calibration checks be completed with de-ionized water (DIW) at deployment and again at recovery. There would also ideally be information about when the instrument clock was set so that an accurate time correction can be determined. Unfortunately, the instrument calibration information was not collected at deployment, so it was necessary to make assumptions which are discussed in the processing steps below.

At deployment and recovery, two samples from the water column were collected from each site and sent to a lab for analysis to compare to the measurements collected by the SUNA. The results from the lab analysis are presented in Table 25 although there is uncertainty surrounding the accuracy of the samples. Samples are typically stable for 12 hours in cold and dark conditions (Strickland and Parsons, 1960); however, this is a general heuristic for nutrients. Nitrate, on the other hand, tends to be one of the more forgiving nutrients. Macdonald and McLaughlin (1982) investigated the impact of quick freezing and regular freezing, thaw time and light exposure on phosphate, nitrate and silicate. Nitrate was not found to be impacted by quick freezing, and no dependence was found on thaw time, up to a maximum thaw time of 24 hours. Additionally, no dependence was found on exposure to light during the thaw process, for nitrate. Further studies by Fellman, D'Arnore and Hood (2007) examined the differences in measured dissolved organic nitrogen, dissolved organic carbon, and total dissolved phosphorus between flash freezing (-50°C) and standard freezer (-7°C). No statistically significant differences were found between the two temperatures. The frozen water samples were stored in a standard freezer.

Table 25.

Water sample nitrate laboratory results analyzed on 2017-11-01.

Sample ID*	Acquisition date [yyyy-mm-dd hh:mm UTC]	Nitrate concentration [$mg \cdot L^{-1}$]**	Hold time [days]
M1R	2017-09-27 22:20	0.118	35
M2R	2017-09-28 21:49	<0.050	34
M1D	2017-10-02 23:21	0.066	30
M2D	2017-10-03 23:12	<0.050	29

*The R and D in the sample IDs indicate recovery and deployment, respectively. **The detection limit is 0.050 $mg \cdot L^{-1}$.

Test measurements of the instrument in DIW were also collected to help correct or two possible sources of sensor drift. The first is due to biofouling due to biological matter accumulating on the optical sensor. The second is due to internal instrument drift due to changes in the battery voltage and lamp brightness. During the first test measurement the instrument was submersed in DIW prior to cleaning. This measured the combined effects of biofouling and internal error. The instrument was then cleaned, and any biofouling removed from the lens. During the second test measurement the instrument was submersed in DIW following this cleaning. This measurement recorded the error due to internal instrument drift. The results from the calibration measurements are available in Table 26. The second measurement should have been be compared to the measurements following calibration at deployment but because this information was not collected it is unknown whether the instrument was properly calibrated, meaning that there may be some error following the application of the drift correction.

Table 26.

Calibration measurements after instrument recovery.

Site	Before cleaning lens	After cleaning lens	Difference
M1	9.920	7.652	2.268
M2	5.427	5.115	0.312

The SUNA data processing consisted of the twelve steps below. The two data sets were somewhat unique requiring customized steps as needed which are described below. Definitions of the flag values used for each site are detailed in Table 27.

1. Extract raw SUNA data from CSV files to ASL .dat/.hdr format. The raw CSV files were structured into three sections. The first section was in XML format and contained information regarding the instrument and data collection parameters. The next section contained instrument specifics and coefficients. The last section contained the measurements collected by the instrument.
2. Up to five samples were collected per hour. These were averaged to create an equispaced time-series with a one-hour sample interval.
3. Correct the sample interval of the data files to account for the effects of instrument clock time drift. The correction is derived from a comparison of instrument start and stop times with coincident readings from an independent clock recorded. No information was available about the initialization time of the instrument clocks; therefore, the time at the start of data acquisition was used as the clock initialization time.
4. Truncate the data files to ensure all data is from a consistent sampling environment. This removed data from times when the instrument was out-of-water and before it had settled to a stable depth.
5. Corrected for drift in nitrate values due to biofouling and internal instrument drift using the values collected after instrument recovery. Biofouling was treated as linear for the duration that the instrument was deployed in-water. Instrument drift depends on the lamp characteristics and on the rate of battery depletion. This instrument drift was non-linear and treated as a function of the lamp time.
6. Interpolate gaps in the nitrate concentration record. Gaps in the data may be due to some factor interfering with proper measurements. Gaps up to 10 records were interpolated. Any gaps exceeding 10 records were flagged as “missing”.
7. Add a data quality channel and use a flag value of ‘2’ to indicate data exceeding the manufacturer specified thresholds for RMSe (>1 x 10-3) and Absorbance (>1.3 AU). There are some records that neighbor these sections that were also flagged due to suspect values.
8. Interpolate sudden and short-lived changes (spikes) exceeding expected values. A threshold change of 1 μM per hour was used as the limit based on previous studies (Balzano et al. 2012; Simpson et al. 2008; Emmerton et al. 2008). Records that were flagged as problematic in the previous step were excluded from this step.
9. Review the automatically interpolated points and identify any remaining points that look suspect for further interpolation.
10. Custom step for M1. Indicate data that looks reasonable but that is exceeding manufacturer thresholds for reliable measurements. Some overlap could exist

with other data quality values, so a second data quality column was added. This is indicated in the data quality column with a value of '4'. The term ‘reasonable’ is defined as data that is non-noisy and similar to neighboring segments where the instrument thresholds are not exceeded. All indicated sections are also instances where the data is not tracking the trend of the Absorbance values.

11. Custom step for M2. Shift sections with negative nitrate concentrations into the positive. Any shifted sections are noted in the data quality column with a flag value of “4”. These negative values could be due to the missing deployment calibration information. If the instrument was not properly calibrated the drift correction could have overcorrected the data. A value of +4.69 μM was used to shift the most negative measurements to a value of 0 μM.
12. Applied to both M1 and M2. Indicate problematic data exceeding typical concentration values in the literature. This is indicated in the second data quality column with a value of '8'. There were some records where the manufacturer quality thresholds were not exceeded but the data looked suspect due to various factors. They may bound segments that exceed the manufacturer thresholds or be part of segments that exceed the expected range of values. For this region, it is expected that nitrate concentrations will not exceed 20 μM.

Table 27.

Flag definitions used in the fully quality controlled time-series of SUNA nitrate results.

Site	Column number	Flag value	Definition
M1	10	2	Exceeds manufacturer threshold for absorbance or RMS error.
	11	4	Exceeds manufacturer threshold for absorbance or RMS error, but looks reasonable
	11	8	Within manufacturer thresholds for valid nitrate measurements, but looks suspect
M2	10	2	Exceeds manufacturer threshold for absorbance or RMS error.
	10	4	Shifted values by a constant offset to remove negative concentration values.
	11	8	Within manufacturer thresholds for valid nitrate measurements, but looks suspect

2.4.7.1 Passive Acoustic Recorder (AURAL)

A hydrophone package (Aural M2) was deployed on mooring M2. The instrument sampled at 16,384 Hz for a useable bandwidth of 10 Hz–8,192 Hz. Acoustic data were recorded for the first 20 minutes of every hour. Data were examined for non-marine mammal acoustic signatures and those were segregated from the rest (Figure 16). Bowhead whales, beluga whales, bearded seals and ringed seals presence was assessed weekly from the acoustic data files. Also detected in fall 2016 were RAFOS signals (used to help gliders navigate or for tomography) and in the first week of September 2017, very loud pulses from seismic airguns were recorded.

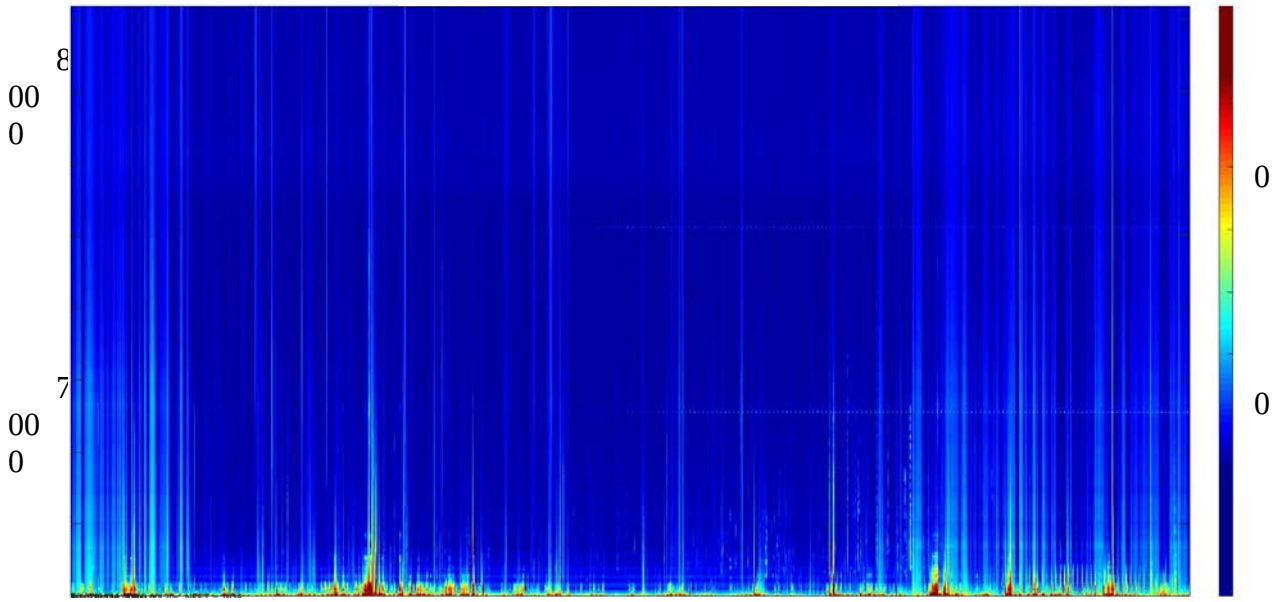

Figure 16. Long term spectrogram of acoustic data, showing the ADCP pings from the M2 mooring as most prominent signals, as well as wind events, ships and some bearded seals.

3 PRELIMINARY DATA ANALYSIS AND INTERPRETATION

3.1 PHYSICAL OCEANOGRAPHY

3.1.1 Currents

3.1.1.1 Sea-Spider

Depth-time plot of de-tided alongstream velocity from the upward-facing ADCP deployed on the Sea-Spider, along with the ice concentration at the site from the AMSR-E satellite are shown in Figure 17. The year-long mean profile is shown as well.

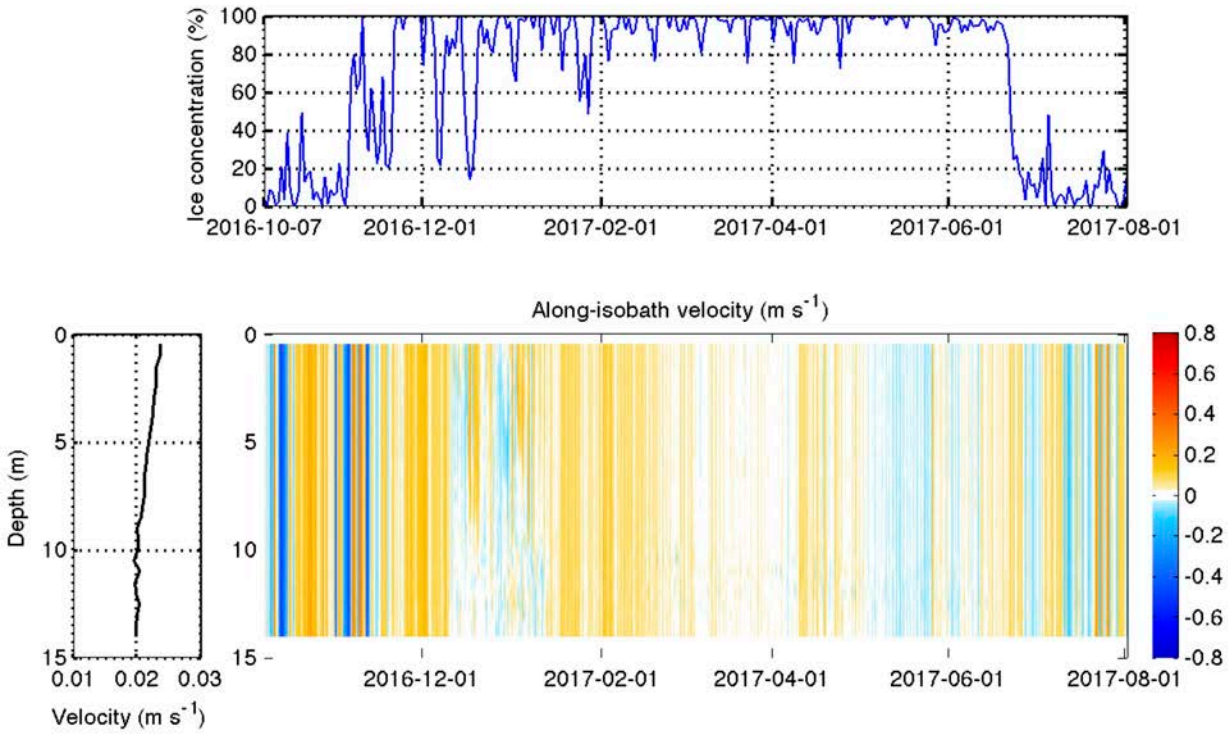

Figure 17. Depth-time plot of de-tided along stream velocity and year-long mean velocity profile from the upward-facing ADCP deployed on the Sea-Spider (bottom panel) compared to ice concentrations from the AMSR-E satellite (top panel).

Averaged over the year, the current is weakly to the east and mainly barotropic. However, before freeze-up (October–November), and after melt-back (mid-June to August), the flow was highly variable and at times quite strong. Once the ice concentration became more consistently between 80–100%, from January through June, the flow weakened. Even during this period; however, there was pronounced variability, the nature of which will be investigated in follow up analyses.

3.1.1.2 M1/M2

Figure 18 through Figure 25 depict observed current speeds and directions at M1 and M2.

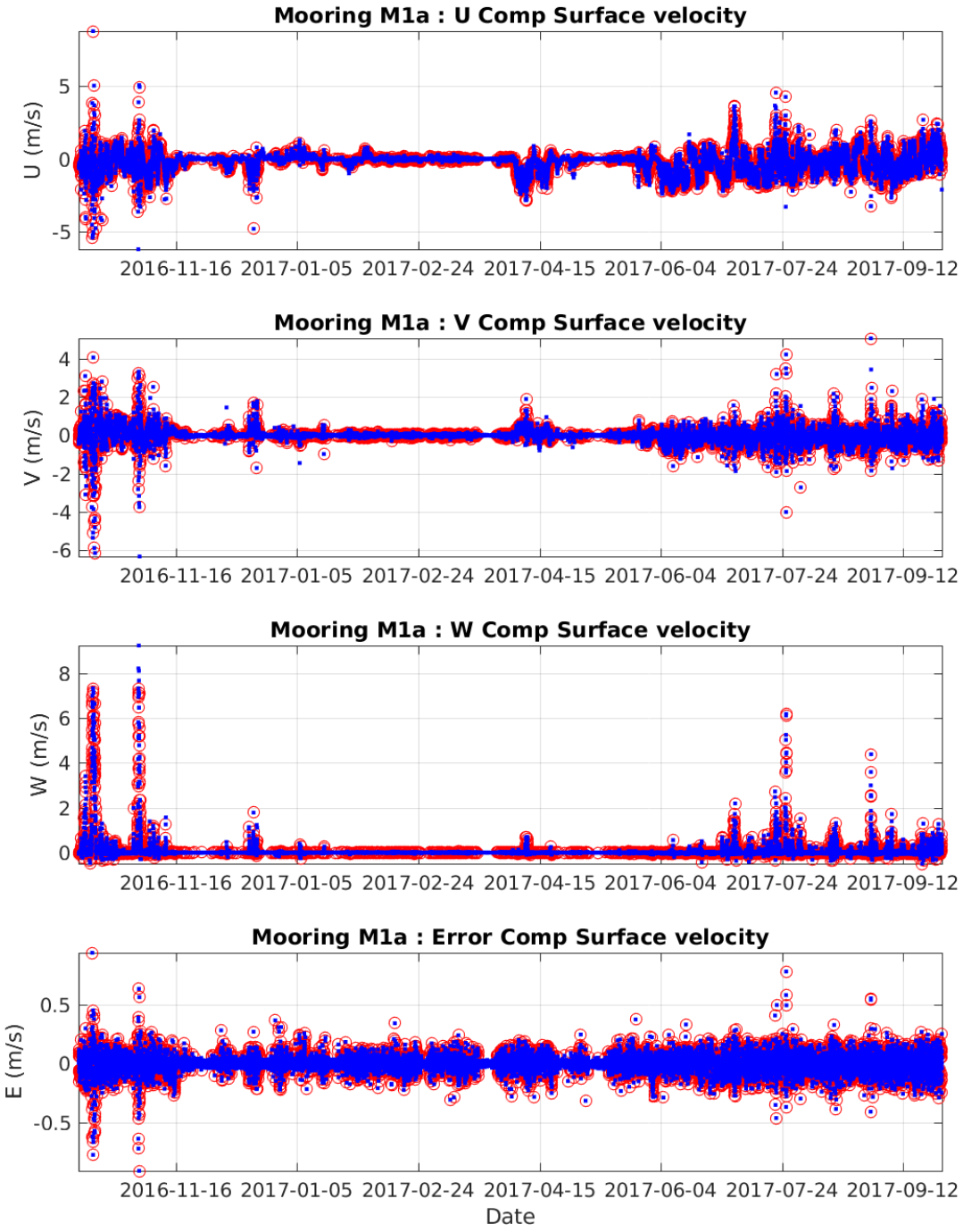

Figure 18. Surface current components (m/sec) for ADCP M1a from 2016-10-6 21:30 to 2017-09-27 23:00.

Current components include the horizontal velocity components u (towards the east when positive) and v (towards the north when positive) and the vertical velocity component w (up when positive).Red represents data that have been flagged for having an error velocity > 5 cm/s. Blue represents data with error velocity < 5 cm/s.

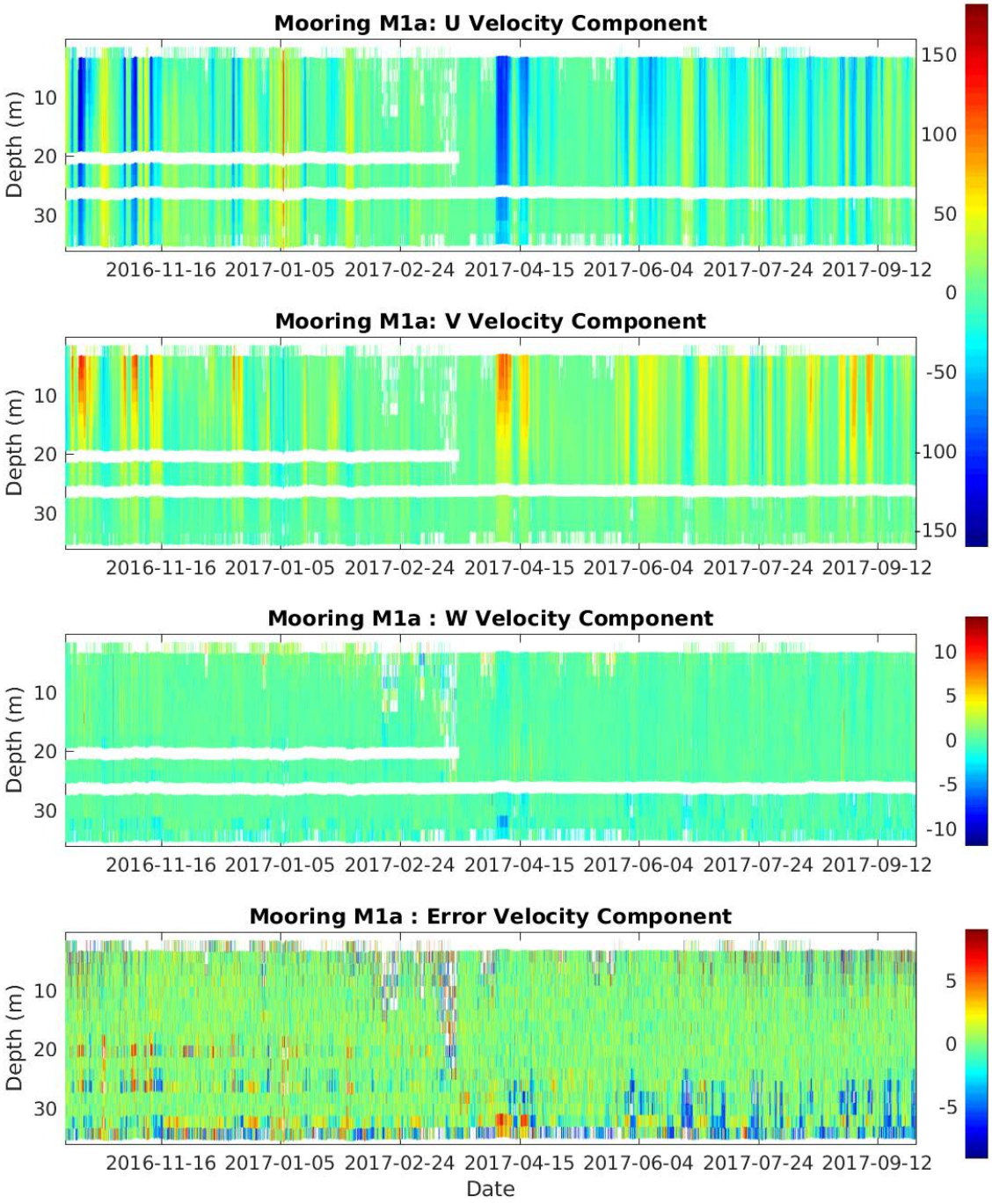

Figure 19. Current components (m/sec) for ADCP M1a across depths from 2016-10-06 21:30 to 2017-09-27 23:00.

Current components include the horizontal velocity components u (towards the east when positive) and v (towards the north when positive) and the vertical velocity component w (up when positive).

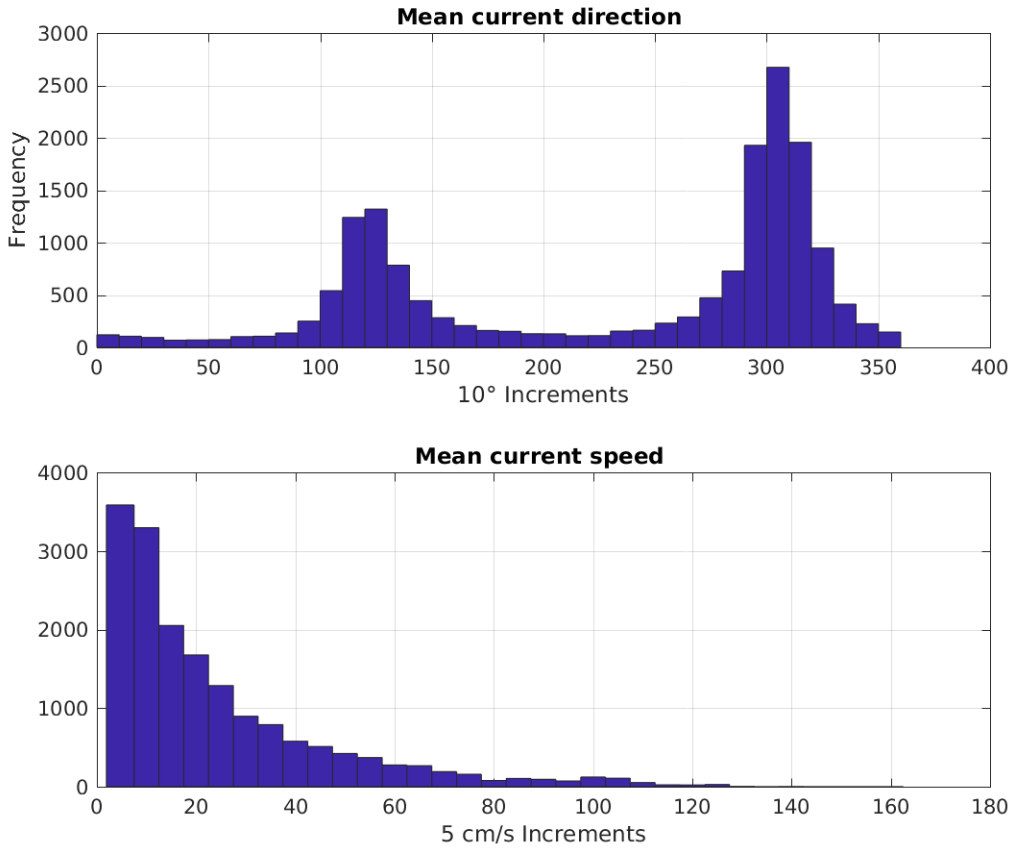

Figure 20. M1a frequency of current direction and velocity between 6 October 2016 and 27 September 2017.

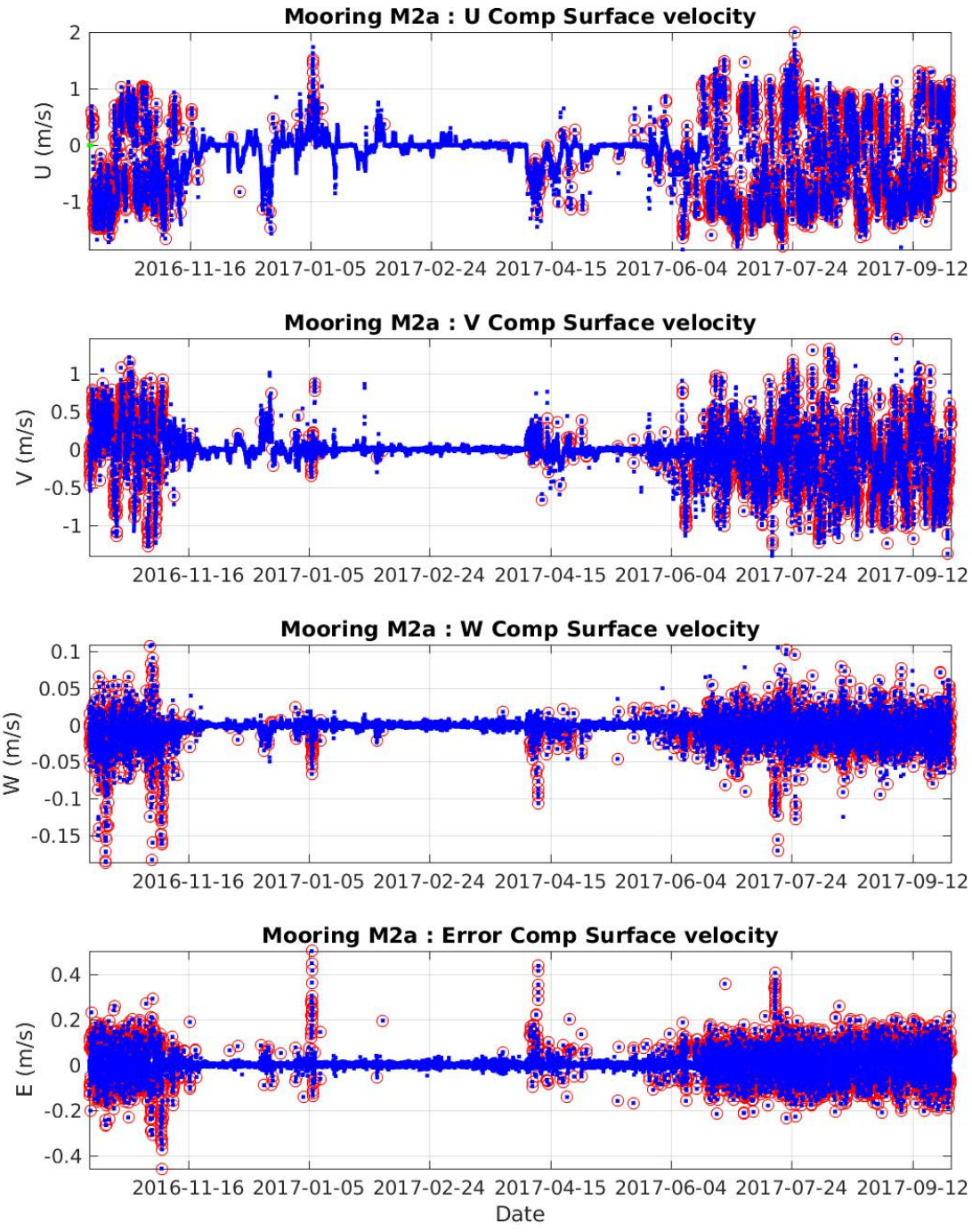

Figure 21. Surface current components (m/sec) for ADCP M2a from 2016-10-05 02:00 to 2017-09-27 20:29:59.

Current components include the horizontal velocity components u (towards the east when positive) and v (towards the north when positive) and the vertical velocity component w (up when positive). Red represents data that have been flagged for having an error velocity > 5 cm/s. Blue represents data with error velocity < 5 cm/s.

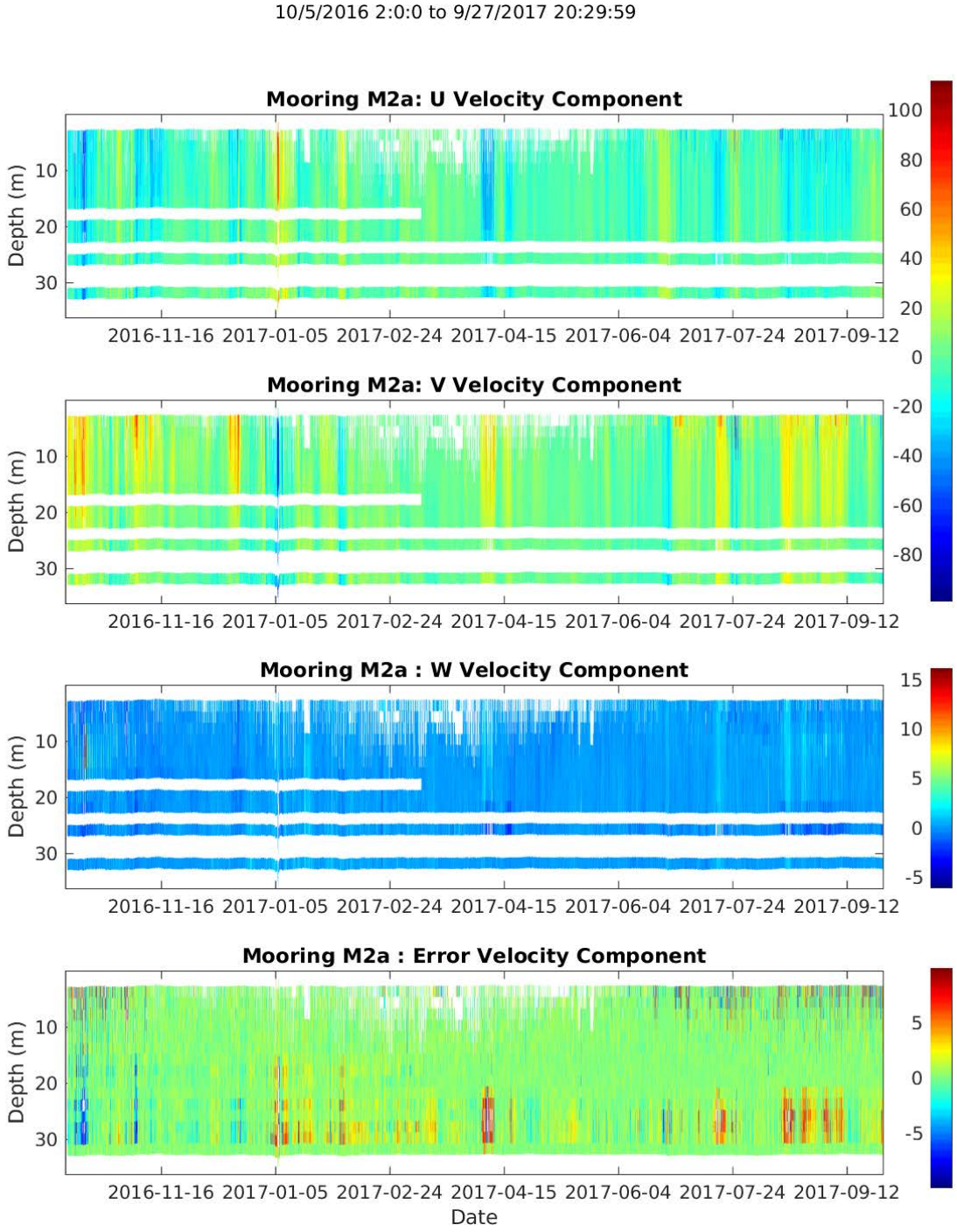

Figure 22. Current components (m/sec) for ADCP M2a across depths.

Current components include the horizontal velocity components u (towards the east when positive) and v (towards the north when positive) and the vertical velocity component w (up when positive).

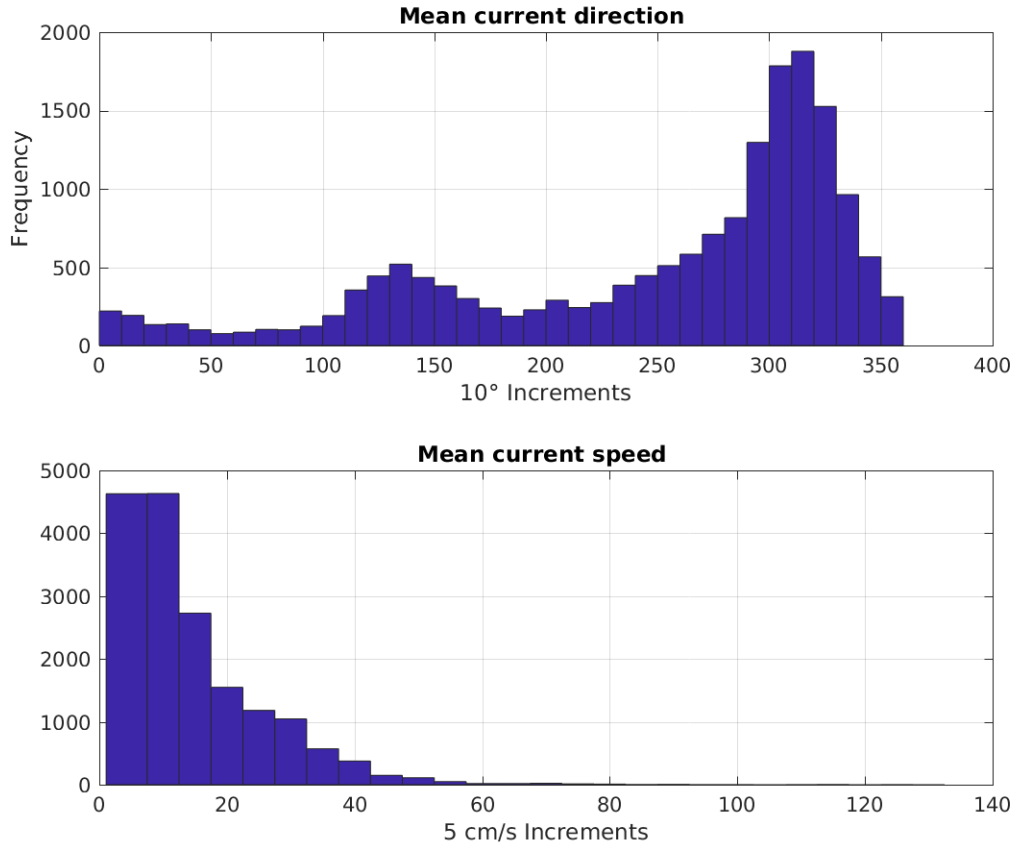

Figure 23. M2a frequency of current angle and velocity between 6 October 2016 and 27 September 2017.

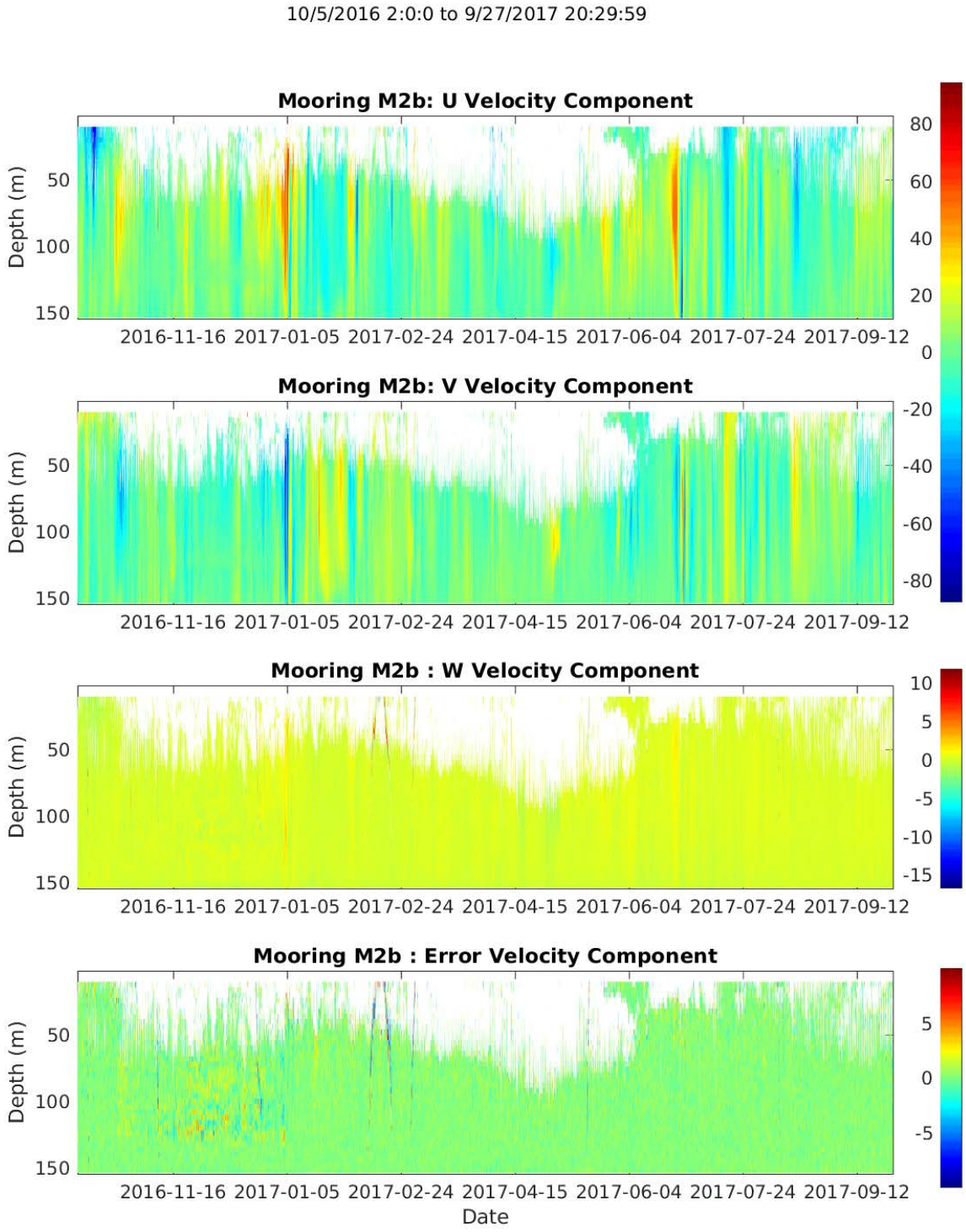

Figure 24. Current components (m/sec) for ADCP M2b across depths.

Current components include the horizontal velocity components u (towards the east when positive) and v (towards the north when positive) and the vertical velocity component w (up when positive).

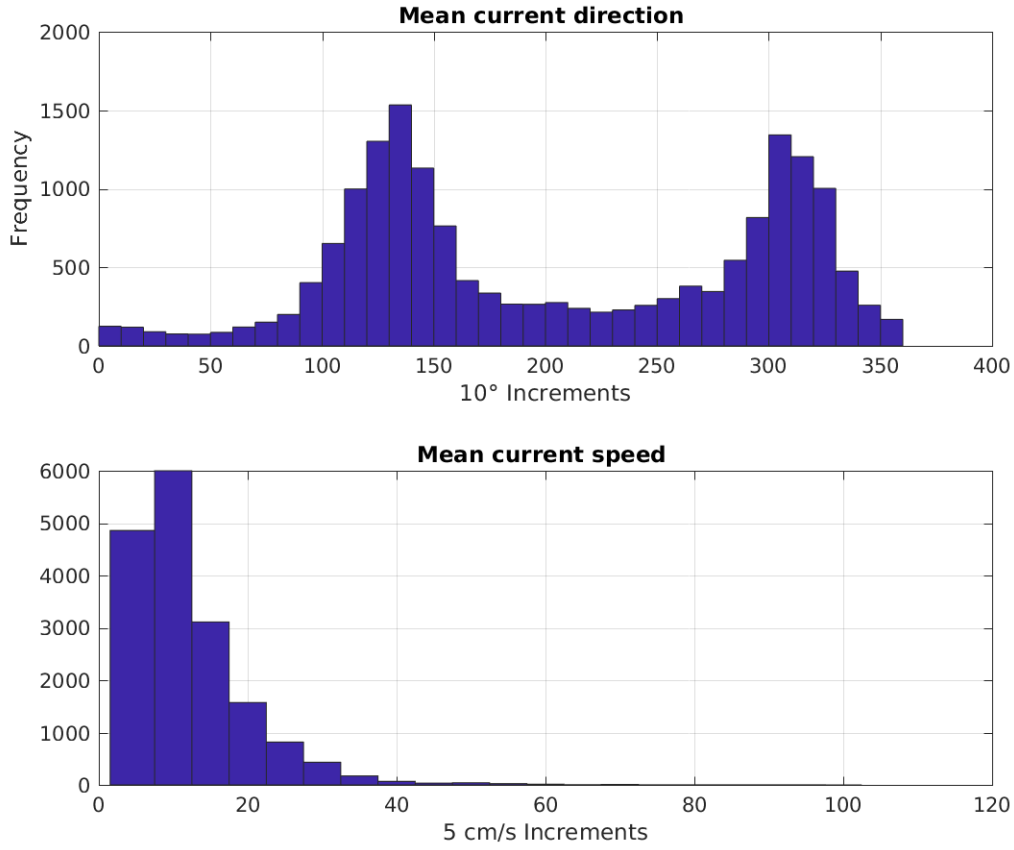

Figure 25. M2b frequency of current angle and velocity between 6 October 2016 and 27 September 2017.

Evident is the presence of a subsurface, eastward-flowing shelfbreak jet. The flow is westward in the upper 40 m and eastward in the depth range of 40–120 m. There is substantial variability of the flow on a variety of timescales, which, to first order, does not seem correlated to the ice cover, at least not at M1.

3.1.1.3 M3 and M4

Each of the M3 and M4 moorings employed two ADCPs at different depths, as described in Section 2.1. This pair of quality-controlled ADCP measurement time-series from each mooring were combined to produce a single time-series of ocean currents with a depth span of 10 to 260 m water depth at M3 and 10 to 310 m at M4. The time-series were combined by interpolating to a common time sequence and vector-averaging the ocean current measurement records acquired in overlapping depth bins. The final combined time-series are reported with a 20-minute interval, as described in Section 2.4.1.5. The results at this high temporal resolution illustrate many features in the current depth profiles; however, to visualize the time-series over the full deployment, it was necessary to average the currents using a 24-hour window.

The daily-averaged ocean currents at M3 and M4 are plotted in Figure 26 and Figure 27, respectively. The color of each cell in the third and fourth panels shows the ocean current speed and direction. Data gaps in the current time-series are plotted as white cells. There are three regions of data gaps: (1) the blanking distance of the deepest ADCP determines the deepest acquired depth cell, (2) side-lobe effects near the longest range target (either the water/air or water/sea-ice interface) limit the reliability of ocean current measurements near the water column surface, and (3) reduced abundance of biological scatterers in the winter months leads to weakened backscattered acoustic signals, particularly at longer distances. The latter effect is particularly evident in the LongRanger ADCP results in bins at longer ranges. The LongRanger ADCPs were configured in broadband mode which is known to provide more precise ocean current measurements while sacrificing range. Future deployments of deep ADCPs should consider the use of narrowband mode to potentially avoid the lack of reliable measurements at long ranges. The ADCP located higher on each mooring was closer to upper measurement cells and thus was less susceptible to the latter effect. This beneficially allowed some data gaps to be filled in the time-series generated by combining each pair of ADCPs. The top three panels of Figure 26 and Figure 27 show the daily-averaged ocean current time-series at specific water depths: 30 m, 90 m, and 152 m at M3; 30 m, 88 m, and 152 m at M4. The dotted lines on the third panel indicate these depths relative to the currents plotted over the full depth span.

Figure 28 shows an example of the ocean currents at M3 in late-June 2017 using the full time-resolution results at 20-minute intervals. The bottom two panels show the ocean current speed and direction and the top two panels show the wind speed and direction. By this time, the water surface is predominantly ice-free with only occasional isolated ice floes transiting past. Under these conditions, wind induced stresses led to a response of the ocean currents near the surface. When the sea surface is entirely ice covered, the wind induced stresses may be in a direction towards which the sea ice is unable to move due to restrictions from the shoreline, landfast ice edge, and high concentration of mobile ice. In these cases, the ice decouples the wind and near-surface currents and little response of the currents to even strong winds can be observed. Other features in Figure 28 are notable. Tidal effects and/or inertial oscillations are evident, for example, in the top 100 m of the ocean current speed on 2017-06-21. The wind direction stabilizes on 2017-06-27 and remains easterly for several days until 2017-07-02. The ocean current during this episode has a strong and deep response with the current speeds reaching 105 $cm \cdot s^{-1}$. Increased currents are evident down to 200 m depth. For a brief episode on 2017-06-29, the currents are observed to increase to the maximum measurable depth of 268 m.

High concentration ice cover does not necessarily lead to decoupling of the winds and ocean currents – for example, see the early-January 2017 event in Figure 29 which occurs during the maximum wind speeds measured at Herschel Island over the mooring deployment timespan. During this event, the ice concentration is approximately 100% according to ice charts and the IPS measurements. The top panel shows the ice velocity which reaches a maximum speed of approximately 127 $cm \cdot s^{-1}$ coincidentally with the maximum wind speed of approximately 34 $m \cdot s^{-1}$ (second panel). Around the time of the maximum wind speed, the wind direction is from the northwest and the ice responds by accelerating and moving towards the southeast. Although the ice cover is heavy, a strong response of the near-surface currents is observed suggesting the ice canopy roughness transfers wind-induced momentum to the near-surface water column in

approximately the upper 30 m. There also appear to be two lobes of motion within the upper 175 m of the water column towards the southeast quadrant which somewhat lag the two wind events.

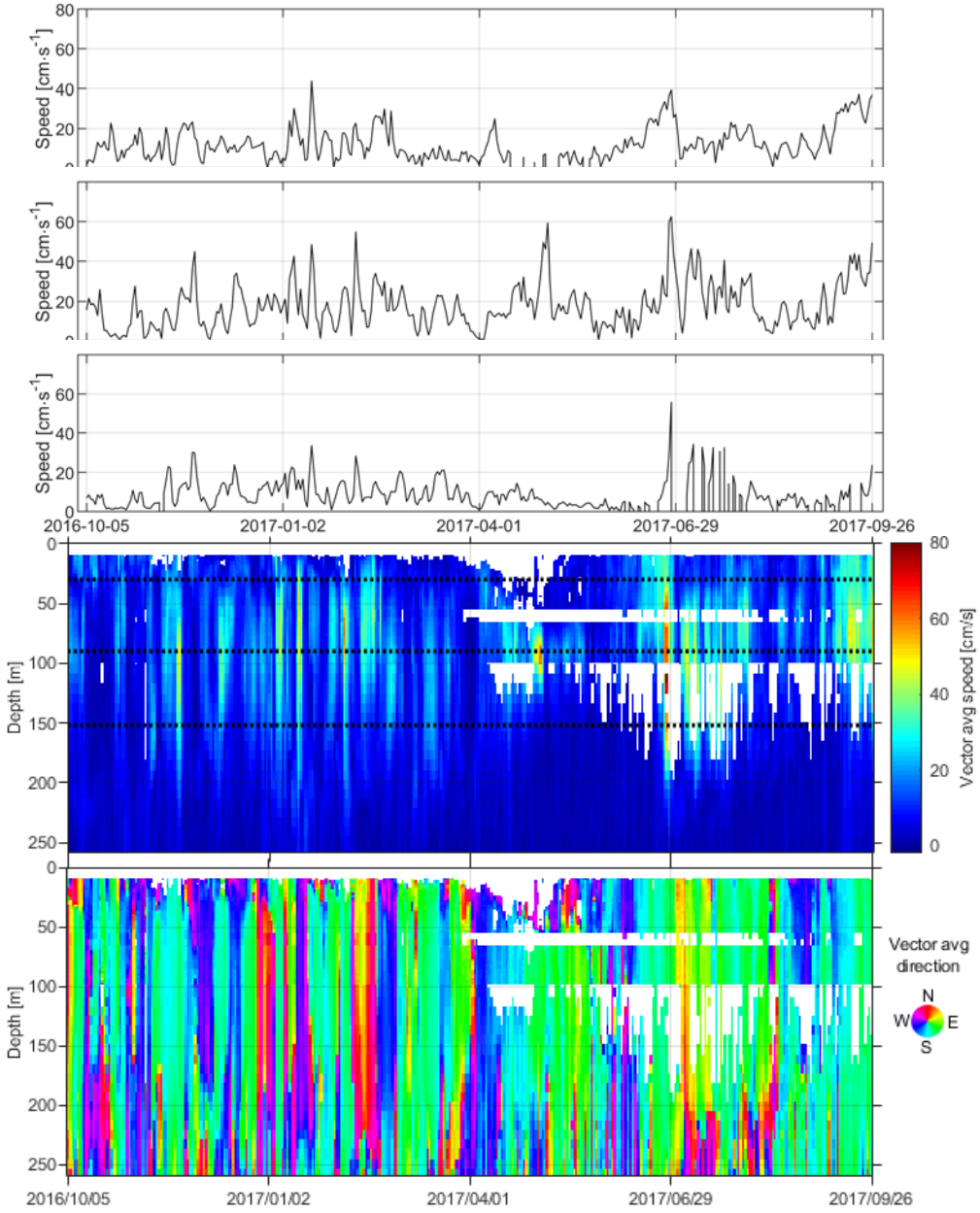

Figure 26. Daily-averaged ocean currents at M3 over the 2016-2017 mooring array deployment. The bottom two panels show the speed and direction of the ocean currents. The vertical extent spans the nearest reliable surface current depth to the closest bin to the ADCP. The top three panels show the current speed at three depths indicated by the dotted line on the fourth panel: 30, 90, and 152 m. These results were constructed by combining the currents measured from ADCPs moored at two depths. Data gaps become more prevalent in the winter when reduced backscatter populations lead to weakened acoustic signals.

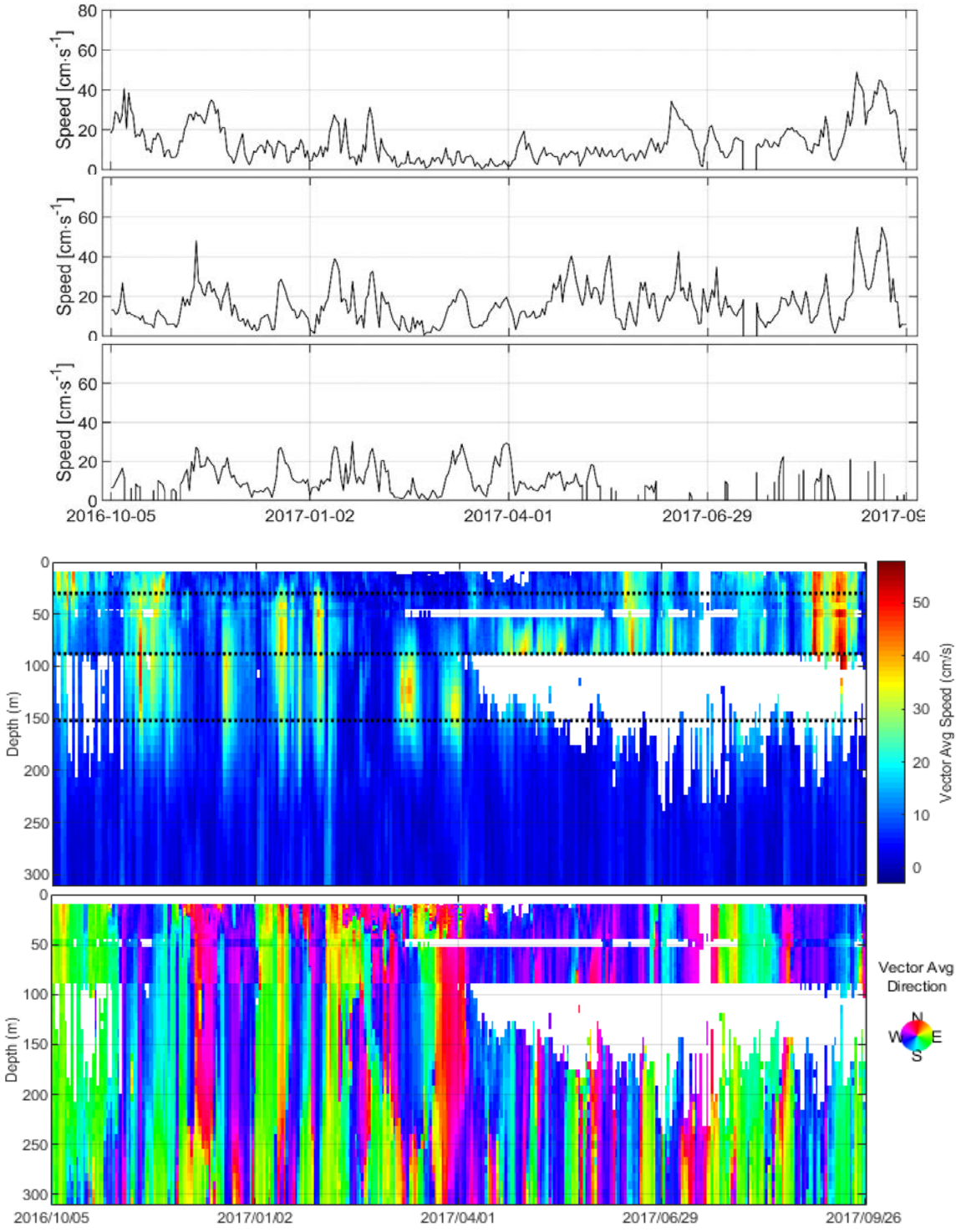

Figure 27. Daily-averaged ocean currents at M4 over the 2016-2017 mooring array deployment. The bottom two panels show the speed and direction of the ocean currents. The vertical extent spans the nearest reliable surface current depth to the closest bin to the ADCP. The top three panels show the current speed at three depths indicated by the dotted line on the fourth panel: 30, 88, and 152 m. These results were constructed by combining the currents measured from ADCPs moored at two depths. Data gaps become more prevalent in the winter when reduced backscatter populations lead to weakened acoustic signals.

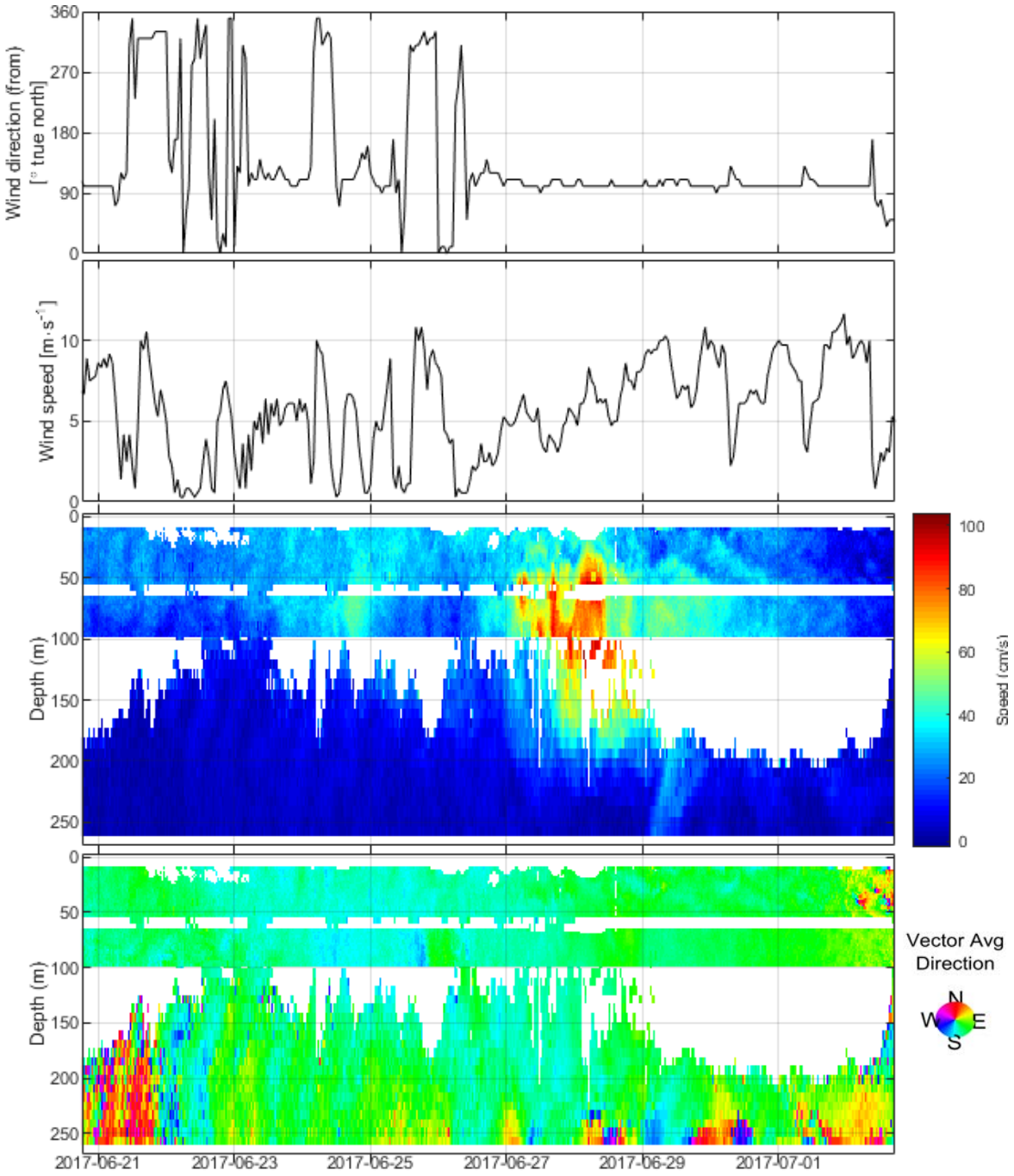

Figure 28. High resolution ocean currents during an ice-free episode in late-June 2017.
The top two panels show the wind direction (from) and speed. The bottom two panels show the ocean current speed and direction (to) observed at M3 based on the results at 20-minute intervals over the measured depth span.

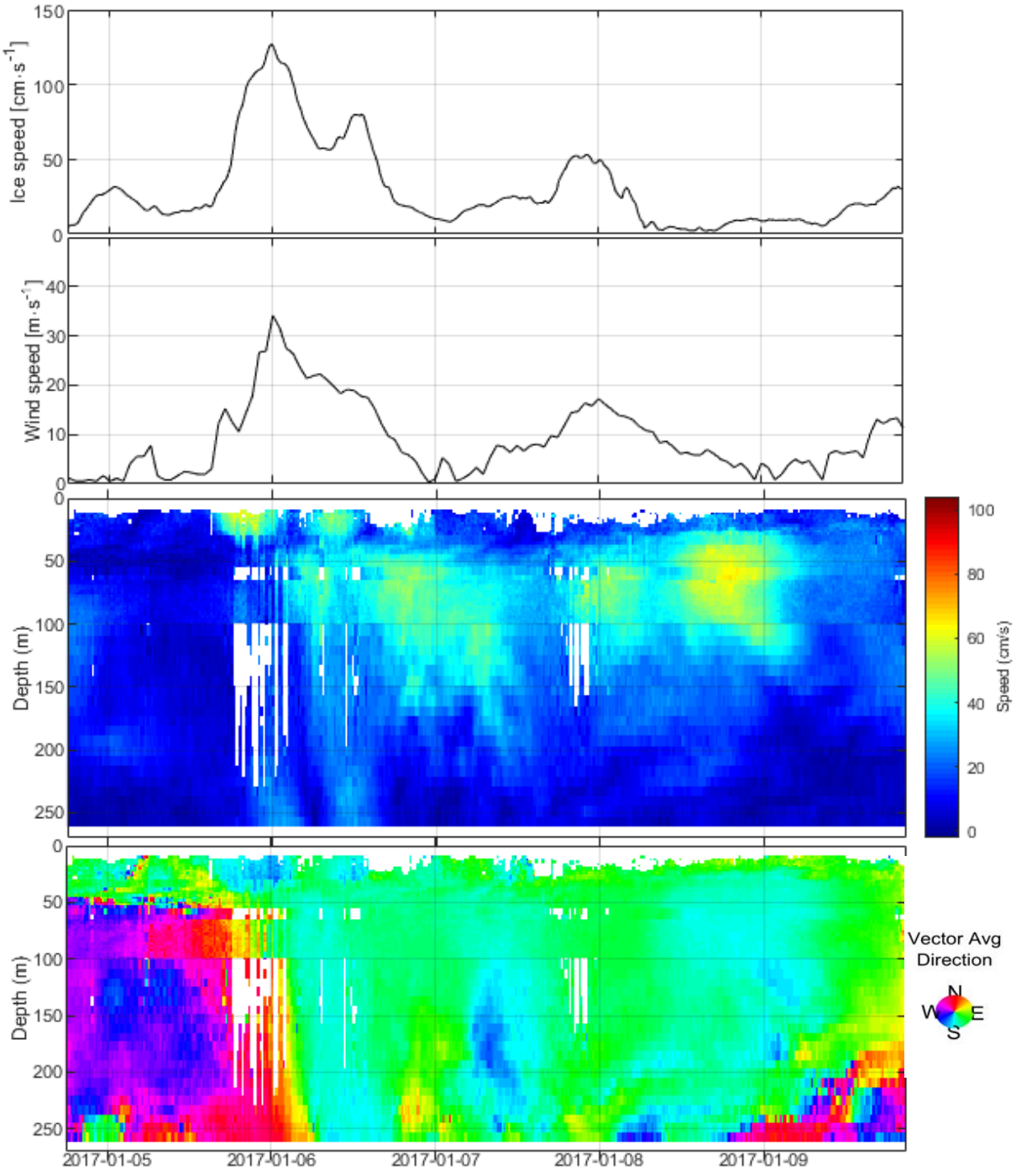

Figure 29. High resolution ocean currents during an episode of heavy ice concentration composed of both level and deformed sea ice in early-January 2017.

The top two panels show the ice and wind speed. The bottom two panels show the ocean current speed and direction (to) observed at M3 based on the results at 20-minute intervals over the measured depth span.

3.1.2 Ice

3.1.2.1 Ice draft derivation

The ice draft of targets acquired during the mooring deployment were calculated using the processed IPS data and the quality-controlled versions of target range, pressure at the instrument depth, and instrument tilt. These parameters are necessary to derive the ice draft, d, of a target as follows:

Equation 6

$$d = \eta - \beta \cdot r \cdot \cos\theta$$

where β is a calibration factor called the range correction factor for the actual depth-averaged sound speed through the water column along the sonar beam (see Section 3.1.2.2), r is the range to the target from the IPS, θ is the total instrument tilt, and η is the water level from the IPS sonar transducer to the air-water interface. Note that the sign convention for ice draft is positive downwards, i.e. a draft of +5 m represents an ice feature which extends 5 m below sea level.

The water level is determined as follows:

Equation 7

$$\eta = \frac{P_{IPS} - P_{SLP}}{\rho g} - \Delta D$$

where P_{IPS} is the pre-processed pressure measured by the IPS, P_{SLP} is the sea-level pressure, g is the local acceleration due to gravity, ρ is the depth-averaged density of sea water above the instrument, and ΔD is the distance of the pressure sensor below the acoustic transducer. The depth-averaged density is determined from the CTD casts performed at deployment and recovery of the IPS (see Section 3.1.3). Table 28 lists the values of these parameters used in the processing of the M3 and M4 IPS data.

Table 28.

Values used in the derivation of water level time-series for each measurement site.

Parameter	M3	M4
$\boldsymbol{g}$ [m·s-2]	9.826125	9.826243
$\Delta\boldsymbol{D}$ [m]	-0.169	-0.169
$\boldsymbol{\rho}$ [kg·m-3]	1,023.36	1,022.46

The total instrument tilt was computed using the pre-processed tilt vector components, θ_x and θ_y, measured by the IPS:

Equation 8

$$\theta = \sqrt{{\theta_x}^2 + {\theta_y}^2}$$

Due to power limitations, the IPS acquired pressure and tilt component observations less frequently relative to the acoustic target measurements. The sampling frequency was carefully selected with a view to minimize the power draw while resolving the anticipated tilt and pressure effects due to mooring motion. The derived water level and total instrument tilt time-series described above was the interpolated to the time sequence of the acoustic target time-series. If the water level and total instrument tilt time-series do not resolve high-frequency signals, this interpolation can lead to aliasing effects in the derived ice drafts. To minimize these effects, the water level and total instrument tilt time-series were smoothed through episodes of unresolved perturbations. These perturbations were often due to mooring strumming as a result of vortex shedding and high-frequency pressure changes due to surface waves.

The final water level and total instrument tilt time-series are presented in Figure 30 and Figure 31. The M3 and M4 IPS instruments remained stable throughout the deployment with a few exceptions where the IPS was pulled down 5 to 10 m in the early part of the deployment at M3. Pulldown events at M4 during this time were smaller at 2 m to 5 m. A large pulldown event of ~24 m occurred at M3 in late June. The M4 IPS had stopped recording by this point. Large tilt values are evident during the pulldown events. Other moderate tilt deviations of less than five degrees from vertical occur throughout both records; however, for most of the deployment the instrument tilt remains sufficiently stable.

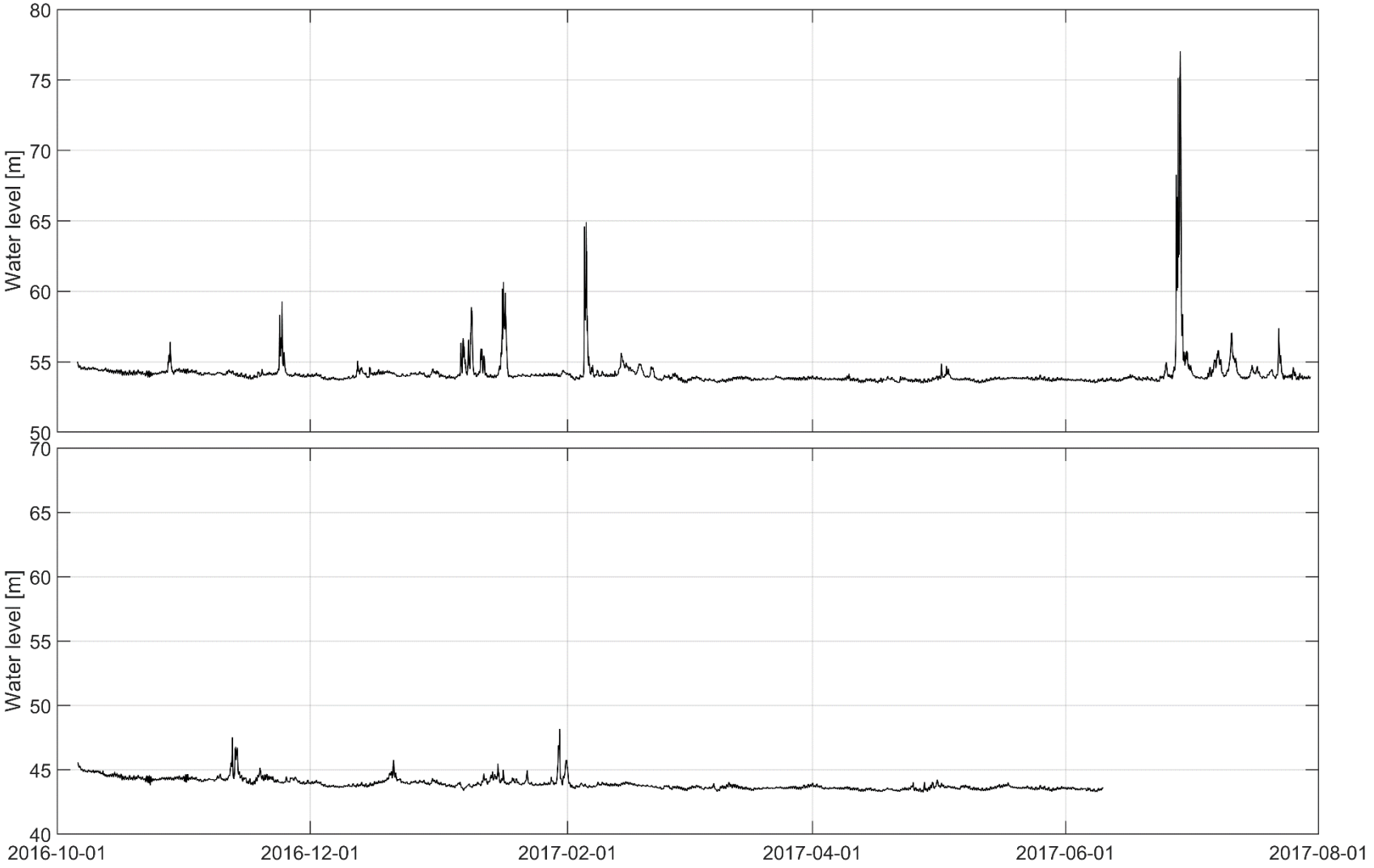

Figure 30. The final water level time-series at M3 (top) and M4 (bottom) as derived from the IPS.

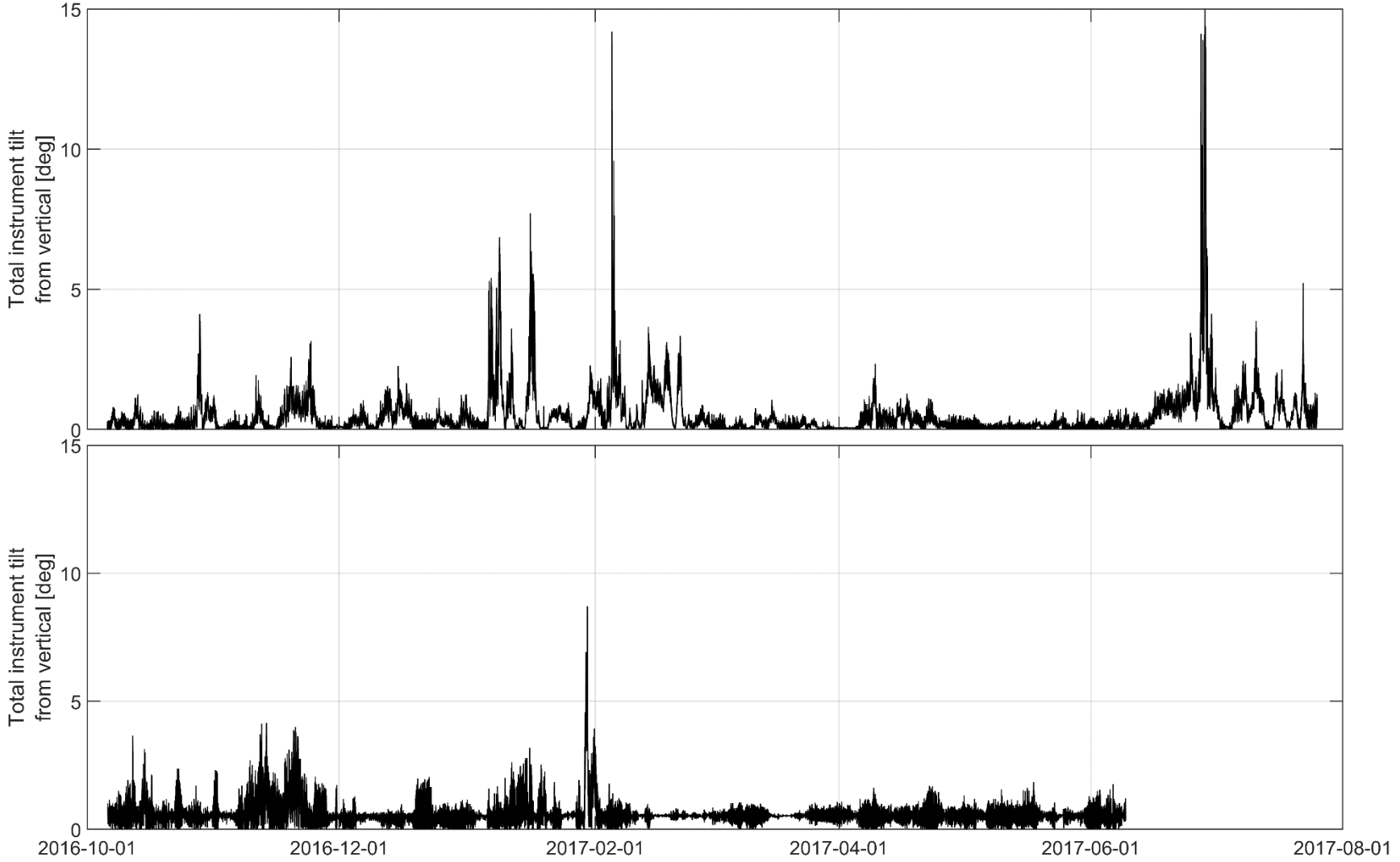

Figure 31. The final total instrument tilt time-series at M3 (top) and M4 (bottom) as derived from the IPS.

3.1.2.2 Ice draft calibration and classification

The factor, β, applied to the measured range in Equation 6 represents the ratio of the actual speed of sound to the assumed value. To determine β, open water segments in the range data set were selected and β was empirically computed. This process involved several iterations with the coarse seasonal sound speed trends developed in the first pass. Subsequent iterations injected modulations for short- and medium-term fluctuations of the sound speed which can include freshwater inputs, major ocean stratification variations due to upwelling and downwelling, solar irradiance fluctuations leading to air temperature changes and radiative heating of the ice and surface water, and vertical motion of the IPS through stratified water masses during mooring pull-down events. Care must be taken during episodes of potential thin ice and/or surface waves that ice targets within the ice draft time-series are not miscategorized as open water. This requires thorough interpretation of all available evidence including meteorology, ice drift, satellite imagery, sea ice charts, and the ice draft time-series itself. The final β time-series for M3 and M4 are plotted in Figure 32.

After the ice draft time-series was calibrated for sound speed variations, each record was classified as either ice or open water. The open water records were set to a flag value of -200. Identification of open water involves an automated classification method followed by a manual review and editing. The automated classification performs a frequency analysis on the ice draft time-series to detect surface waves and generate a time-series of ‘significant wave height’. The ‘significant wave height’ time-series is used to separate features within the ice draft time-series that are due to wave oscillations from those due to the topography of the ice undersurface. During calm sea state, a short segment of values around each ice draft record was investigated. The probability distribution of these values was used to classify the segment as either thin ice or open water. Summary statistics of the extent of open water classification in each of the M3 and M4 ice draft time-series are listed in Table 21 and Table 22 in Section 2.4.3.2, respectively.

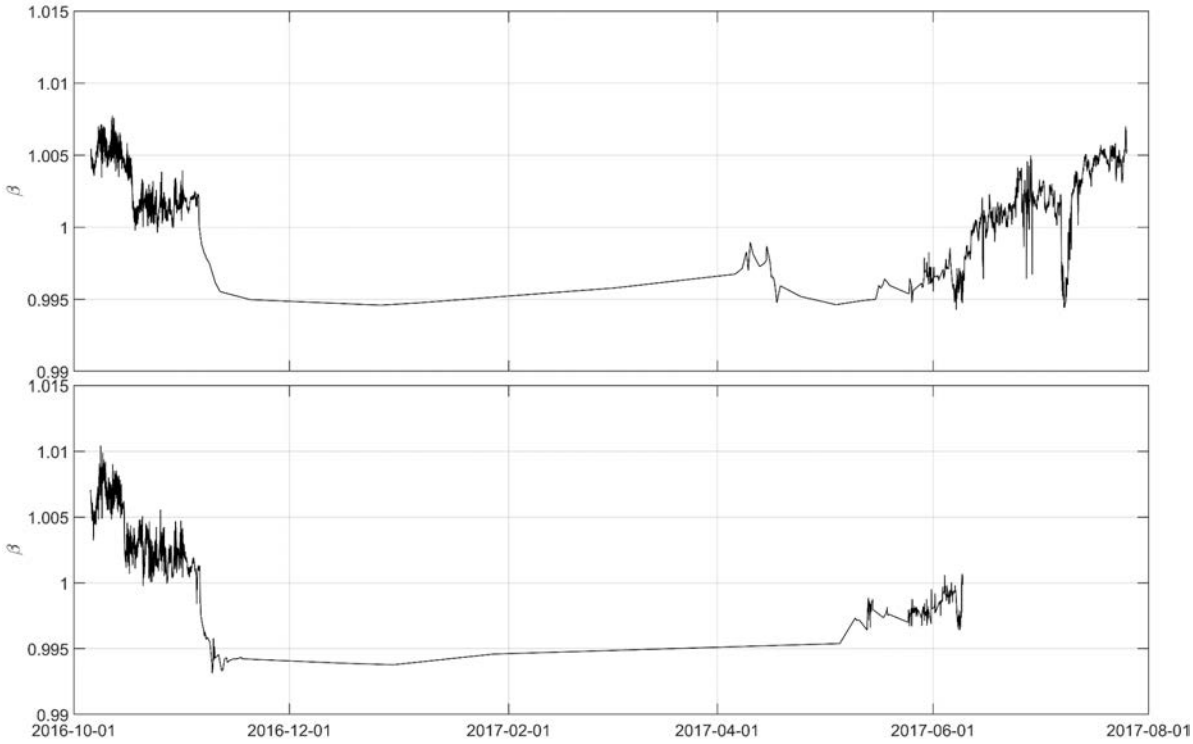

Figure 32. The final $\boldsymbol{\beta}$ time-series at M3 (top) and M4 (bottom).

3.1.2.3 Ice draft spatial-series

Ice draft time-series were converted to a distance (or spatial) series using the quality-controlled ADCP ice velocity time-series (see Section 2.4.1.6). The cumulative distance was calculated using the east and north displacements for each sample from beginning to end.

The ice draft was sampled at regular time intervals but due to the irregular motion of the ice cover, the resulting distance series was unevenly spaced. To account for this, the distance series was interpolated to regular increments using a double-weighted double-quadratic interpolation scheme:

Equation 9

$$y(x_i) = \frac{Y_1[y(u_{i+2}) - y(u_{i+1})][x_i - x(u_{i+1})] + Y_2[y(u_i) - y(u_{i-1})][x_i - x(u_i)]}{[y(u_{i+2}) - y(u_{i+1})][x_i - x(u_{i+1})] + [y(u_i) - y(u_{i-1})][x_i - x(u_i)]}$$

As shown in Figure 33, the value Y_1 represents the value obtained from a quadratic interpolation using two points to the left and one to the right of x_i and Y_2 represents the interpolated value using two points to the right and, one to the left of x_i. In the figure, the desired regularly spaced interpolation point is x_i, and the measurement locations are given by u_{i-1}, u_i, u_{i+1} and u_{i+2}. The two interpolated values were then averaged using a weighting factor based on the distance between points and on the change in draft between points. The double weighting

scheme, as shown in Figure 33, was adopted to avoid overshoots in regions of high draft gradients. In order to represent the ice drafts at low ice velocities, the ice draft data were interpolated to 0.10 m distances then block averaged to 1.0 m distances.

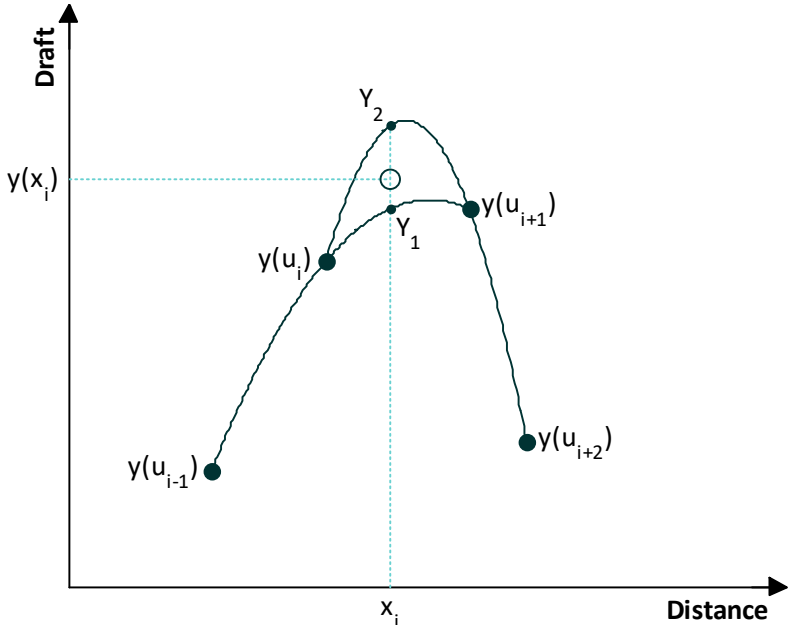

Figure 33. The double quadratic interpolation method used to convert the ice draft time series into a spatial series.

3.1.2.4 Ice Dynamics

Sea ice freeze-up began in late-October 2016 in the region of the MARES array and heavy (9-10 tenths) ice concentration was established by mid-November (Figure 34). The sea ice concentration remained high throughout the deployment with further evolution of the landfast ice edge until early-March 2017 where this feature remained at a maximum extent. The regional ice break-up and clearing began in early-June 2017. A notable exception to the sustained high ice concentrations near the MARES array occurred in April 2017 when changes in the wind forcing led to a region-wide fracturing and offshore motion event, generating large leads in the sea ice which eventually reversed and closed in early-May. This event is presented in further detail below. The ice motion throughout the deployment expressed many episodes of both appreciable drift and low to zero speeds. Under certain conditions, relative immobility can be indicative of higher internal stresses within the ice pack. Low motion occurred most during February and March 2017.

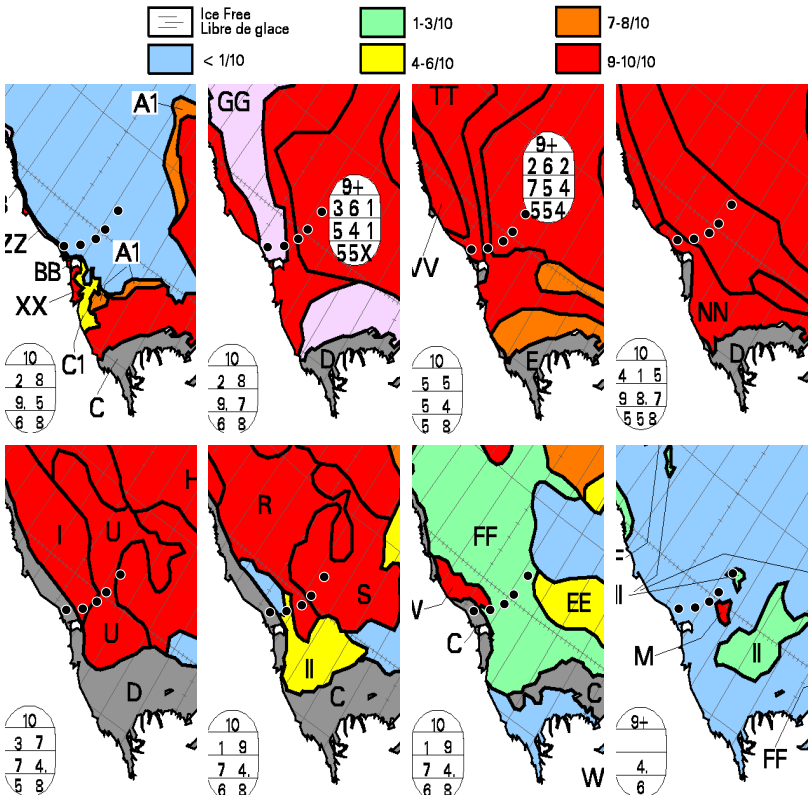

Figure 34. Sea ice concentration in tenths of coverage in the region of the MARES array as reported by Canadian Ice Services ice charts (Archive Search 2017).

The top row shows the beginning of the ice season conditions on (from left to right) 2016-10-31, 2016-11-07, 2016-11-14, and 2016-11-21. The bottom row shows the ice break-up during (from left to right) 2017-05-22, 2017-06-05, 2017-06-19, and 2017-07-03. Grey polygons illustrate regions of landfast ice. The MARES mooring locations are shown by the black circles with white outline.

The depth-averaged sound speed through the water column above each IPS unit is plotted in Figure 32 in Section 3.1.2.2. This time-series is notable as it contributes most to the accuracy in the final ice draft time- and spatial-series. As the sound speed time-series are empirically derived, they are influenced by effects in addition to sound speed, for example, bias within the IPS sensors and uncertainty in selection of open water events. The advantage of the empirical approach is that these effects are corrected for; however, caution should be used when interpreting the β time-series for insight into sound speed. The β time-series follow the seasonal trends in air temperature with the highest values occurring in the shoulder seasons—October to November 2016 and mid-May to late-July 2017. The high-frequency fluctuations during these episodes are due to the heat cycling through daylight hours, short-term perturbations due to cold water masses accompanying massive ice features, upwelling of water masses, pulses of freshet, and mooring pulldown through stratified water. Conversely, the β time-series through the winter is relatively constant with a notable exception in April 2017 at M3.

During April 2017, a large fracturing event occurred across the wider region around the MARES mooring array (Figure 35). During the days leading up to April 4, where fracturing is clear in the Aqua MODIS imagery, and for the first few days as the leads grew, the wind speed remained modest at about 5 $m \cdot s^{-1}$. It was the shift in wind direction, however, that drove the early part of this event shift. The wind direction changed from the northwest to from the southeast—a direction away from the shore and landfast ice edge. Through the rest of April, the winds varied, and the ice concentration increased again by mid-May.

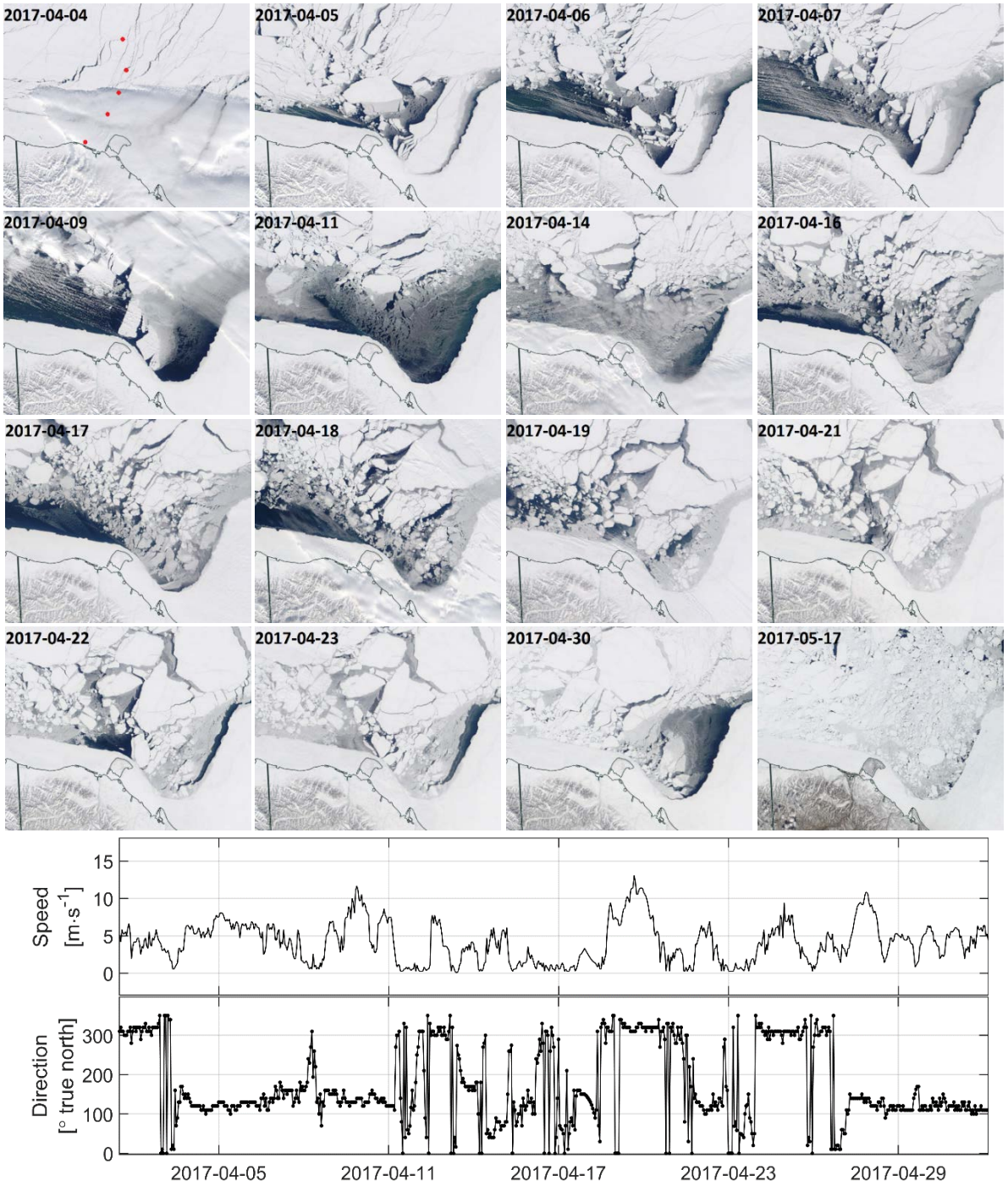

Figure 35. Time-series collage of large ice fracturing event in April 2017 in the region of the MARES mooring array shown by red dots in upper left panel as evident in Aqua MODIS satellite imagery (NASA Worldview 2017). The bottom two panels show the wind speed and direction (from) through the event as measured at Herschel Island (Hourly Data Report…2017).

The time-series of daily minimum, maximum and mean ice draft measured at M3 and M4 are presented in Figure 36. Note that the mean ice draft is computed for ice observations only and therefore does not include a bias due to the presence of open water. At M3, the average daily ice draft throughout the deployment was 1.90 m. The maximum draft of 26.32 m occurred on 2017-04-10. The average daily ice draft at M4 was 1.71 m and the maximum draft was 26.59 m on 2017-04-09. The mean and maximum ice draft values for the entire deployment for each site are presented in Table 29.

Table 29.

Full deployment mean and maximum ice draft values at each site.

Site	Mean ice draft (ice-only) [m]	Mean ice draft (all records) [m]	Maximum ice draft [m]
M3	1.90	1.54	26.32
M4	1.71	1.66	26.59

The high sampling frequency and ice draft accuracy available from the M3 and M4 IPS results enabled observation of episodes of surface waves transiting through the ice pack (Figure 37). During these episodes, the ice draft time-and spatial-series are superpositions of the ice and waves signals. This is readily found in some circumstances in the spectrogram generated from the M3 ice draft time-series shown in Figure 38. The detailed power spectral density during early-February clearly distinguished the ice and surface wave frequency bands since the ice was slow moving and therefore contributed relatively less to the variance. When the ice concentration was low, the separation of the ice and waves were also distinguishable as in the example in mid-July. The spectral distribution of ice and waves, however, was generally more mixed as the roughness of sea ice tended to span a large frequency band. This is an area of active research (Mudge et al. 2018) as marginal ice zones continue to evolve with shortening ice seasons, strengthening wind storms, and weakening ice leading to higher likelihood of propagation of waves through the ice pack.

The ice speed at M3 and M4 is plotted in Figure 39. The mean speed over the full deployment was 0.12 $m \cdot s^{-1}$ at both sites. The maximum ice speed occurred on January 5, 2017 and reached 1.27 and 0.94 $m \cdot s^{-1}$ at M3 and M4, respectively. This event corresponded with the maximum wind speed reached over the deployment of 34 $m \cdot s^{-1}$ as measured at Herschel Island. The ice speed amplitudes were generally similar at the two locations with M4 leading M3 by a variable phase of up to approximately 15 hours. The ice flow direction was generally from east to west following the general circulation pattern in the region of the MARES array; however, there were many deviations from this average motion throughout the deployment. The progressive vector diagrams in Figure 40 illustrate this. In these diagrams, the Eulerian-based ice velocity measurements were integrated and plotted. These diagrams are thus illustrative of the complex ice drift patterns and are not meant to show the true particle path in the Lagrangian sense.

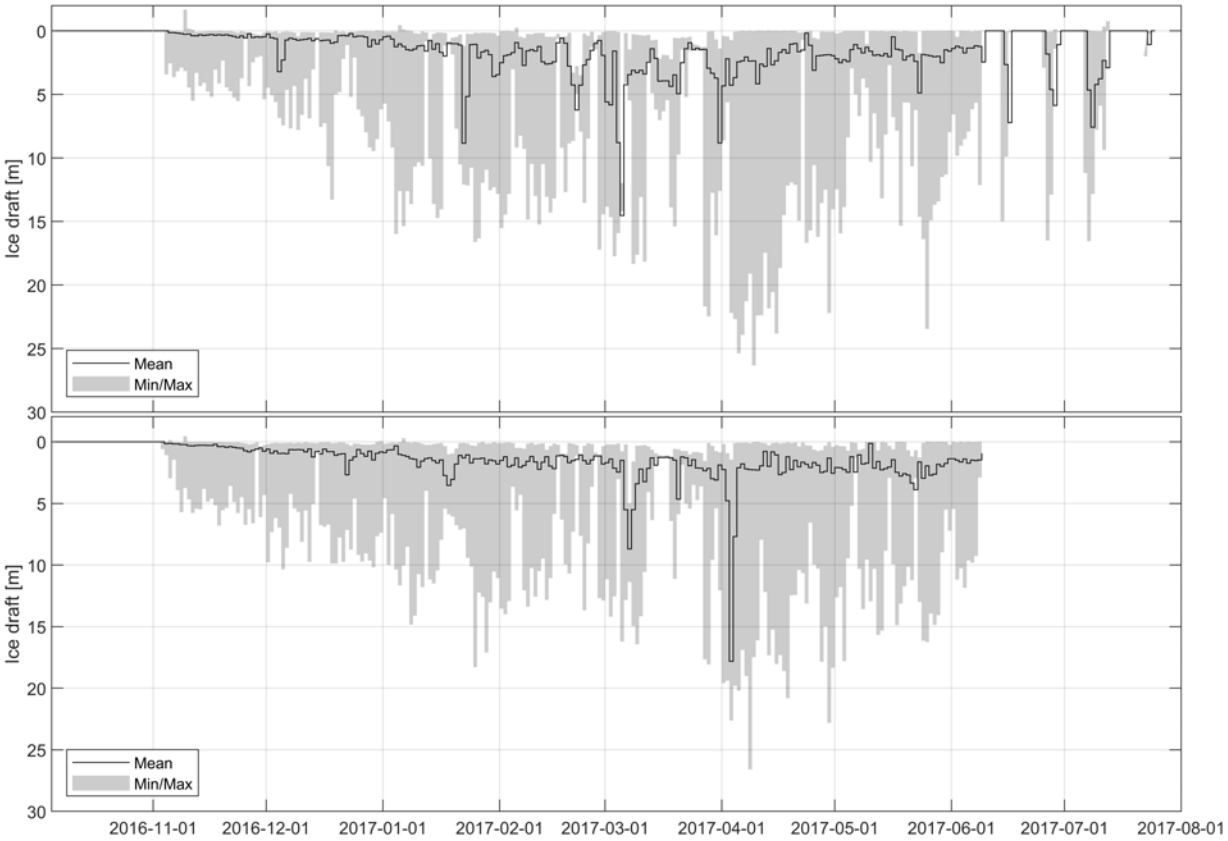

Figure 36. Daily minimum, maximum, and mean ice draft for M3 (top) and M4 (bottom). Open water records are omitted from the statistics.

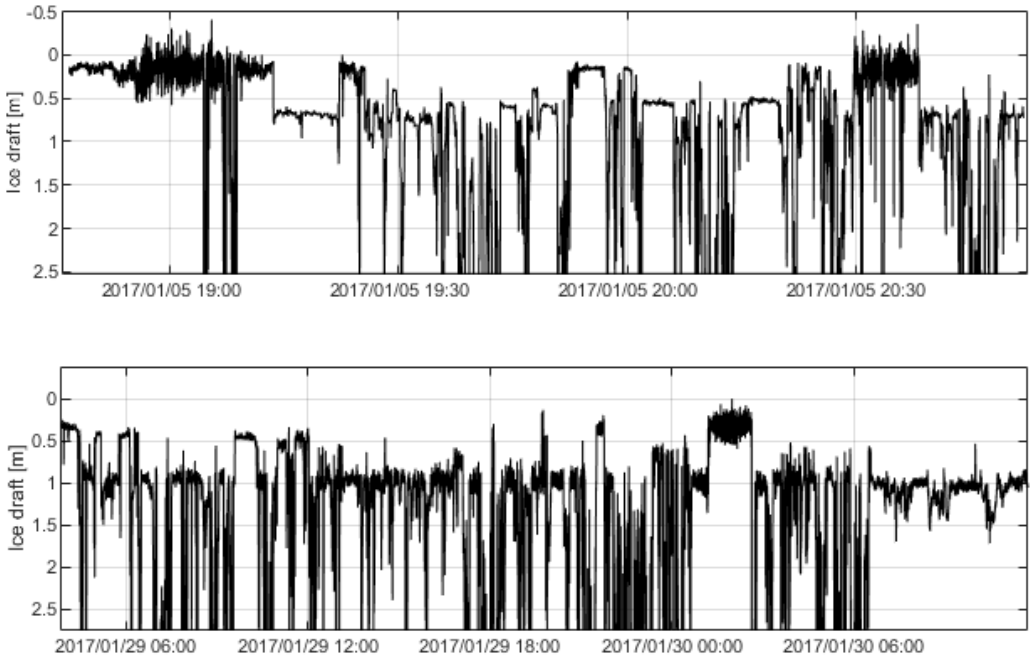

Figure 37. Examples of surface waves propagating through sea ice during January 4, 2017 at M3 (top) and late-January 2017 at M4 (bottom).

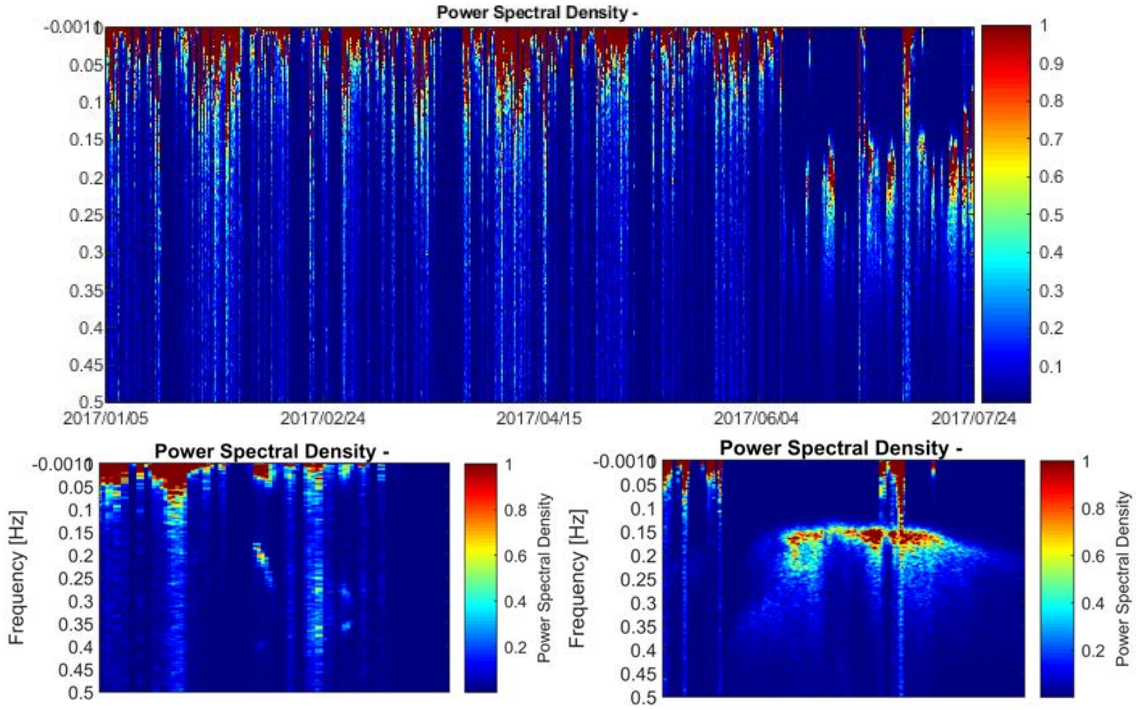

Figure 38. A spectrogram (top) based on the M3 ice draft time-series.
The color indicates the normalized power spectral density. The two detailed insets (bottom) show episodes when the ice and surface wave signals are readily separated during either slow drifting ice on February 4, 2017 (bottom left) and abundant open water on July 12, 2017 (bottom right).

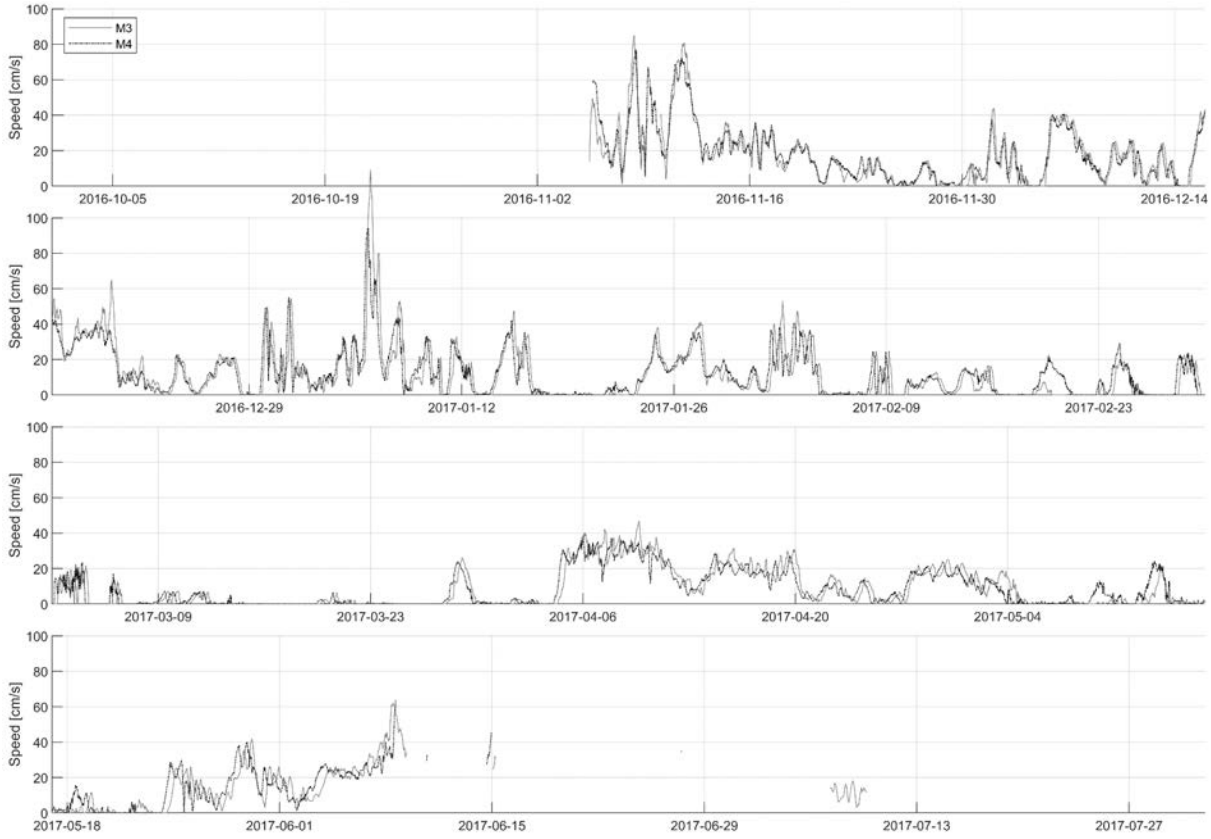

Figure 39. Horizontal ice speed at M3 and M4 over the 2016-2017 deployment.

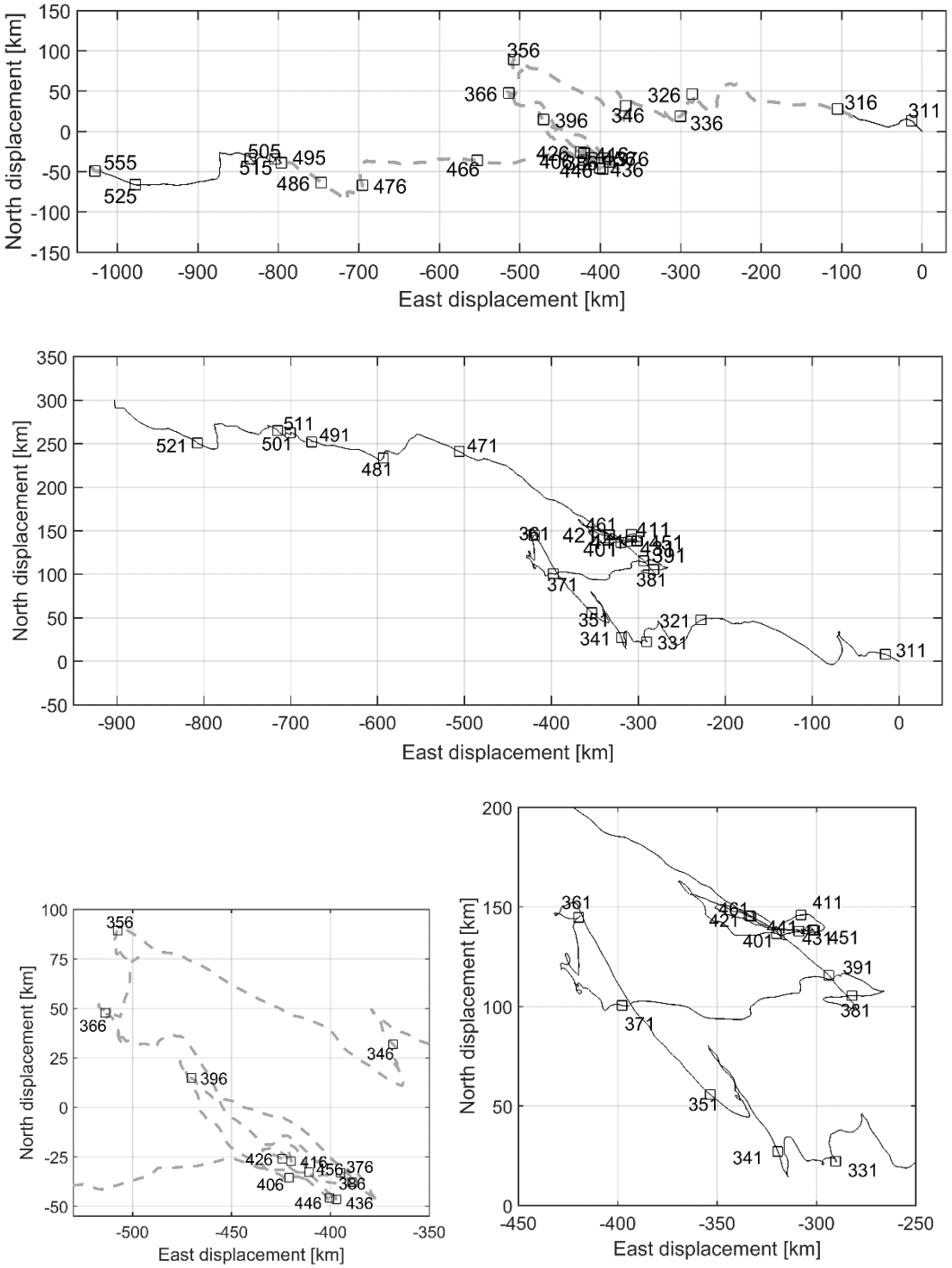

Figure 40. Progressive vector diagrams created through integration of the ice velocity time-series for M3 (top) and M4 (middle) over the full 2016-2017 deployment.

The labels indicate every tenth ordinal day of the year. The bottom panels (M3 – left, M4 – right) show a detailed view of approximately days 370 (early-January) to 450 (late-March) during which time the ice speeds were generally lower and several episodes of very low and zero-motion occurred.

The fusion of the ice draft and ice velocity time-series' enables the derivation of equispaced ice draft spatial-series following the method described in Section 3.1.2.3. The resulting total horizontal distance of ice that transited over M3 and M4 is plotted in Figure 41. This time-series itself is divided into segments of continuously measured ice velocity as summarized in Table 30 and Table 31. The total integrated ice distance was 2,159 km at M3 and 2,186 km at M4. The total cross-sectional area of ice that transited past M3 and M4 was 2.98 and 2.85 km^2, respectively.

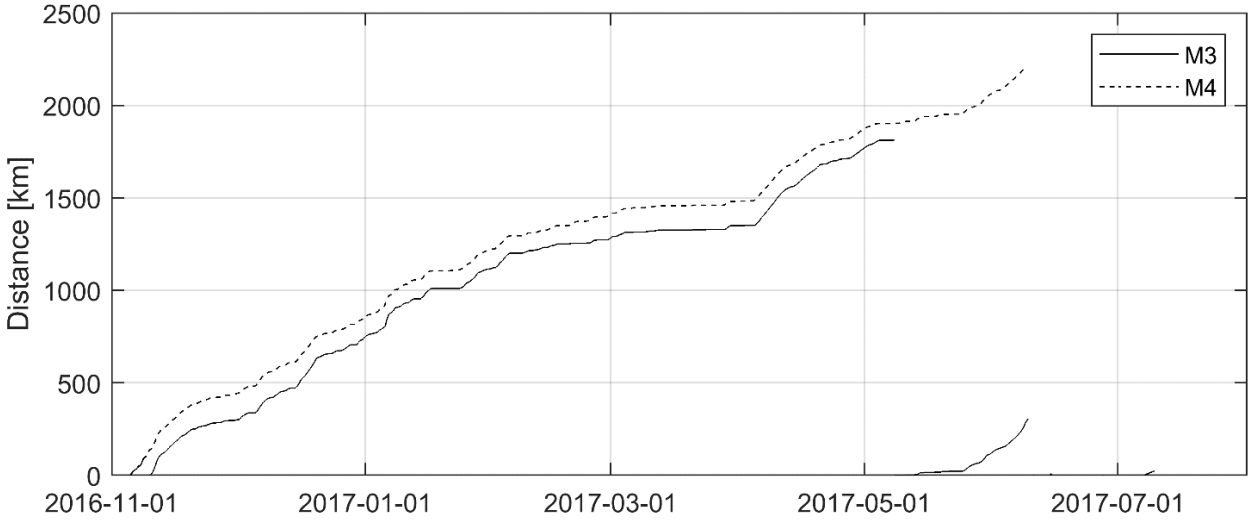

Figure 41. Time-series of the horizontal extent of ice that transited over the M3 and M4 measurement locations.

Table 30.

The horizontal spatial extents of episodes of continuous ice velocity at M3.

Segment	Start date [yyyy-mm-dd HH:MM:SS UTC]	End date [yyyy-mm-dd HH:MM:SS UTC]	Horizontal ice distance [km]	Total integrated ice distance [km]
1	2016-11-05 10:26:05	2016-11-09 05:55:37	105	106
2	2016-11-10 03:17:55	2017-05-08 05:08:09	1,805	1,812
3	2017-05-08 05:51:10	2017-06-09 09:31:36	226	306
4	2017-06-15 01:05:59	2017-06-15 06:26:26	5	5
5	2017-06-27 10:37:18	2017-06-27 12:17:23	1	2
6	2017-07-07 07:22:16	2017-07-09 17:48:09	17	24

The second last column indicates the horizontal extent for those records in the ice draft spatial-series that correspond to ice only. The last column indicates the horizontal extent for all records in the ice draft spatial-series including open water.

Table 31.

The horizontal spatial extents of episodes of continuous ice velocity at M4.

Segment	Start date [yyyy-mm-dd HH:MM:SS UTC]	End date [yyyy-mm-dd HH:MM:SS UTC]	Horizontal ice distance [km]	Total integrated ice distance [km]
1	2016-11-05 15:10:00	2017-08-06 16:09:59	2,186	2,211

The second last column indicates the horizontal extent for those records in the ice draft spatial-series that correspond to ice only. The last column indicates the horizontal extent for all records in the ice draft spatial-series including open water.

3.1.3 Temperature and Salinity

3.1.3.1 SeaSpider CTD

Timeseries of potential temperature and salinity from the CTD situated near the bottom, along with the ice concentration at the site from the AMSR-E satellite are shown in Figure 42.

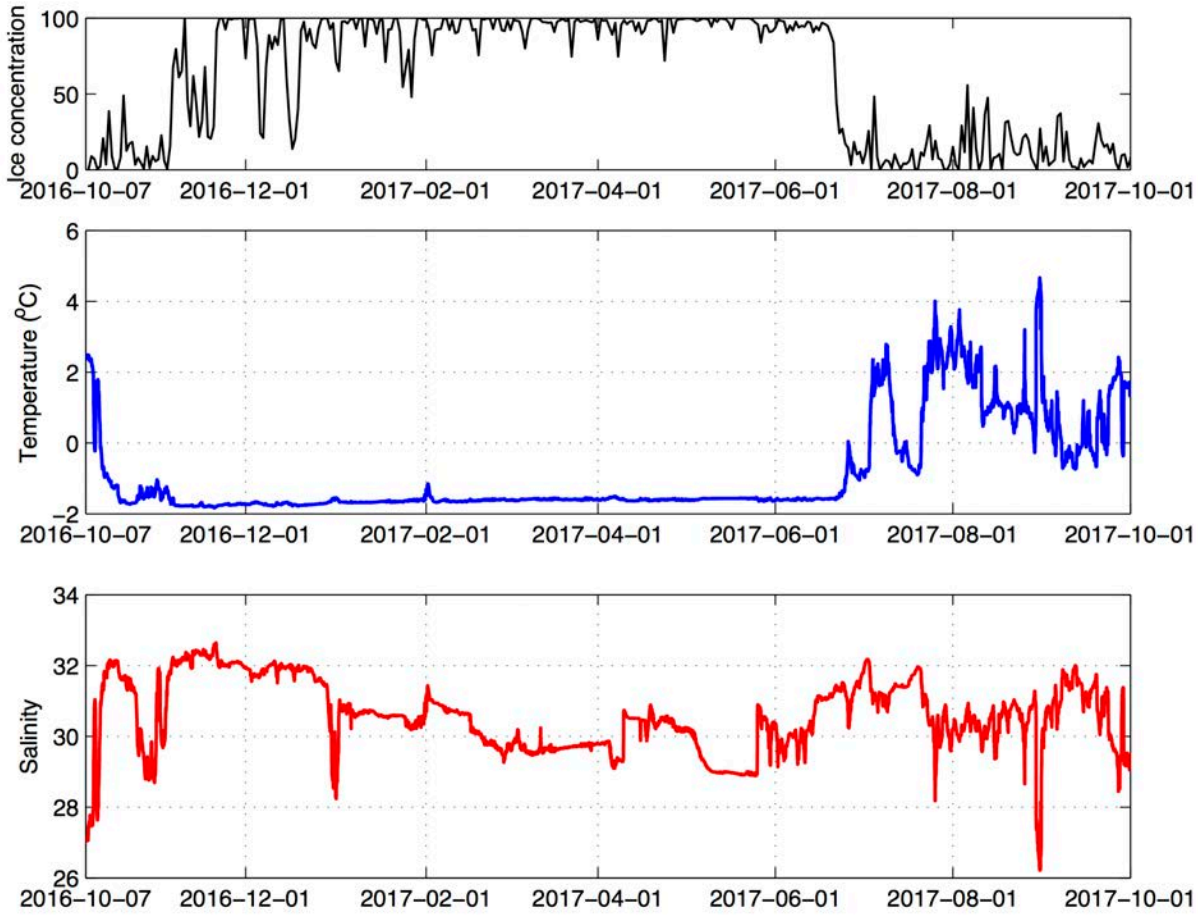

Figure 42. Timeseries of potential temperature and salinity from the SeaSpider CTD
Situated near the bottom (approximately 11 m depth), along with the ice concentration at the site from the AMSR-E satellite.

During the period of substantial ice cover from November through June, the water was just below the freezing point. However, there was considerable variability in the salinity during this time. The nature of this variability is one of the things we will be exploring in the follow-up scientific analysis.

3.1.3.2 MicroCATs

Figure 43 and Figure 44 show time series of temperature, salinity, and sensor depth at M1 and M2. Note that the shallowest MicroCAT (MC) of both M1 and M2 underwent a depth change roughly half-way through the deployment. We presume that the top floatation of the tripod/moorings was destroyed by ice, leading it to sink below the second deepest MicroCAT. The floatation originally between the top and middle MicroCATs then became the shallowest element of the mooring.

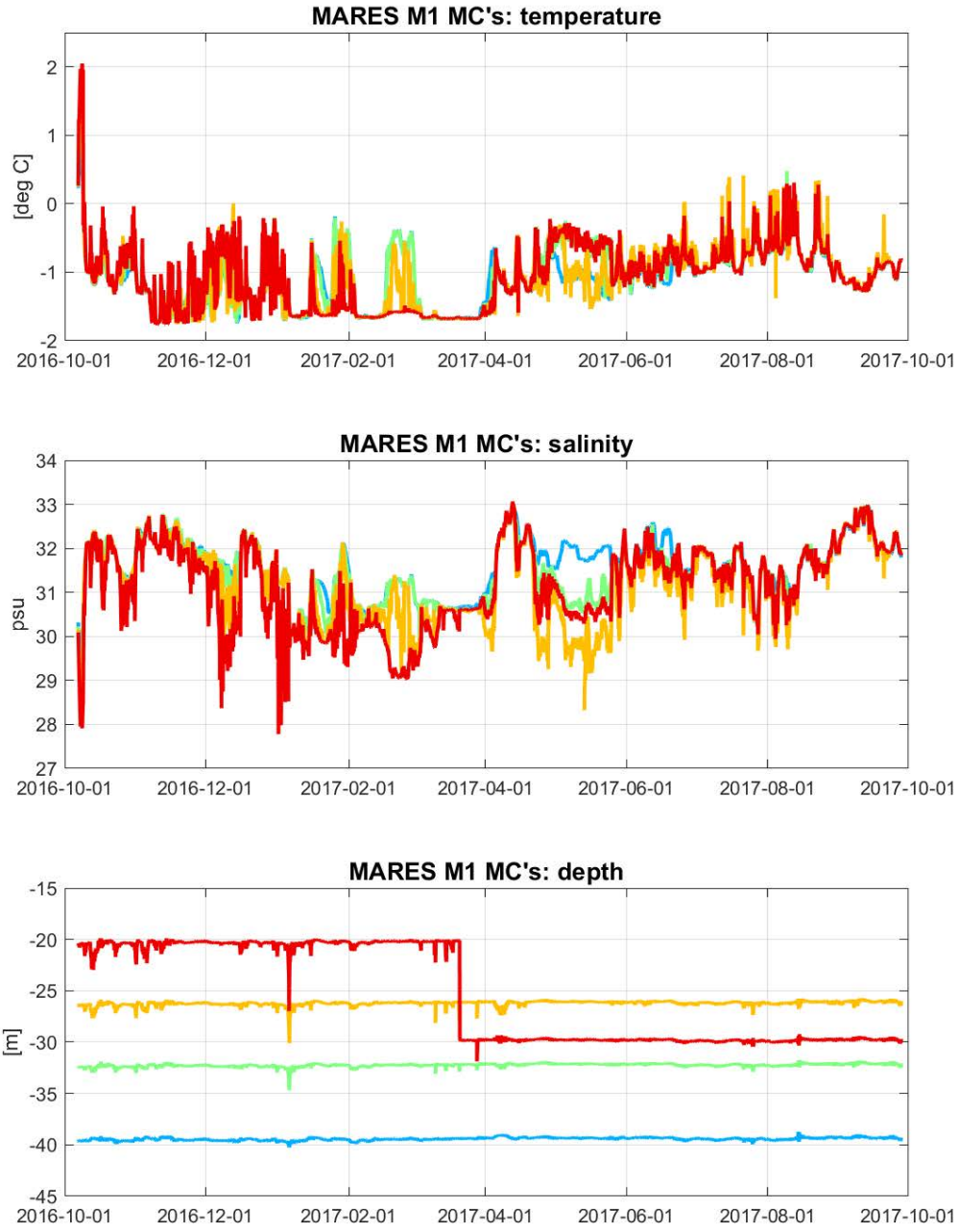

Figure 43. M1 MicroCAT (MC) time series of temperature (top), salinity (middle), and sensor depth (bottom). Colors represent the four MicroCATs deployed at different depths at the M1 mooring, depths and colors as per the bottom graph.

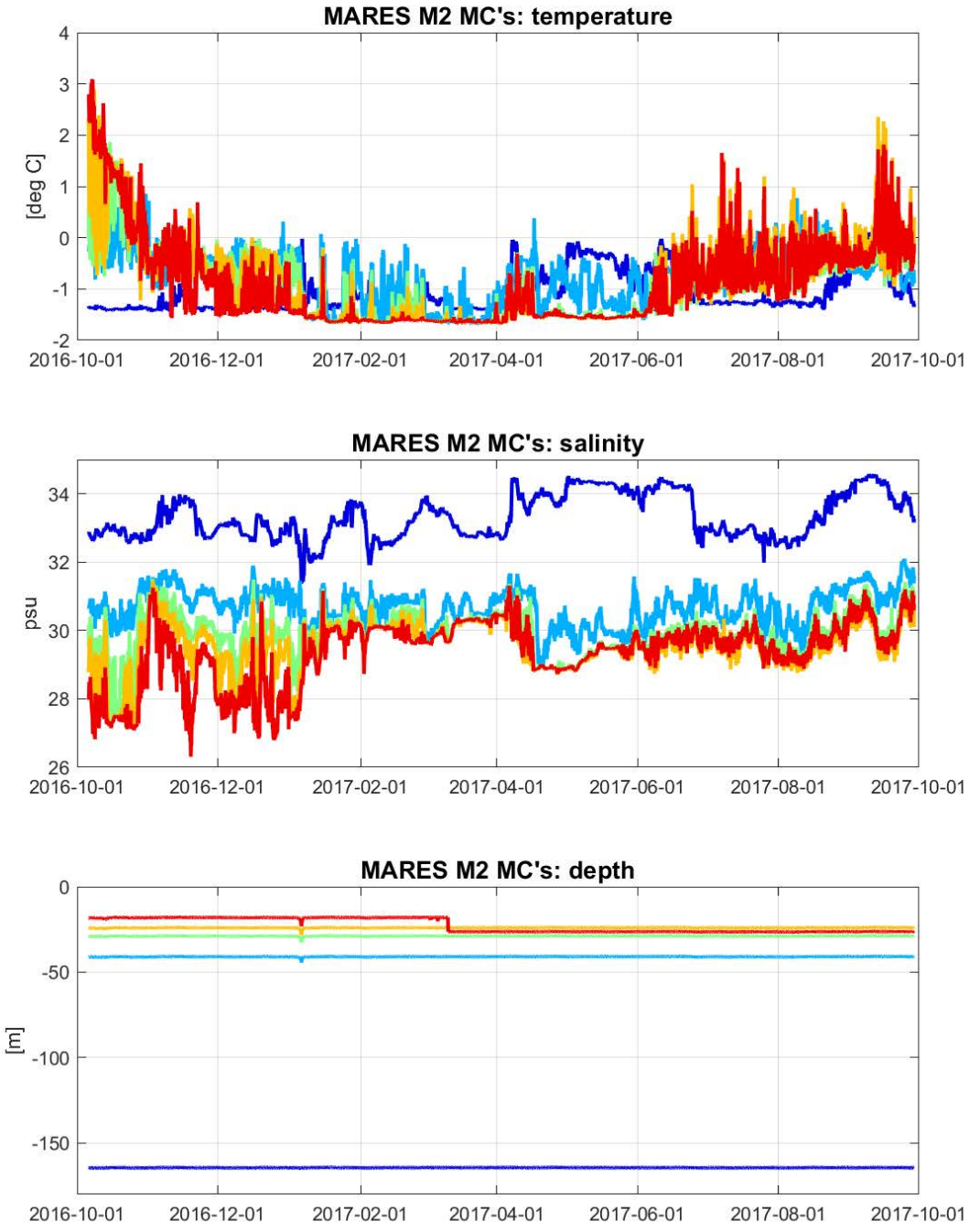

Figure 44. M2 MicroCAT (MC) time series of temperature (top), salinity (middle), and sensor depth (bottom). Colors represent the four MicroCATs deployed at different depths at the M2 mooring, depths and colors as per the bottom graph.

3.1.3.3 McLane Moored Profiler (MMP)s

In addition to the MicroCATs, the McLane Moored Profiler at M2 also collected temperature and salinity profiles (Figure 45 and Figure 46).

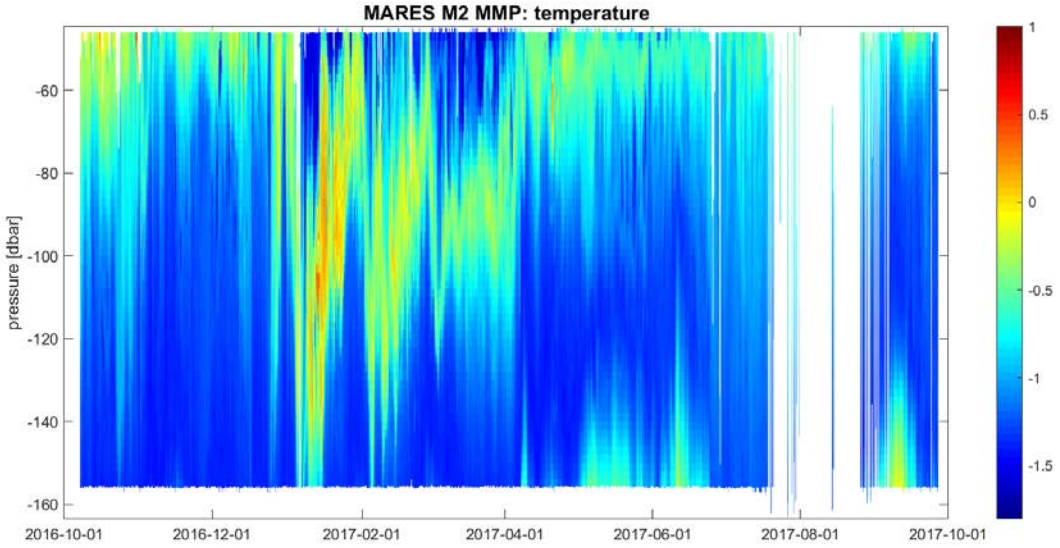

Figure 45. MMP temperature time series at M2.

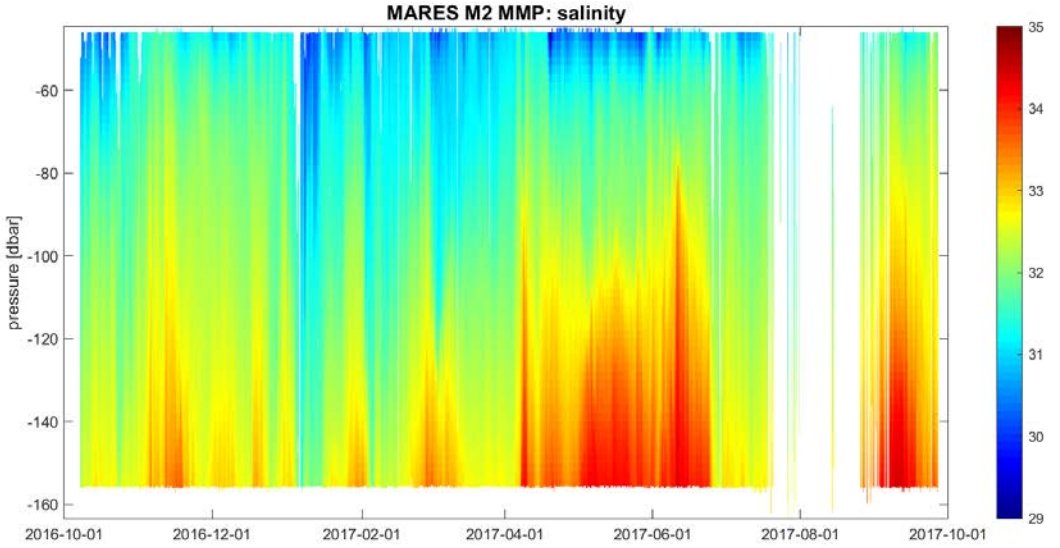

Figure 46. MMP temperature salinity time series at M2.

3.1.3.4 M3 and M4

Figure 47 and Figure 51 show the quality-controlled temperature time-series acquired from sensors on the M3 and M4 moorings, respectively. The results from the CT sensors have been supplemented with the temperature records from the co-deployed ADCP instruments. Figure 48 and Figure 52 show the quality-controlled salinity time-series acquired from sensors on the M3 and M4 moorings, respectively. Figure 49 and Figure 53 show the density time-series derived from the temperature, salinity, and pressure time-series. Figure 50 and Figure 54 show the same temperature, salinity, and density results; however, the results have been interpolated over the full water depth span and the depth of each sensor is shown.

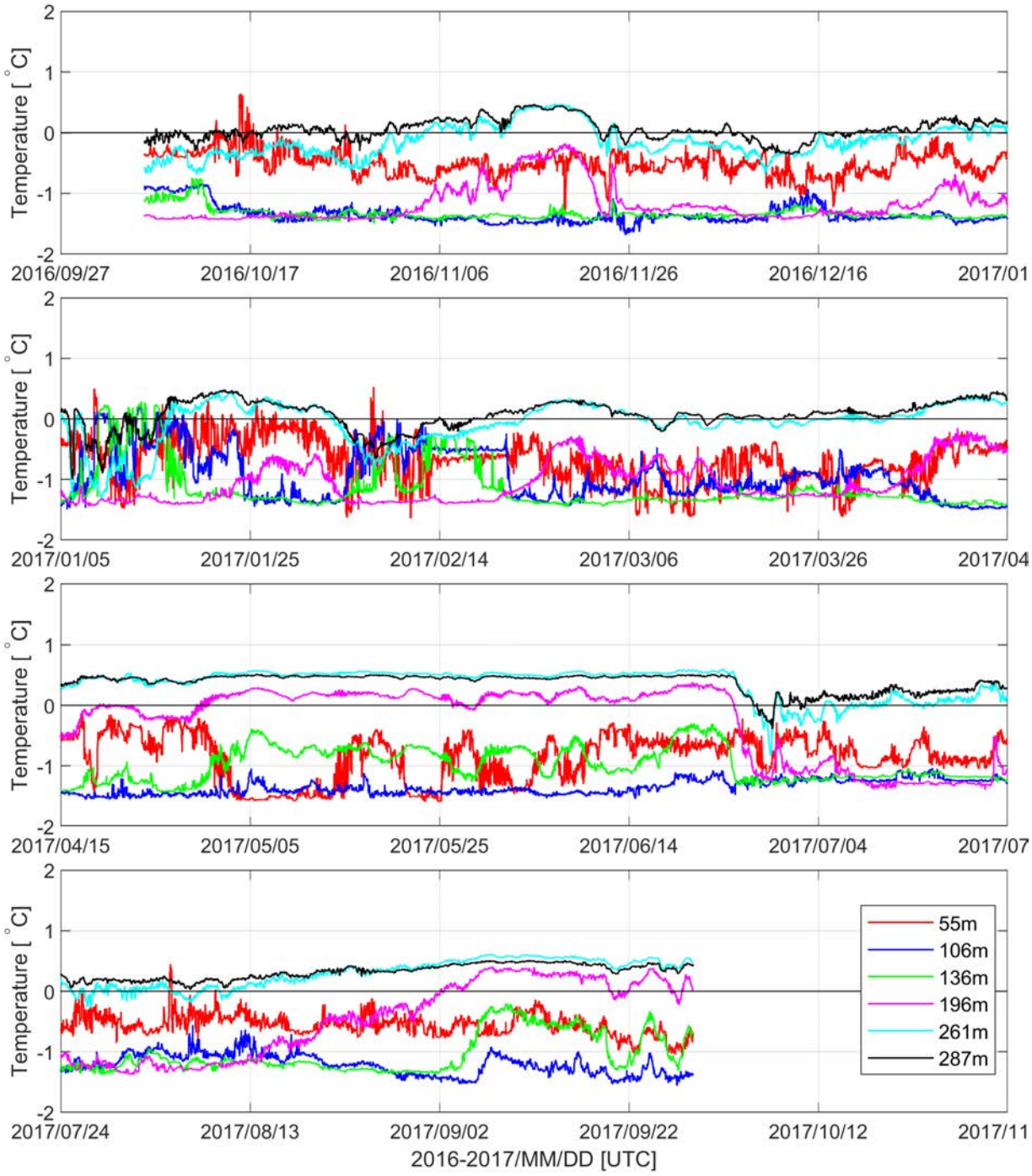

Figure 47. Temperature time-series as measured by sensors on M3 at various depths.
The 106 m depth curve (blue) and 287 m depth curve (black) originate from the ADCPs. The other curves originate from MicroCAT CTs located at different depths

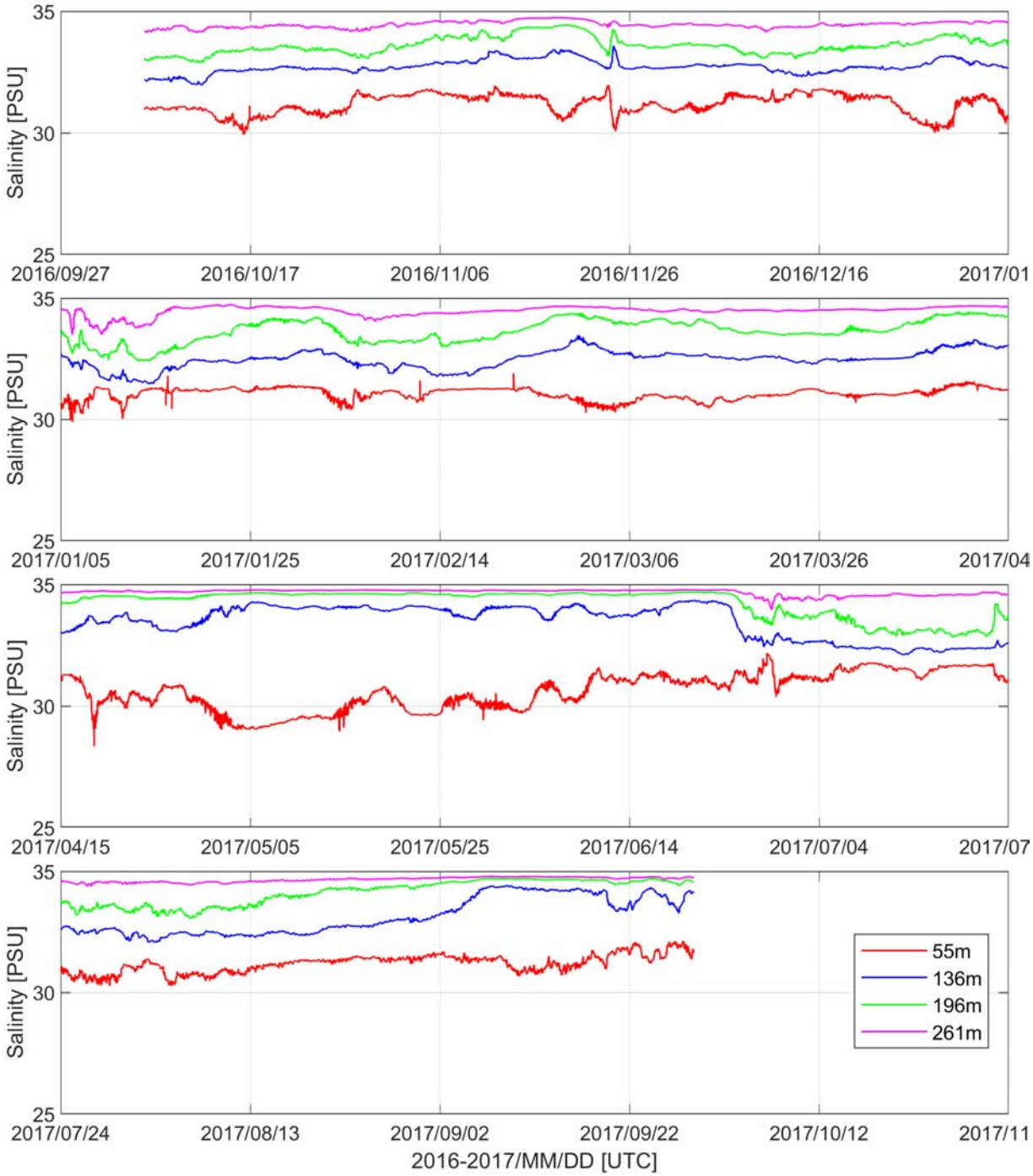

Figure 48. Salinity time-series as measured by CT sensors on M3 at various depths.

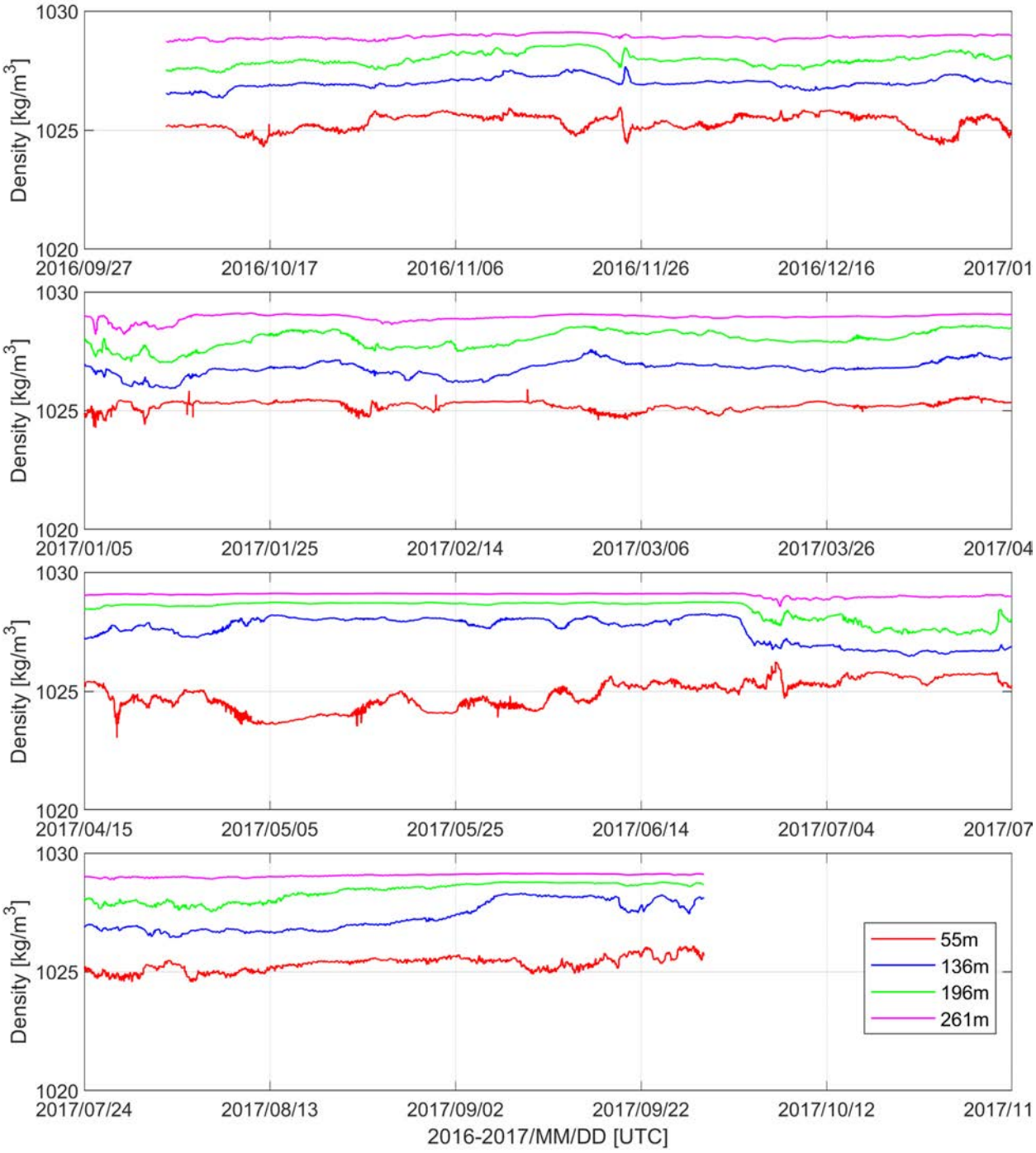

Figure 49. Density time-series derived from CT sensor measurements on M3 at various depths.

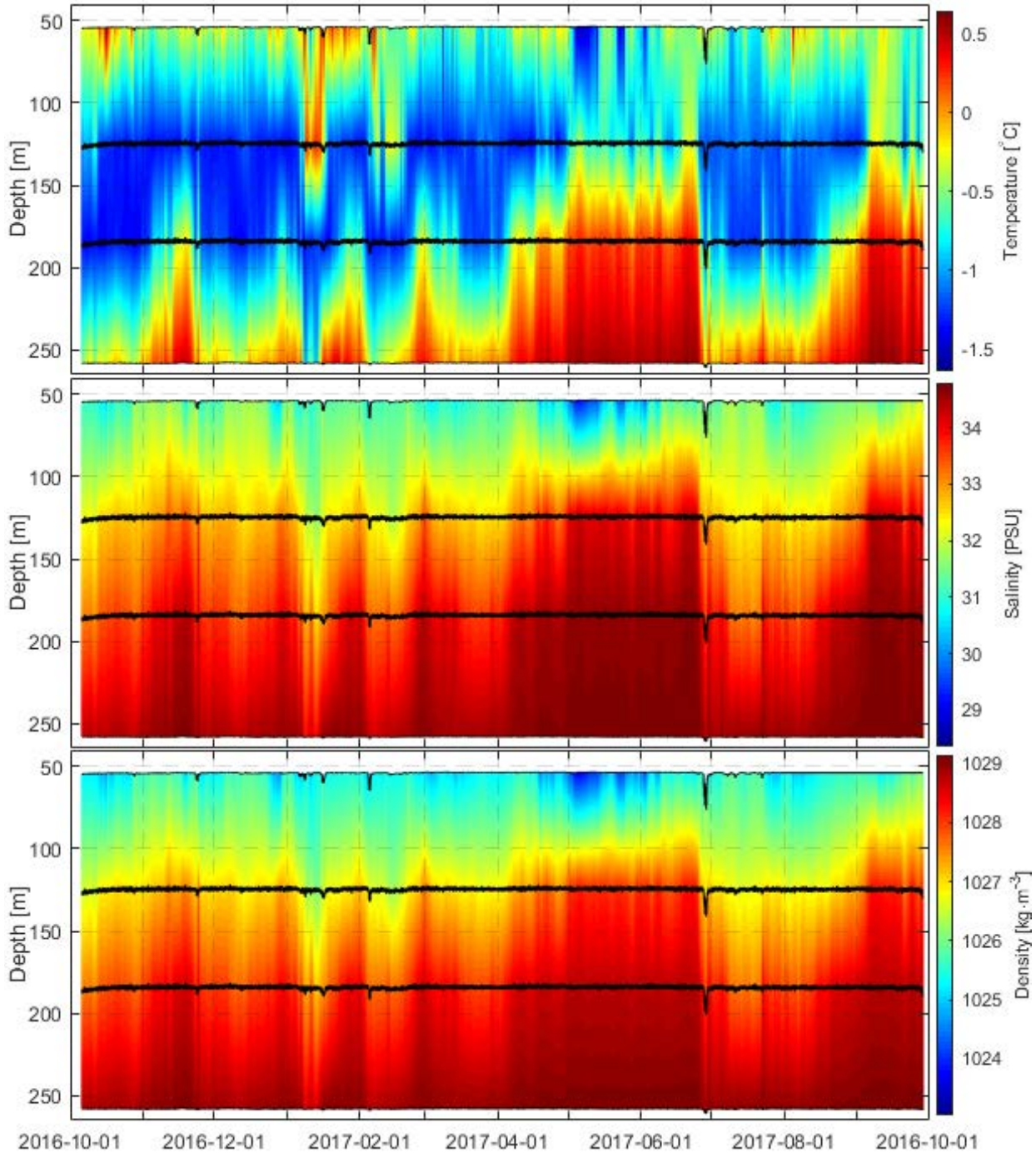

Figure 50. Temperature, salinity, and density time-series from CT sensors on M3 and interpolated over the full sampled water depth span. The black curves show the depth of each sensor used in the interpolation.

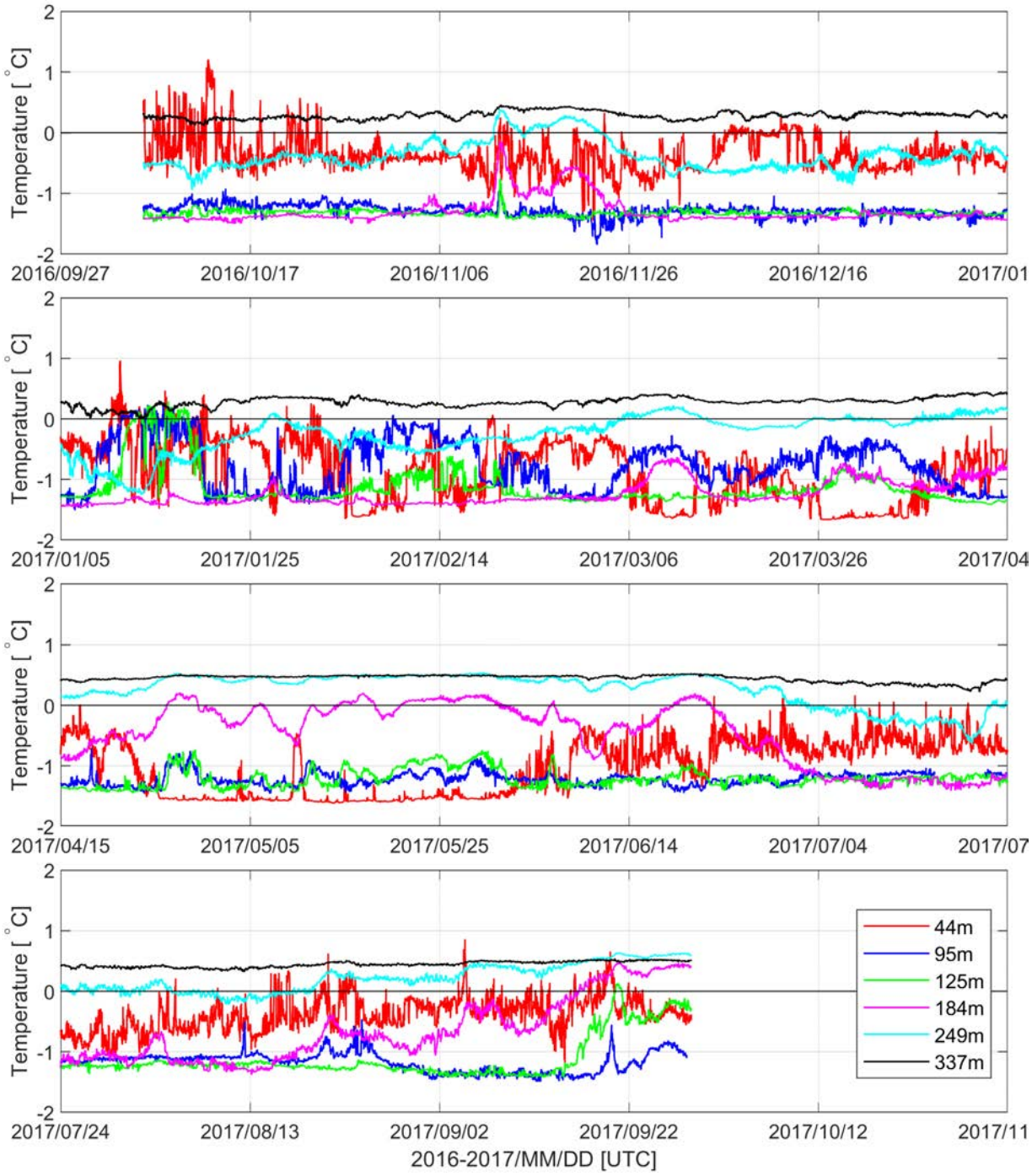

Figure 51. Temperature time-series as measured by sensors on M4 at various depths.
The 95 m depth curve (blue) and 337 m depth curve (black) originate from the ADCPs. The other curves originate from MicroCAT CTs at various depths.

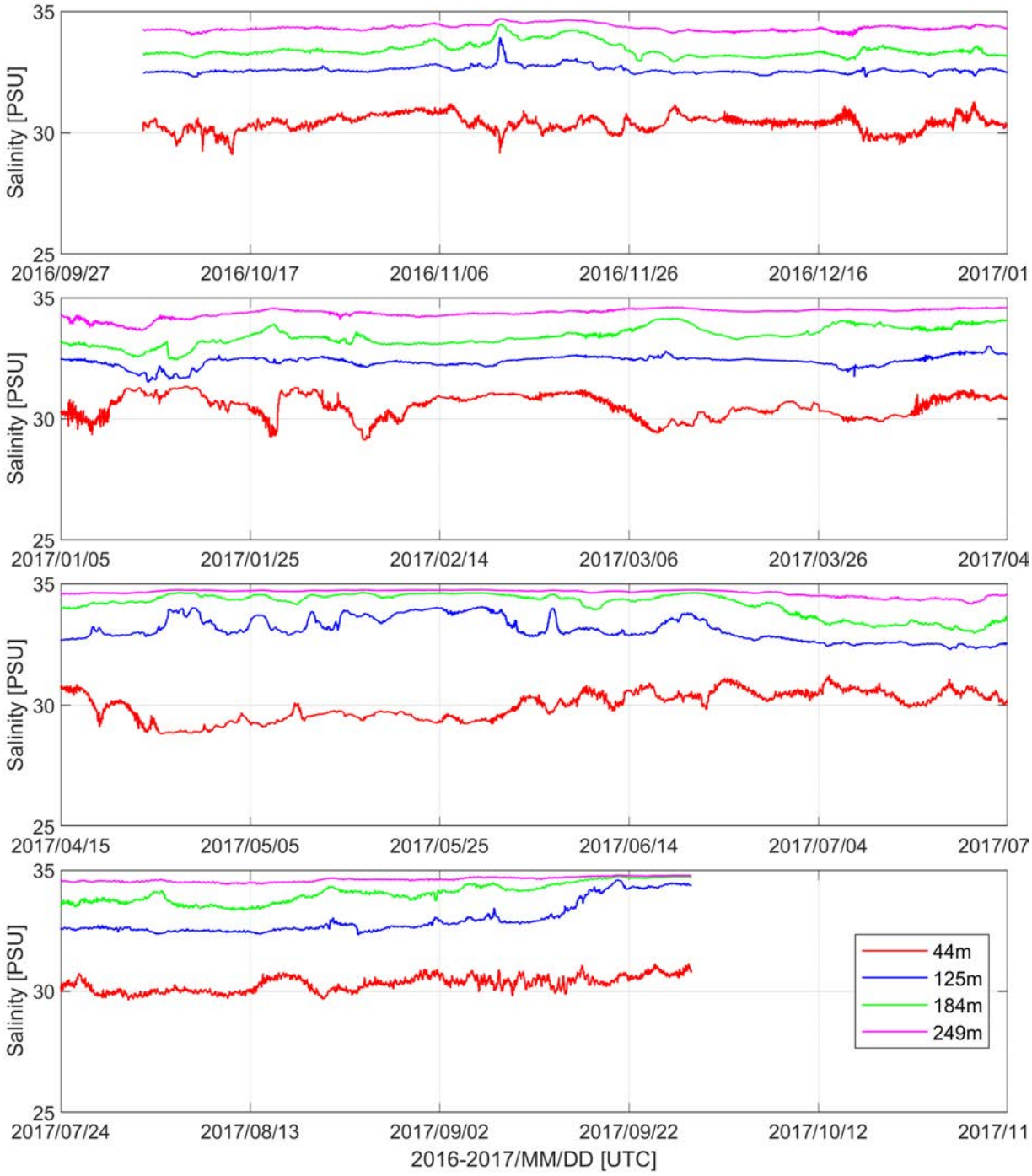

Figure 52. Salinity time-series as measured by CT sensors on M4 at various depths.

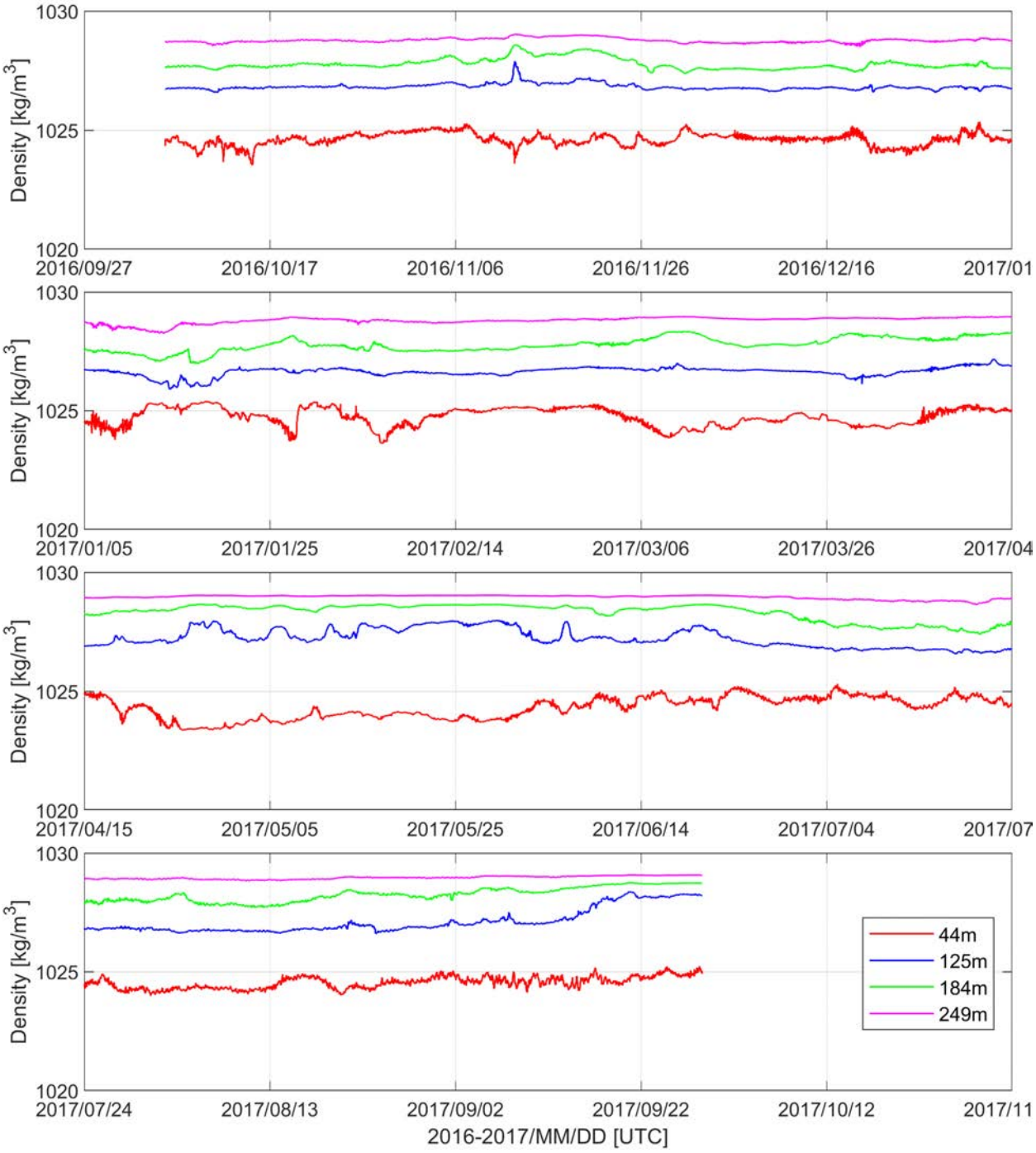

Figure 53. Density time-series derived from CT sensor measurements on M4 at various depths.

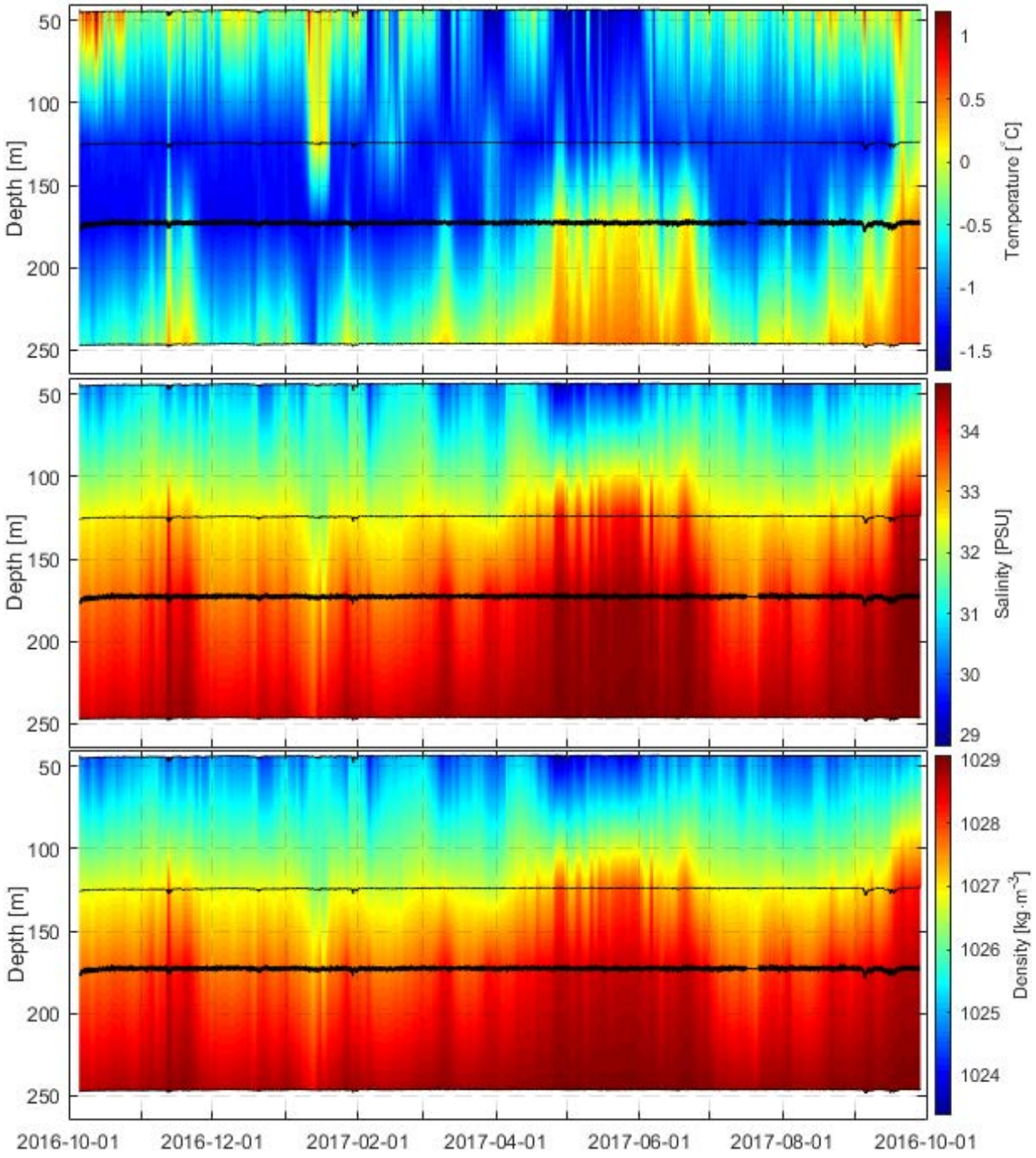

Figure 54. Temperature, salinity, and density time-series from CT sensors on M4 and interpolated over the full sampled water depth span. The black curves show the depth of each sensor used in the interpolation.

3.1.4 Turbidity

In addition to temperature and salinity, the MMP at M2 also collected water turbidity profiles (Figure 55). The most visible increases in turbidity were observed during the first three weeks of March and in mid May.

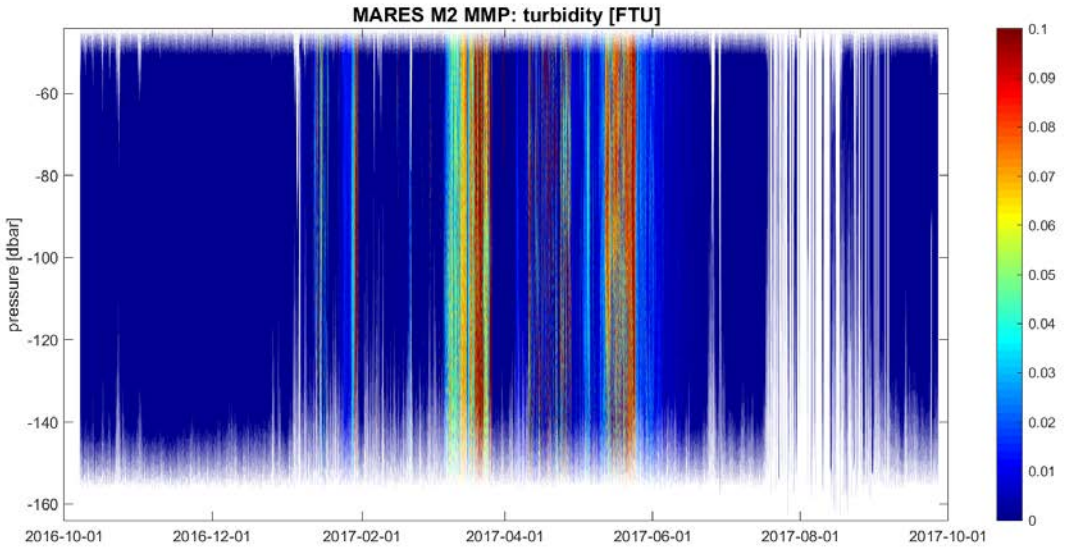

Figure 55. MMP turbidity time series at M2, in Formazin Turbidity Units (FTU).

3.1.5 Photosynthetically Active Radiation (PAR)

The MMP also collected photosynthetically active radiation (PAR), the spectral range of solar radiation from 400 to 700 nanometers that photosynthetic organisms are able to use in photosynthesis (Figure 56). Although the profiles seem reasonable, a PAR sensor at depth would normally be used in conjunction with "surface PAR", a second sensor at the ocean surface. Without it, it is not possible to distinguish between variability in oceanic light transmission and fluctuations in solar input at the surface (mostly due to cloud changes). Most evident increase in PAR was observed in April, coinciding with the opening of the ice lead discussed in Section 3.2 above.

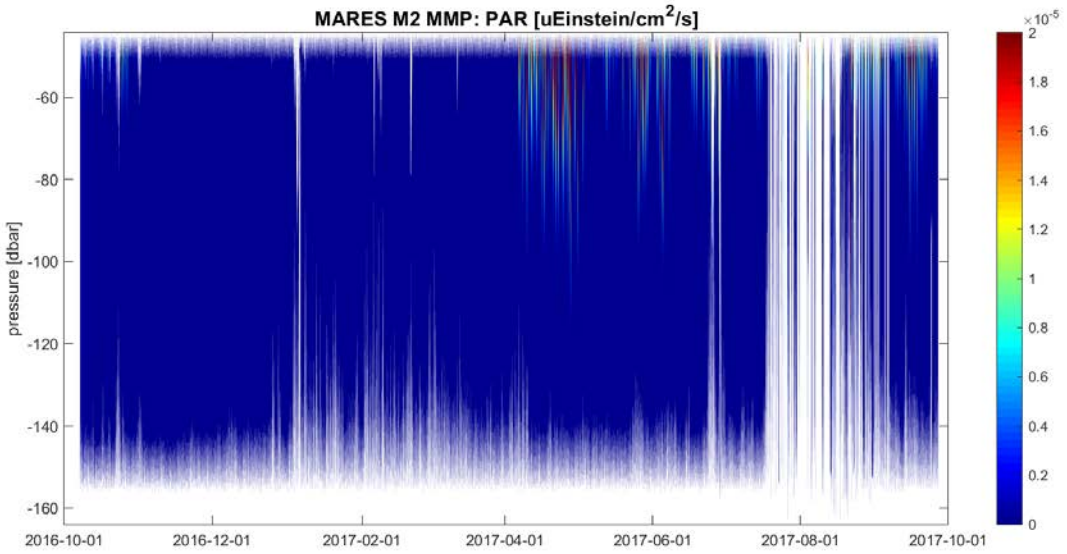

Figure 56. MMP PAR time series at M2.

3.2 CHEMICAL OCEANOGRAPHY AND PRODUCTIVITY

3.2.1 Oxygen (DO)

The SBE43 dissolved oxygen sensor on the MMP at M2 collected reasonable looking profiles for nearly the whole deployment (Figure 57). Seven profiles late in the record (#1937:1943) were removed because of unrealistically low values, presumably due to a fouled sensor. However, as is typical for this type of membrane sensors, the data frequently showed slight differences between up- and down-profiles ("up/down hysteresis"). Further, the oxygen calibration could not be inspected for drift due to the lack of independent information such as oxygen bottle samples. At present the data should be treated with caution, primarily due to the lack of an independent reference.

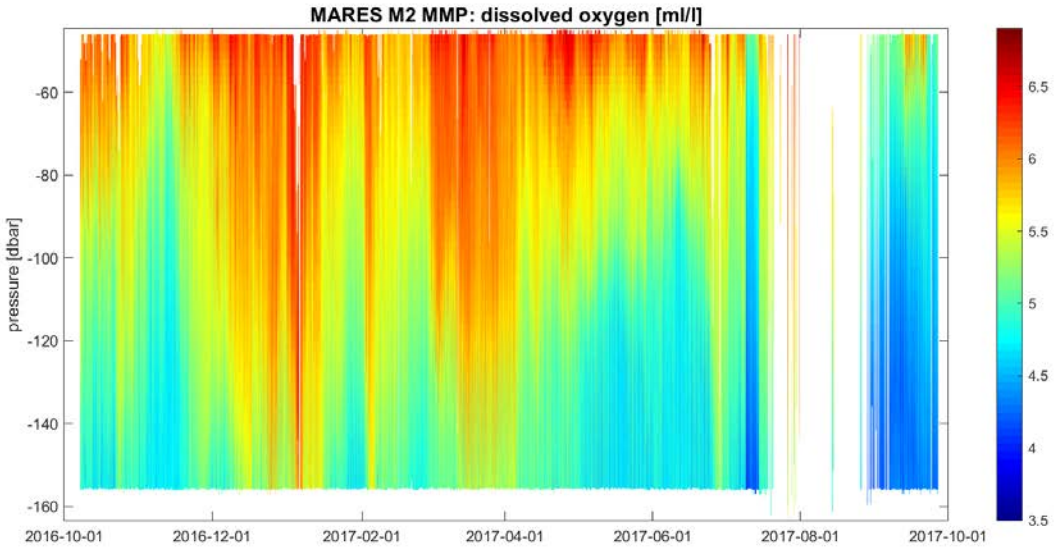

Figure 57. MMP dissolved oxygen time series at M2 (units are ml/L)

3.2.2 Nitrates

At M1, it appears that the SUNA experienced optically dense conditions early in the deployment and again towards the end of the deployment, which led to extended integration time per sample. During these events the RMS error and absorbance values exceeded the manufacturer thresholds so that no valid data was collected. As a result of the extended lamp-time, the instrument battery was rapidly depleted and no valid nitrate concentration data was collected after 2017-07-19. The instrument was still operating until recovery and continued to record other data, but the battery voltage dropped too low to acquire nitrate readings. At M2, the instrument was affected by optically dense conditions as well, but only towards the end of the deployment. As a result of these conditions much of the data following mid-July 2017 was unreliable, except for an episode from late-August to early-September. The quality-controlled nitrate time-series for M1 and M2 are displayed in Figure 58.

In the raw data for M1 there were 3,722 (43.6%) records with missing data. In the final quality-controlled time-series, there is 3,666 (42.9%) records with missing data. This decrease in the amount of missing data was accomplished by interpolating across short gaps in the record. In the final quality-controlled time-series, there were 1,490 (17.4%) records identified that exceeded the manufacturer threshold for reliable data. Of these, 308 (3.6%) records were identified as being possibly acceptable. There were another 175 (2.1%) records identified as being suspect due to other reasons, such as exceeding expected values, or being noisy.

In the raw data for M2 there were 582 (6.8%) records with missing data. In the final quality-controlled time-series, there is 506 (5.9%) records with missing data. As with M1, there was a decrease in the amount of missing data by interpolating across short gaps in the record. In the

delivered data, there were 1,087 (12.7%) records identified that exceeded the manufacturer threshold for reliable data. There were 1,002 (11.7%) negative records that were shifted into the positive by an offset of +4.69 µM. There were another 193 (2.3%) records identified as being suspect due to other reasons, such as exceeding expected values, or being noisy.

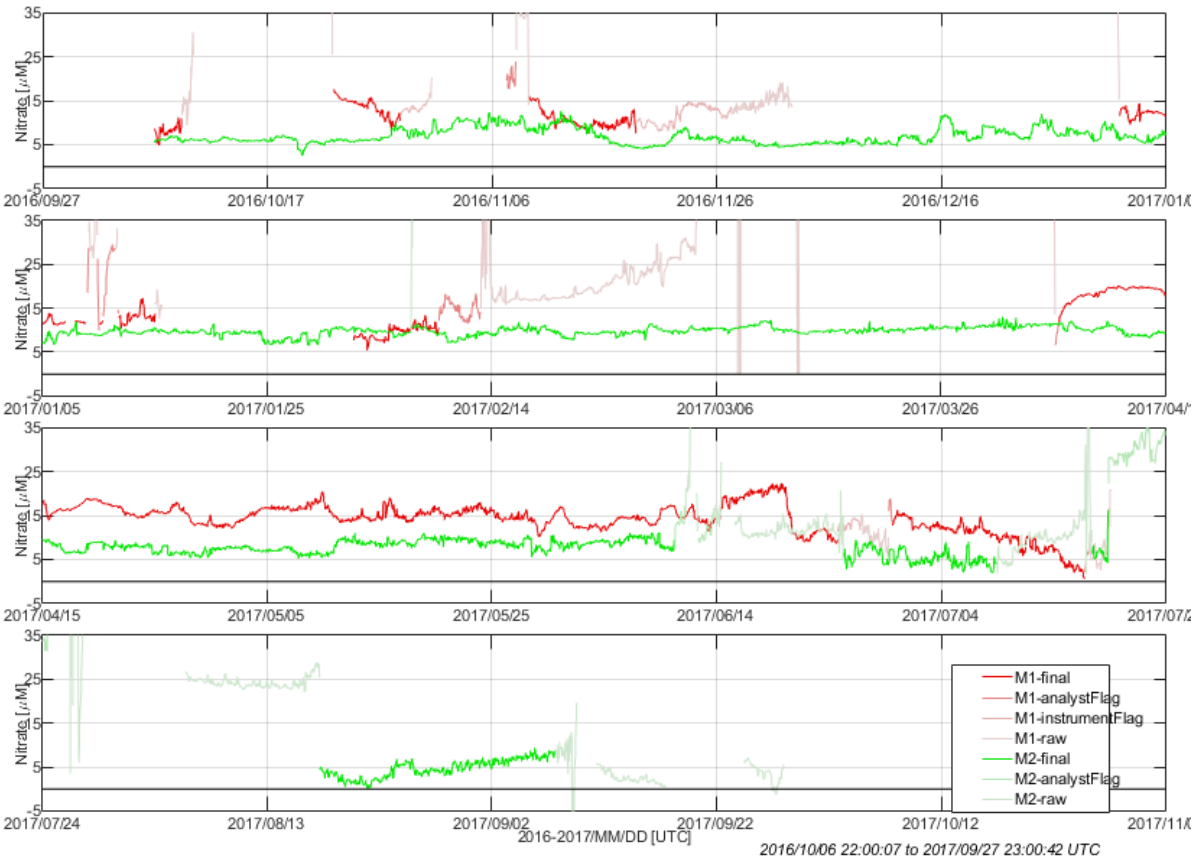

Figure 58. Comparison of M1 and M2 quality-controlled nitrate time-series.
Colors correspond to values in the data quality channels.

The values of high confidence nitrate concentration were between 0.6 to 22.3 µM at M1, and between 0.0 to 13.0 µM at M2. Typical nitrate concentrations in this region have been below 20 µM.

During episodes of low (no) biological productivity, the concentration of nitrates generally follows that of biologically inert compounds such as salinity. The salinity is compared to the nitrate concentration in Figure 59 and Figure 60. The salinity has been scaled (de-meaned, divided by standard deviation of salinity, multiplied by standard deviation of nitrate and added to the mean value of nitrate) to be readily compared to the nitrate concentration. Productivity usually diminishes when the number of daylight hours decrease, or when ice is present, so we would expect that the trend of nitrate concentration should be relatively consistent during the winter. Some

increase in nitrate concentration may occur over the winter if deepwater is advected to the upper ocean. Generally, though, during episodes of low productivity, the nitrate concentration should follow a similar trend to the salinity. The number of daylight hours over the deployment are shown in Figure 61. This trend was observed at M2 with the nitrates and salinity following a similar trend from October 2016 through to early-June 2017 when the ice break-up occurred, and the high-confidence nitrate concentrations decrease. At M1, the trends of salinity and nitrate were similar in the first few days of deployment and from about April 5 to April 23, 2017. Other than this, the trend in the nitrate concentration was erratic and inconsistent during the winter when no biological productivity was expected. It is possible that strong upwelling may have occurred bringing in nitrate rich waters, but this is unclear. Further comparison to other instruments may help to resolve this anomalous signal.

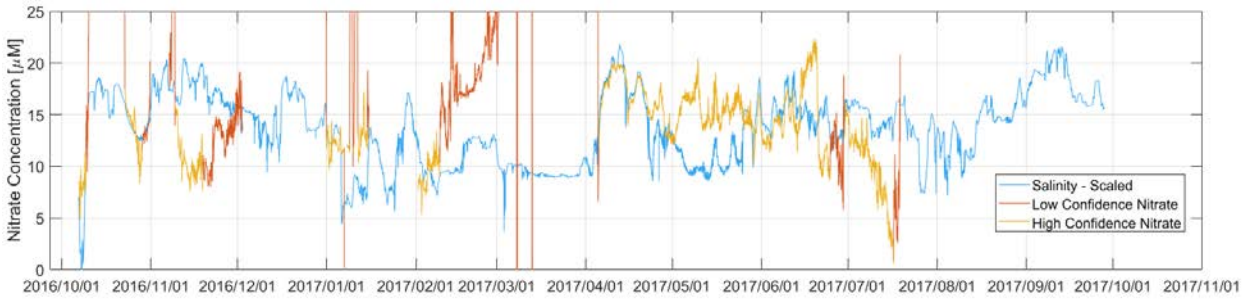

Figure 59. Comparison of Nitrates and Salinity at M1.

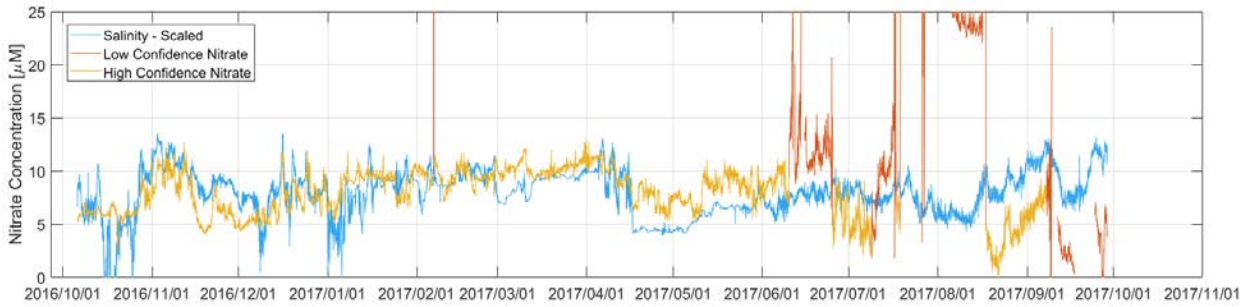

Figure 60. Comparison of Nitrates and Salinity at M2.

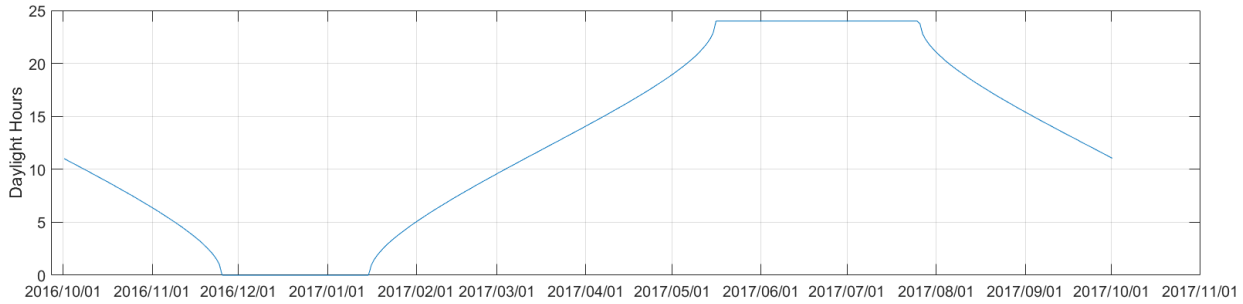

Figure 61. Number of hours of daylight over the deployment.

3.3 CARBON DIOXIDE (pCO_2)

The pCO_2 data recovered from SAMI C0009 at M1 are shown in Figure 62. The pCO_2 values ranged from 349 to 1088 µatm. Calibration samples collected at the end of the deployment did not compare well, so this data should be treated with extreme caution. Moored pCO_2 values at the end of the deployment were found to be much higher than the calibration samples collected at both sites (much more so at M1), even though the precision from the triplicate water samples taken was within our expected sampling error (<1%) and the sampling occurred according to protocol.

The most notable feature in the data record is a rapid increase in pCO_2 occurring on 05 April 2017 at M1, which is also when the ice lead started to open (Figure 35). While there are a variety of natural processes that can cause pCO_2 to increase, such an interpretation is not supported by the broader data collected by the program. Temperature variability is insufficiently large across the entire deployment to result in such a large variation in pCO_2. Additionally, other chemical oceanography data collected does not indicate a respiration event that could have produced non-conservative increases in CO_2. While nitrate data from the SUNA is not available during this period, we note that no high nitrate concentrations are found throughout the deployment (see Section 3.2.2). Additionally, no corresponding drop in oxygen values, indicating bacterial respiration, were detected (see Section 3.2.1). While lateral or vertical transport may have exposed the sensor to a new water mass, and a new water mass does appear to be present concurrent with this rise, that water mass passes out of the area within a few weeks. Meanwhile, the pCO_2 data continued to remain anomalously high. As a result, we do not believe that this rise is real.

Instead, we suggest a mechanical failure that may be related to the stress to the mooring caused by the dislodged surface MicroCAT (see Section 3.1.3; Figure 43). The hanging instrument then dropped to approximately 30 m depth, very near to the SAMI instrument. While this occurs a few days prior to the rise in CO_2 concentrations, we note that on the day of our suspected mechanical malfunction, there is a spike in the depth reading for this sensor again (Figure 43). Simultaneously, there is a jump in surface velocity (see Section 3.1.1.2; Figure 18 and Figure 19). We believe that this represents a wind event that disturbed the water column, perhaps causing the freely swinging MicroCAT to contact the mooring line and disturb the SAMI pH sensor. Because this percussive impact occurred much closer to the sensor than the original impact with ice suspected to have

dislodged the MicroCAT, it could have been more damaging. Cumulative stress from both impacts could also underlie this malfunction.

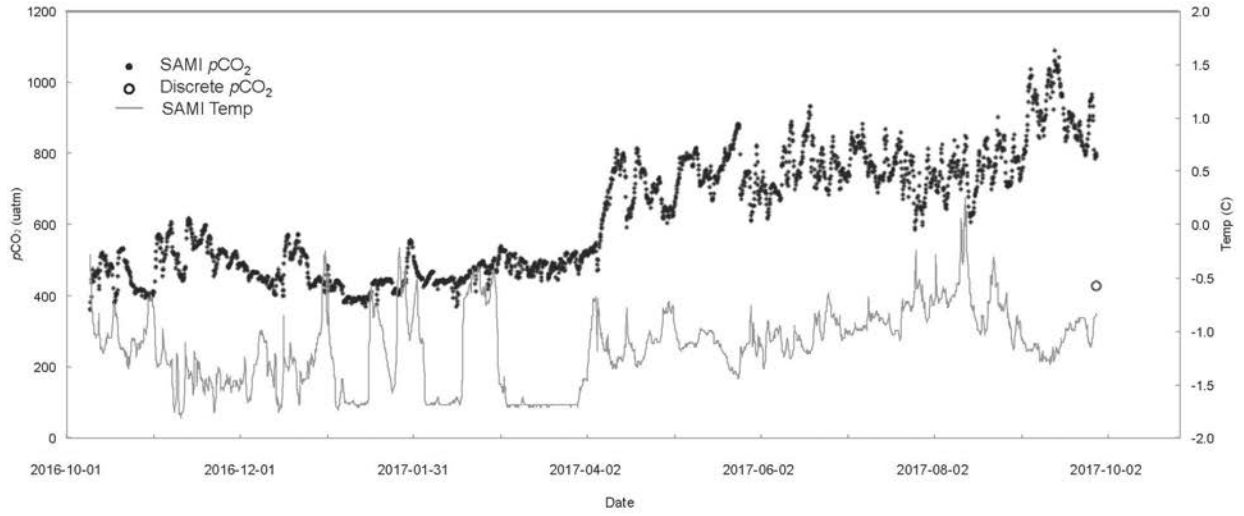

Figure 62. SAMI data from M1 (C0009) 36 m.
Black dots are pCO_2 (µatm) measured every three hours. Open circle is the calculated pCO_2 from the discrete sample collected upon recovery of the sensor. The gray line is the temperature data from the SAMI.

The pCO_2 data recovered from SAMI C0021 at M2 are shown Figure 63. The pCO_2 values at this location had a tighter range as compared to M1, from 283 to 755 µatm. While the data record here looks more reasonable, end of deployment calibration samples for M2 also did not compare well, and resultantly the data should be treated with caution. At this site, a surface MicroCAT was also dislodged, falling to 30 m. We note that the surface velocity change associated with our hypothesized April 5 wind event was much weaker at M2 than at M1 (see Section 3.1.1.2, Figure 21 and Figure 22). The depth of the freely swinging MicroCAT sensor at M2 also appears more stable, perhaps indicating a lack of impact similar to that experienced at M1 (see Section 3.1.3, Figure 44). The mismatch between the calibration sample and the moored record is more difficult to explain in this case. We note that the calibration sample was collected during a time of high variability in the data record.

The daily average for both sites are shown in Figure 64. The M2 data are generally lower than values seen at the M1 site, particularly after the stepped increase observed at M1 after April 2017. Noise even in the smoothed data is evident in the M2 record after late April, possibly associated with surface water mass variability. A sensor was redeployed at the M1 mooring site for the 2017-2018 field season, and we hope these new data will aid in the interpretation of the 2016-2017 data record.

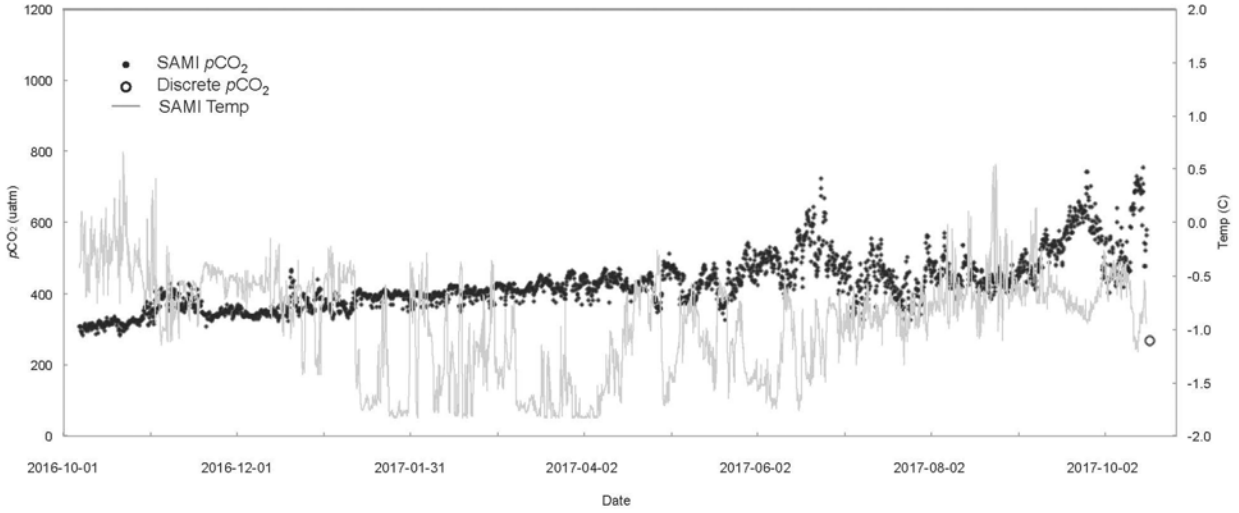

Figure 63. SAMI data from M2 (C0021) 36 m.
Black dots are pCO_2 (μatm) measured every three hours. Open circle is the calculated pCO_2 from the discrete sample collected upon recovery of the sensor. The gray line is the temperature data from the SAMI.

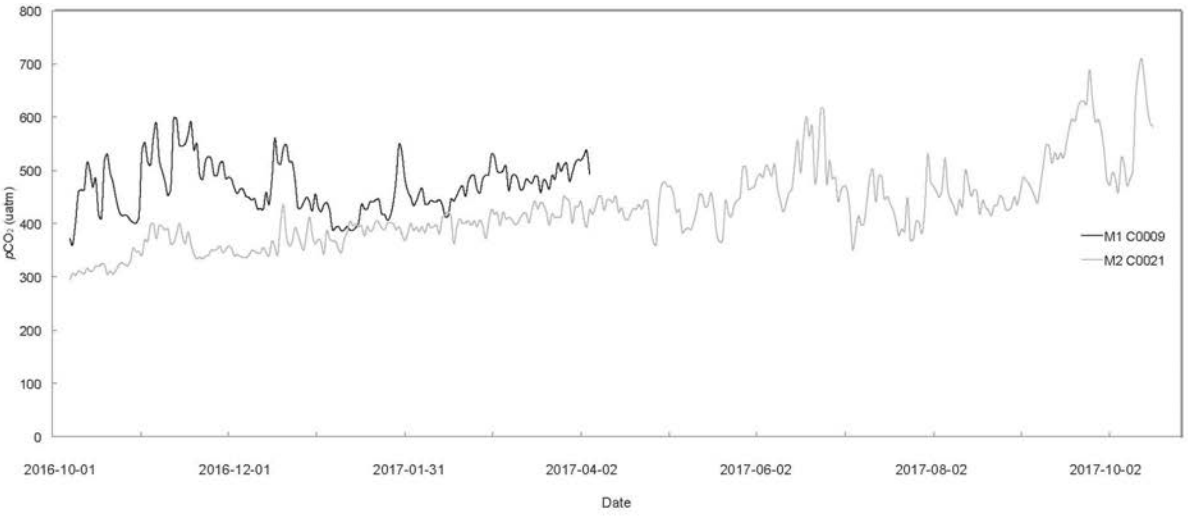

Figure 64. Daily averaged SAMI data from M1 and M2.

3.4 BIOLOGICAL OCEANOGRAPHY

3.4.1 Primary Productivity

Similar to oxygen, the analog MMP sensors measuring fluorescence, collected what appeared to be reasonable profiles (Figure 65). Again, however, they are of reduced quality compared to temperature and salinity data. Nonetheless, it appears that we may have captured a fall bloom event that seemed to have been ongoing at the time of deployment (late September 2016), and increased fluoresce was detected again in spring of 2017 (mid-June) and September 2017 just before recovery.

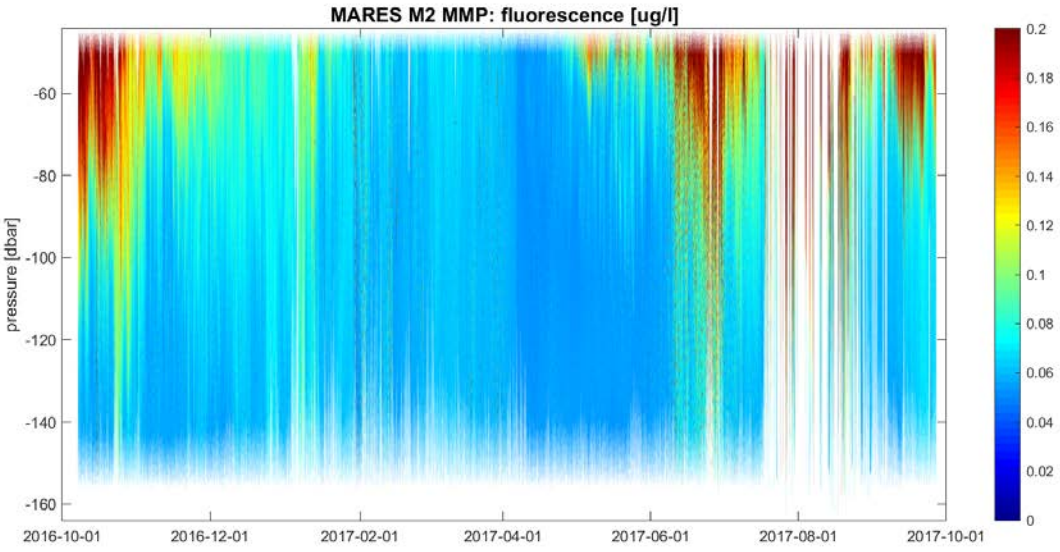

Figure 65. MMP fluorescence time series at M2.

3.4.2 Zooplankton and Fish

3.4.2.1 Comparing AZFP and ADCP

We investigated the suitability of the AZFP as a performance benchmark and compared the acoustic backscatter between the ADCP and AZFP. Figure 66 and Figure 67 show a one-week example of coincident AZFP and ADCP acoustic backscatter measurements, respectively. The full set of AZFP and ADCP acoustic backscatter depth profile time-series plots are included in the MARES Research Workspace project archive.

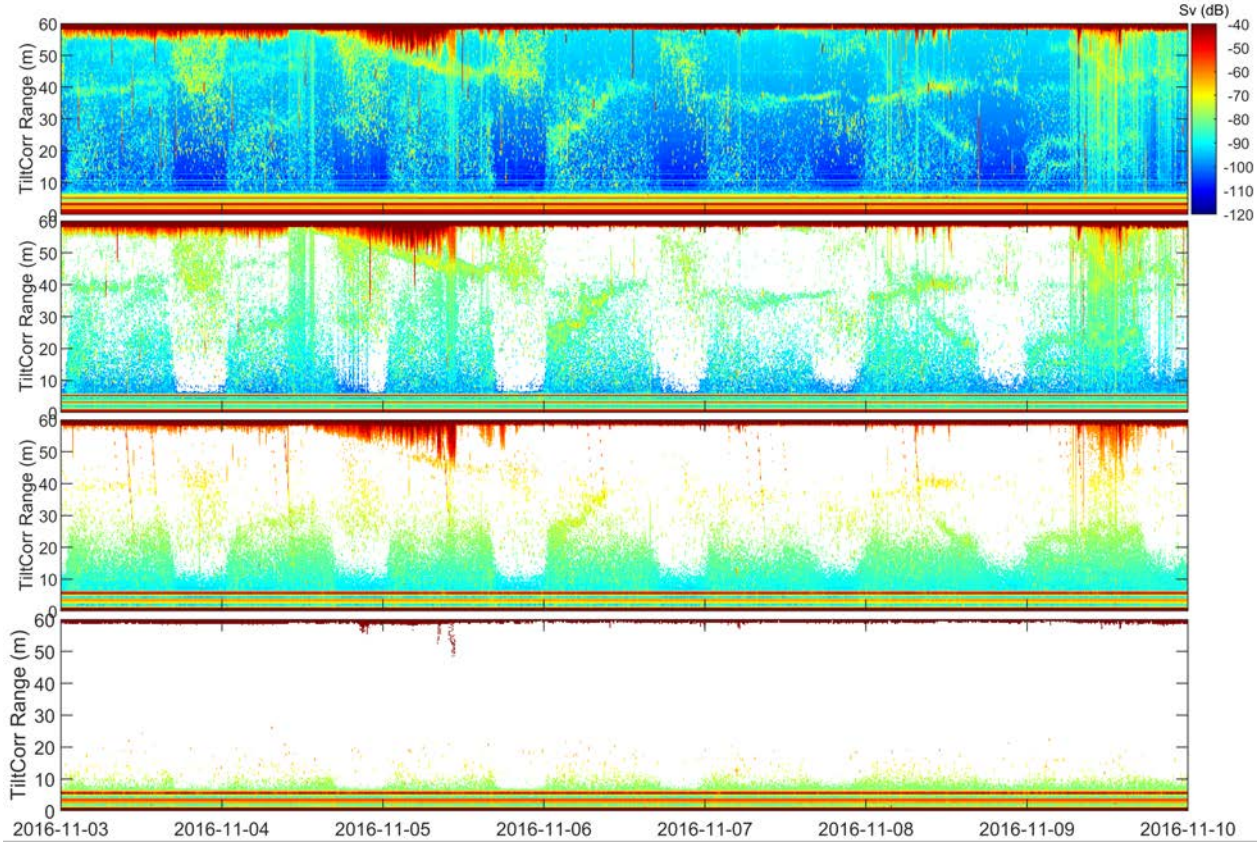

Figure 66. Acoustic backscatter depth profile time-series for the AZFP at 59 m water depth on the M3 mooring.

This plot shows a one-week sample in early November 2016. Each panel corresponds to a single frequency of (from top to bottom) 125, 200, 455, and 769 kHz.

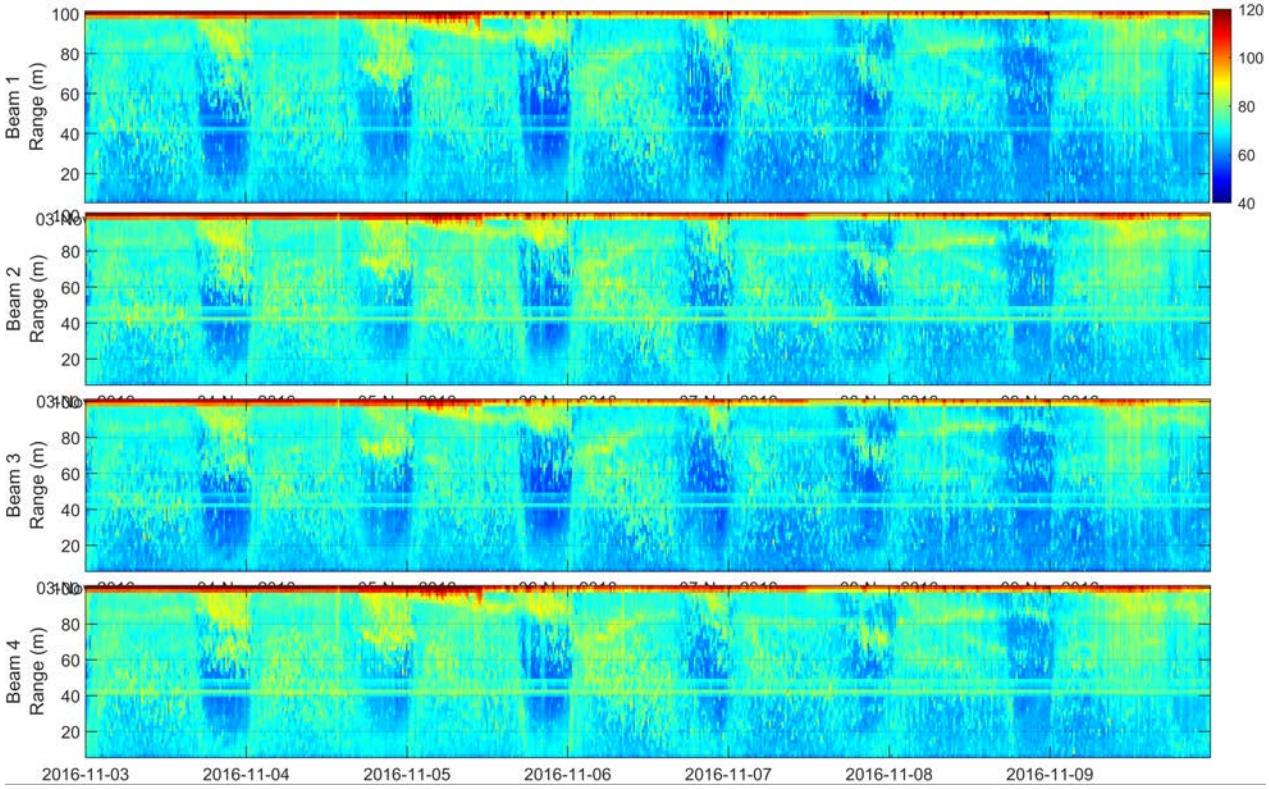

Figure 67. Acoustic backscatter depth profile time-series for the 150 kHz Workhorse Quartermaster ADCP at 104 m water depth at M3.

This plot shows a one-week sample in early November 2016. Each panel correspond to one of the four sonar beams used by the ADCP.

AZFP 55089, deployed on M3, was located slightly below mooring floatation. Precise distances to this floatation were not measured during deployment or recovery, but AZFP data clearly indicate two strong, unsaturated, and consistent targets within view during the entire deployment. These targets are therefore assumed to be mooring floatation. The consistent and persistent nature of these targets makes them well-suited for establishing that the AZFP maintains its calibration throughout the 12-month deployment, i.e. a consistent target appears with a consistent target strength; the target does not appear to weaken as the AZFP battery is depleted.

The first such target is located at 3.3 m range corresponding to the range bin with index 16. Figure 68 and Figure 70 show the A/D counts and Sv for this first target at 125 kHz and 200 kHz, respectively. Daily mean A/D counts are also plotted (cyan dots), along with the 12-month mean (solid cyan line) and daily standard deviations (green dots).

The second target that was visible to AZFP 55089 was located at 5.4 m range corresponding to the range bin with index 26. Again, this target is assumed to be mooring floatation. Figure 69 and Figure 71 plot the data corresponding to this second target, as seen at 125 kHz and 200 kHz, respectively.

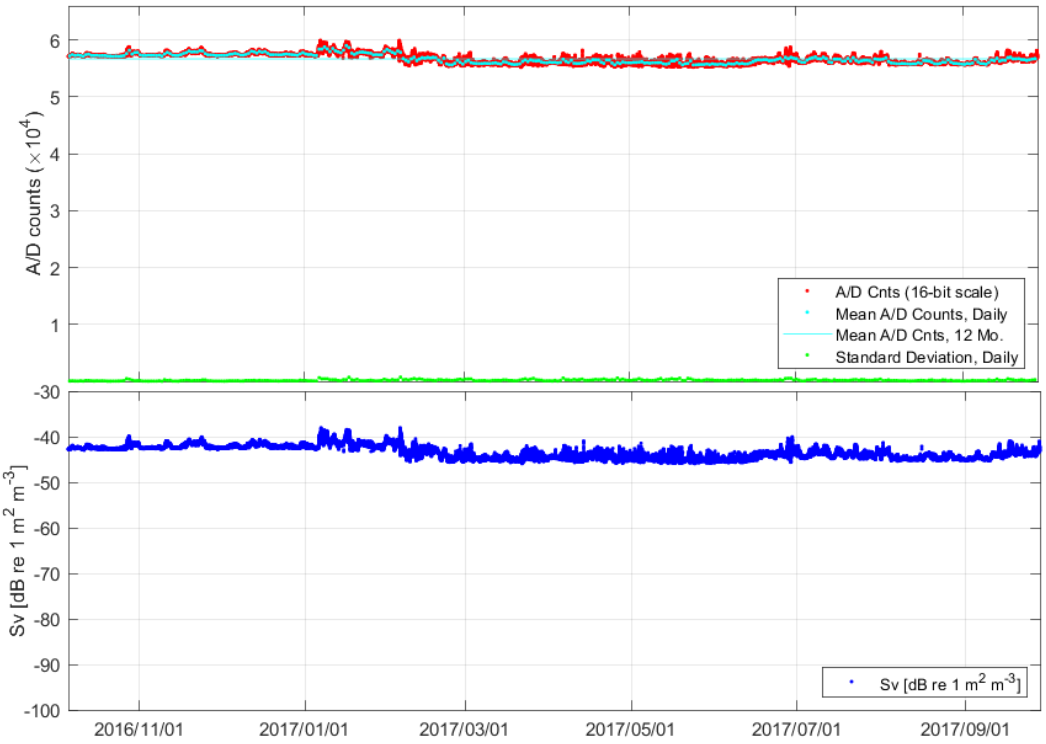

Figure 68. Close range (bin 16, 3.3 m) target as seen by AZFP 55089, 125 kHz.

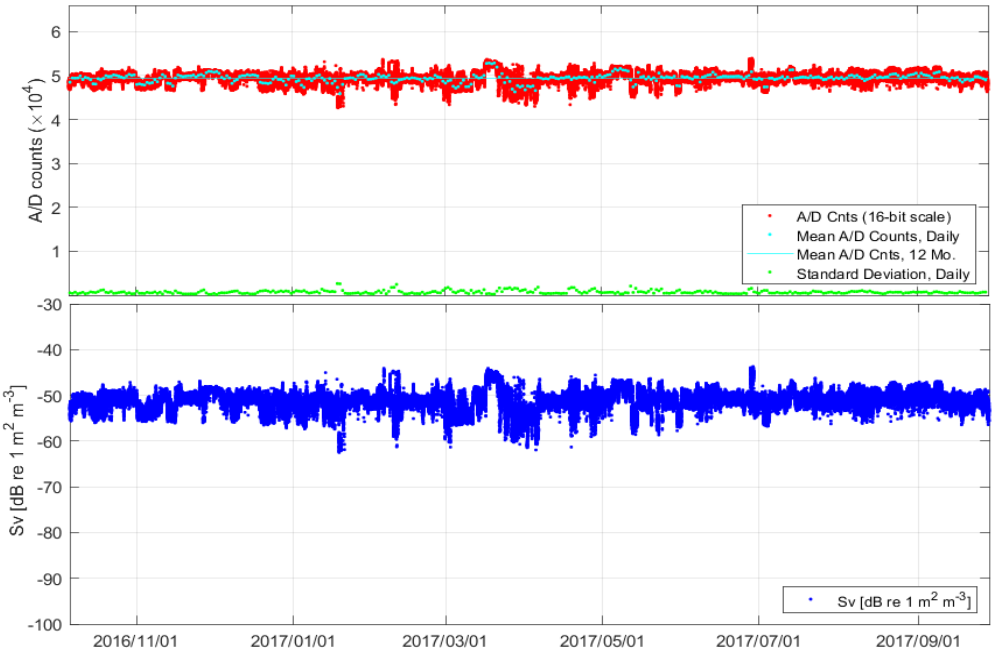

Figure 69. Close range (bin 26, 5.4 m) target as seen by AZFP 55089, 125 kHz.

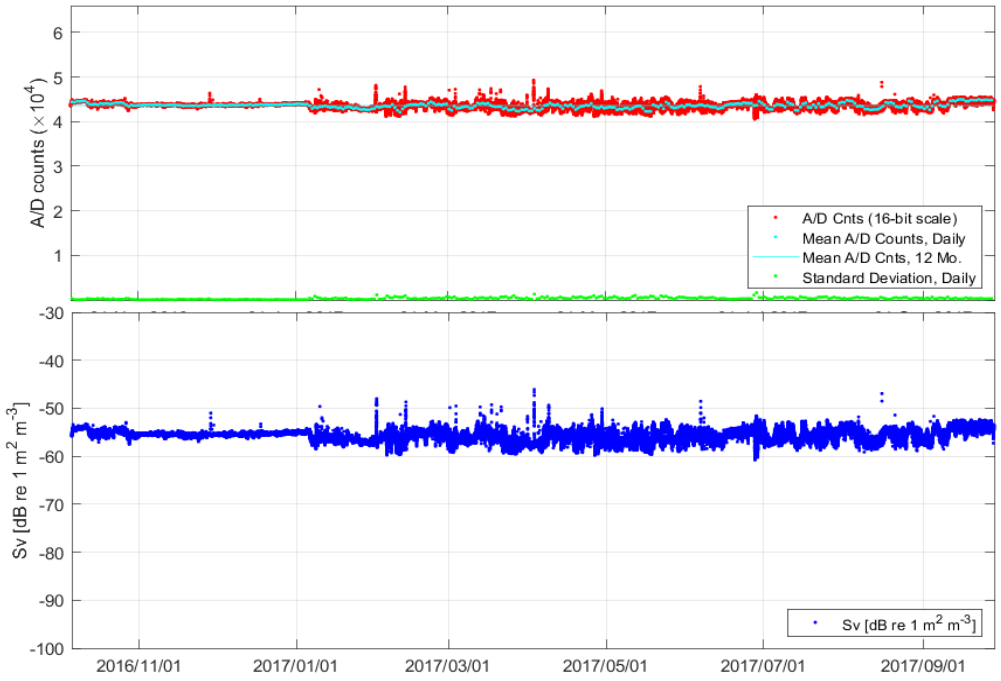

Figure 70. Close range (bin 16, 3.3 m) target as seen by AZFP 55089, 200 kHz.

Figure 71. Close range (bin 26, 5.4 m) target as seen by AZFP 55089, 200 kHz.

The AZFP provided a suitable performance benchmark against which to assess the performance of the ADCPs at estimating backscatter strength for targets such as zooplankton. The first part of this analysis established that the AZFP provided consistent volume backscattering measurements when looking at persistent and consistent targets (i.e. mooring floatation) over the full 12-month deployment. The variability of the acoustic return was quite low. At 125 kHz the maximum standard deviation was approximately 734 A/D counts, but typical values were approximately 194 A/D counts. This variability is remarkably small, especially considering that small motions of the target (e.g. from water currents) can lead to motion within the beam and effects on the acoustic return. At 200 kHz, this variability in the acoustic return from the first target was larger than at 125 kHz but was still remarkably small. The maximum daily standard deviation was approximately 1620 A/D counts, and typical values were approximately 356 A/D counts. It is worth noting that the 200 kHz channel has a reduced beamwidth of approximately 7 degrees at -3 dB one-way, compared to approximately 8 degrees at -3 dB one-way for the 125 kHz channel. This makes the channel more sensitive to small motions of any target within the beam.

The second close-range target, at a distance of 5.4 m, provided a similar demonstration of the AZFP's consistency as a calibrated instrument over the course of the 12-month deployment. Figure 69 and Figure 71 show the A/D counts and Sv corresponding to the second close-range target at 125 kHz and 200 kHz, respectively. At 125 kHz, the maximum daily standard deviation was approximately 2650 A/D counts, compared to typical daily standard deviations of 707 A/D counts. At 200 kHz, the maximum daily standard deviation was approximately 2620 A/D counts while typical daily values were approximately 695 A/D counts. This slightly increased variation in the intensity of the acoustic backscatter is expected, since the target is at a greater range and thus may move greater distances throughout the beam. Nevertheless, both targets are remarkably consistent throughout this year-long deployment. The consistency of these measurements demonstrates that the AZFP provides a suitable performance benchmark against which ADCP backscatter intensity measurements may be compared.

After establishing the suitability of the AZFP as a performance benchmark against which to compare ADCP backscatter intensity measurements, a preliminary comparison between the instruments was performed. The purpose of this comparison is to provide an initial and preliminary assessment of the suitability of the ADCP as a tool for zooplankton study. In the present project, the scope of this analysis is limited; results are plotted, and initial comparisons are drawn, but the analysis is not exhaustive.

The comparison is limited to the 125 kHz and 200 kHz channels of the AZFP, since these channels straddle the 150 kHz center frequency of the Workhorse Quartermaster ADCPs. In Figure 72 the Sv measurements from AZFP 55089 are compared to the backscatter intensity measurements of ADCP 16215. An offset *C* is applied to the ADCP data such that this data is brought into approximate registration with AZFP data at the beginning of the deployment. The offset was determined empirically. Comparing the ADCP data (dash-dot blue curve) to AZFP data, it is apparent that these ADCP backscatter measurements roughly correspond to the 200 kHz Sv measurements (red curve) and show weaker correspondence to the 125 kHz Sv measurements. The extent of the correspondence between ADCP and AZFP backscatter measurements has not been quantified; however, to a large extent the ADCP tracks similar trends in backscatter intensity,

although ADCP backscatter measurements fluctuate more pronouncedly than AZFP measurements. These fluctuations are potentially attributable to the narrower main lobe of the ADCP, and to the frequency difference between the instruments. One exception to this trend is noteworthy: the high-intensity values shown during the April 2017 timeframe. During this time, large ice floes were passing over M3 and M4, and these peaks in the backscattering measurements are attributed to the acoustic signals scattering off the ice. The greater sensitivity of the ADCP to this ice is likely attributable to ADCP sidelobes.

Figure 73 compares AZFP 55089 Sv measurements to ADCP 16216 backscatter intensity measurements. Note that ADCP 16216 was located on M4, while AZFP 55089 was located on M3; the devices did not interrogate identical portions of the water column, and thus it is expected that there will be dissimilarity in the acoustic backscatter. This comparison indicates, in a general sense, that ADCP 16216 tracked roughly similar trends compared to the 200 kHz channel on AZFP 55089. As with ADCP 16215, ADCP 16216 was highly sensitive to the presence of ice floes.

Figure 74 shows the acoustic backscatter from both ADCPs. General trends in acoustic backscatter are similar (e.g. large ice floes visible around April 2017, weaker acoustic returns in mid-May) but, as expected, the ADCPs did not observe the same targets because they were not co-located.

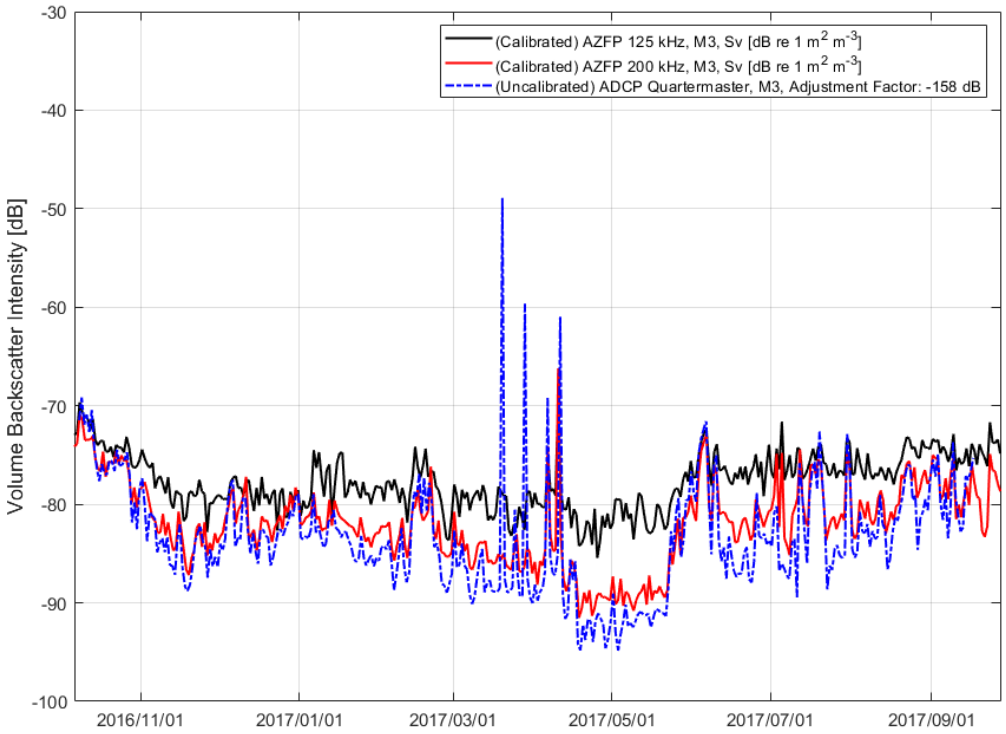

Figure 72. AZFP 55089 volume backscatter intensity (S_v) vs. ADCP 16215 backscatter.

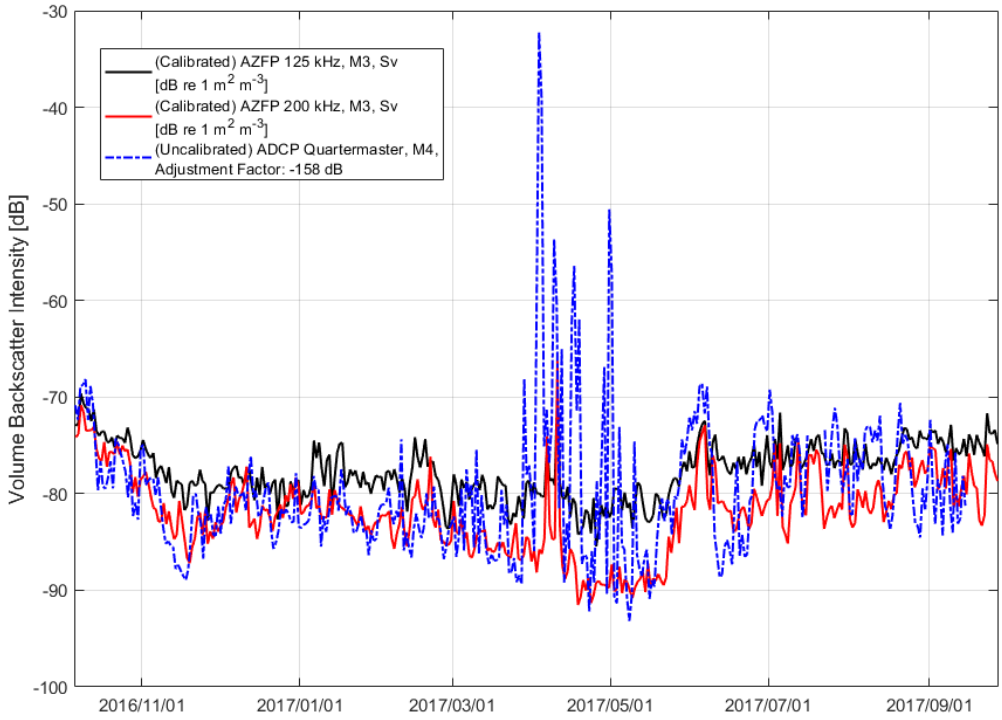

Figure 73. AZFP 55089 volume backscatter intensity (S_v) vs. ADCP 16216 backscatter.

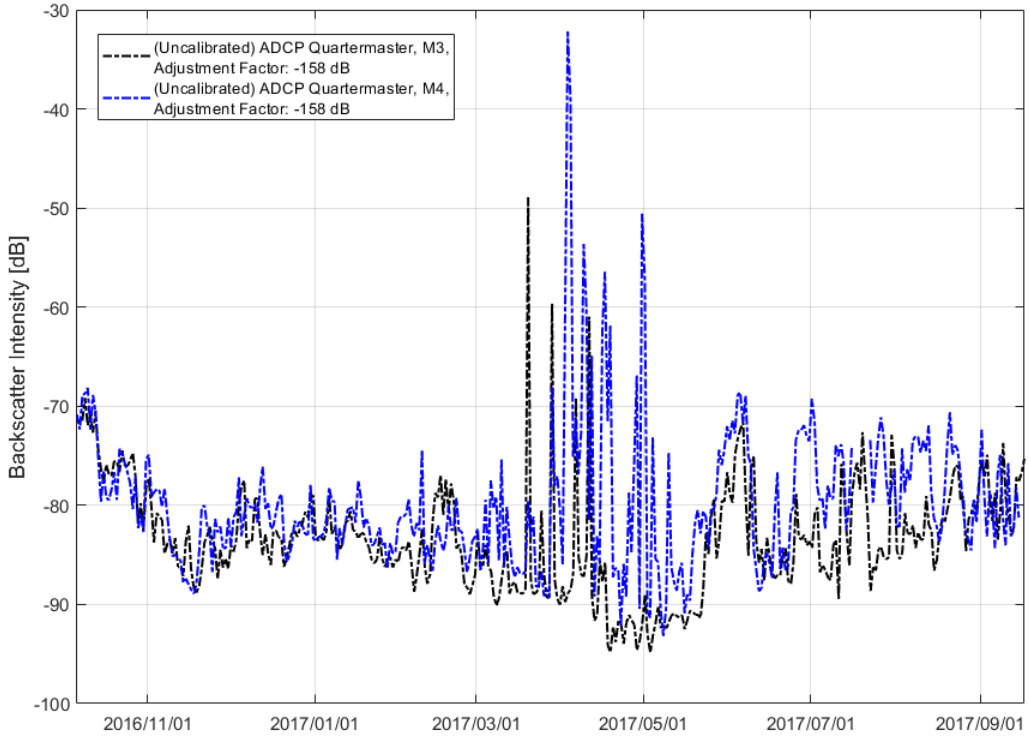

Figure 74. ADCP 16215 backscatter intensity measurements vs ADCP 16216 backscatter intensity measurements.

There are three primary lessons that arise from the comparison between AZFP S_v measurement and ADCP backscatter measurement in the application of zooplankton study:

1. The ADCP requires sufficient battery life such that the transmit signal level will be minimally altered over the course of the deployment. A Workhorse Quartermaster ADCP has been seen to track, to a large extent, acoustic backscatter trends that are evident in AZFP Sv measurements, but the ADCP had only used 3.3 of the 4 battery packs during the deployment.
2. The Workhorse Quartermaster ADCP was observed to be more sensitive to the passage of large ice floes than the AZFP, and this increased sensitivity is suspected to result from comparatively high sidelobe levels. Users are advised to take care such that strong targets, seen through sidelobes, will not dominate weak scattering by zooplankton.
3. The presence of a calibrated AZFP in the vicinity of the ADCP allows the user to empirically estimate an offset C that may bring ADCP backscatter data into approximate registration with Sv measurements that are reported on an absolute scale. Based off estimates of C, it may also be possible to quantify changes in ADCP transmit signal level result from changes in ADCP battery level. This may assist users in analysis of ADCP data over a time series where the battery

is known to have depleted, but the implications of the changing battery level are not obvious.

3.4.2.2 AZFP: Abundance and Phenology

To goal of the AZFP deployment was to describe the temporal cycle of zooplankton and fishes from summer 2016 to summer 2017, and to ultimately determine how these cycles might relate to environmental conditions observed from other moored sensors.

The nautical area scattering coefficient (NASC) derived from acoustic signal strength is proportional to fish and zooplankton density and is thus used here as an index of abundance. Patterns of abundance at mooring M3 were detected on an annual scale. The bulk of adult arctic cod abundance occurred between October and March, with peak abundance observed in December (Figure 75). Most adult arctic cod targets were detected below 200 m (Figure 78). Juvenile arctic cod were present near the surface from July to October, mainly in the upper 40 m (Figure 76 and Figure 79) but with a potentially interesting peak of abundance from end of May to beginning of June. Juveniles were absent from the surface layer between November and June.

Copepods were present in the upper water column mostly from June to February (Figure 77 and Figure 80) and were at least partly responsible for the daily vertical migration pattern observed (Figure 81). Diel migration patterns were observed throughout the year (not shown).

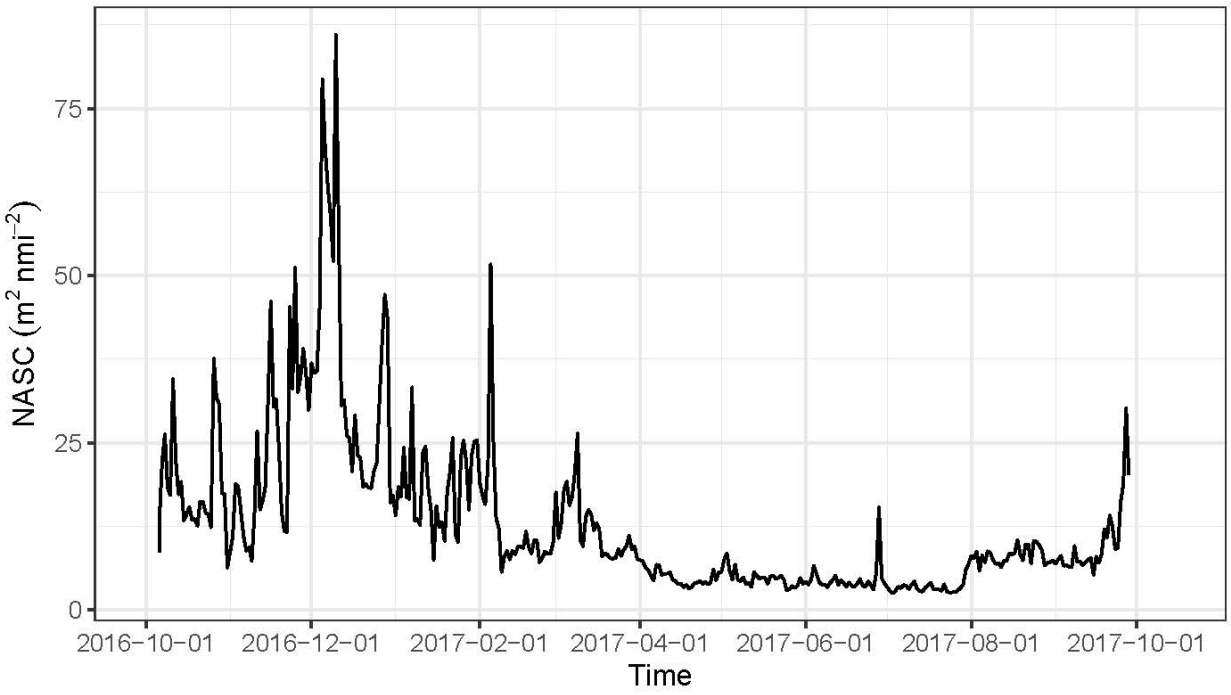

Figure 75. Nautical area scattering coefficient (NASC) as a function of time for adult arctic cod at site M3 in the Beaufort Sea, from October 2016 to October 2017.

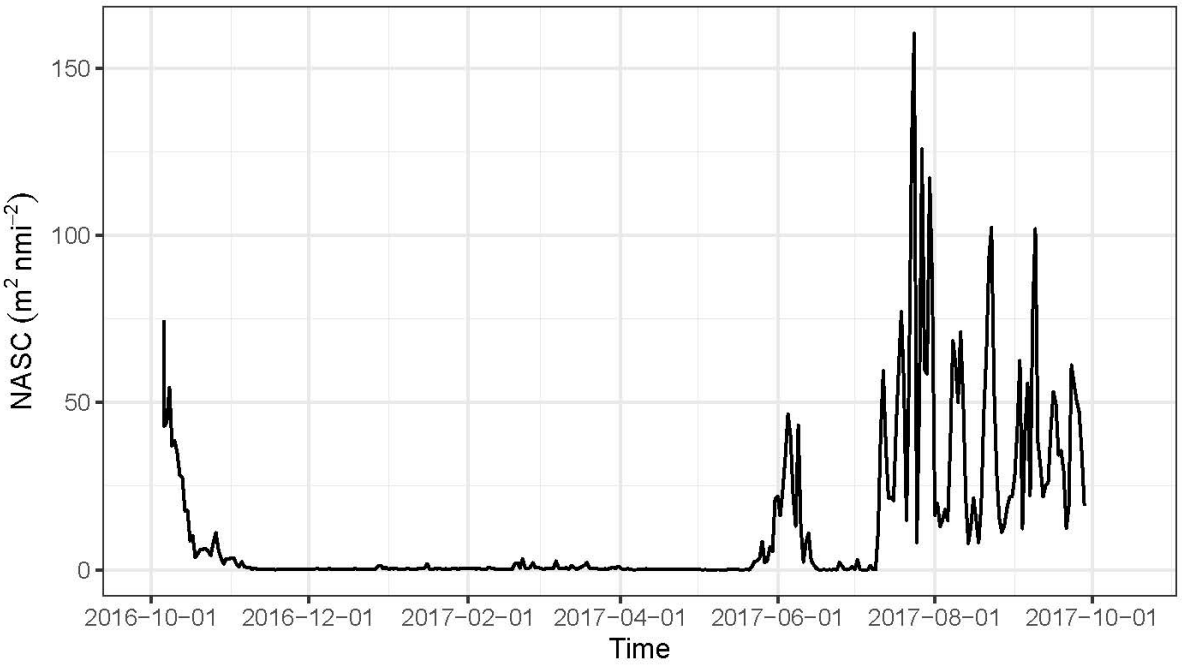

Figure 76. Nautical area scattering coefficient (NASC) as a function of time for juvenile arctic cod at site M3 in the Beaufort Sea, from October 2016 to October 2017.

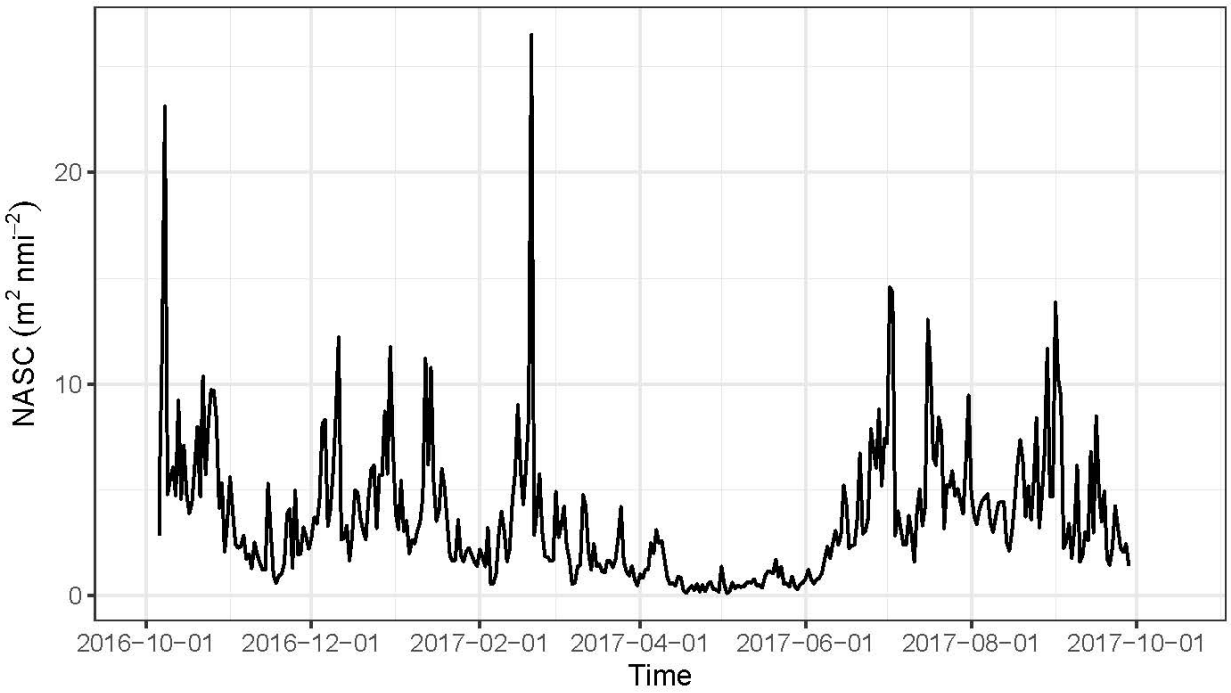

Figure 77. Nautical area scattering coefficient (NASC) as a function of time for copepods at site M3 in the Beaufort Sea, from October 2016 to October 2017.

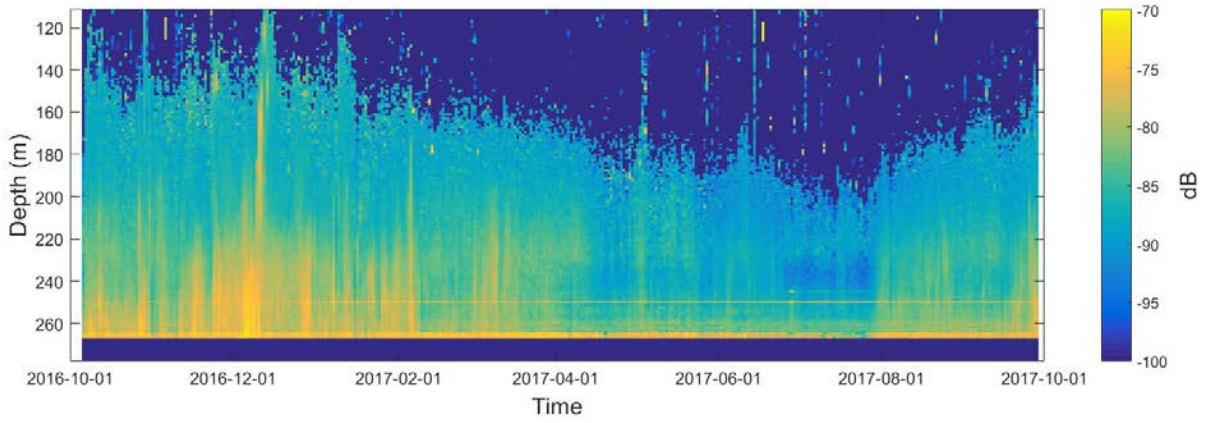

Figure 78. Echogram of 38 kHz backscatter (S_v) corresponding to adult arctic cod at site M3 in the Beaufort Sea, from October 2016 to October 2017.

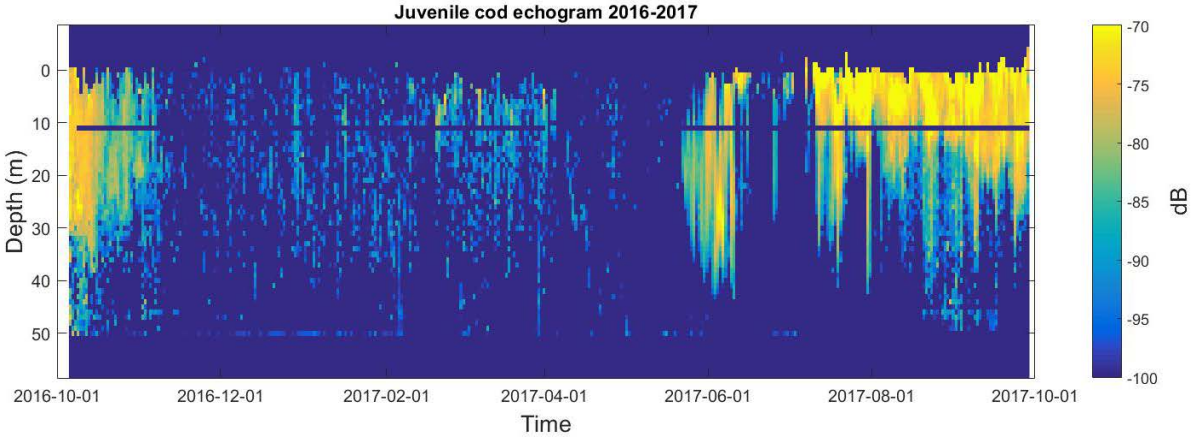

Figure 79. Echogram of 125 kHz backscatter (S_v) corresponding to juvenile arctic cod at site M3 in the Beaufort Sea, from October 2016 to October 2017.

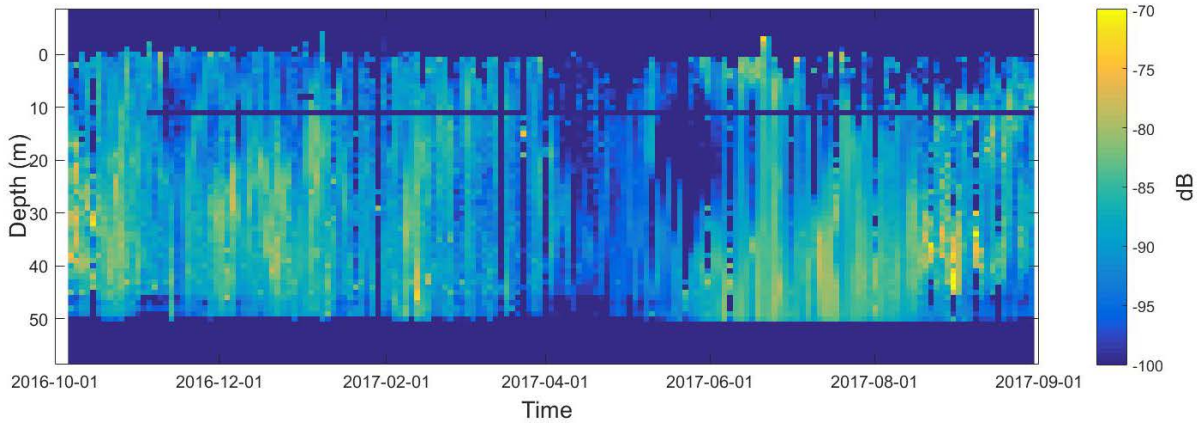

Figure 80. Echogram of 200 kHz backscatter (S_v) corresponding to copepod at site M3 in the Beaufort Sea, from October 2016 to October 2017.

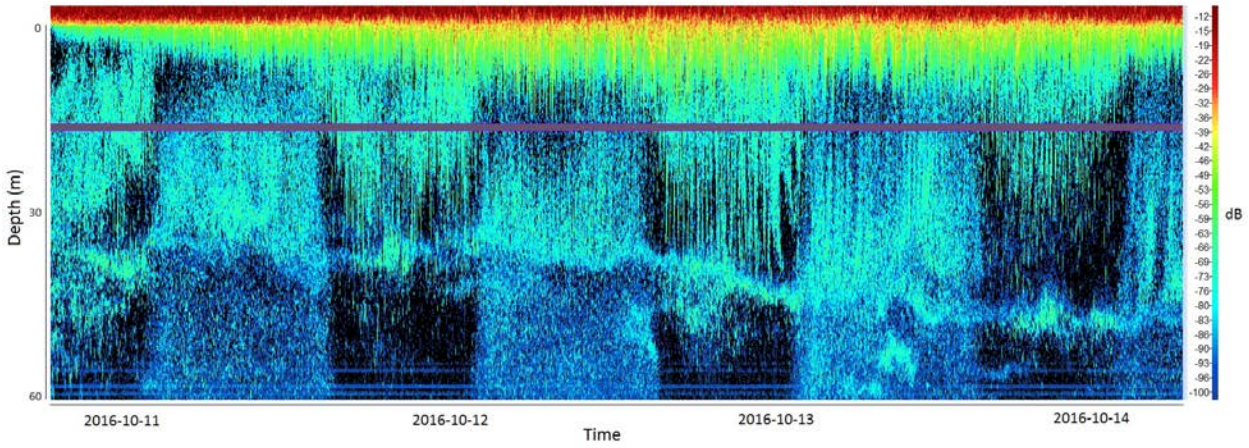

Figure 81. Echogram of 125 kHz backscatter (S_v) showing daily migration pattern at site M3 in the Beaufort Sea, from October 11 to 14, 2016.

3.4.2.3 Acoustic Backscatter

Two of the ADCPs (M1a, M2b) recorded data over almost the entire water column depth (excluding the few meters below the instrument and the blanking intervals at the surface and near the transducers). To examine changes in water column backscatter and associations of those changes with hydrography and currents, mean backscatter and u and v velocities were calculated for each profile from these two instruments. This removed any diel signal in the vertical distribution of backscatter and vertical shear in velocities. Daily means then were calculated for the 48 time periods within each decimal date for backscatter (S_v), u and v velocities and for temperature and salinity from the CTD located on each mooring.

All three records showed substantial variation throughout the year, and greatest backscatter near the surface with lower scattering at mid-depth and lowest backscatter at depth (Figure 82 to Figure 84). Backscatter at M2 (both instruments) was substantially greater than that seen at M1. Smoothing the profiles evened out smaller-scale variability and successfully produced realistic values for bins where data were missing due to scattering of sound from floats in M2a.

The mean backscatter (S_v; Figure 85 and Figure 86, middle panel) represented the total variations in water column backscatter over the period of the deployment. There was considerable profile-to-profile variability in mean backscatter that was reduced by calculating both a 5-day running mean of the profile means and by calculating the daily mean backscatter (mean of all mean profile backscatter with in a 24 hour period) (Figure 85 and Figure 86, lower panel). The five-day running averages of all profiles (middle panel) and of the daily means (lower panel) were virtually identical.

Backscatter from the two instruments (M1a, M2b) that profiled the entire water column was compared using the daily mean backscatter data smoothed using a 5-day running mean (Figure 87). The daily anomalies from the mean daily backscatter for the entire records (backscatter anomaly) also were computed and compared. Backscatter was greater at the M2, the instrument moored at 149 m bottom depth, than at M1 that was located on the shelf at 40 m bottom depth. However, both instruments showed similar trends in backscatter over the period of the deployments, with higher backscatter in early fall (October 2016) and summer (June–September 2017) and lowest backscatter in May 2017. Values were average in winter (December 2016–February 2017) and declined steeply to minima in May 2017 after which values increased rapidly to maxima in June. Shorter-term maxima and minima were seen throughout the record, most notably in January 2017, early April 2017, late April 2017, and early June 2017. These episodic variations occurred over time scale of days and must be driven by advection of different populations of plankton, with differing abundances, over the sites since these time scales are shorter than the production response time of mesozooplankton at these water temperatures. Backscatter (both daily means and anomalies) between M1a and M2b were positively correlated ($r = 0.79$, $p<0.01$, $n = 357$).

Daily water column means, smoothed means, and anomalies from the mean smoothed mean also were calculated for the u and v component of velocity for the two instruments. For each record, the water column mean for each time point was calculated. The mean of all water column means within a numerical day (48 values for a full 24 hours) then was calculated and smoothed with a five-day running average (Figure 88). Anomalies were calculated from the smoothed daily means (anomalies not shown since the patterns were essentially identical to the smoothed daily means as for backscatter). For each instrument, the daily smoothed u and v velocities were negatively correlated ($r = -0.9645$ for M1a, $r = -0.86$ for M2b). Most of the currents ran either on the shelf (to the south) or off of the shelf (to the north). For more description and analyses of the currents, see Section 3.1.1.

Mean daily water column velocities were compared to the daily mean backscatter anomalies for each mooring (Figure 89 to Figure 91). For M1a, many of the episodic variations in the backscatter anomalies were associated with peaks in velocities, with a short lag. A number of maxima in the backscatter anomaly occurred shortly after maxima in velocities to the north (see in

particular October and November and April) and many minima in the backscatter anomaly occurred shortly after maxima in velocities to the south. Correlations between the mean backscatter anomalies and daily mean u and v were statistically significant but low (-0.2120 for S_v and u; 0.2668 for S_v and v). By contrast, little association was observed between episodic peaks in the mean backscatter anomalies and velocities at M2b. For both sites, little correspondence was observed between the winds and currents in this very preliminary comparison.

Backscatter anomalies also were compared to the temperature and salinity recorded by the CTD moored near the ACDP on each mooring (Figure 92 and Figure 93). For M1a, some maxima or minima in backscatter were positively associated with peaks in salinity (r = 0.28) or temperature (r = 0.35). For M2b, the large period of low backscatter seen in April-June was associated with warmer, more saline water while the elevated backscatter seen immediately afterwards in June-September was associated with lower salinity, colder water. On a shorter time period, some maxima and minima in backscatter were negatively associated with maxima or minima in salinity (-0.39) and temperature (-0.24). Note that the prominent peak in backscatter in January corresponded to warmer, fresher water. It is interesting to note that temperature and salinity were not correlated at M1a (r = 0.04) but highly correlated at M2b (r = 0.83).

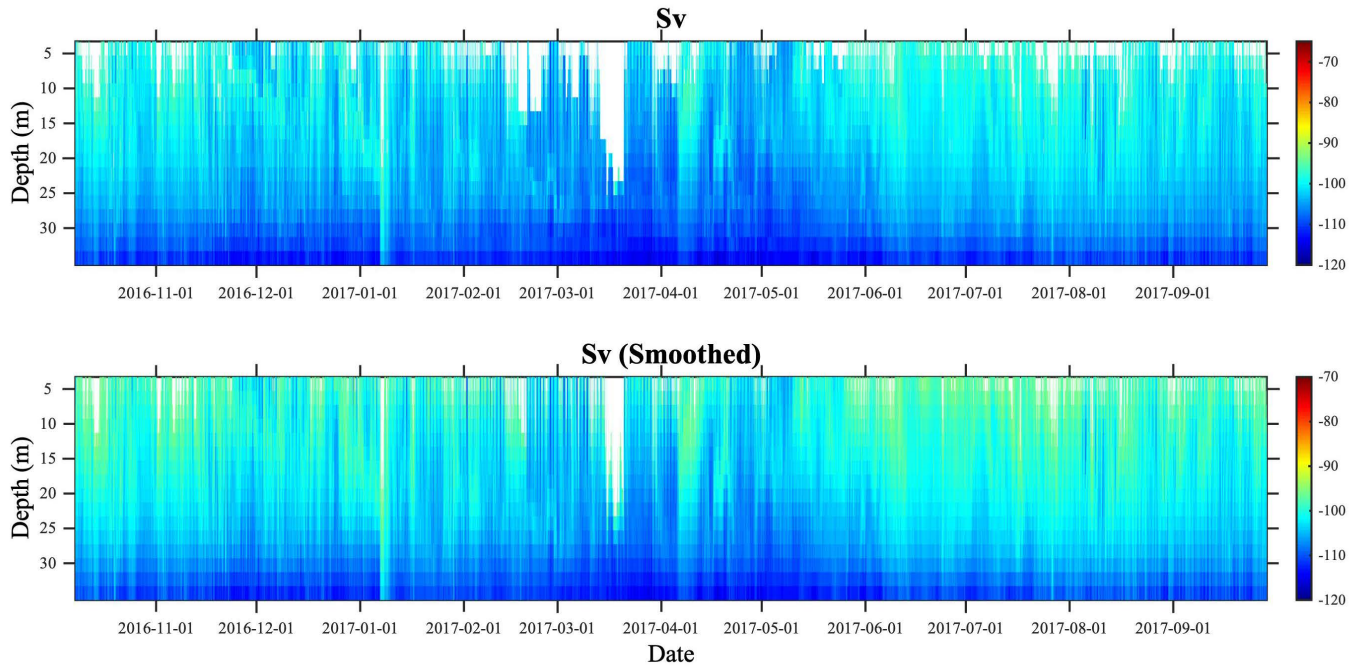

Figure 82. Absolute backscatter (top) and smoothed absolute backscatter (bottom) from mooring M1. All profiles plotted, with no interpolation.

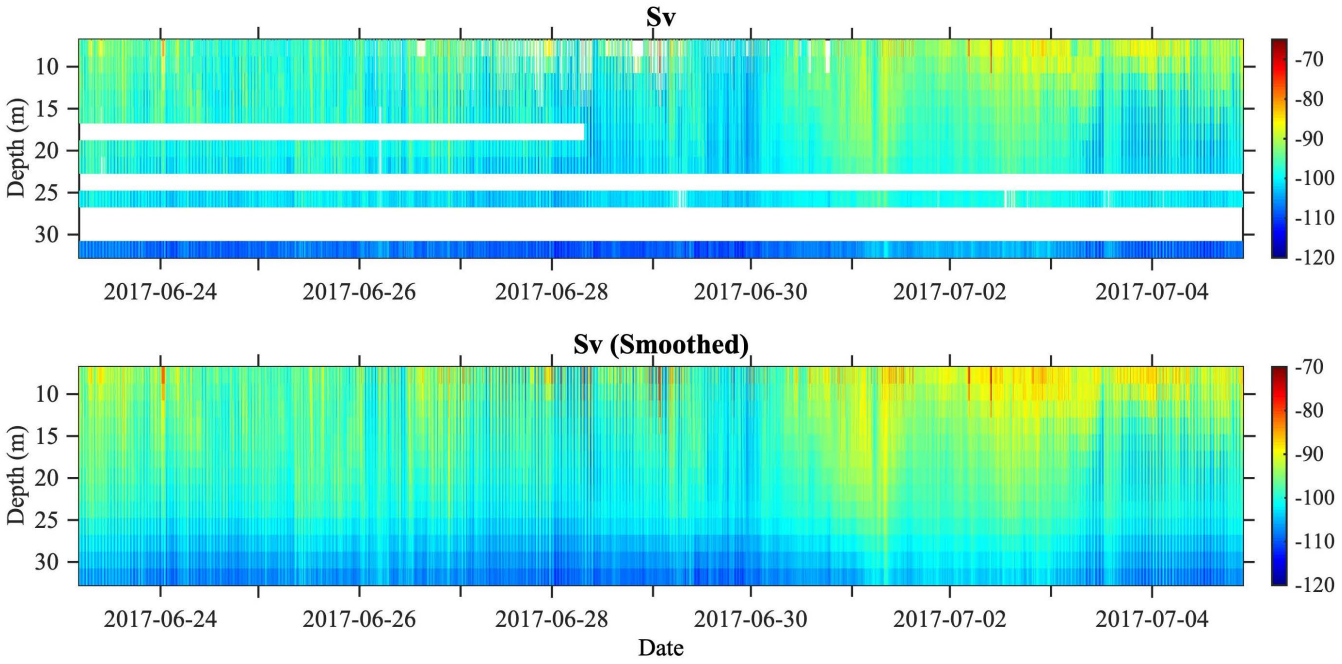

Figure 83. Absolute backscatter (top) and smoothed absolute backscatter (bottom) from mooring M2, upper instrument (at ~39 m water depth; 2a).

All profiles plotted, with no interpolation.

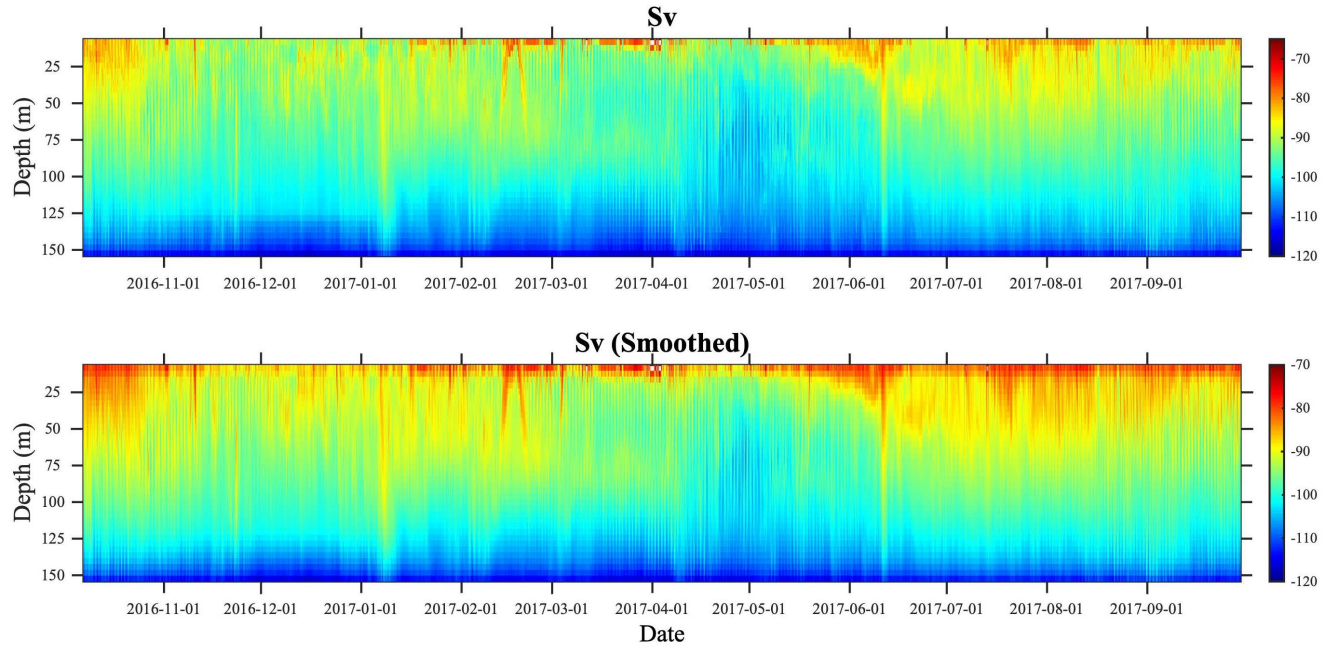

Figure 84. Absolute backscatter (top) and smoothed absolute backscatter (bottom) from mooring M2, bottom moored instrument (2b).

All profiles plotted, with no interpolation.

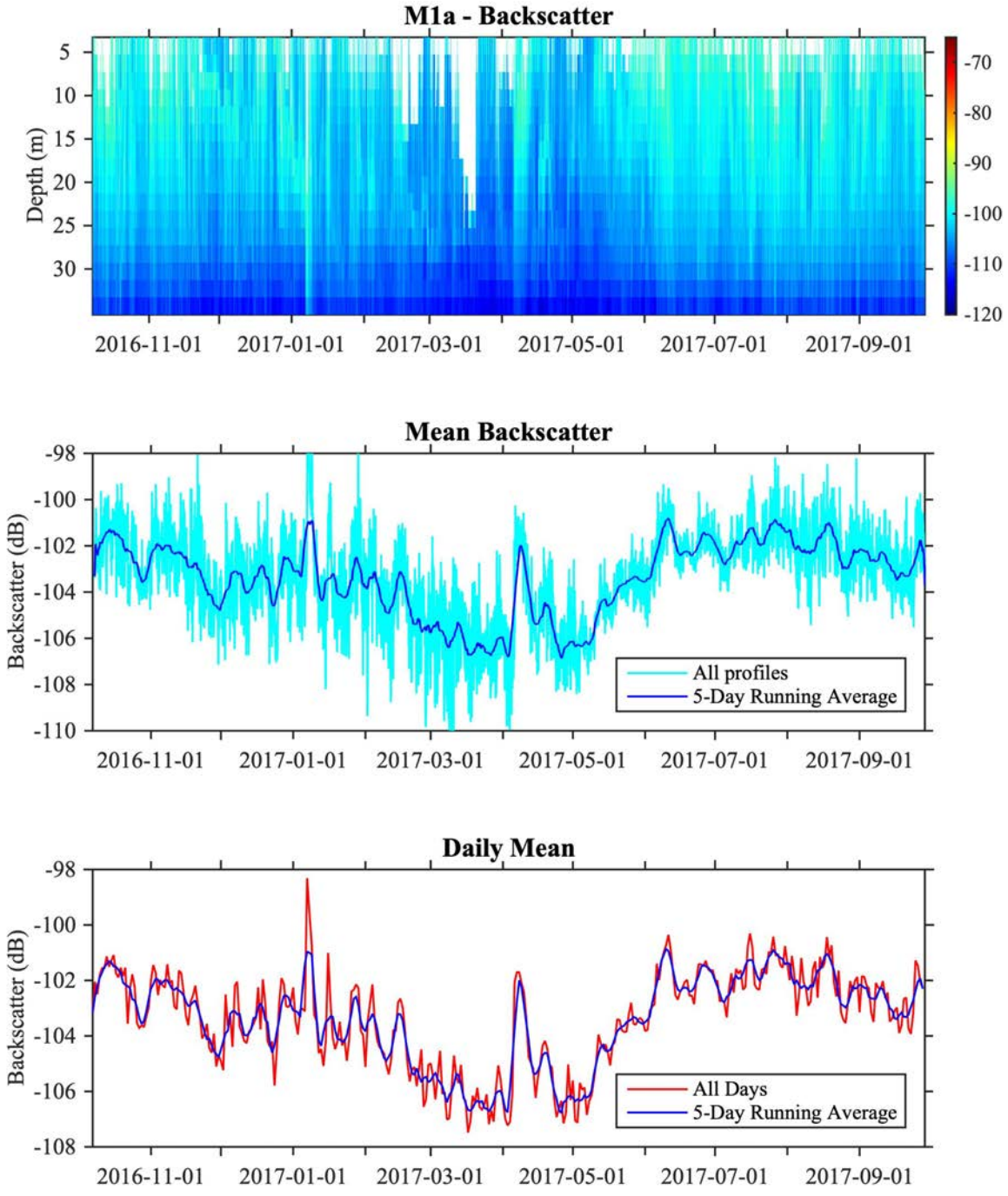

Figure 85. Backscatter (upper), mean and 5-day running average mean backscatter for each profile (middle), and daily mean and 5-day running average mean backscatter (lower) for M1a.

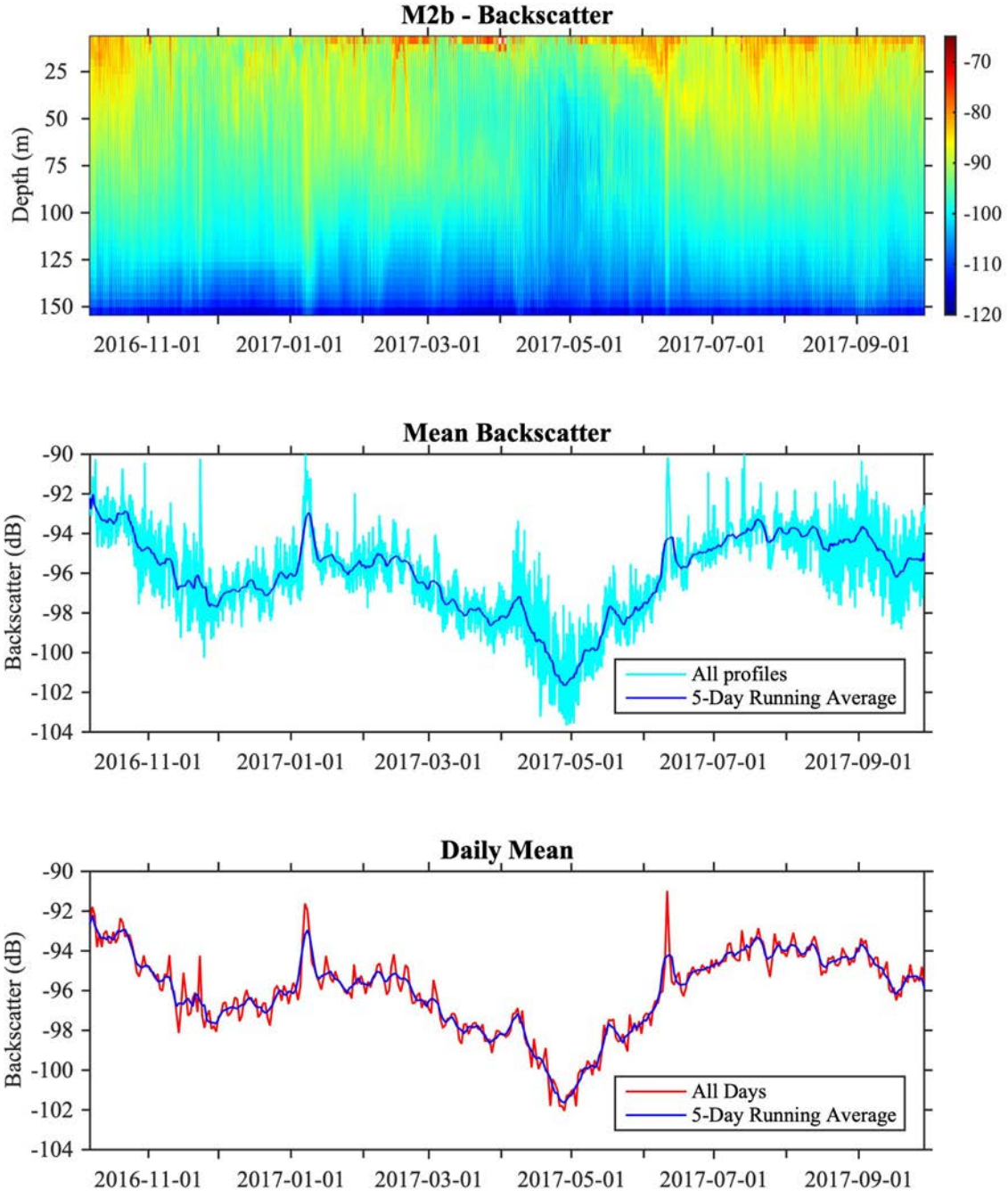

Figure 86. Backscatter (upper), mean and 5-day running average mean backscatter for each profile (middle), and daily mean and 5-day running average mean backscatter (lower) for M2b.

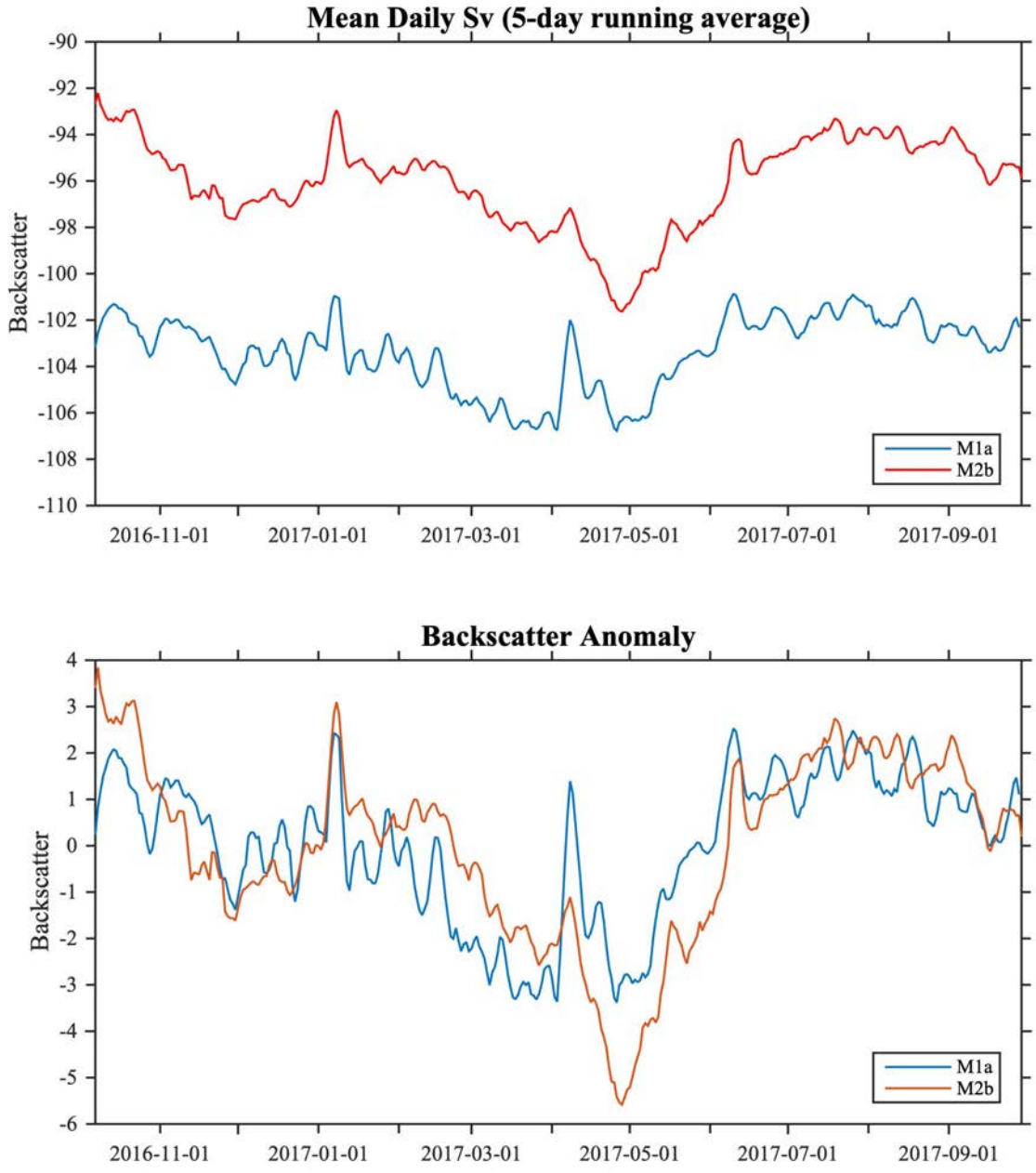

Figure 87. Mean daily water column S_v smoothed with 5-day running average (upper) and anomalies from the mean daily water column S_v (lower) for M1a and M2b.

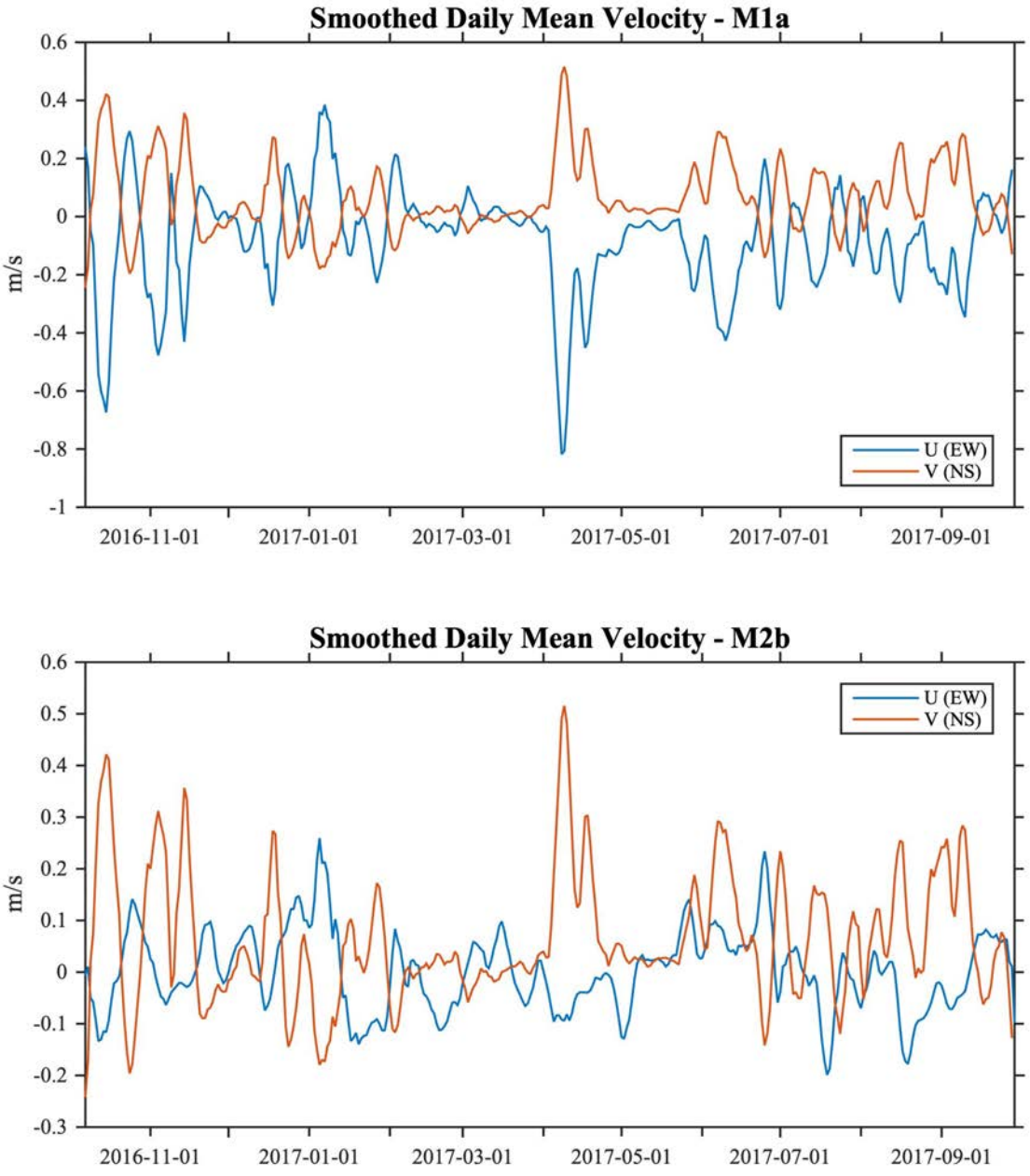

Figure 88. Smoothed daily mean velocity components (u and v) from M1a (upper) and M2b (lower).

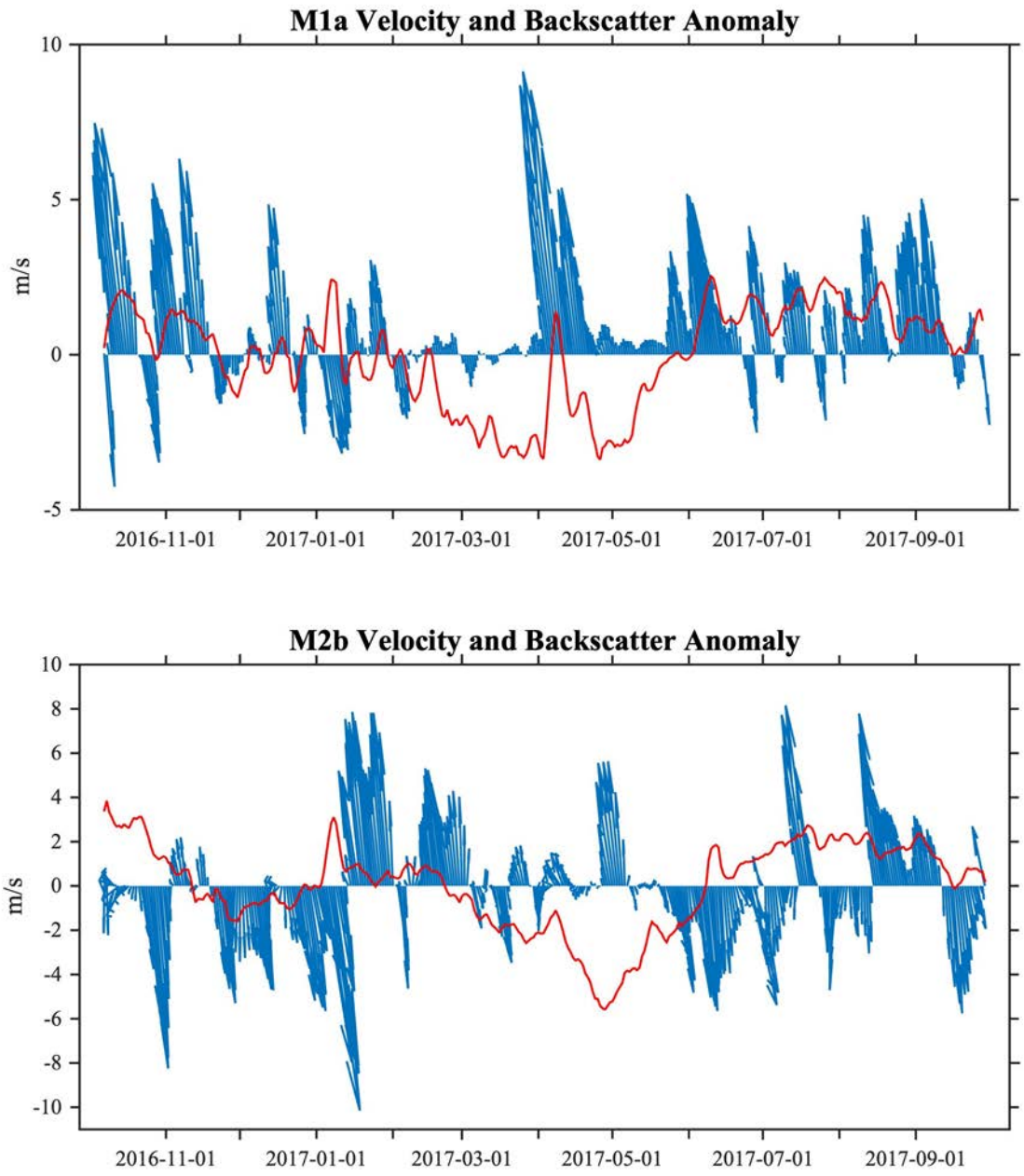

Figure 89. Quiver plot of mean daily water column velocities (smoothed with 5-day running average) and mean daily backscatter anomaly (red line) from M1a (upper) and M2b (lower). Mean daily backscatter anomalies doubled to better show episodic variations on the scale of the velocities.

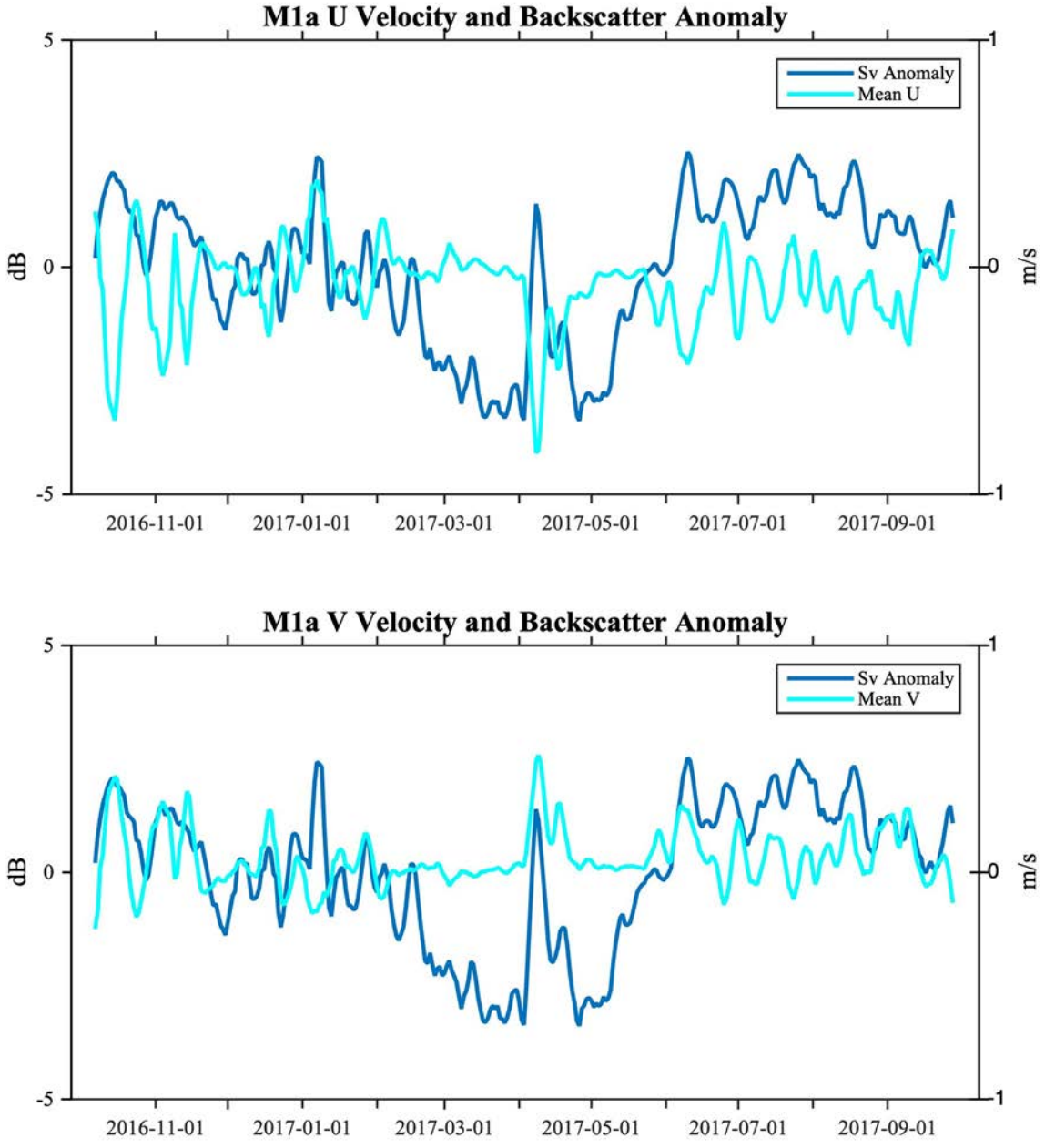

Figure 90. Mean daily backscatter anomalies and mean daily u velocity (upper panel) and v velocity (lower panel) for M1a, all smoothed with 5-day running average.

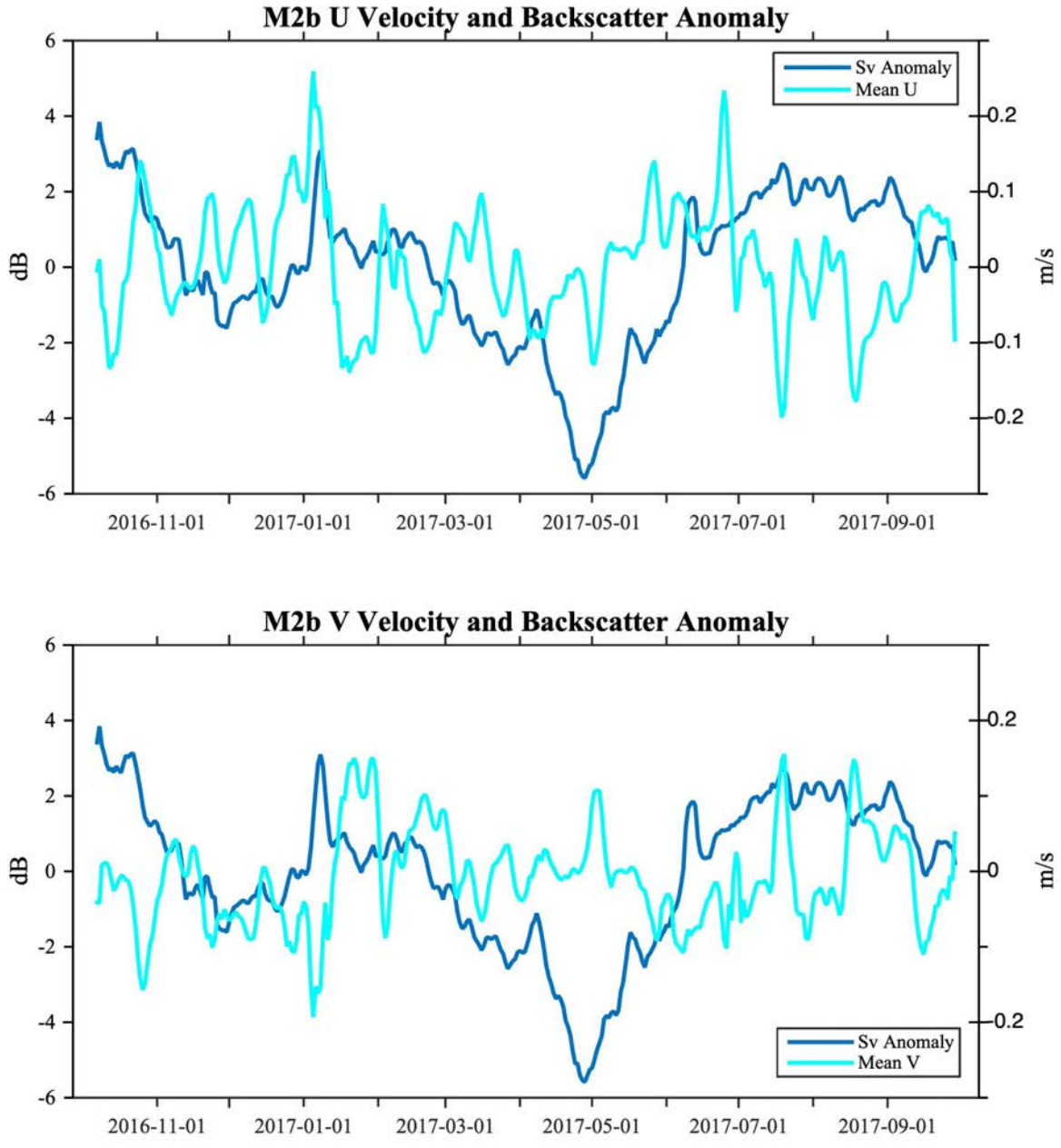

Figure 91. Mean daily backscatter anomalies and mean daily u velocity (upper panel) and v velocity (lower panel) for M2b, all smoothed with 5-day running average.

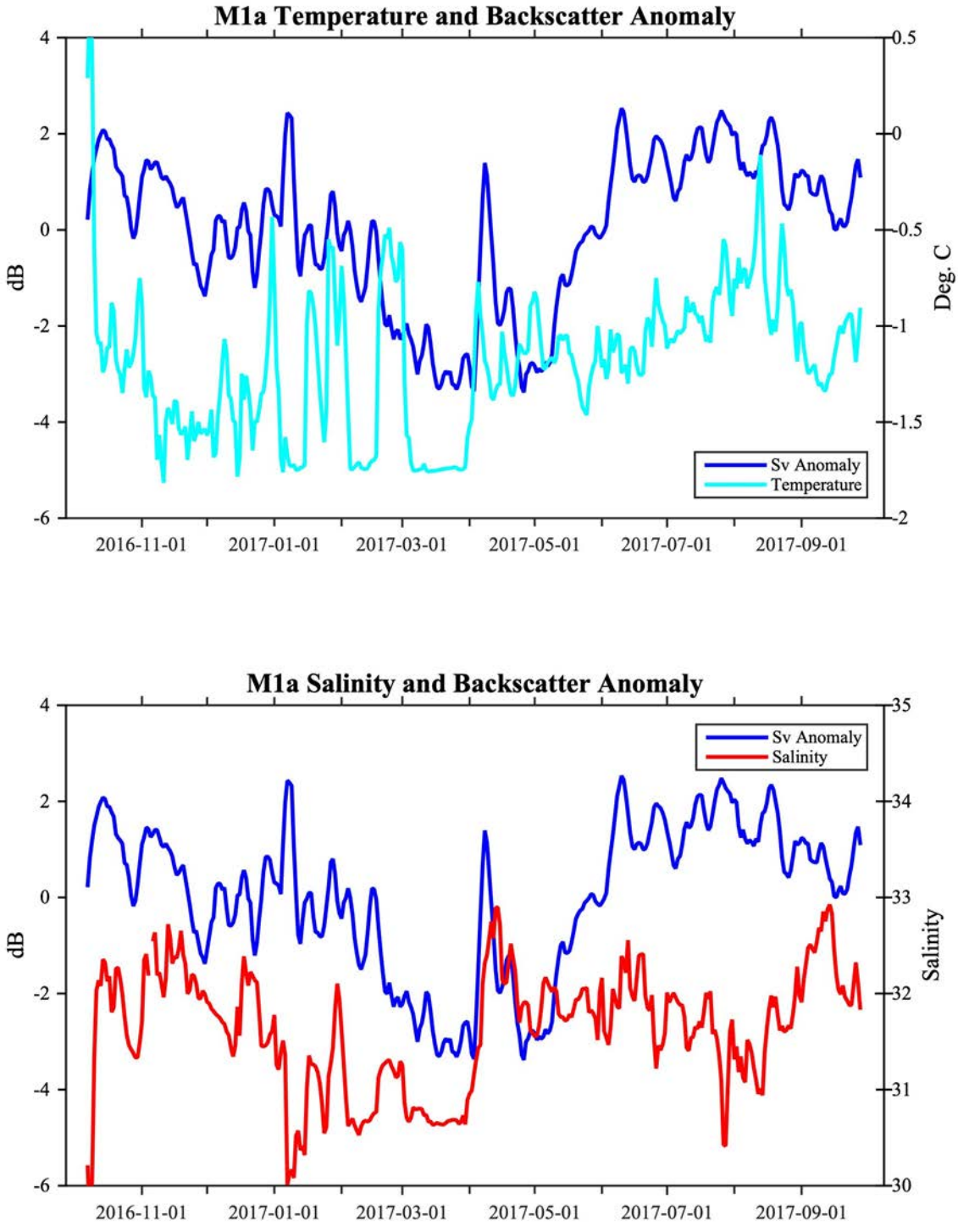

Figure 92. Daily mean backscatter anomaly and temperature (upper) and salinity (lower) at mooring M1.

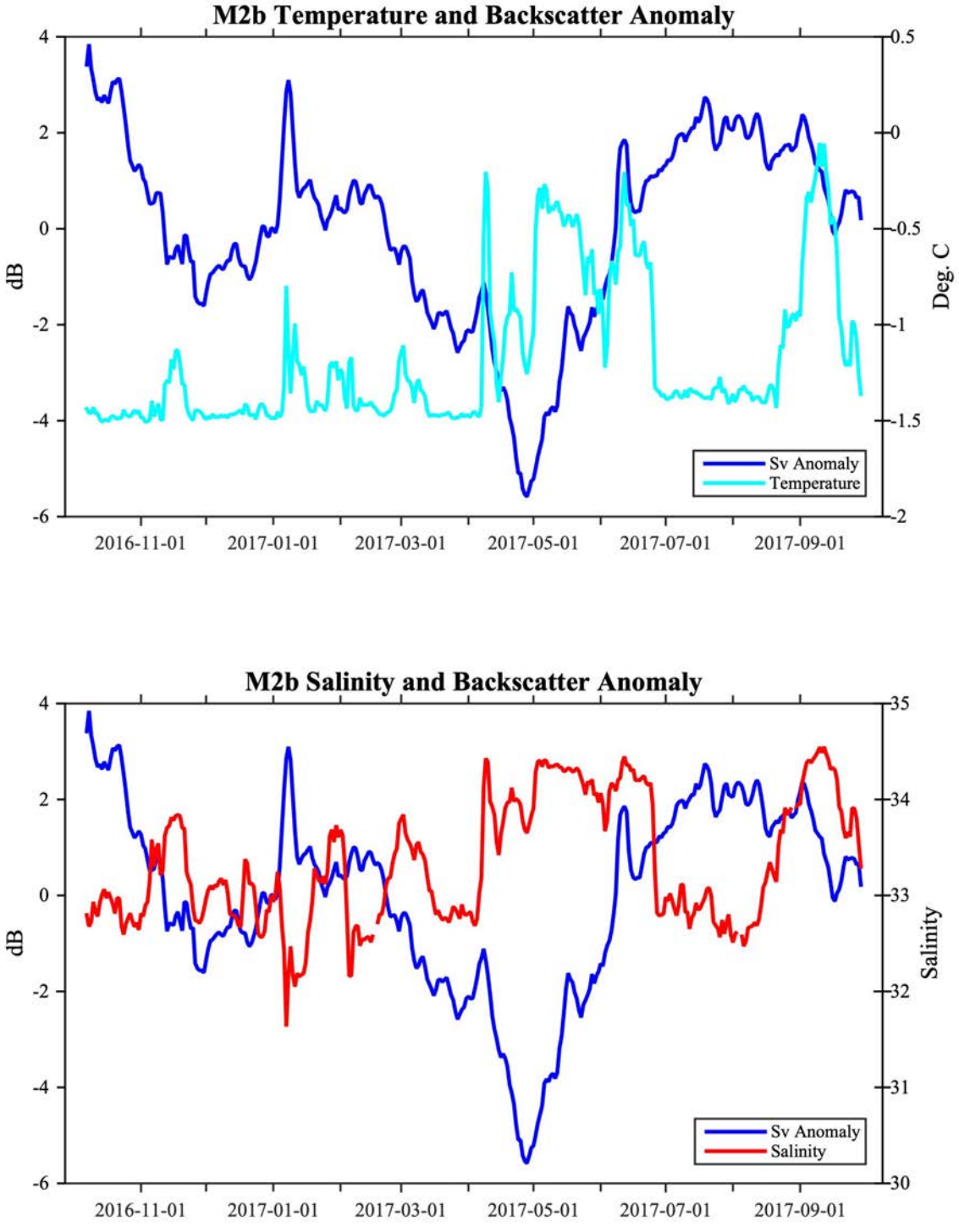

Figure 93. Daily mean backscatter anomaly and temperature (upper) and salinity (lower) at mooring M2.

Identifying periods of DVM was much more complex than originally anticipated due days-weeks changes in the depths at which the deep backscatter was found (independent of diel re-organizations). Greatest backscatter was seen at the surface throughout the record; this discussion focuses on backscatter patterns at depths greater than ~ 15 m. Three types of patterns were identified and are demonstrated using data from Mooring M2b (Figure 94). For one pattern, the bulk of the backscatter was located at depths shallower than 110 m, with a marked diel signal with migration of backscatter to the near surface during the night hours (centered at midnight) and migration back to depth (~90 m during daylight (centered at noon) (Figure 94, upper panel). Vertical redistribution of biomass occurred in association with times of sunrise and sunset. Backscatter at 82 m within each day for this pattern would have a minimum at midnight, because most backscatter was near the surface, and a maximum at noon when most backscatter was at ~90 m depth (Figure 95). In a second pattern, distinct tracks of upward and downward migrating backscatter were associated with times of sunrise and sunset but backscatter during the day at mid-depths was very low, suggesting that the migrating backscatter was located below the instrument, near the sea floor, during the day while backscatter was higher during the night (Figure 94, middle panel). In contrast to the first pattern, backscatter at 82 m within each day for these profiles would have a maximum at midnight, because backscatter was near the surface, and a minimum at noon when most backscatter was at ~90 m depth (Figure 96). The third panel (Figure 94, lower panel) showed little to no diel redistribution of backscatter. (For the week selected for demonstration, backscatter was elevated in the upper 50 m). Backscatter at 82 m for this pattern shows no consistent association of peaks with specific times of the day (Figure 97). The changing pattern of water column backscatter between the first and second patterns, with the attendant changes in the times of day at which maximum backscatter at 82 m was observed, means that the sinusoid curves that would yield low sums of squares (SS) and detect DVM should vary between the patterns, with the first peaking at noon (Figure 95) and the second peaking at midnight (Figure 96).

The daily SS thus were calculated for each record using two different reference sinusoid curves, one with a peak at noon and a second with a peak at midnight. Comparison of the two curves for the two moorings (Figure 98) shows that the two sets of SS for each mooring varied almost inversely but for both calculations, there were periods when the SS was less than ~0.15 for extended periods. This was particularly intriguing for M2b during the mid-February to mid-June period during which DVM was typical but switched in early April between the backscatter being in the mid-water column to being deeper (Note, the prominent switch in SS in mid-May resulted from spurious backscatter data rather than being real). Diel vertical migration occurred much more frequently at mooring M2b, moored at ~150 m on the slope, than at mooring M1a that was located shallower on the shelf (~35 m), as shown by the higher SSs at M1a than at M2b.

Looking at when one or the other of the SS were less than 0.15, it can be seen that DVM at Mooring 2b was prominent from the start of the deployment until early November, from late November until January, and for a protracted period from mid-February until mid-June, and then briefly in early August and finally at the end of the record. As expected, DVM was weak during the middle of the period of constant daylight (mid-June to mid-July), although DVM was present both early (mid-May to mid-June) and late (mid-late July) in the period of constant daylight. Although the sun was above the horizon during these weeks, the low elevation would have provided periods of reduced light for a portion of each 24 hour period, providing cues for DVM.

During total darkness in late November-mid-January, a diel signal was present for the first half of December, which was surprising. For mooring M1a, DVM was prominent primarily during early December (in the dark period) and during mid-February to mid-April. It is notable that backscatter at both moorings demonstrated DVM during early December, suggesting some sort of common biological response or change in backscatter populations.

The backscatter anomalies were compared to the SS for each of the moorings. For this comparison, the minimum SS of the two SS curves for each day was used to obtain a single metric of DVM for the period of the deployment (Figure 99). However, there was little correspondence between changes in the backscatter and the presence of a DVM signal.

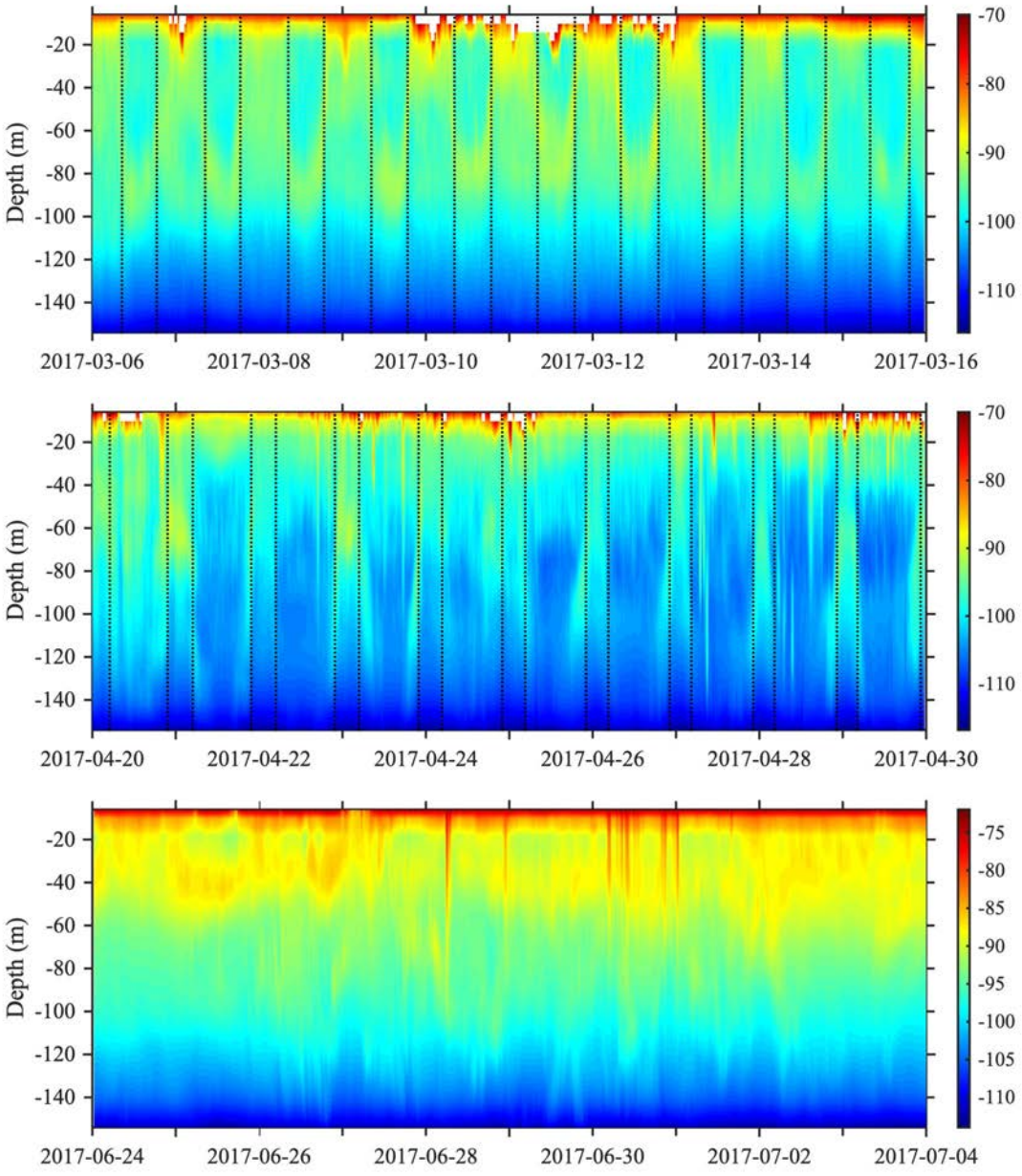

Figure 94. Ten-day periods showing three patterns of vertical distribution of backscatter at Mooring 2. Times are in local Alaskan time. Times of sunrise and sunset are shown as dashed lines in the top two panels with sunset preceding midnight and sunrise following midnight. Data in the bottom panel were collected during period of 24-hour light. Upper Panel: Diel vertical migration originating mid-water column at ~80-100 m. Middle Panel: Diel vertical migration originating below the moored instrument. Lower Panel: No vertical migration.

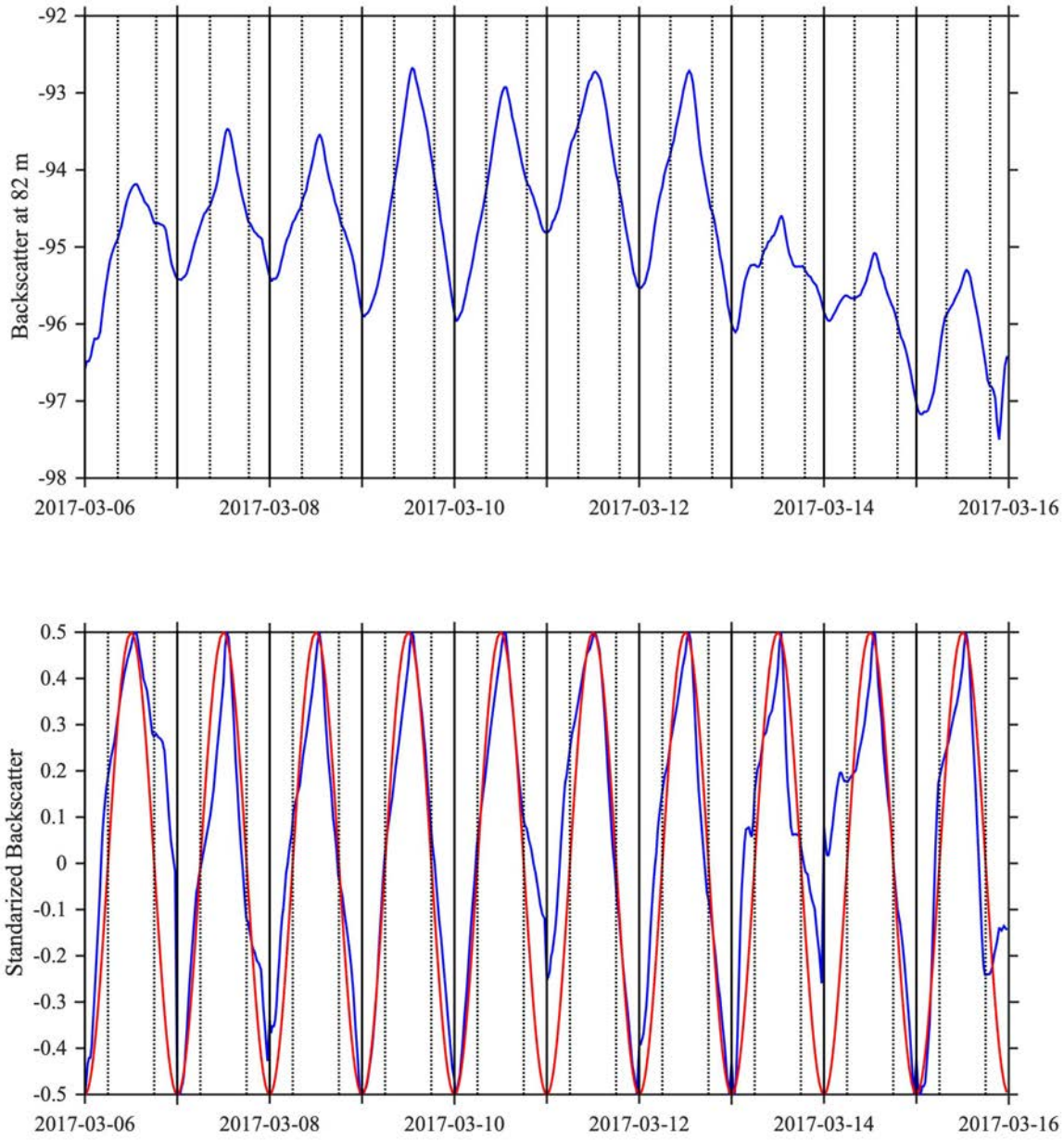

Figure 95. (Upper panel) Backscatter at 82 m from mooring M2b from March 6-16 (see Figure 13) during which time the sun was rising and setting, and diel vertical migration was occurring. Times are in local Alaskan time. Times of sunrise and sunset (dashed lines) and midnight (solid lines) are shown. (Lower panel). Backscatter (blue line) standardized to maximum (0.5) and minimum (-0.5) for each day of that period and with times set so that sunrise is at 6 AM and sunset is at 6 PM and an idealized sinusoid curve (red line) for which the greatest value occurs at noon and the least value occurs at midnight. The sums of squares between the data and the sinusoid ranged from 0.051–0.076.

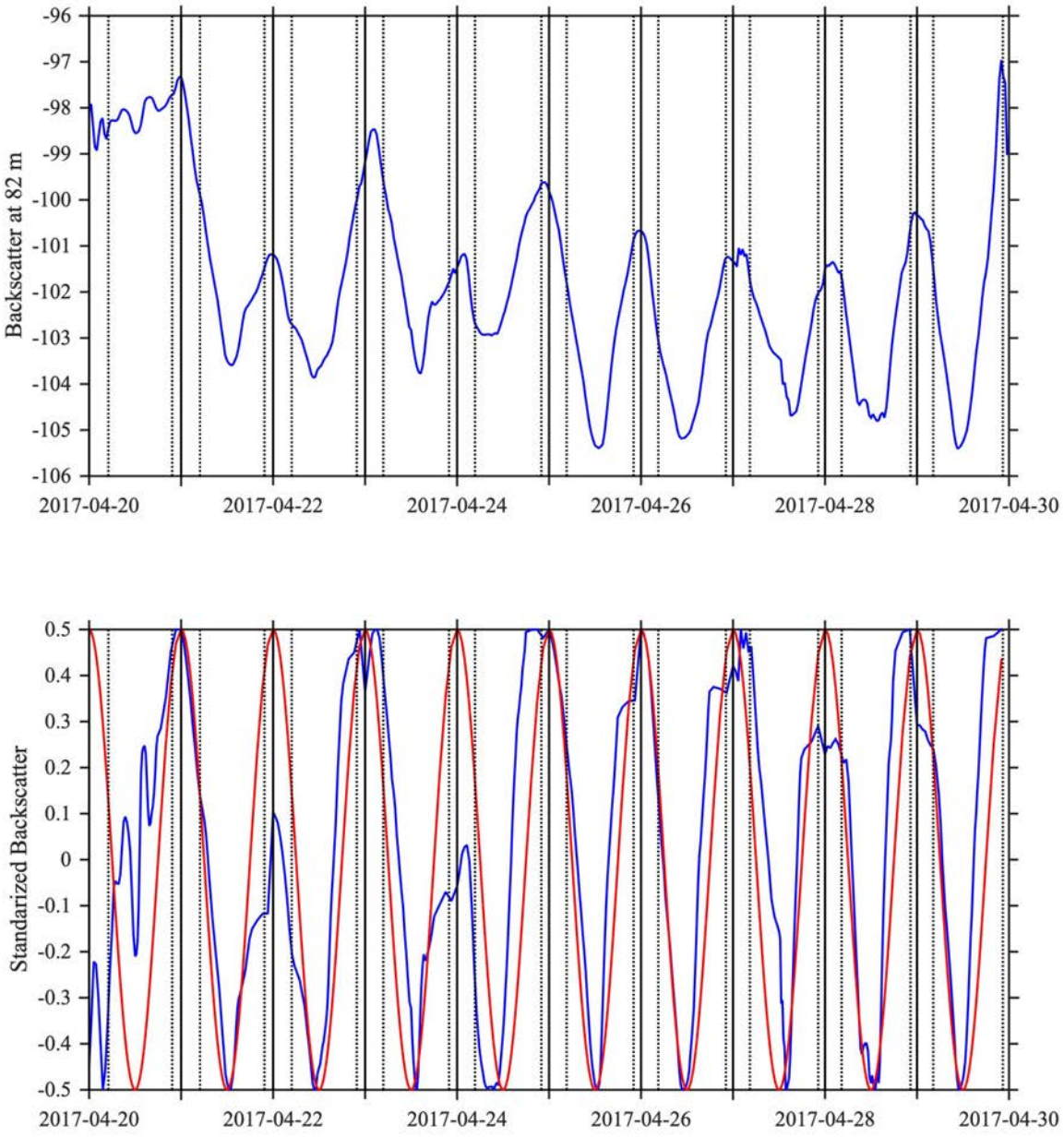

Figure 96. (Upper panel) Backscatter at 82 m from mooring M2b from May 20-29 (see Figure 13) during which time the sun was rising and setting, and diel vertical migration was occurring with the backscatter migrating upwards at night from below the instrument. Times are in local Alaskan time. Times of sunrise and sunset (dashed lines) and midnight (solid lines) are shown. (Lower panel). Backscatter (blue line) standardized to maximum (0.5) and minimum (-0.5) for each day of that period and with times set so that sunrise is at 6 AM and sunset is at 6 PM and an idealized sinusoid curve (red line) for which the greatest value occurs at noon and the least value occurs at midnight. The sums of squares between the data and the sinusoid ranged from 0.023 – 0.23.

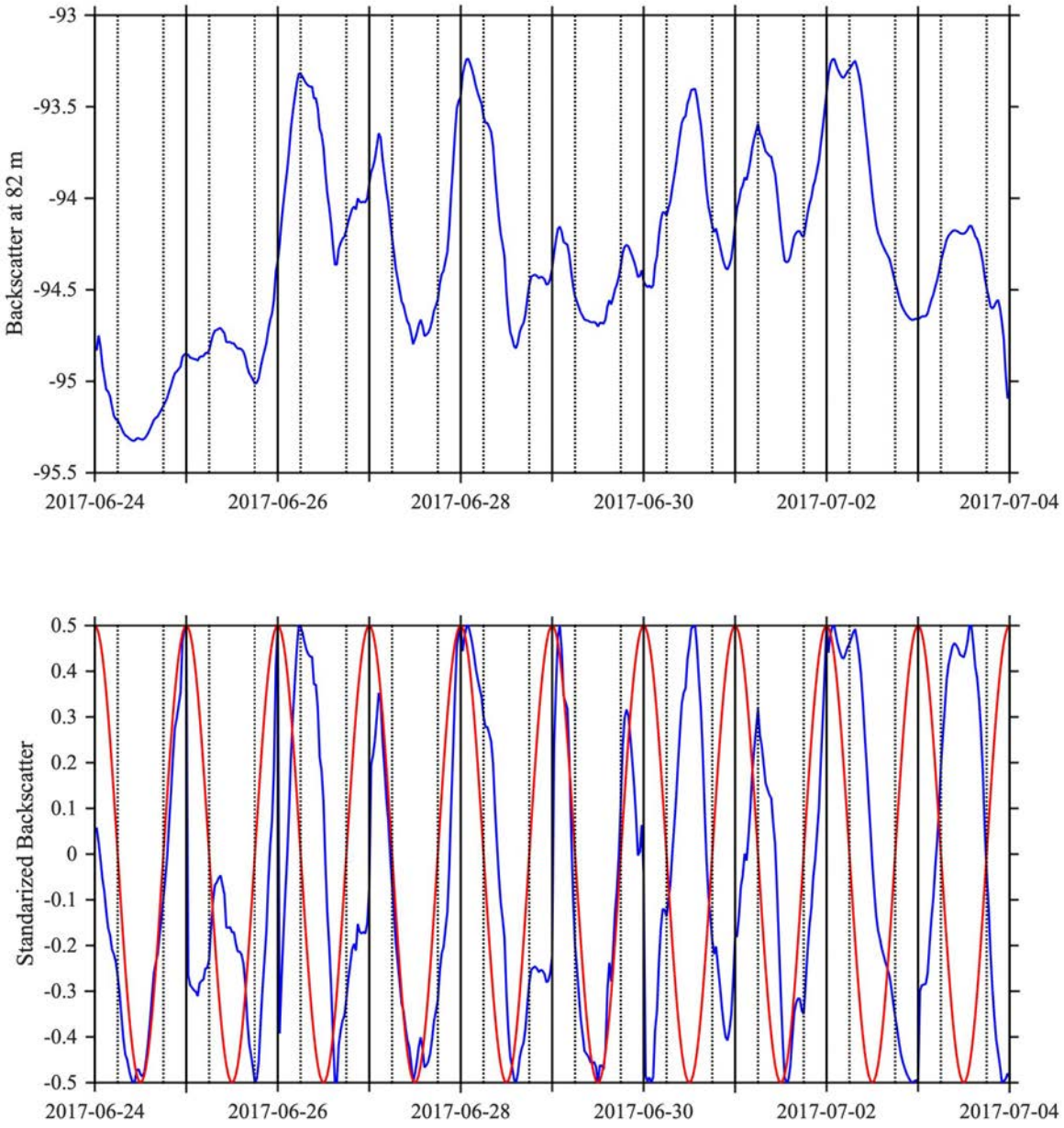

Figure 97. (Upper panel) Backscatter at 82 m from mooring M2b from June 24-July 4 (see Figure 13) during which time the sun was not setting (constant daylight) and diel vertical migration occurring only infrequently.

Times are in local Alaskan time. Times of midnight (solid lines) are shown. Dashed lines indicate 6 AM and 6 PM. (Lower panel). Backscatter (blue line) standardized to maximum (0.5) and minimum (-0.5) for each day of that period, with no modification of times of the observation since there was no sunrise or sunset and an idealized sinusoid curve (red line) for which the greatest value occurs at noon and the least value occurs at midnight. The sums of squares between the data and the sinusoid ranged from 0.013 (July 3) to 0.447 (June 27).

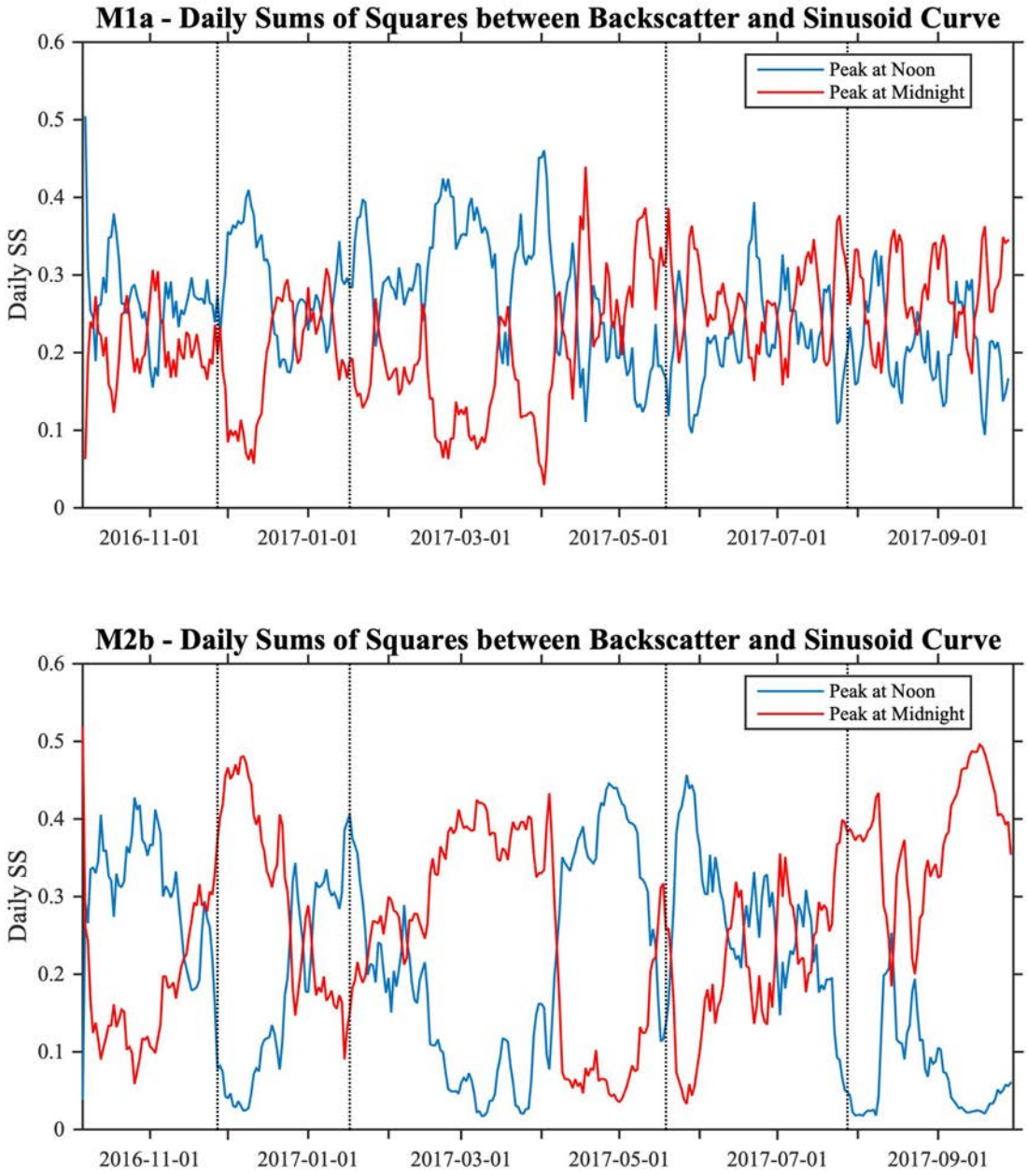

Figure 98. The daily sums of squares between standardized backscatter and sinusoid curves. Sinusoid curves with a peak at noon are those with migrating biomass originating from mid-water column while sinusoid curves with a peak at midnight are those with biomass originating below the instrument. Periods of total darkness (December–mid January) and total daylight (late May–late July) shown with dotted lines.

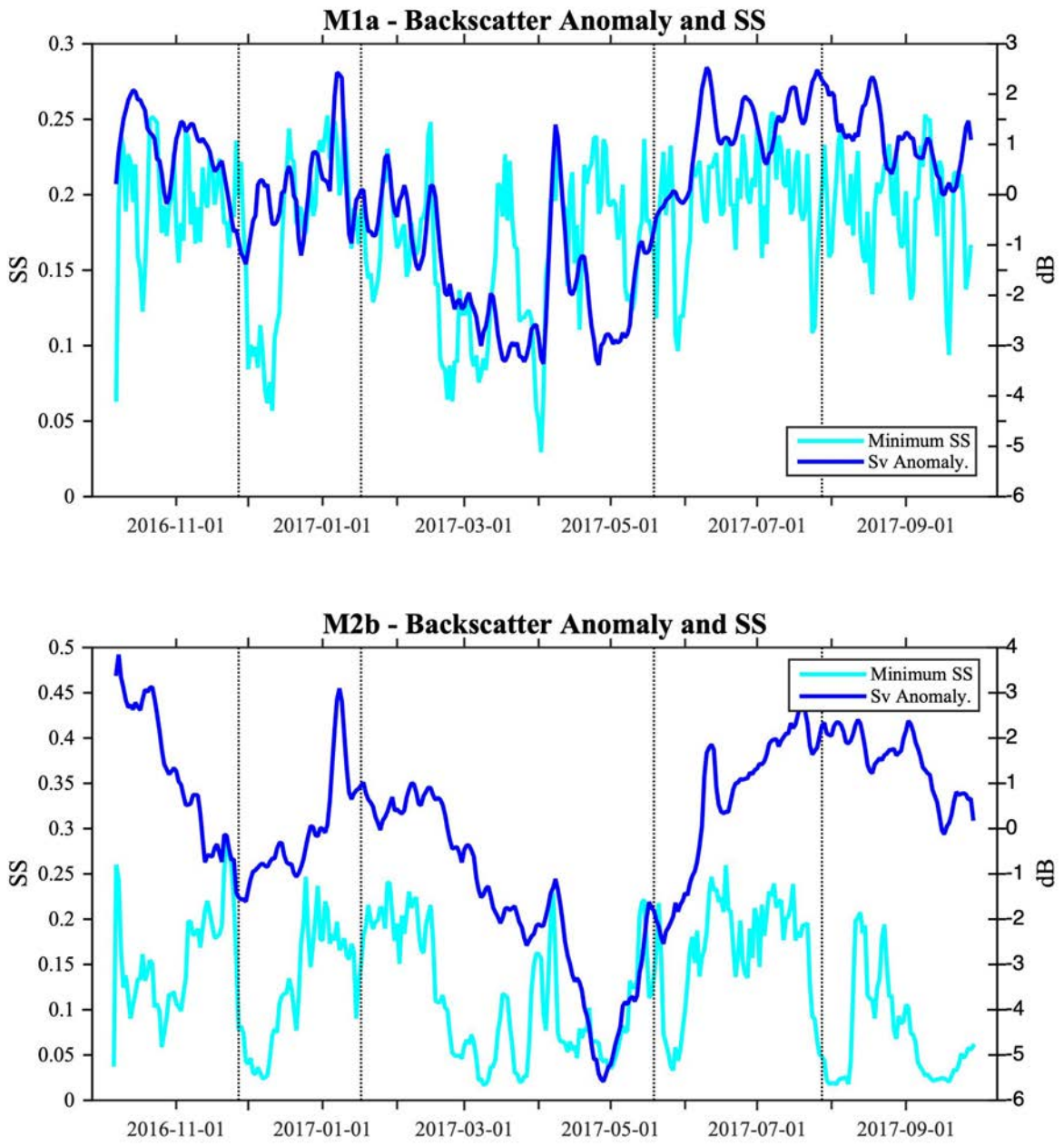

Figure 99. Combined daily sums of squares from the two curve types (see Figure 17) and the backscatter anomalies for both moorings.

All data smoothed with five-day running average. Periods of total darkness (December–mid January) and total daylight (late May–late July) shown with dotted lines. Periods with diel vertical migration have a SS less than ~0.15.

3.5 MARINE MAMMALS

Bearded seals were detected nearly year-round with the exception of summer months (July-August) while both bowhead and beluga whales were recorded from late spring through fall (Figure 100). Ringed seals were only recorded sporadically. Also detected in fall 2016 were RAFOS float signals (used to help gliders navigate or for tomography) and in the first week of September 2017, very loud pulses from seismic airguns were recorded.

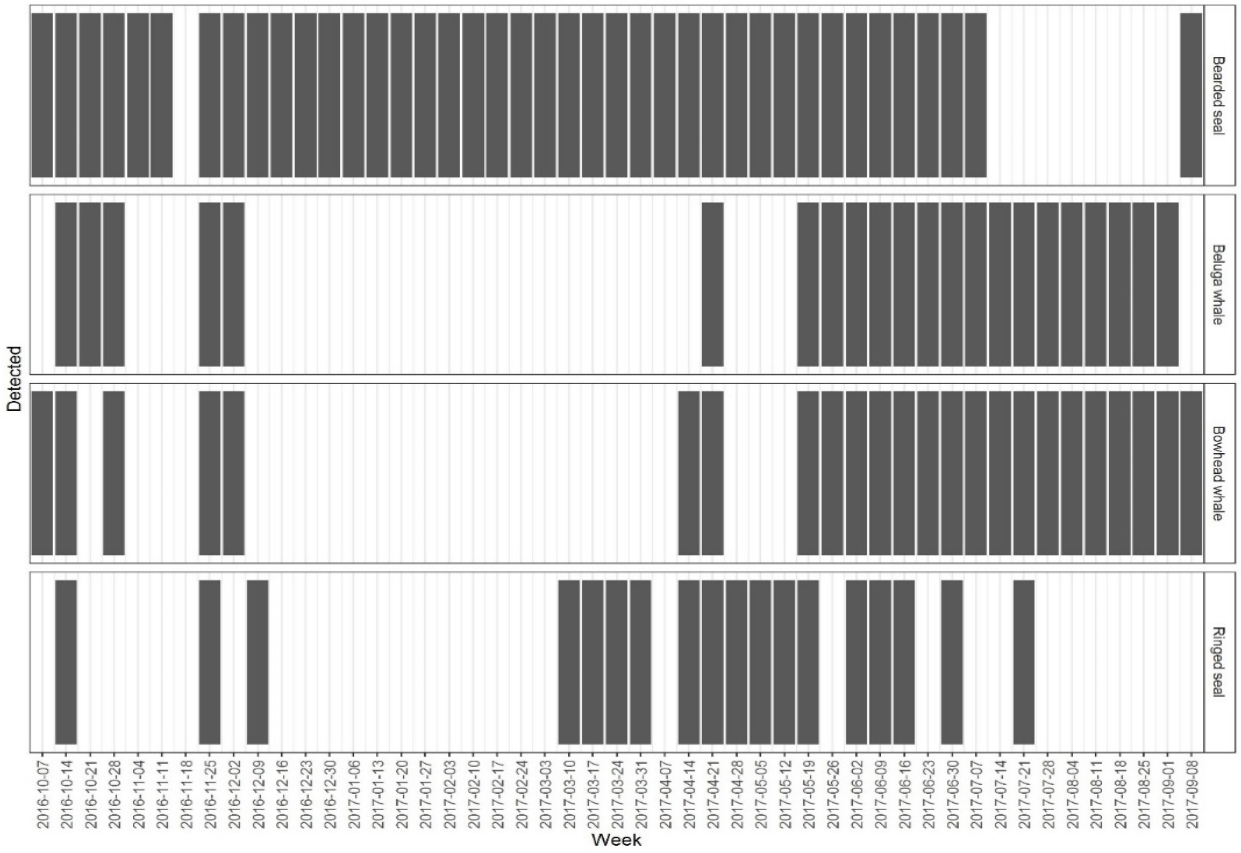

Figure 100. Marine mammal detections by week from October 2018 through September 2017.

4 DISCUSSION

4.1 PHYSICAL OCEANOGRAPHY

Figure 101 shows the cross-section of the mooring array, with the locations of the hydrographic and velocity sensors indicated. The bathymetry is from the ship's echosounder. The spatial coverage of the velocity data and temperature/salinity data are shown in right two panels. The excellent cross-stream coverage will allow construction of timeseries of vertical sections.

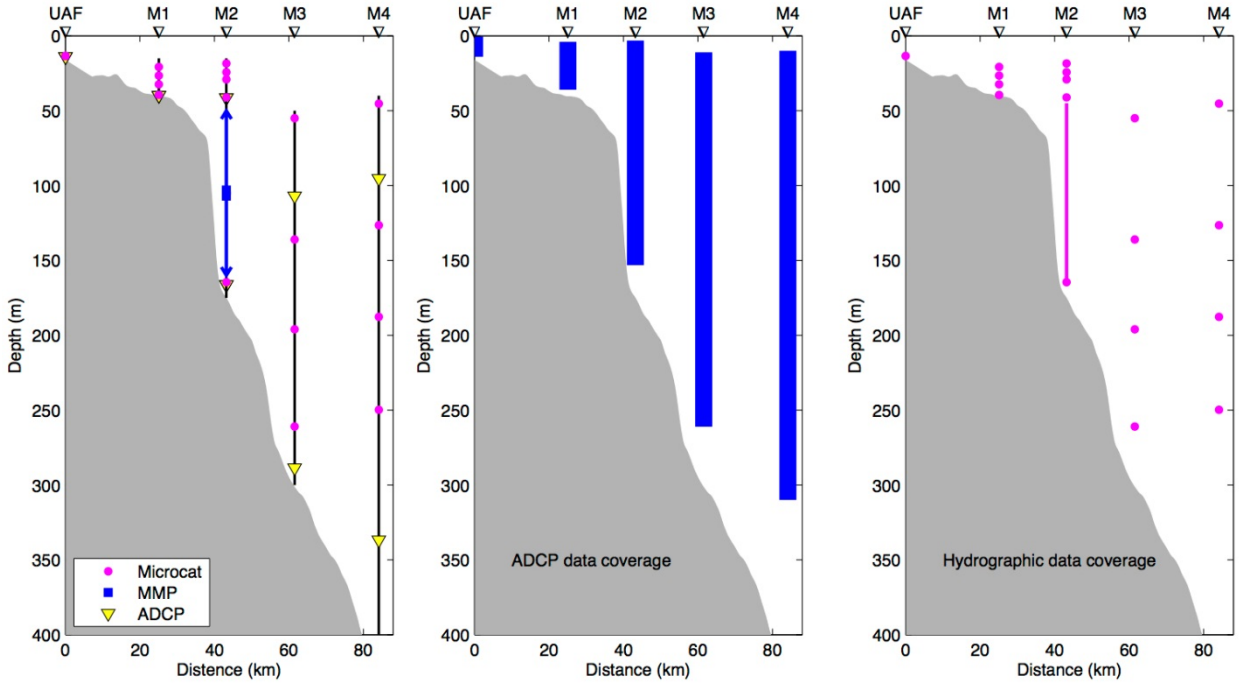

Figure 101. Cross section of the MARES mooring array.

One of the unique aspects of the MARES array was the placement of three MicroCATs above the top floats of the moorings on the outer shelf (M1) and the upper slope (M2; Figure 101). Using an inductive modem, the instruments transmitted their data to loggers on the top floats in case of damage due to ridging ice. As it turned out, only the upper-most MicroCAT on each mooring was hit. Furthermore, the instruments were not torn away. Rather, after losing their flotation, they dropped to a deeper part of the water column and continued to sample. Figure 102 shows when the MicroCAT on mooring M1 lost its flotation. It lasted through much of the ice season until the middle of March, returning valuable hydrographic data ~20 m from the sea surface.

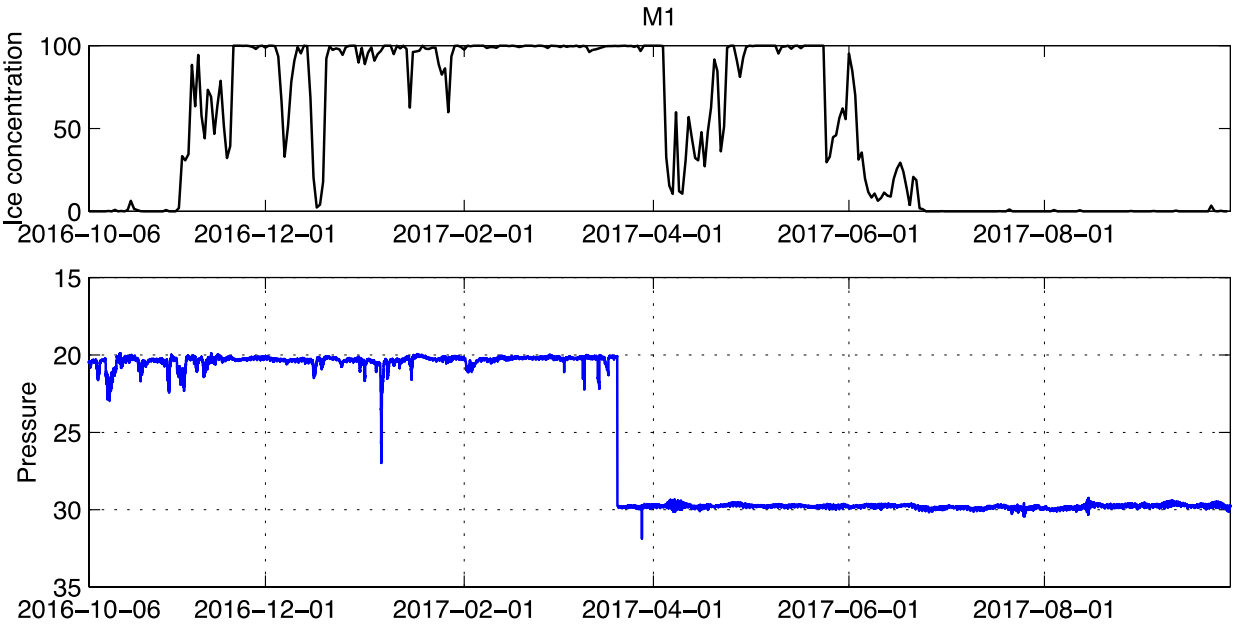

Figure 102. Depth of MicroCAT on M1 (lower panel) and the ice concentration (upper panel) during deployment.

One of the interesting findings from the array data is the presence of a subsurface, eastward-flowing shelfbreak jet. Figure 103 shows the along-isobath velocity at site M2 in relation to the ice cover. In the mean, the flow is westward in the upper 40 m and eastward in the depth range of 40–120 m. There is statistically significant variability of the flow on a variety of timescales, which, to first order, is not correlated to the ice cover. This velocity feature will be analyzed in detail and related to what we know about the circulation farther upstream in the Alaskan Beaufort Sea.

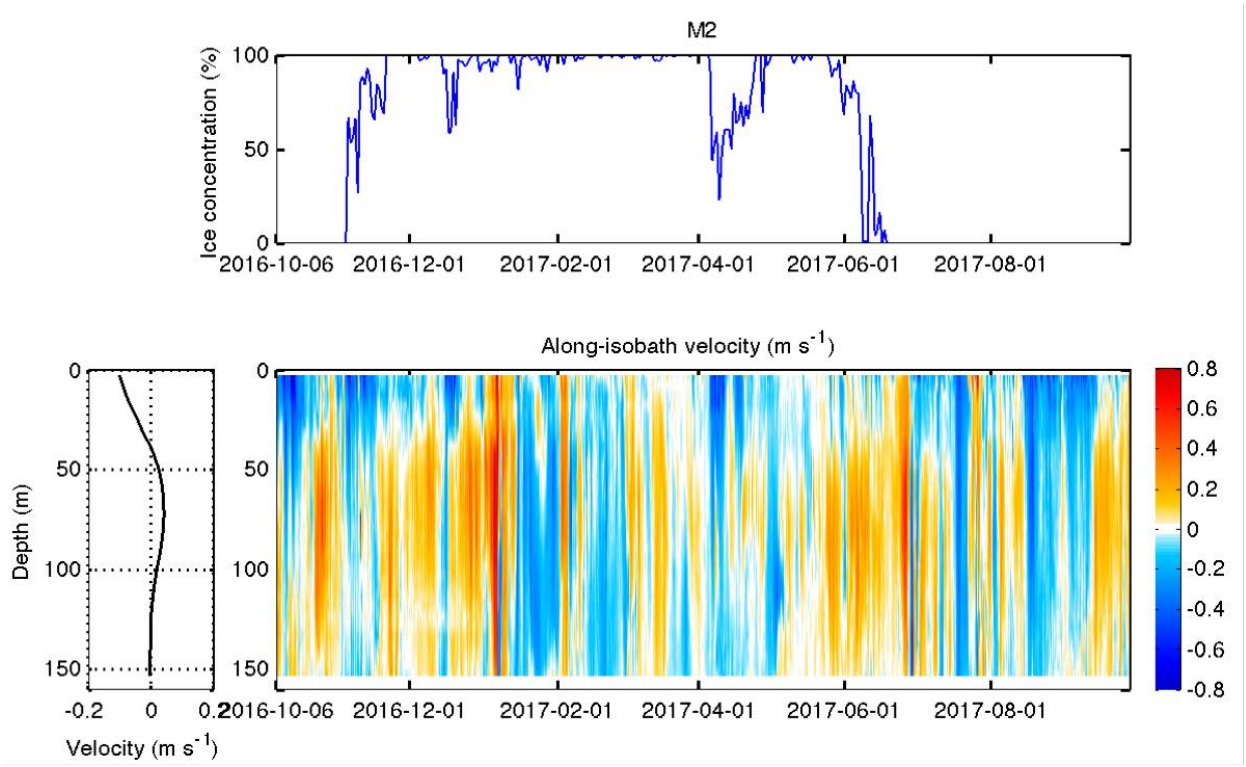

Figure 103. Along-isobath velocity at M2 (lower panel) in relation to ice concentration (upper panel).

One of the things we will focus on during future analyses is the impact of ice cover on the circulation and shelf-basin exchange. Towards this end, the ADCPs on the MARES moorings measured ice velocity in addition to water column velocity. Figure 104 shows the ice velocity at site M2 in relation to the ice concentration. Not surprisingly, ice velocities were largest during periods of reduced concentration (e.g., at the beginning of freeze-up in November, and also in April during a polynya event). However, there was also substantial ice movement when concentrations were near 100% (e.g., in January). In addition, the ice was fast at M2 for much of February and March. It will be interesting to see how the changing ice-ocean stress impacts the circulation, including upwelling and downwelling.

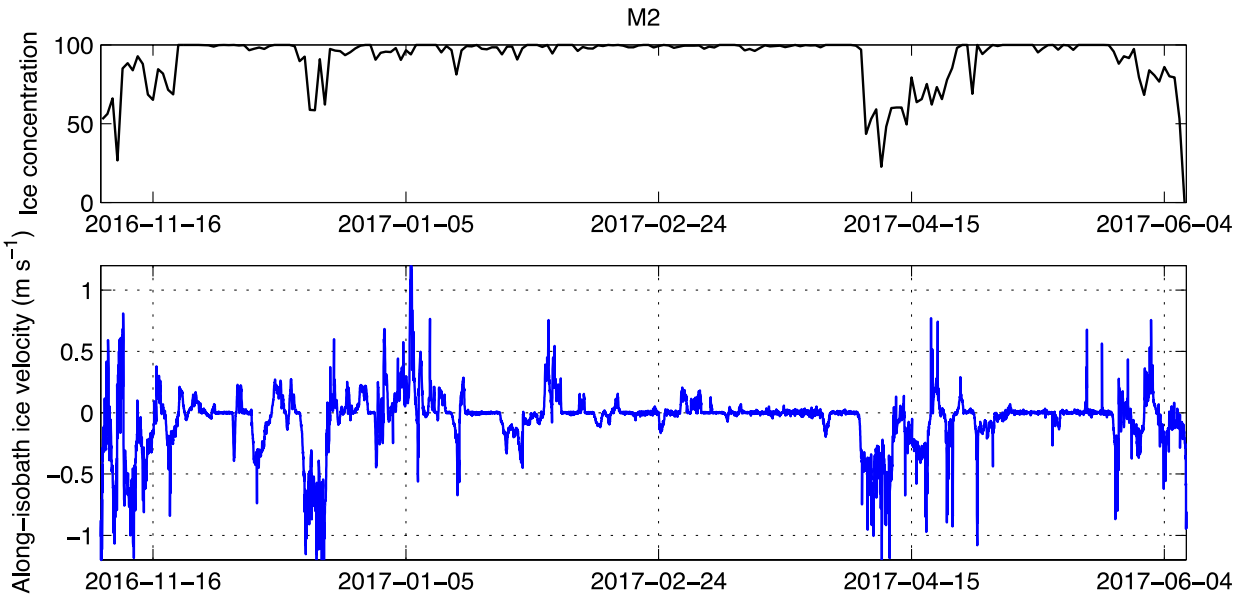

Figure 104. Along isobath ice velocity (lower panel) in relation to ice concentration (upper panel) at M2.

The MMP at mooring M2 lasted nearly the entire deployment period, returning high-resolution vertical profiles of temperature and salinity every four hours (it also measured turbidity, fluorescence, and PAR). Figure 105 shows the evolution of potential temperature (color) and potential density (contours) over the full year, in relation to the ice cover. These MMP records contain a wealth of information, including the presence of newly-ventilated winter water (colder than -1.7°C) during the period of ice cover, and substantial amounts of Atlantic Water at depth during the months of April, May, June, and October. The nature of these seasonal signals, as well as the high frequency variability, will be explored during future analyses.

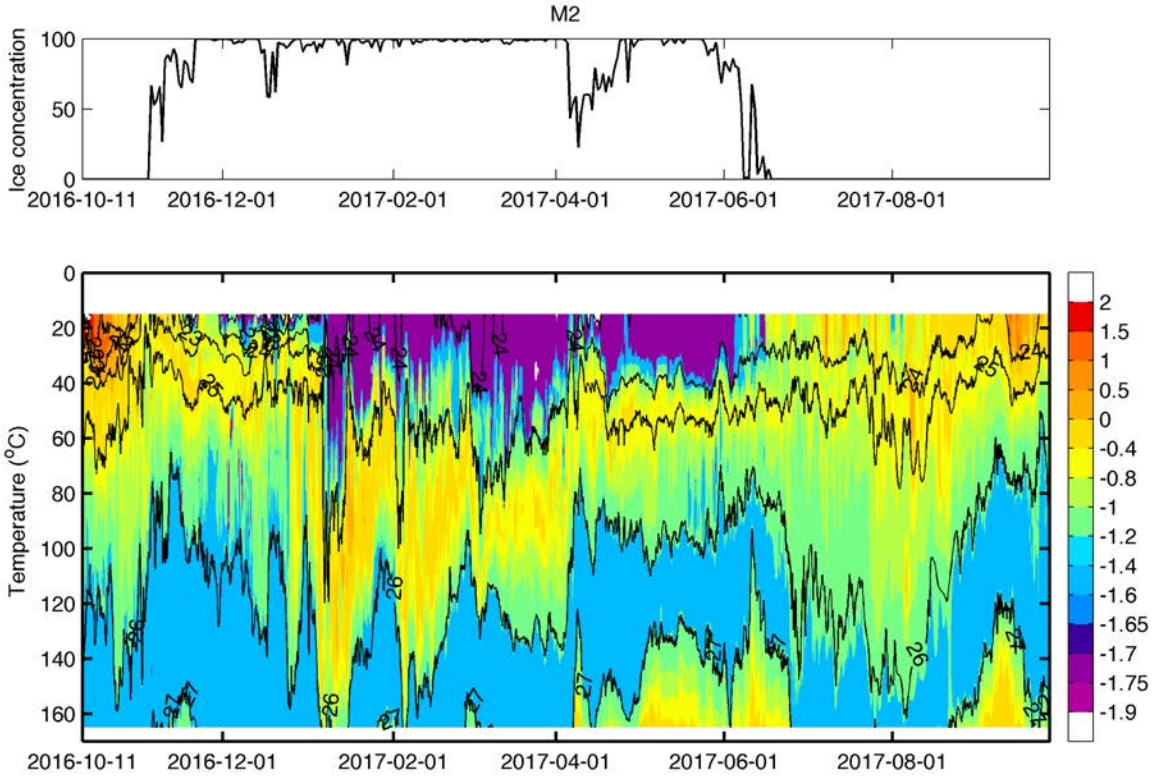

Figure 105. Temperature (lower panel) and ice concentration (upper panel) at M2.

Combining the above with some of the key results from the physical oceanography and sea ice mooring data sets across the other moorings, a few interesting characteristics jump out which will be examine further in the future:

Repeated episodes of large-scale upwelling on the shelf and slope regions on the western flank of the Mackenzie Trough were present under open water conditions. A particularly interesting episode occurred in late June 2017 and is most evident at M3 about two weeks following the breach of the landfast ice in Mackenzie Bay and Shallow Bay. Other episodes of synoptic scale upwelling are being identified and analyzed for the summer and early autumn months.

The mooring data, along with readily available satellite imagery of Mackenzie River plume water and sea ice floes, provide unprecedented information on the process of the combined ice breakup and the entry of Mackenzie River freshet discharges into Mackenzie Bay and the shelf/slope region to the west of the Mackenzie Trough. The river freshet peaked in late May of 2017 and the full study area cleared of sea ice in the first half of June. The detailed process of this clearing of the ice and the inundation of the River water in June, and the physical linkages and processes involved in this, could be quantified through the mooring based measurements of ocean currents, sea ice drafts and velocities, water properties (temperature, salinity, turbidity and other

parameters), ocean waves as well as mapped surface observations from satellites, the river discharges from gauged River channels and the measured winds.

The development of highly concentrated and thickening sea ice cover during the freeze-up period from mid-October through December was characterized by a high level of dynamic processes involving rapid heat loss from the ocean to the atmosphere, episodic winds from the east and northwest, and the resulting ice formation and drift as individual ice floes along with areas of open water and thinner ice cover. Ocean waves propagating within the ice cover were also observed thanks to the mooring-based ice sensors.

The development of highly concentrated and thicker sea ice cover from the first half of January to March 2017 led to a marked reduction in sea ice drift as internal ice stresses developed which inhibited ice motion. In April 2017, the sea ice regime changed markedly with extensive large-scale fracturing in the sea ice cover (as observed by satellite observations) and accompanying episodes of rapid ice motion (for early spring conditions) of up to 40 cm/s. This departure of the sea ice regime from the conditions in the winter months and the slower ice movements in May indicate that the ice regime was quite distinct in April 2017. The sea ice morphology and dynamics for this time-period will be further examined to provide insight into the physical processes driving this, and the nature of the sea ice in terms of its potential role as habitat for marine life.

4.2 CHEMICAL OCEANOGRAPHY AND PRIMARY PRODUCTIVITY

The SUNA instruments had issues obtaining reliable measurements at times throughout the deployment due to optically dense conditions. During these times, the absorbance and RMSe exceeded the manufacturer thresholds of 1.3 AU and 10^{-3}, respectively. To better understand whether this was an instrument error or due to oceanographic conditions we extracted the MMP data for comparison. We had predicted that such conditions would be caused by high turbidity but found that the SUNA generally functions well in turbid conditions. It appears that the problematic conditions in the latter half of the deployment were due to high fluorescence. In the oceans, the main sources of fluorescence are microscopic algae and colored dissolved organic matter.

Prior to the rise in fluorescence at the M2 site, from June 8 to 10, 2017, the nitrate concentrations were approximately 7 to 11 μM. After the initial rise in fluorescence, the nitrate concentrations had fallen to below 5 μM by July 2, 2017. This suggests that the increase in fluorescence was driven by a bloom in biological activity that collapsed after the nitrate concentrations were depleted. Prior to the bloom, there was substantial ice presence, and high turbidity levels until approximate May 25, 2017 which may have prevented the bloom from occurring earlier (Figure 106).

Before the next bloom occurs, from July 19 to 24, 2017, the nitrate concentrations rose to between 26 and 35 μM. This is flagged in the final quality controlled time-series in the data channel named AnalystFlags because it exceeds the typical concentrations for the area, and because it borders a section of data where the manufacturer thresholds for RMSe and Absorbance are exceeded (Figure 107); however, it is possible that this rise in nitrate concentrations could be real and the cause of the increase in fluorescence from July 24 to August 24, 2017. This sudden rise in

nitrate could have been caused by an influx of river water from the McKenzie delta or upwelling of nitrate rich waters from greater depths. Near the tail end of this bloom, the nitrate concentrations have once again fallen below 5 μM.

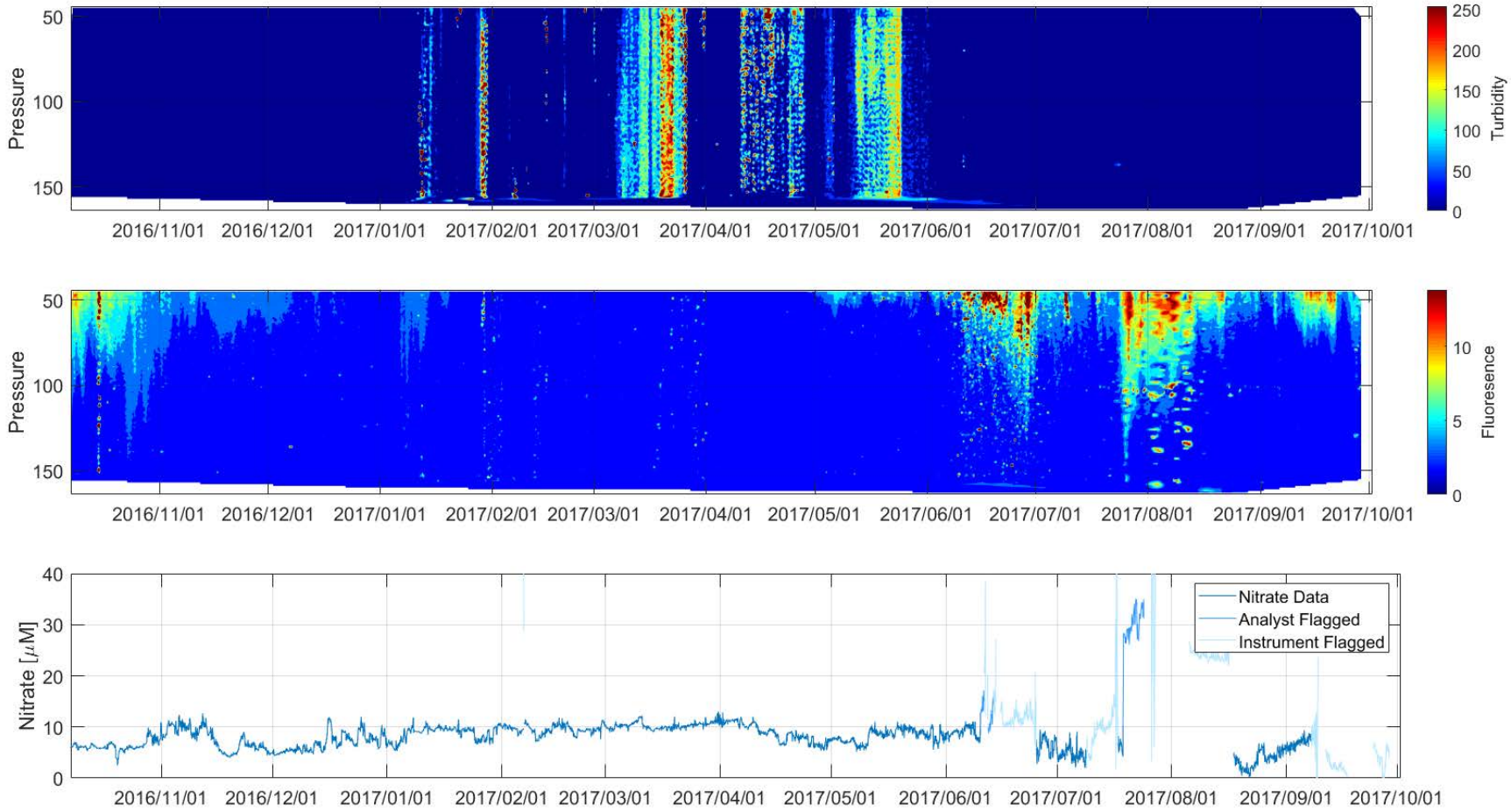

Figure 106. MMP turbidity (top) and fluorescence (middle) and SUNA nitrate concentrations (bottom) at M2.

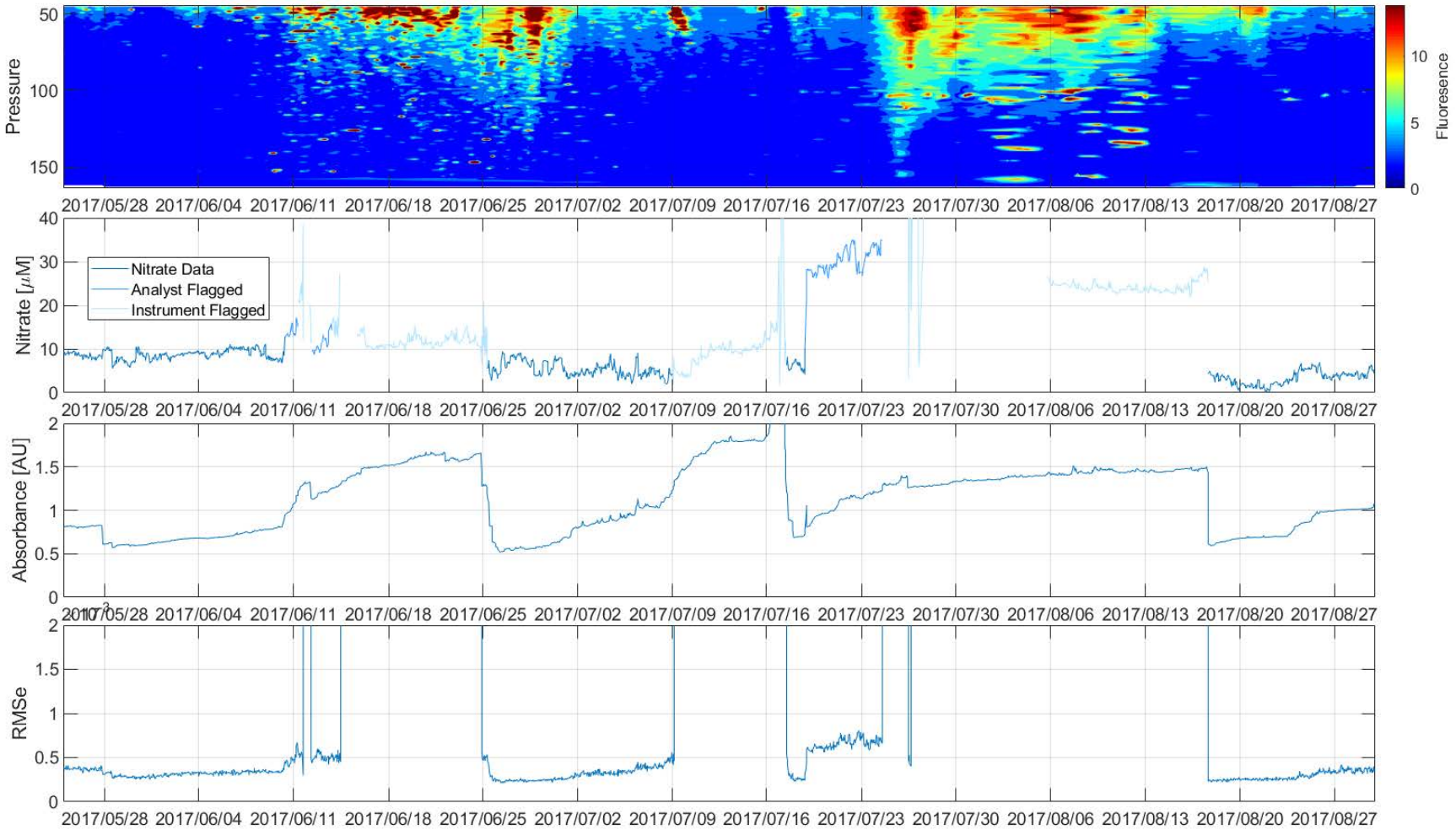

Figure 107. MMP fluorescence (top), SUNA nitrate concentration, absorbance, and instrument quality channels (bottom) at M2 for May 25 to August 30, 2017.

There was no MMP instrument on the M1 mooring so it is difficult to draw any conclusions between the nitrate concentrations at this site with productivity in the area; however, if the instrument is affected by turbidity and fluorescence in the same way as at M2 it would suggest similar driving conditions. In other words, we might expect that there were periodic blooms of high fluorescence or CDOM from the time the instrument was deployed in October 2016 through to early April 2017. The absorbance and RMSe sporadically exceeded manufacturer thresholds between October 2016 and April 2017.

4.3 ZOOPLANKTON AND FISH

Using analysis of acoustic backscatter and identification of target taking a multi frequency approach we were able to discern patterns of distribution of zooplankton and larval and adult arctic cod. The bulk of adult cod abundance at mooring M3 occurred below 200 m between October and March, with peak abundance observed in December. Juvenile cod were present near the surface from July to October (absent from the surface layer between November and June) which complements adult abundances seen October to March; this potentially represents and ontogenic shift from larval to adult cod. Juveniles were seen mainly in the upper 40 m.

Copepods were found in relatively high abundance high in the water column from June to February, and at lower abundance high in the water column March to May. Copepods were at least partly responsible for the daily vertical migration patterns which were observed throughout the year.

Most patterns investigated to date were derived from observations across the year. There are potential additional patters to be explored across smaller temporal and spatial scales as may be suggested by certain oceanographic events observed with the other co-tethered sensors. Such patterns and relationships will be explored in future analyses. In addition, we display one year of data and there may be year to year variation observed which might emerge once we also examine data from the 2017-2018 deployment. In sum we have detected what appear to be meaningful patterns in the movement and relative abundance of zooplankton and fish, two critical ecosystem components. The synoptic analysis to follow will serve to inform the patterns seen here and likely provide considerable insight into biological patterns and their physical and chemical drivers in the eastern Beaufort Sea.

4.4 MARINE MAMMALS

Detections of whales were limited to bowhead whales and beluga whales, with both species detected from late spring through fall. The bowhead whale detections may be reflecting migration into the area for summer feeding (e.g., Moore and Laidre 2006). The beluga whale detections could be of either the Eastern Beaufort Sea or Eastern Chukchi Sea populations, as both have been recorded to utilize the region in summer (Hauser et al. 2014).

Bearded seals were detected nearly year-round, with the exception of July and August. A similar trend of decreased calling activity in July-August has been observed in the western Beaufort Sea (MacIntyre et al. 2013, Jones et al. 2014). Ringed seal detections occurred primarily

from mid-March to the end of July, and some detections sporadically recorded from October to December. The sporadic detections of ringed seals, and no calls occurring during summer months has also observed in the western Beaufort Sea (Jones et al. 2014).

5 CONCLUSIONS

General Program

- The 2016-2017 mooring program was successful. The equipment and data recovery rate was very high.
- Upper-most MicroCAT on each mooring (which was partially experimental) remained intact through the ice season providing unique and valuable hydrographic data ~20 m from the sea surface.
- All field operations were conducted safely with no incidents or accidents.

Preliminary Analyses

- The preliminary analysis performed to date suggest that the physical oceanographic processes that were expected to be present in the study area were in fact observed and can be further characterized explored in future more in-depth analyses.
- The excellent cross-stream coverage of the mooring array will allow construction of timeseries of vertical sections.
- Flow was westward in the upper 40 m and there was a subsurface, eastward-flowing shelfbreak jet in the depth range of 40–120 m.
- Ice velocities were largest during periods of reduced concentration (e.g. at the beginning of freeze-up in November, and also in April during a polynya event). However, there was also substantial ice movement when concentrations were near 100% (e.g. in January). In addition, the ice was fast at this mooring site for much of February and March.
- There were clear indications of phytoplankton blooms in spring and fall with associated drawdowns of nutrients and possible relationships with the Mackenzie plume.
- Copepods were found in relatively high abundance high in the water column from June to February, and contributed to the daily vertical migration patterns which were observed throughout the year.
- There was substantial variation in acoustic backscatter between M1 and M2 throughout the year, with greatest backscatter near the surface, for M1 and M2, with lower scattering at mid-depth and lowest backscatter at depth.
- Backscatter at M2 was substantially greater than that seen at M1.

- Some maxima or minima in backscatter at M1 were positively associated with peaks in salinity or temperature.
- The long period of low backscatter seen in April-June at M2 was associated with warmer, more saline water while the elevated backscatter seen immediately afterwards in June-September was associated with lower salinity and colder water.
- Juvenile arctic cod were present near the surface from July to October.
- Adult arctic cod abundance was observed mostly below 200 m between October and March, with peak abundance observed in December.
- Bearded seals were detected nearly year-round with the exception of summer months (July-August), while both bowhead and beluga whales were recorded from late spring through fall (Figure 100). Ringed seals were only recorded sporadically.

Lessons Learned

- The deployment configuration of sensors on the 2017-2018 moorings was refined based on lessons learned through examination of the measurement data collected during 2016-2017. It was found that the LongRanger ADCPs in wideband mode led to considerable fading of target strengths later in the deployment leading to configuration of future sensors using the ADCP narrowband mode. The IPS and SUNA sampling plans were revised to reduce the estimated power draw.
- SAMI-CO2 at M1 had a possible malfunction after April 5, 2017 when one of the top sensors was knocked off during a polynya event. The calculated pCO_2 at M1 and M2 from the discrete sample did not validate the in situ pCO_2 and should be considered with caution until the second year of data are available.

6 REFERENCES

Archive Search. 2017. Government of Canada, Canadian Ice Service; [accessed 23 October 2017]. http://iceweb1.cis.ec.gc.ca/Archive.

Ashjian, CJ, Smith SL, Flagg CN, Wilson C. 1998. Patterns and occurrence of diel vertical migration of zooplankton in the Mid-Atlantic Bight measured by the acoustic Doppler current profiler. Continental Shelf Research 18: 831-858.

Ashjian, CJ, Smith SL, Flagg CN, Idrisi N. 2002. Distribution, annual cycle, and vertical migration of acoustically derived biomass across a 900 km transect in the Arabian Sea during 1994-1995. Deep-Sea Research II, 49: 2377-2402.

ASL Environmental Sciences Inc. 2017. Ice Profiler Processing Toolbox User's Guide. Report by ASL Environmental Sciences Inc., Victoria, BC, Canada. xii + 107 p.

Balzano S, Marie D, Gourvil P, Vaulot D. 2012. Composition of the summer photosynthetic pico and nanoplankton communities in the Beaufort Sea assessed by T-RFLP and sequences of the 18S rRNA gene from flow cytometry sorted samples. ISME J. 6(8): 1480-1498. doi: 10.1038/ismej.2011.213.

Benoit D, Simard Y, Fortier L. 2008. Hydroacoustic detection of large winter aggregations of Arctic cod (*Boreogadus saida*) at depth in ice-covered Franklin Bay (Beaufort Sea). Journal of Geophysical Research 113, C06S90, doi:10.1029/2007JC004276.

Benoit D, Simard Y, Fortier L. 2013. Pre-winter distribution and habitat characteristics of polar cod (*Boreogadus saida*) in southeastern Beaufort Sea. Polar Biology DOI 10.1007/s00300-013-1419-0.

Deines K. 1999. Backscatter Estimation Using Broadband Acoustic Doppler Current Profilers. In: Proc. Sixth Working Conf. on Current Measurement, San Diego, CA. IEEE, 249-253.

DeRobertis A, Higginbottom I. 2007. A post-processing technique to estimate the signal-to-noise ratio and remove echosounder background noise. ICES Journal of Marine Science 64: 1282–1291.

Dickson AG, Sabine CL, Christian JR. (Eds.) 2007. Guide to Best Practices for Ocean CO2 Measurements. PICES Special Publication 3, 101 pp.

Emmerton C, Lesack L, Vincent W. 2008. Mackenzie River nutrient delivery to the Arctic Ocean and effects of the Mackenzie Delta during open water conditions. Global Biogeochem. Cycles. 22(GB1024). doi: 10.1029/2006GB002856.

Evans W, Mathis JT, Cross JN, Bates NR, Frey KE, Else BGT, Papkyriakou TN, DeGrandpre MD, Islam F, Cai W, Chen B, Yamamoto-Kawai M, Carmack E, Williams WJ, Takahashi T. 2015.

Sea-air CO2 exchange in the western Arctic coastal ocean, Global Biogeochem. Cycles 29: doi:10.1002/2015GB005153.

Fellman, J, D'Arnore D, Hood E. 2009. An evaluation of freezing as a preservation technique for analyzing dissolved organic C, N and P in surface water samples. Science of the Total Environment. 392(2-3): 305-312. doi: 10.1016/j.scitotenv.2007.11.027.

Fissel D, Marko J, Melling H. 2008. Advances in upward looking sonar technology for studying the processes of change in Arctic Ocean ice climate. Journal of Operational Oceanography. 1(1): 9-18. doi: 10.1080/1755876X.2008.11081884.

Hauser DDW, Laidre KL, Suydam RS, Richard PR. 2014. Population-specific home ranges and migration timing of Pacific Arctic beluga whales (*Delphinapterus leucas*). Polar Biology 37(8): 1171-1183.

Hourly Data Report for September 01, 2016 - Climate - Environment and Climate Change Canada. 2017. Government of Canada; [accessed 23 October 2017]. http://climate.weather.gc.ca/climate_data/hourly_data_e.html?StationID=1560.

Jones JM, Thayre BJ, Roth EH, Mahoney M, Sia I, Merculief K, Jackson C, Zeller C, Clare M, Bacon A, Weaver S, Gentes Z, Small RJ, Stirling I, Wiggins SM, Hildebrand JA. 2014. Ringed, bearded, and ribbon seal vocalizations north of Barrow, Alaska: Seasonal presence and relationships with sea ice. Arctic 67(2): 203-222.

Korneliuss RJ, Ona E. 2002. An operational system for processing and visualizing multi-frequency acoustic data. ICES Journal of Marine Science 59: 293–313.

Kitamura M, Amakasu K, Kikuchi T, Nishino S. 2017. Seasonal dynamics of zooplankton in the southern Chukchi Sea revealed from acoustic backscattering strength. Continental Shelf Research 133: 47–58.

MacDonald R, McLaughlin F. 1982. The effect of storage by freezing on dissolved inorganic phosphate, nitrate and reactive silicate for samples from coastal and estuarine waters. Water Research 16(1):95-104. doi: 10.1016/0043-1354(82)90058-6.

MacIntyre KQ, Stafford KM, Berchok CL, Boveng PL. 2013. Year-round acoustic detection of bearded seals (*Erignathus barbatus*) in the Beaufort Sea relative to changing environmental conditions, 2008-2010. Polar Biology 36(8): 1161-1173.

Mathis JT, Cross JN, Bates NR. 2011. Coupling primary production and terrestrial runoff to ocean acidification and carbonate mineral suppression in the eastern Bering Sea, J. Geophys. Res., 116: C02030, doi:10.1029/2010JC006453.

Melling H, Johnston P, Riedel D. 1995. Measurements of the underside topography of sea ice by moored subsea sonar. J. Atmospheric and Oceanic Technology. 13(3): 589-602. doi: 10.1175/1520-0426(1995)012<0589:MOTUTO>2.0.CO;2.

Moore SE, Laidre, KL. 2006. Trends in sea ice cover within habitats used by bowhead whales in the Western Arctic. Ecological Applications 16(3): 932-944.

Mullison J. 2017. Backscatter Estimation Using Broadband Acoustic Doppler Current Profilers – Updated. Presented at ASCE Hydraulic Measurements & Experimental Methods Conference, Durham, NH.

Mudge T, Borg K, Slonimer A. 2018. Spectral Analysis of Sea Ice Draft from Sonars. Poster session presented at: 2018 AMSS. Proceedings of the 2018 Alaska Marine Science Symposium; Anchorage, AK.

NASA Worldview. 2017. NASA/Goddard Space Flight Center Earth Science Data and Information System; [accessed October 2017 through September 2018]. https://worldview.earthdata.nasa.gov/.

Parker-Stetter SL, Horne JK, Weingartner TJ. 2011. Distribution of polar cod and age-0 fish in the U.S. Beaufort Sea. Polar Biology 34: 1543-1557.

Robbins LL, Hansen ME, Kleypas JA, Meylan SC. 2010. CO2calc- a user-friendly seawater carbon calculator for Windows, Mac OS X, and iOS (iPhone). US Geological Survey Open-File Report, 2010–1280, 17 pp. Available at https://pubs.usgs.gov/of/2010/1280/.

Ryan TE, Downie RA, Kloser RJ, Keith G. 2015. Reducing bias due to noise and attenuation in open-ocean echo integration data. ICES Journal of Marine Science doi:10.1093/icesjms/fsv121.

Simpson K, Tremblay J, Gratton Y, Price N. 2008. An annual study of inorganic and organic nitrogen and phosphorus and silicic acid in the southeastern Beaufort Sea. J. of Geophysical Research. 113(C7): doi: 10.1029/2007JC004462.

Strickland J, Parsons R. 1960. A manual of sea water analysis. Bulletin No. 125. Nanaimo, BC, Canada: Fisheries Research Board of Canada, Pacific Oceanography Group. 192 pages.

Wiese FK, Harvey HR, McMahon R, Neubert P, Gong D, Wang H, Hudson J, Pickard R, Ross E, Fabijan M, Gryba RD. 2018. Marine Arctic Ecosystem Study—Biophysical and chemical observations from glider and benthic surveys in 2016. Anchorage (AK): US Department of the Interior, Bureau of Ocean Energy Management. OCS Study BOEM 2018-024. 98 p. https://www.boem.gov/BOEM-2018-024/

Department of the Interior (DOI)

The Department of the Interior protects and manages the Nation's natural resources and cultural heritage; provides scientific and other information about those resources; and honors the Nation’s trust responsibilities or special commitments to American Indians, Alaska Natives, and affiliated island communities.

BOEM
Bureau of Ocean Energy Management

Bureau of Ocean Energy Management (BOEM)

The mission of the Bureau of Ocean Energy Management is to manage development of U.S. Outer Continental Shelf energy and mineral resources in an environmentally and economically responsible way.

BOEM Environmental Studies Program

The mission of the Environmental Studies Program is to provide the information needed to predict, assess, and manage impacts from offshore energy and marine mineral exploration, development, and production activities on human, marine, and coastal environments. The proposal, selection, research, review, collaboration, production, and dissemination of each of BOEM’s Environmental Studies follows the DOI Code of Scientific and Scholarly Conduct, in support of a culture of scientific and professional integrity, as set out in the DOI Departmental Manual (305 DM 3).